

# **Dual-functional carbon–based Interlayers towards high-performance Li-S batteries**

**Ruwei Yi**

**2020/08**

A DISSERTATION SUBMITTED TO THE DEPARTMENT OF CHEMISTRY AND  
THE COMMITTEE ON GRADUATE STUDIES OF UNIVERSITY OF LIVERPOOL  
IN PARTIAL FULFILLMENT OF THE REQUIREMENTS FOR THE DEGREE OF  
DOCTOR OF PHILOSOPHY

## Abstract

For reducing carbon emission and alleviating pollution, people are gradually replacing the fossil fuel-employing combustion engines with new energy devices. The secondary batteries with high energy storage have become a hot alternative to power sources due to its zero emission during their operation. In recent years, as the most popular energy storage equipment in the battery market for mobile devices, lithium-ion battery is gradually showing a decline in the field of power battery, because its energy density ( $\sim 150 \text{ Wh kg}^{-1}$ ) has been unable to meet the demands of power equipment, and the current research has almost reached the theoretical capacity of lithium-ion battery electrode materials, and leaves little space for improvement. Therefore, academic research began to seek a variety of new battery systems to meet the needs of the industry. As a battery system based on the non-topological reaction between lithium anode and sulfur anode, lithium sulfur battery has a very high theoretical energy density ( $2567 \text{ Wh kg}^{-1}$ ) and theoretical specific capacity ( $1672 \text{ mAh g}^{-1}$ ), which is good enough to meet the energy density requirements ( $500\text{-}600 \text{ Wh kg}^{-1}$ ) of power battery. Meanwhile, sulfur is of low cost and environmentally friendly, which is suitable for large-scale commercialization. Therefore, it is considered as a strong competitor of the next generation power supply. However, a series of shortcomings of lithium sulfur battery limit its large-scale application at present stage; for examples, the sluggish reaction kinetics of active sulfur and the degraded cyclic stability from shuttle effect. The improvement of both can ameliorate the rate performance and cycle stability of lithium sulfur battery, which are crucial to the practical application of power battery.

In this thesis, in order to solve the above problems, the author first used a facile and scalable method to prepare carbon black/ PEDOT:PSS. The modified separator was applied to lithium sulfur battery as an improved interlayer of the cathode. The principle of improving sulfur cathode by the interlayer was studied by the electrochemical analysis. The high conductivity and polysulfide adsorption ability of the coating delivers an initial specific capacity of  $1315 \text{ mAh g}^{-1}$  at  $0.2 \text{ C}$  current, and  $699 \text{ mAh g}^{-1}$  at a high rate of  $2 \text{ C}$  current; secondly, for the purpose of reducing the density of the cathode interlayer, a three-dimensional graphene foam was chosen as the conductive substrate of the interlayer, and modified with the zinc oxide by atomic layer deposition (ALD), creating the self-standing three-dimensional graphene foam / nano zinc oxide interlayer. This interlayer leads to an initial specific capacity of  $1051 \text{ mAh g}^{-1}$  at

a 0.5 C rate. Its low area density ( $0.15 \text{ mg cm}^{-2}$ ) also reduces the influence on the energy density of the cathode. As a step forward, the two-dimensional  $\text{Ti}_3\text{C}_2\text{T}_x$  nanosheet (MXene) with high conductivity and polysulfide adsorption characteristics was selected as an alternative material of zinc oxide to modify the graphene foam (GFMX), which simplifies the synthesis process and enhances the electronic conductivity of the interlayer. After 120 cycles at 0.2 C, the lithium sulfur batteries still maintain a specific capacity of  $867 \text{ mAh g}^{-1}$  and  $755 \text{ mAh g}^{-1}$  at 2 C high rate current with the GFMX interlayer. In light of the significant improvement of the interlayer by MXene, the modified the MXene by an in-situ growth of nitrogen and nickel doped carbon nanosheets has been studied. Results show that the stacking of MXene is greatly reduced and the specific surface area of the material is increased, moreover, the adsorption capacity of polysulfides has been largely improved by the nitrogen doping. When using the obtained composite material as the separator coating, the lithium sulfur batteries exhibit  $943 \text{ mAh g}^{-1}$  specific capacity after 100 cycles at 0.2 C current, and  $588 \text{ mAh g}^{-1}$  specific capacity after 500 cycles at 1 C. The average cycle capacity decay rate is 0.069%, and the specific capacity of the high sulfur loading cathode ( $3.8 \text{ mg cm}^{-2}$ ) is  $946 \text{ mAh g}^{-1}$ , highlighting its potential applications in the high-performance lithium sulfur batteries.

# 摘要

出于对减少碳排放, 缓解环境污染的考虑, 近年来人们开始逐渐使用新能源设备来替代采用化石能源的内燃机设备, 而具有高储能的二次电池由于在使用过程中的零排放, 成为了倍受瞩目的动力能源替代方案。作为近年来在移动设备的电池市场上最受欢迎的储能设备, 锂离子电池在动力电池领域逐渐显现颓势, 因为其能量密度 ( $\sim 150 \text{ Whkg}^{-1}$ ) 已经无法满足动力设备的需求, 而目前的研究也已逐渐逼近锂离子电池的电极材料理论容量, 难以再有明显提升。因此学术研究开始寻求各种新的电池体系来满足业界需求。锂硫电池作为建立在金属锂负极和硫正极的非拓扑反应上的电池体系, 具有极高的理论能量密度 ( $2567 \text{ Whkg}^{-1}$ ) 和理论比容量 ( $1672 \text{ mAhg}^{-1}$ ), 足以满足动力电池的能量密度要求 ( $500\text{--}600 \text{ Whkg}^{-1}$ ), 同时硫具有价格低廉、环境友好的特点, 更适宜大规模的商业化的需求, 被认为是下一代动力电源的有力竞争者。然而锂硫电池中的一系列缺点限制了其目前阶段在规模化应用上的推广; 其中在正极方面, 最关键挑战包括对活性物质硫的反应动力学的提高和对穿梭效应的抑制。这两者的改善能够提高锂硫电池的倍率性能与循环稳定性, 而这些都对动力电池表现至关重要。

在本论文中, 为解决以上问题, 作者首先使用了一种简便且可规模化的方法制备了碳黑/PEDOT:PSS 涂层修饰的电池隔膜, 并应用于锂硫电池中作为正极改良的中间层, 同时从电化学分析角度解释了中间层对于硫正极提高的原理。其涂层的高电导率和多硫化物吸附能力使得电池在  $0.2 \text{ C}$  电流下具有  $1315 \text{ mAhg}^{-1}$  的初始比容量, 在高倍率  $2 \text{ C}$  电流下仍有  $699 \text{ mAhg}^{-1}$  比容量; 其次, 为了减轻正极中间层的密度, 选择三维石墨烯泡沫作为中间层导电基底, 并使用原子层沉积 (ALD) 方法进行氧化锌修饰, 得到自支撑的三维石墨烯泡沫/纳米氧化锌中间层, 使得锂硫电池在  $0.5 \text{ C}$  倍率下也具有  $1051 \text{ mAhg}^{-1}$  的初始比容量, 而其较低的密度 ( $0.15 \text{ mg cm}^{-2}$ ) 也减少了对正极能量密度的影响; 在此基础上, 作者选择同时具有高电导率和多硫化物吸附特性的  $\text{Ti}_3\text{C}_2\text{T}_x$  二维纳米片 (MXene) 作为氧化锌替代材料, 对石墨烯泡沫进行修饰, 简化了合成难度的同时提升了中间层的电子导电性。使用改进后的中间层让锂硫电池在  $0.2 \text{ C}$  下循环 120 次后仍具有  $867 \text{ mAhg}^{-1}$  的比容量,  $2\text{C}$  的高倍率电流下具有  $755 \text{ mAhg}^{-1}$  的比容量; 基于 MXene 对中间层的显著提升, 作者接着将 MXene 进行原位生长氮、镍掺杂碳纳米片以进行修饰, 这减少了 MXene 的堆叠, 提高了材料比表面积, 同时掺杂元素提升了对多硫化物的吸附能力。得到的复合材料用于涂层材料以修饰电池隔膜。使用该隔膜使得锂硫电池在  $0.2 \text{ C}$  电流下循环 100 次后具有  $943 \text{ mAhg}^{-1}$  比容量, 且  $1 \text{ C}$  循环 500 次后具有  $588 \text{ mAhg}^{-1}$  的稳定比容量, 平均循环容量衰减率为  $0.069\%$ , 并使得  $3.8 \text{ mg cm}^{-2}$  高载硫量电极呈现  $946 \text{ mAhg}^{-1}$  的比容量, 体现了在高容量锂硫电池中的应用潜力。

## Acknowledgments

The four-year time as a Ph.D. student is a valuable journey in my life, during which I have received munificent support from all people around me. Their help is the indispensable light to guide me in finishing this thesis.

In the first place, I would like to send my unpretending gratitude to my first supervisor, Dr. Li Yang. Ever since our first contact online four years ago, she has been a patient and kind director during all my Ph.D. career. Her meticulousness and guidance on my research are the guarantee of my academic achievements; her consideration of my life supports my career in XJTLU. I will never forget those touching moments in her supervisory. It is my great fortune to have her as a Ph.D. supervisor.

My secondary supervisor, Prof. Cezhou Zhao, is a generous group leader. He provided numerous assistances in my experiment and brilliant project plan. Here I want to give my special appreciation to him.

I would also express my thanks to my supervisor in UoL, Prof. Laurence Hardwick, and his student Mr. Alex Neale. Their academic guidance helped me smoothly starting the research in UoL. Thank all the people in Stephenson Institute of Renewable Energy who helped me during my first-time abroad experience.

I also want to send my gratitude to the staff of the Chemistry Department: Dr. Ruiyao Wang, Dr. Lifeng Ding, Dr. Graham Dawson for sharing research experience and concerning of my Ph.D. progress.

Moreover, my gratefulness also belongs to my dear senior fellows: Dr. Qian Zhang, Dr. Yifei Mu, Dr. Qifeng Lu, Dr. Ruize Sun, Dr. Yanfei Qi. Their experiences are a precise fortune in my research career. I would also thank other fellows in my dear research group: Dr. Chenugang Liu, Dr. Yinchao Zhao, Mr. Xianwei Geng, Ms. Yi Sun, Mr. Xiangfei Lin, Ms. Shuhui Tao, Ms. Miao Cui, Mr. Yutao Cai, Mr. Yuxiao Fang, Mr. Zongjie Shen, Mr. Qihan Liu, Mr. Tianshi Zhao, Ms. Xiaoping Chen, and Ms. Xinkai Xie. This huge family gave me essential happiness and energy to work and live for this unforgettable four-year time. Thank you very much.

In the end, special gratitude is sent to my parents who are always willing to generously backup me to come through all the difficulties. Although one thousand kilometers away from them, I was inspired and powered as if they had always stood by my side. I love you.

Ruowei Yi

Aug. 2020

## List of Publications

### Journal Articles

---

- [1] **Ruowei Yi**, Xiangfei Lin, Yinchao Zhao, Chenguang Liu, Yinqing Li, Laurence J. Hardwick, Li Yang, Cezhou Zhao, Xianwei Geng, and Qian Zhang, *Fabrication of a Light-Weight Dual-Function Modified Separator towards High-Performance Lithium-Sulfur Batteries*. ChemElectroChem, 2019,**6** (14): p. 3648-3656.
- [2] **Ruowei Yi**, Chenguang Liu, Yinchao Zhao, Laurence J. Hardwick, Yinqing Li, Xianwei Geng, Qian Zhang, Li Yang, and Cezhou Zhao, *A Light-weight Free-standing Graphene Foam-based Interlayer towards Improved Li-S Cells*. Electrochimica Acta, 2019,**299** p. 479-488.
- [3] Xianwei Geng, **Ruowei Yi**, Zhiming Yu, Cezhou Zhao, Yinqing Li, Qiuping Wei, Chenguang Liu, Yinchao Zhao, Bing Lu, and Li Yang, *Isothermal sulfur condensation into carbon nanotube/nitrogen-doped graphene composite for high performance lithium-sulfur batteries*. Journal of Materials Science: Materials in Electronics, 2018,**29** (12): p. 10071-10081.
- [4] Xianwei Geng, **Ruowei Yi**, Xiangfei Lin, Chenguang Liu, Yi Sun, Yingchao Zhao, Yinqing Li, Ivona Mitrovic, Rui Liu, Li Yang, and Cezhou Zhao, *A high conductive TiC-TiO<sub>2</sub>/SWCNT/S composite with effective polysulfides adsorption for high performance Li-S batteries*. Journal of Alloys and Compounds, 2020,p. 156793.
- [5] Yudan Yuan, **Ruowei Yi**, Yi Sun, Jianqiao Zeng, Jiaqi Li, Jiahao Hu, Yinchao Zhao, Wei Sun, Chun Zhao, Li Yang, and Cezhou Zhao, *Porous Activated Carbons Derived from Pleurotus eryngii for Supercapacitor Applications*. Journal of Nanomaterials, 2018,**2018** p. 1-10.
- [6] Chenguang Liu, Yinchao Zhao, **Ruowei Yi**, Yi Sun, Yinqing Li, Li Yang, Ivona Mitrovic, Stephen Taylor, Paul Chalker, and Cezhou Zhao, *Alloyed Cu/Si core-shell nanoflowers on the three-dimensional graphene foam as an anode for lithium-ion batteries*. Electrochimica Acta, 2019,**306** p. 45-53.
- [7] Chenguang Liu, Yinchao Zhao, **Ruowei Yi**, Yi Sun, Yinqing Li, Li Yang, Ivona Mitrovic, Stephen Taylor, Paul Chalker, and Cezhou Zhao, *Alloyed Cu/Si core-shell nanoflowers on the three-dimensional graphene foam as an anode for lithium-ion batteries*. Electrochimica Acta, 2019,**306** p. 45-53.

- [8] Yinchao Zhao, Chenguang Liu, Yi Sun, **Ruowei Yi**, Yutao Cai, Yinqing Li, Ivona Mitrovic, Stephen Taylor, Paul Chalker, Li Yang, and Cezhou Zhao, *3D-structured multi-walled carbon nanotubes/copper nanowires composite as a porous current collector for the enhanced silicon-based anode*. Journal of Alloys and Compounds, 2019,**803** p. 505-513.
- [9] Yinchao Zhao, Chenguang Liu, **Ruowei Yi**, Ziqian Li, Yanbing Chen, Yinqing Li, Ivona Mitrovic, Stephen Taylor, Paul Chalker, Li Yang, and Cezhou Zhao, *Facile preparation of  $\text{Co}_3\text{O}_4$  nanoparticles incorporating with highly conductive MXene nanosheets as high-performance anodes for lithium-ion batteries*. Electrochimica Acta, 2020,**345** p. 136203.
- [10] Qian Zhang, Shuhui Tao, **Ruowei Yi**, Chunhui He, Cezhou Zhao, Weitao Su, Alexander Smogunov, Yannick J. Dappe, Richard J. Nichols, and Li Yang, *Symmetry Effects on Attenuation Factors in Graphene-Based Molecular Junctions*. The Journal of Physical Chemistry Letters, 2017,**8** (24): p. 5987-5992.
- [11] Qian Zhang, Chenguang Liu, Shuhui Tao, **Ruowei Yi**, Weitao Su, Cezhou Zhao, Chun Zhao, Yannick J. Dappe, Richard J. Nichols, and Li Yang, *Fast and straightforward analysis approach of charge transport data in single molecule junctions*. Nanotechnology, 2018,**29** (32): p. 325701.
- [12] Yifei Mu, Yuxiao Fang, Ce Zhou Zhao, Chun Zhao, Qifeng Lu, Yanfei Qi, **Ruowei Yi**, Li Yang, Ivona Z. Mitrovic, Stephen Taylor, and Paul R. Chalker, *Total Dose Effects and Bias Instabilities of  $(\text{NH}_4)_2\text{S}$  Passivated Ge MOS Capacitors With  $\text{Hf}_x\text{Zr}_{1-x}\text{O}_y$  Thin Films*. IEEE Transactions on Nuclear Science, 2017,**64** (12): p. 2913-2921.
- [13] Yanfei Qi, Chun Zhao, Ce Zhou Zhao, Wangying Xu, Zongjie Shen, Jiahuan He, Tianshi Zhao, Yuxiao Fang, Qihan Liu, **Ruowei Yi**, and Li Yang, *Enhanced resistive switching performance of aluminum oxide dielectric with a low temperature solution-processed method*. Solid-State Electronics, 2019,**158** p. 28-36.

## Conference Paper

---

- [1] **Ruowei Yi**, Xiangfei Lin, Yinchao Zhao, Chenguang Liu, Yinqing Li, Laurence J. Hardwick, Li Yang, Ce Zhou Zhao, Xianwei Geng, Qian Zhang. “A Light-weight Dual-functional Modified Separator via Facile Fabrication towards High Performance Li-S Batteries.” *The 2nd International Conference on Green Energy and Environment Engineering (CGEEE)*, 2019.
- [2] **Ruowei Yi**, Yinchao Zhao, Chenguang Liu, Li Yang, Cezhou Zhao. “The Facile Fabrication of a Light-weight Dual-functional Modified Separator towards High Performance Li-S Batteries.” *The 71st Annual Meeting of the International Society of Electrochemistry*, 2020..
- [3] Yinchao Zhao, Chenguang Liu, **Ruowei Yi**, Yi Sun, Li Yang, and Ce Zhou Zhao. “3D Copper Sponges-Supported Si Hollow Nanowires as Advanced Anode Materials for Lithium-Ion Battery.” *The 2nd International Conference on Green Energy and Environment Engineering (CGEEE)*, 2019.
- [4] Chenguang Liu, Yinchao Zhao, Ran Shi, **Ruowei Yi**, Yi Sun, Li Yang, and Ce Zhou Zhao. “In-situ measurement of stress evolution and pulverization in a composite silicon electrode by high frequency capacitance characterization.” *The 2nd International Conference on Green Energy and Environment Engineering (CGEEE)*, 2019.
- [5] Yi Sun, Chenguang Liu, Yinchao Zhao, **Ruowei Yi**, Li Yang, and Ce Zhou Zhao. “Graphene oxides mixed in hierarchical porous polyacrylonitrile-based carbons for supercapacitor electrodes.” *The 2nd International Conference on Green Energy and Environment Engineering (CGEEE)*, 2019.

## Patents

---

- [1] **Ruowei Yi**, Li Yang, Cezhou Zhao, Yinchao Zhao, Chenguang Liu, Xianwei Geng. *Three-dimensional dendritic nitrogen-doped graphene nanotube and its preparation method*. Publication patent No.: CN 108039460 B, Patent granted No.: ZL201711170934.X
- [2] **Ruowei Yi**, Li Yang, Cezhou Zhao, Chenguang Liu, Yinchao Zhao, Xianwei Geng. *Lithium-sulfur battery using nitrogen-doped graphene foam sheet as interlayer and its preparation*. Publication patent No.: CN 107887557 B, Patent granted No.: ZL201711006380.X
- [3] **Ruowei Yi**, Li Yang, Cezhou Zhao, Chenguang Liu, Yinchao Zhao, Xianwei Geng. *Method for manufacturing interlayer of conductive polymer compound for lithium-sulfur batteries*. Patent Application No.: 201711170978.2
- [4] **Ruowei Yi**, Li Yang, Cezhou Zhao, Yudan Yuan, Chenguang Liu, Yinchao Zhao, Xianwei Geng, Xiangfei Lin. *Composite separator for lithium-sulfur battery and its preparation method and application*. Patent Application No.: 201811442542.9
- [5] **Ruowei Yi**, Li Yang, Cezhou Zhao, Yudan Yuan, Chenguang Liu, Yinchao Zhao, Xiangfei Lin. *Cathode for lithium-sulfur battery and its preparation method and application*. Patent Application No.: 201811449059.3
- [6] Yudan Yuan, **Ruowei Yi**, Jiaqi Li, Yi Sun, Yinchao Zhao, Chenguang Liu, Wei Sun, Li Yang, Chun Zhao, Cezhou Zhao. *The preparation of the polyacrylonitrile / molybdenum disulfide composite for supercapacitors*. Publication patent No.: CN 108305789 B, Patent granted No.: ZL201711481492.0
- [7] Li Yang, **Ruowei Yi**, Cezhou Zhao. *The lithium-sulfur battery using nitrogen-doped carbon nanotube coated graphene foam as the interlayer*. Publication patent No.: CN 107959045 B, Patent granted No.: ZL201711006349.6

## List of Figures

<b>Figure 1.1</b> Schematic comparison of theoretical gravimetric and volumetric energy densities between LIB (graphite/LiCoO <sub>2</sub> ) and Li-S batteries. A 500 km distance is used as a benchmark for the future requirement of EV energy storage [3].	3
<b>Figure 1.2</b> Schematic of the discharge process of a Li-S battery with the metallic lithium anode and S-containing cathode, with an organic liquid electrolyte [16].	4
<b>Figure 1.3</b> The schematic of a theoretical charge/discharge profile of the Li-S battery [15]. Note that due to the sluggish solid phase reduction of Li <sub>2</sub> S <sub>2</sub> to Li <sub>2</sub> S, the practical final reduction products are usually a mixture of Li <sub>2</sub> S <sub>2</sub> and Li <sub>2</sub> S.	5
<b>Figure 1.4</b> The schematic of some intrinsic and extrinsic drawbacks of Li-S batteries [13].	6
<b>Figure 1.5</b> The schematic of different issues faced by the Li metal anode during practical application [27].	7
<b>Figure 1.6</b> The schematic of the high-dimensional phases to the low-dimensional phases [28].	8
<b>Figure 1.7</b> (A–F) Surface morphology evolution characterized by scanning electronic microscope (SEM) of the P-rGO/Li anodes. (A–F) correspond to the different charge/discharge states in (G) [36].	9
<b>Figure 1.8</b> <i>In-situ</i> optical microscopy study of the Li <sub>2</sub> S <sub>8</sub> and LiNO <sub>3</sub> effect on lithium dendrite formation. (a) Schematic illustration of the <i>in-situ</i> observation equipment. (b–f) The cross-section of the cell with the addition of both Li <sub>2</sub> S <sub>8</sub> and LiNO <sub>3</sub> , showing the dendrites evolution process versus increasing lithium deposition time. (g–k) The comparison with only LiNO <sub>3</sub> addition at the same condition. All the scale bars are 100 μm [37].	10
<b>Figure 1.9</b> The <i>in-situ</i> microscopy comparative observation of Li metal deposition in electrolyte (a) with and (b) without thiourea additive [30].	11
<b>Figure 1.10</b> The demonstration of low flammability of the DEGDM-E-LiTFSI-LiNO <sub>3</sub> electrolyte by direct ignition test [32].	12
<b>Figure 1.11</b> The CV curves of the Li-S cell with PP14-RTIL electrolyte. The 1 <sup>st</sup> , the 2 <sup>nd</sup> , and the 10 <sup>th</sup> cycles are shown in solid line, dot line, and dashed line, respectively [50].	13
<b>Figure 1.12</b> The schematic of the concept of Solvent-in-Salt electrolyte. (a) A conclusion of currently	

available electrolytes and classification. (b) The distribution map of different non-liquid organic electrolytes based on volume ratio and weight ratio of salt-to-solvent [52].....	14
<b>Figure 1.13</b> The schematic of Li-S battery configurations with different types of SSEs: (A) polymer SSE, (B) oxide SSE, and (D) sulfide SSE. The illustration of galvanostatic charge/discharge profiles of battery systems with (C) quasi-solid and (E) solid electrolytes [65]. .....	15
<b>Figure 1.14</b> (a) The schematic of fabrication process of the HGs/S composite by template approach. (b) A performance comparison between superior HGs/S composite and reduced graphene/sulfur (RGO/S) during cycling [74].....	17
<b>Figure 1.15</b> (a)(b) The high-resolution of GQDs. The insert is the size distribution of GQDs. (c) The SEM image of GQDs-S/CB composite. (d) Schematics of GQDs-S/CB composite structure and (e) the magnified illustration near sulfur surface [75].....	17
<b>Figure 1.16</b> Schematic of the nano-size effect on the sulfur particle in sulfur cathode: (a) a comparison between theoretical and practical galvanostatic discharge profiles of sulfur cathodes. (b) The dissolution of sulfur at the beginning discharge stage results in electrochemical disconnection with the electrode. (c) The diffusion of polysulfides during discharge process. (d) During the polysulfides reduction, the $\text{Li}_2\text{S}_2/\text{Li}_2\text{S}$ layer blocks the electron and Li ion transfer in electrode with large sulfur particle size. For the large sulfur particle, large Li ion flux may form blocking layer of $\text{Li}_2\text{S}$ on (e) sulfur and (f) $\text{Li}_2\text{S}_2$ surface [76].....	19
<b>Figure 1.17</b> (a) $\text{N}_2$ adsorption/desorption isotherms of the microporous carbon spheres with the insert of pore size distribution. (b) XRD patterns of sulfur, microporous carbon spheres, and microporous carbon spheres/sulfur composite. (c) The galvanostatic charge/discharge profiles of the carbon spheres/sulfur composite. (d) Cycling performance of carbon spheres/sulfur composite with 42% and 51% sulfur weight percent at $40 \text{ mA g}^{-1}$ [78]. .....	19
<b>Figure 1.18</b> SEM (a) and TEM (b) of the DCNTs prepared by the AAO-template method. Cycling performance (c) and Coulombic efficiency (d) of sulfur loaded CNTs (SDCNTs) samples with different sulfur impregnation temperatures [82]. .....	21
<b>Figure 1.19</b> Schematics of (a) VA-CNT/S electrode preparation [83] and (b) S-CNT electrode fabricated by AAO template and acetylene reduction of sulfate-AAO [84].....	21
<b>Figure 1.20</b> (a) The schematic of nano S-SACNT fabrication process. The SEM image shows the morphology of the S-SACNT electrode with an insert of optical graph [85]. (b) The schematic of	

theoretical sulfur content calculation in a SWCNT network with uniform sulfur coating. The right image is the TEM characterization of a fabricated sulfur coated SWCNTs electrode [86]. ..... 22

**Figure 1.21** Synthesis schematic (a) and SEM characterization (b) of GO-S-Amy composite. Cycling performance at 2 mg cm<sup>-2</sup> and 6 mg cm<sup>-2</sup> sulfur loading is shown in (c). ..... 23

**Figure 1.22** (a) The self-assembling schematic of rGO-S film with corresponding optical image to each stage. The TEM image (b) and EDS mapping result (c). Macroscale image (d) and flexible demonstration (e) of the film. Rate performance comparison (f) and galvanostatic charge/discharge profiles (g) with the rGO-S mixture electrode, correspondingly [89]. ..... 23

**Figure 1.23** (a) Schematic of the Li-S battery with porous-graphene/sulfur (P-G/S) with large and small pore sizes as the cathode and their cycling performance at 0.5 C (c) [91]. (b) The illustration of 3D sulfur@ porous carbon composite (3D-S@PGC) preparation and its cycling performance (d) [92]. ..... 24

**Figure 1.24** (a) Structural illustration of pure graphene (p-G) and different N-doping configurations like graphitic N (N<sub>C</sub>), pyridinic N (N<sub>PD</sub>), and pyrrolic N (N<sub>PL</sub>). Anchoring of NH<sub>2</sub> groups are configurations of the N<sub>A</sub> at the edge and the N<sub>A'</sub> on the basal plane. (b) The conclusion of calculated binding energy between polysulfides and different N-dope configurations [101]. ..... 25

**Figure 1.25** (a) A schematic of the PANI-S composite's variation during the charge/discharge cycle, and related cycling performance at different rates [103]. (b) Schematic illustration of the SPANI-NT/S composite structure and its cyclic voltammetry [105]. ..... 26

**Figure 1.26** (a-e) The binding energies of Li<sub>2</sub>S<sub>8</sub> on different metal oxides surface with optimized geometries. (f-k) The Li ion diffusion paths on different metal oxides, and the potential energy of the diffused Li ion on different sites of oxides [106]. ..... 27

**Figure 1.27** The “Goldilocks” principle of the redox between metal oxides and polysulfides: the resulted production as a function of redox potential vs. Li/Li<sup>+</sup> [107]. ..... 27

**Figure 1.28** (a) Schematic of different polysulfides adsorption mechanisms of oxidized CoP and reduced CoP (CoP-R). (b) The cycling performance with S cathodes modified with CNT, CoP-CNT, and CoP-R-CNT [116]. ..... 28

**Figure 1.29** Top-view SEM images of expansion-tolerance electrode (a,b) with growing magnifications and related schematic of web-like binder bonds holding particles while leaving expansion space. (d) The cycling performance of the expansion-tolerance electrode with high sulfur loading [117].

.....	29
<b>Figure 1.30</b> (a-c) and (d-f): Top-view optical image, cross-section SEM image, and top-view SEM image of thermal-dried sulfur electrode (TDS) and freeze-dried sulfur electrode (FDS), respectively. (g) The cycling performance of freeze-dried-and-compressed (FDS-C) electrode with different sulfur loading at current density of $0.5 \text{ mA cm}^{-2}$ [118].	29
<b>Figure 1.31</b> A schematic comparison of Li-S cells with (a)(b) and without (c)(d) a carbon-coated separator as a polysulfide diffusion barrier region, showing the polysulfide-stabilization effect of interlayer [128].	30
<b>Figure 1.32</b> SEM images of MWCNT paper before (a)(c) and after cycling (b)(c), in which the agglomerated sulfur particles and denoted by red circles. (e)The EDS mapping of sulfur on the surface of cycled MWCNT interlayer [120].	31
<b>Figure 1.33</b> Adsorption test of nano-TiO <sub>2</sub> with Li <sub>2</sub> S <sub>6</sub> solution: (a) optical image comparison, (b) UV-vis spectra of Li <sub>2</sub> S <sub>6</sub> solution before and after adsorption, and (c) XPS of Ti 2 <i>p</i> of TiO <sub>2</sub> before and after adsorption test [142].	31
<b>Figure 1.34</b> (a) Open circuit potential (OCP) test of cells with and without GO membrane interlayer [144]. Galvanostatic charge/discharge profiles of cells with MoS <sub>2</sub> /CNT interlayer (b) and without interlayer (c) over 200 cycles [145].	32
<b>Figure 1.35</b> Cycling performance of cells with CB/PEDOT:PSS interlayer, with 2 layers of Celgard separator and electrochemically isolated CB/PEDOT:PSS interlayer at 0.2 C. The schematic shows the structure of the isolated cell.	33
<b>Figure 1.36</b> EIS of cells with and without MWCNT paper (a) [120]; the EIS of cells with MTO-CNTs, CNTs interlayers and PP separators before and after 2 cycles [124].	33
<b>Figure 1.37</b> EIS of Ti <sub>3</sub> C <sub>2</sub> T <sub>x</sub> separator, Ti <sub>3</sub> C <sub>2</sub> T <sub>x</sub> @ carbon nanotube (T@C) separator, Ti <sub>3</sub> C <sub>2</sub> T <sub>x</sub> @ carbon nanotube/polyethyleneimine (PEI) (T@CP) separator, and pristine glass fiber (GF) separator [147].	34
<b>Figure 1.38</b> (a) Schematic of the sulfur species precipitation on the cathode surface during charge/discharge process. SEM images of cycled cathode without conductive interlayer:(b) the cross-section image with an optical insert of corresponding separator; the magnified images of the precipitation layer: (c) the cross-section and (d) the top-view images. (e) The schematic illustration of the activate function of the conductive interlayer. (f) The cross-section image of a	

cell with interlayer; the insert shows the corresponding separator. The magnified SEM images of this cathode: the cross-section (g) and the top-view (h) images [127].	35
<b>Figure 1.39</b> The cycling performance of Li-S batteries of GO interlayer with various mass loadings: (a) cycling performance at 0.1 C and (b) corresponding Coulombic efficiency; (c) rate performance and (d) corresponding Coulombic efficiency.(e)(f) SEM images of the GO interlayer: bird-view and cross-section, respectively [144].	37
<b>Figure 1.40</b> SEM images of (a) GP and (b) MnO <sub>2</sub> /GP surface. Nitrogen adsorption/desorption curves of samples with different MnO <sub>2</sub> content were shown in (c), and their performance in cycling test were shown in (d) [159].	38
<b>Figure 1.41</b> SEM (a) and TEM (b) images of the porous nitrogen and phosphorus dual doped graphene (p-NP-G) composite. (c) Rate performance of cells with different heteroatoms doped graphene interlayers. (d) <i>I-V</i> curves of these interlayers [99].	39
<b>Figure 1.42</b> (a) Schematic of the exfoliation of the Ti <sub>3</sub> C <sub>2</sub> T <sub>x</sub> MXene [162]; (b) SEM images of the Ti <sub>3</sub> AlC <sub>2</sub> , the etched Ti <sub>3</sub> C <sub>2</sub> T <sub>x</sub> , and the delaminated Ti <sub>3</sub> C <sub>2</sub> T <sub>x</sub> , respectively. The HRTEM images are Mo <sub>2</sub> TiAlC <sub>2</sub> , and etched Mo <sub>2</sub> TiC <sub>2</sub> T <sub>x</sub> . The bright field TEM image is a single-layer Ti <sub>3</sub> C <sub>2</sub> T <sub>x</sub> flake [165]. (c) The density of states (DOS) calculation results of Ti <sub>3</sub> C <sub>2</sub> with all -OH terminations [166]. (d) The folded Ti <sub>3</sub> C <sub>2</sub> T <sub>x</sub> filtrated paper and its flexibility demonstration [167].	40
<b>Figure 1.43</b> (a-d) The optimized adsorption configurations of S <sub>8</sub> , Li <sub>2</sub> S <sub>8</sub> , Li <sub>2</sub> S <sub>4</sub> , and Li <sub>2</sub> S on the Ti <sub>3</sub> C <sub>2</sub> O <sub>2</sub> surface and their corresponding adsorption energy, respectively [176]. (e) The schematic of polysulfides reservation mechanism by the formation of a continuous sulfate protecting layer on the surface during deep cycling [171].	41
<b>Figure 1.44</b> (a) Schematic of the fast ion transportation in a compact and nano porous MXene film (CN-MX) and the slow transportation in a tightly restacked MXene film fabricated by the vacuum filtration [177]. (b) The bird-view SEM image of pure Ti <sub>3</sub> C <sub>2</sub> T <sub>x</sub> film surface with the insert of optical observation of its flexibility. (c) The rate performance of cells with and without Ti <sub>3</sub> C <sub>2</sub> T <sub>x</sub> film as interlayer [172]. (d) The bird-view SEM image of Nafion-modified Ti <sub>3</sub> C <sub>2</sub> T <sub>x</sub> MXene (MX-NF) film. (e) The height profiles measured by AFM of single layer Ti <sub>3</sub> C <sub>2</sub> T <sub>x</sub> nanosheet and NF-MX nanosheet. (d) The rate performance cells with various interlayers and without interlayer [179].	42
<b>Figure 1.45</b> (a) The self-assembly fabrication schematic of T@CP interlayer and its SEM images of (b) the surface and (c) the cross-section. (d) The rate test of cells with T@CP, T@C, and Ti <sub>3</sub> C <sub>2</sub> T <sub>x</sub>	

interlayer [147].	44
<b>Figure 1.46</b> The schematic of N-Ti <sub>3</sub> C <sub>2</sub> /C interlayer fabrication (a), and the TEM images of Ti <sub>3</sub> C <sub>2</sub> /ZIF-67 (b) and N-Ti <sub>3</sub> C <sub>2</sub> /C (c). The rate performance comparison of cells with N-Ti <sub>3</sub> C <sub>2</sub> /C, Ti <sub>3</sub> C <sub>2</sub> interlayer and without interlayer is shown in (d) [180].	44
<b>Figure 2.47</b> Schematic of the physical signals from the interaction between electron beam and specimen in the SEM system (Adapted from Ref. [6]).	66
<b>Figure 2.48</b> The schematic of the optical path in the TEM system (adapted from Ref. [7]).	67
<b>Figure 2.49</b> The schematic of the oxidation and reduction peaks in a cyclic voltammetry (CV) [8].	68
<b>Figure 2.50</b> A schematic Nyquist plot of the Randles equivalent circuit for an electrochemical cell [14].	70
<b>Figure 3.51</b> Preparation of CB/PEDOT:PSS modified separator.	73
<b>Figure 3.52</b> (a) Side view of the CB/PEDOT:PSS modified separator; the thickness of the separator and coating layer were marked by arrows. (b) SEM image of the CB/PEDOT:PSS interlayer.	75
<b>Figure 3.53</b> Nitrogen adsorption-desorption isotherms of the CB/PEDOT:PSS coating. The insert shows the pore size distribution curves.	75
<b>Figure 3.54</b> Current-voltage (I-V) curves for pristine Celgard, CB, and CB/PEDOT:PSS modified separators.	76
<b>Figure 3.55</b> Configuration of the Li-S cell with the CB/PEDOT:PSS interlayer.	77
<b>Figure 3.56</b> Charge and discharge profiles (a) at 0.2 C the second cycle of cells without an interlayer, with CB and CB/PEDOT:PSS interlayers (the insert shows the enlarged part where two discharge plateaus meet); (b) at different rates of a cell without an interlayer, (c) at different rates of a cell with CB, and (d) at different rates of a cell with CB/PEDOT:PSS interlayers.	78
<b>Figure 3.57</b> Cyclic voltammetry profiles of pristine cell and cell with CB/PEDOT:PSS interlayer for the first cycle.	79
<b>Figure 3.58</b> The linear fitting result of the Tafel range in the CV curves ( <b>Figure 3.57</b> ): the comparison of (a) peak A and (b) peak B in different batteries.	81
<b>Figure 3.59</b> (a) The cyclic discharging specific capacities and Coulombic efficiency of a cell without an interlayer, with CB or CB/PEDOT:PSS interlayer at 0.2 C current density. (b) The rate capacities of cells with CB or CB/PEDOT:PSS interlayer. (c) Long-term cycling of CB/PEDOT:PSS cell at 1 C.	82

**Figure 3.60** (a) Scheme of the cell with the isolated CB/PEDOT:PSS interlayer structure. (b) Cycling performance of cells with 2-layer Celgards separator, isolated CB/PEDOT:PSS interlayer, and CB/PEDOT:PSS interlayer. .... 83

**Figure 3.61** CV curves recorded at different scan rates for Li-S batteries with (a) CB/PEDOT:PSS modified separator and (c) without interlayer. Linear fits of CV peak current dependence based on the scan rate of Li-S batteries with (b) CB/PEDOT:PSS modified separator and (d) without interlayer. .... 85

**Figure 3.62** (a) The wide survey spectra of CB/PEDOT interlayer before and after 50 cycles at 0.5 C. The deconvoluted S 2*p* and Li 1*s* XPS spectra of (b)(d) pristine CB/PEDOT:PSS interlayer and (c)(e) CB/PEDOT:PSS interlayer after 50 cycles at 0.5 C. .... 87

**Figure 3.63** (a) Electrochemical impedance spectra of pristine Li-S cell and cells with CB and CB/PEDOT:PSS interlayers before and after 10 cycles at 0.2 C. (b) The corresponding equivalent circuits of all the cells (i), except the cycled cell without interlayer (ii). .... 88

**Figure 4.64** The average growth rate of ZnO by ALD from a total 150 cycles at each temperature, measured by the ellipsometry. .... 95

**Figure 4.65** A Li-S battery incorporated with a GF-based interlayer, with an insert showing a free-standing GF interlayer. The scale bar is 10 mm. .... 97

**Figure 4.66** (a) The Raman spectra of GF and GF@ZnO. (b) High resolution C 1*s* and Zn 2*p* XPS spectra of GF@ZnO. (c) SEM image of GF. The insert shows the fractured graphene triangular prism and its hollow interior space. (d) TEM image of the as-prepared GF@ZnO. (e) The HRTEM of GF@ZnO denoted with crystal lattice fringes with d-spacing of the (002) plane of the ZnO. The insert shows the layer structure of graphene edge. .... 99

**Figure 4.67** Cyclic voltammetry profiles of the initial five cycles of the S-C cell and cells with 2 GF, GF@ZnO and GF/GF@ZnO interlayers, respectively. .... 100

**Figure 4.68** The initial galvanostatic charge-discharge profiles of S-C cell and cells with 2 GF, GF@ZnO and GF/GF@ZnO interlayers at 0.5 C. .... 101

**Figure 4.69** Electrochemical performance of Li-S cells with different interlayers: (a) cyclic test performance of cells with different interlayers measured at 0.5 C and (b) the corresponding cycling specific capacity based on cathode and interlayer mass. (c) Rate performance and (d) electrochemical impedance spectra of cells with different interlayers before cycling; and (e) the

corresponding equivalent circuit: (i) pristine Li-S battery and (ii) cells with different interlayers.	104
<b>Figure 4.70</b> The cycling performance of cells with different GF@ZnO interlayers: interlayers with 20, 60 and 80 ALD cycles.	104
<b>Figure 4.71</b> The cycling performance of cells with GF/GF@ZnO and GF@ZnO/GF interlayers at 0.5 C.	105
<b>Figure 4.72</b> The cycling performance of cells with GF/GF@ZnO and GF/GF/GF@ZnO interlayers at 0.5 C.	105
<b>Figure 4.73</b> (a) Scheme of the cell with an isolated interlayer. (b) The cyclic discharge specific capacity performance of the cell with GF@ZnO interlayer, isolated GF@ZnO interlayer and pristine cathode at 0.5 C.	106
<b>Figure 4.74</b> (a) SEM image of the GF/GF@ZnO interlayer of the GF side after 100 cycles at 0.5 C; (b) corresponding EDS carbon elemental mapping and (c) corresponding EDS sulfur elemental mapping.	107
<b>Figure 4.75</b> (a) SEM image of the GF/GF@ZnO interlayer of the GF@ZnO side after 100 cycles at 0.5 C; (b) the corresponding EDS carbon elemental mapping and (c) sulfur elemental mapping. ....	107
<b>Figure 4.76</b> (a) SEM image of the GF interlayer and (b) GF@ZnO interlayer after for 50 cycles at 0.5 C. Insert tables show the corresponding quantitative results of elements.	108
<b>Figure 5.77</b> The schematic of the fabrication of GFMX interlayer and its application in the Li-S battery. The insert is the macroscale optical image of the synthesized free-standing GFMX interlayer.	119
<b>Figure 5.78</b> The physical characterization of GF and GFMX: The SEM images of (a)(c) GFMX and (b)(d) GF with different magnifications. (e) The TEM bright field image of GFMX and the corresponding (f) SEAD patterns. (g) The corresponding STEM-HADDF image and EDS element mapping of Ti, C, and O. The Raman spectra comparison of GF and GFMX is shown in (h). ...	121
<b>Figure 5.79</b> (a) The comparison of CV curves of GFMX, GF, and pristine Li-S batteries. (b) Linear fit results of the CV curves in the Tafel range, with slopes denoted on the plot.	123
<b>Figure 5.80</b> The galvanostatic characterizations of pristine cell, GF cell, and GFMX cell: (a) cycling performance at 0.2 C. (b) The rate performance at 0.2 C, 0.5 C, 1 C, and 2 C current densities. The exhibited galvanostatic charge and discharge profiles belong to (c) GFMX cell and (d) GF cell,	

respectively.....	124
<b>Figure 5.81</b> The EIS comparison of different cells: the pristine, the GF, and the GFMX cell.....	125
<b>Figure 6.82</b> The fabrication process of the N-doped MXene@carbon nanosheets-Ni (N-M@CNi)...	133
<b>Figure 6.83</b> (a) SEM image and (b) TEM bright-field image of N-M@CNi. The insert is a SEM cross-section of a $Ti_3C_2T_x$ filtrated film (scale bar, 5 $\mu$ m). (c) The TEM bright-field image of the carbon nanosheets showing the Ni nanoparticles and their typical diameters. (d) The HRTEM image of the Ni and C lattice fringes. (e) HAADF images and corresponding elemental mapping of Ti, N, C, Ni, and O elements. ....	133
<b>Figure 6.84</b> Nitrogen adsorption-desorption isotherm of the (a) N-M@CNi and (b) MXene powder. The insert shows the pore size distribution acquired using the Barrett-Joyner-Halenda (BJH) method.....	134
<b>Figure 6.85</b> (a) XRD patterns and the (b) Raman patterns of N-M@CNi powder and $Ti_3C_2T_x$ film...	135
<b>Figure 6.86</b> The deconvoluted XPS of (a) N 1s and (b) Ti 2p of the N-M@CNi sample.....	136
<b>Figure 6.87</b> (a) OCP test of cells with N-M@CNi or CB modified separator, or with pristine Celgard separator. (b) Cyclic voltammetry curves of cells with N-M@CNi or CB modified separator, or with pristine Celgard separator. The sulfur loading in the tested cathode was $\sim 2.3$ mg $cm^{-1}$ .....	137
<b>Figure 6.88</b> (a) The CV of the symmetric cells (coating/Celgard/Celgard/coating) with different separators. The insert shows the resistance of different separators measured by the four-probe method. (b) The impedance plots of the stainless steel/modified separator/ stainless steel cells with different separators. The insert table summarizes the calculated ionic conductivity values of the Celgard, the CB and the N-M@CNi separators. ....	138
<b>Figure 6.89</b> The typical galvanostatic charge and discharge (GCD) curves of (a) CB, (b) N-M@C and (c) N-M@CNi cells at 0.2 C, 0.5 C, 1 C, 2 C, and 3 C. The rate performance (d) of the Celgard, the CB, the N-M@C and the N-M@CNi cells at a current of 0.2 C. (e) The cycling performance comparison of N-M@CNi cells with different sulfur mass loading cathodes at 0.2 C. (f) The long-term cycling performance of Celgard and N-M@CNi cells at 1 C. ....	140
<b>Figure 6.90</b> The EIS plots of Celgard, CB, and N-M@CNi cells before (solid dots) and after 10 cycles (hollow dots) at 0.2 C.....	143
<b>Figure 6.91</b> The deconvoluted XPS of the cycled N-M@CNi separator: (a) S 2p and (b) Ti 2p. The adsorption of LiPS and the presence of the Ti-S bond are demonstrated in the deconvoluted	

results ..... 143

## List of Tables

<b>Table 3.1</b> The specific resistivity values of three separators were measured by the four-probe method. .....	76
<b>Table 3.2</b> The calculated Li-ion diffusion coefficients of pristine cell and cell with CB/PEDOT:PSS modified separator. ....	85
<b>Table 3.3</b> Fitted values of the impedance spectra in <b>Figure 3.14</b> . ....	88
<b>Table 4.1</b> ALD growth data of ZnO on silicon wafer at different temperatures. ....	94
<b>Table 4.2</b> Analysis of Raman spectrum of GF@ZnO .....	98
<b>Table 4.3</b> The fitting results of Re, Rct, Rst and Rtotal values of cells with GF/GF@ZnO interlayer and without interlayer. ....	104
<b>Table 5.1</b> The fitted parameters of the EIS curves in <b>Figure 5.5</b> . ....	125

## Table of Content

Abstract.....	II
Acknowledgments.....	V
List of Publications .....	VII
List of Figures.....	XI
List of Tables.....	XXI
Table of Content.....	XXII
List of Abbreviations and Acronyms.....	XXV
Chapter 1: Literature reviews.....	1
1.1    Introduction of Li-S batteries .....	1
1.1.1    From fossil fuel to green energy: the background of Li-S batteries' emerging .	1
1.1.2    The development and advantages of Li-S batteries.....	2
1.1.3    The mechanism and challenges of Li-S batteries .....	3
1.2    Current research reviews of Li-S batteries.....	6
1.2.1    Li anode.....	7
1.2.2    Electrolyte .....	10
1.2.3    S-based cathode.....	15
1.2.4    Multi-functional interlayers.....	29
1.3    2D materials (graphene and MXene) and their applications in Li-S battery interlayer	
36	
1.3.1    Graphene .....	36
1.3.2    MXene.....	39
1.4    Aim of study and proposals of the thesis .....	45
1.4.1    Aim of study.....	45
1.4.2    The outline of thesis .....	45
1.5    References.....	47
Chapter 2: Experimental section.....	64
2.1    Structure and morphology characterization .....	64

2.1.1	Raman spectrum.....	64
2.1.2	X-ray diffraction.....	64
2.1.3	Scanning electron microscopy .....	65
2.1.4	Transmission electron microscopy .....	66
2.2	Electrochemical tests.....	67
2.2.1	Cyclic voltammetry .....	67
2.2.2	Galvanostatic charge and discharge .....	68
2.2.3	Electrochemical impedance spectroscopy .....	69
2.3	References.....	70
Chapter 3: Carbon/ Poly (3,4-ethylene dioxythiophene) : Poly (styrene sulfonate) (CB/PEDOT:PSS)		
composite modified separator as a dual-function separator for high-performance Li-S batteries ..		
3.1.	Introduction.....	72
3.2.	Experiment part.....	73
3.2.1.	Fabrication of Carbon/ Poly (3,4-ethylene dioxythiophene) : Poly (styrene sulfonate) (CB/PEDOT:PSS) modified separator .....	73
3.2.2.	Electrode preparation .....	73
3.2.3.	Materials Characterization .....	74
3.2.4.	Electrochemical Measurements.....	74
3.3.	Characterization results of the CB/PEDOT:PSS interlayer and relevant analysis .....	74
3.4.	Conclusions.....	89
3.5.	References.....	90
Chapter 4: Graphene foam-based free-standing interlayer as a light-weight dual-function cathode cover for high-performance Li-S batteries .....		
4.1.	Introduction.....	92
4.2.	Experiment part.....	93
4.2.1.	Fabrication of graphene foam (GF).....	93
4.2.2.	Atomic layer deposition (ALD) of ZnO on GF.....	94
4.2.3.	Electrode preparation .....	95
4.2.4.	Materials characterization .....	95
4.2.5.	Electrochemical measurements .....	96

3.6.	Characterizations of the graphene foam-based interlayer and relevant analysis.....	96
4.3.	Conclusions.....	110
4.4.	References.....	110
Chapter 5 Graphene foam@ Ti <sub>3</sub> C <sub>2</sub> T <sub>x</sub> as an interlayer for stable Li-S batteries .....		115
5.1	Introduction.....	115
5.2	Experimental part.....	116
5.2.1	Synthesis of graphene foam (GF).....	116
5.2.2	Synthesis of graphene foam @ Ti <sub>3</sub> C <sub>2</sub> T <sub>x</sub> (GFMX) interlayer.....	116
5.2.3	Physical characterization.....	117
5.2.4	Electrochemical characterization .....	117
3.7.	Characterizations of the graphene foam@MXene interlayer and relevant analysis..	118
5.3	Conclusions.....	125
5.4	References.....	126
Chapter 6 N-doped MXene@carbon nanosheets-Ni composite modified separator for stable Li-S batteries .....		128
6.1.	Introduction.....	128
6.2.	Experiment part.....	129
6.2.1.	Preparation of the delaminated Ti <sub>3</sub> C <sub>2</sub> T <sub>x</sub> (MXene).....	129
6.2.2.	Preparation of the nitrogen-doped MXene@nitrogen-doped carbon nanosheet-nickel (N-M@CNi) .....	130
6.2.3.	Preparation of the N-M@CNi modified separator .....	130
6.2.4.	Physical characterization.....	130
6.2.5.	Electrochemical characterization .....	131
6.3.	Characterization results of the N-M@CNi interlayer and relevant analysis .....	132
6.4.	Conclusions.....	143
6.5.	References.....	144
Chapter 7 Conclusion and perspective.....		149

## List of Abbreviations and Acronyms

Abbreviations	Complete spelling
1D one-dimensional	1D one-dimensional
2D two-dimensional	2D two-dimensional
3D three-dimensional	3D three-dimensional
Al	Aluminum
ALD	Atomic layer deposition
Ar	Argon
CB	Carbon black
CH <sub>4</sub>	Methane
CV	Cyclic voltammetry
CVD	Chemical vapor deposition
DCDA	Dicyandiamide
DI	Deionized water
DME	Dimethoxyethane
DOL	Dioxolane
EDS	Energy dispersive X-ray spectrometer
EIS	Electrochemical impedance spectroscopy
GF	Graphene foam
GFMX	Graphene foam @ MXene
GF@ZnO	Graphene foam @ ZnO
HCl	Hydrogen chloride
H <sub>2</sub>	Hydeogen
LiF	Lithium fluoride
LIBs	Lithium-ion batteries
Li-S	Lithium-sulfur
LiTFSI	Lithium bis (trifluoromethanesulfonyl) imide

Ni	Nickel
N-M@CNi	N-doped MXene@carbon nanosheets-Ni composite
NMP	N-Methyl-2-pyrrolidone
MAX	Ti <sub>3</sub> AlC <sub>2</sub>
MXene	2-D metal carbides
OCP	Open-circuit potential
PEDOT:PSS	poly (3,4-ethylene dioxythiophene):poly (styrene sulfonate)
PVDF	Poly(vinylidene fluoride)
S	Sulfur
sccm	Standard cubic centimeter per minute
SEI	Solid-electrolyte interphase
SEM	Scanning electron microscopy
TEM	Transmission electron microscopy
XPS	X-ray photoelectron spectroscopy
XRD	X-ray diffraction
ZnO	Zinc oxide

## Chapter 1: Literature reviews

### 1.1 Introduction of Li-S batteries

#### 1.1.1 From fossil fuel to green energy: the background of Li-S batteries' emerging

It cannot be denied that the booming economy and the flourishing human society of the past century are based on the growing energy consumption. Currently, the development of many modern industries has heavily depended on the combustion of many resources, like biomass and fossil fuels, causing a massive and ever-growing carbon emission during the past decades. From 1971 to 2010, the world's carbon dioxide emissions grew from 20.1 billion tones to 32.7 billion tones [1]. Meanwhile, the massive carbon emission produced by the fossil fuel combustion arises international recognized concerns about global climate change and environmental pollution [2]. To ameliorate this situation without economic stagnation, an essential solution is to replace these fossil fuels with long-term sustainable energy alternatives. Up to now, most of these green energy resources, including solar energy, hydropower, and wind power, are considered as intermittent power sources [3]. Therefore, an effective approach to utilize these power sources is to develop high energy storage devices that can be substituted for combustion engines.

To this day, the most popular electrochemical energy storage system is the rechargeable Li-ion battery (LIB). It has replaced other energy devices like Ni-Cd cells and Ni-metal hydride cells since the Japanese company Sony has developed the cells consisting of lithium cobalt oxide as a cathode and graphite as an anode in 1991 [4]. The LIB has dominated the rechargeable battery market by a factor of 2.5 of any other related battery technologies due to its high value of energy density, typically of 150 Whkg<sup>-1</sup> and 650 Whl<sup>-1</sup> [5]. This feature has made the LIB as the first choice in portable electronic market, including mobile phones, laptop computers, and digital cameras.

Due to its success in the electronic market, the LIB has also been employed as the power source for the electric vehicles (EVs). Nevertheless, the LIB encounters several setbacks in meeting the requirements of EV industry. One of the most important issues is the insufficient energy density [6]. Compared with the portable electronic device, EVs requires remarkable advance in the energy density of

LIBs to compete with combustion engines. However, the typical target for an electric vehicle is to drive a 500 km distance after a single-pass charging, and a future proposal for the battery in electric vehicles is to reach an energy density of 500 Whkg<sup>-1</sup> by 2030 [7], both of which far beyond the theoretical limit of LIBs [8, 9]. Therefore, it is exigent to explore other novel energy storage systems with novel electrochemistry that can surpass the energy limit of LIBs.

### 1.1.2 The development and advantages of Li-S batteries

The key factor limiting the theoretical energy density of LIBs is its topotactical insertion chemistry, which only allows specific sites in the crystal of electrode materials to accommodate the lithium ions [10]. Hence, different battery mechanisms should be put forward to make breakthrough in the energy density. One of the most attractive candidates is the lithium sulfur (Li-S) battery, whose concept was firstly proposed by Herbet and Ulam in a U.S. patent in 1962 [11, 12]. The Li-S battery is based on a non-topotactic reaction mechanism between a lithium metal anode and a sulfur cathode. The lithium metal is an attractive anode providing a low reduction potential of -3.04 V (Li/Li<sup>+</sup>) versus standard hydrogen electrode (SHE) and a high theoretical capacity of 3862 mAh g<sup>-1</sup> owing to its low density (0.534 g cm<sup>-3</sup>) [13]. Meanwhile the lithium metal can be used directly as the anode without conductive additives and binder, delivering a more attractive energy density performance in practical application. On the other hand, the sulfur element is the cathode material with the highest theoretical capacity (1673 mAh g<sup>-1</sup>) among all solid elements [12]. Thus, the combination of Li and S presents an alluring theoretically energy density of 2567 Wh kg<sup>-1</sup> or 2199 Wh l<sup>-1</sup> [8], as shown in **Figure 1.1**, which exceeds the requirement of a 500 km-drive for EVs and surpasses the performance of a commercial LIB. Another attractive characteristic of Li-S batteries is the abundance of the raw material of the cathode, for that the sulfur is the 10<sup>th</sup> most abundant element in the universe and it is the by-product of the gasoline refining process [14], which is expected to meet the criterion cost requirement of the EV (less than \$125/kWh) [15]. Besides, the sulfur also shows more human and environment benignant than electrode materials in LIBs [16], thus causing less pollution problems. In conclusion, the Li-S battery is regarded as a promising energy storage system for the next-generation EV power source.

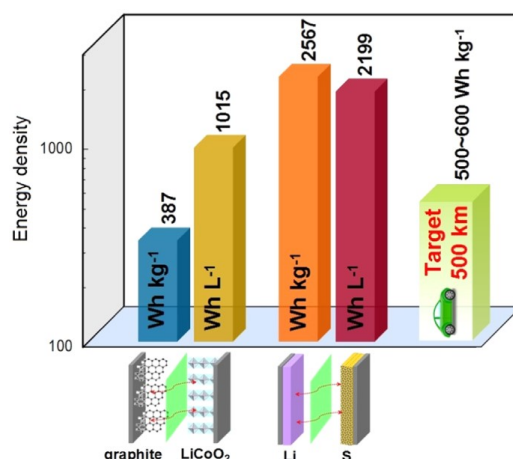
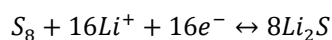


**Figure 1.1** Schematic comparison of theoretical gravimetric and volumetric energy densities between LIB (graphite/LiCoO<sub>2</sub>) and Li-S batteries. A 500 km distance is used as a benchmark for the future requirement of EV energy storage [3].

### 1.1.3 The mechanism and challenges of Li-S batteries

Unlike the Li ion insertion mechanism of LIBs, the Li-S battery works similar to conventional batteries through charge transfer reactions [12]. Despite that the earliest prototype battery uses the molten KCl-LiCl mixed salt as electrolyte at high-temperature (>400 °C) [17], modern Li-S battery is operated at room temperature, consisting of Li metal anode, S-containing cathode, and the organic electrolyte. During a discharge process, the Li anode is oxidized to Li ion (Li<sup>+</sup>) which is driven to the S cathode while electrons move through the external load in the same direction, as illustrated in **Figure 1.2**. For a charge process, the Li ion and electron flows go reversely. An overall reversible redox reaction for this battery can be described as:



**Equation 1.1**

The average potential of this couple is 2.15 V (versus Li<sup>+</sup>/Li), which is lower than that of most commercial LIBs. However, this drawback can be compensated by the much higher gravimetric capacity of S, accompanied with the increased safety at lower operation voltage [11, 12].

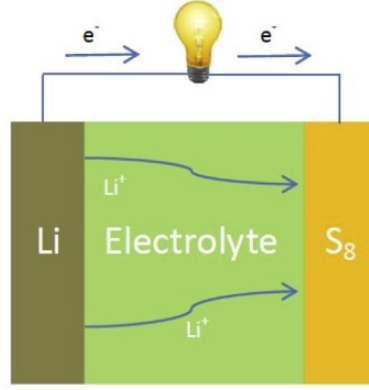
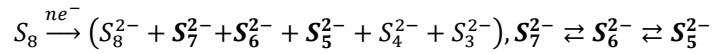


**Figure 1.2** Schematic of the discharge process of a Li-S battery with the metallic lithium anode and S-containing cathode, with an organic liquid electrolyte [16].

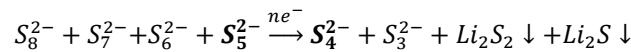
Although in **Equation 1.1** the battery reaction seems to be a simple redox process, the actual reactions happen in the discharging cathode are much more complexed, which involve a series of polysulfides conversion due to the dynamic chemical equilibria between them. Generally speaking, the discharge process can be divided into three parts [18]:

For cathode potential  $>2.3$  V, the first discharge plateau (major species are in bold):



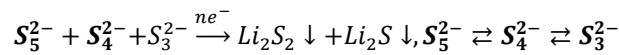
**Equation 1.2(1)**

2.1~2.3 V (major species are in bold):



**Equation 1.2(2)**

$<2.1$  V, the second discharge plateau (major species are in bold):



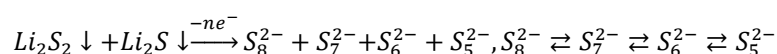
**Equation 1.2(3)**

The final discharge product is usually a mixture of  $Li_2S_2/Li_2S$ , not the fully reduced  $Li_2S$ . This is due to the sluggish solid/solid reaction that hinders the transformation.

Compared with the discharge process, the oxidation reaction of the cathode is relatively simpler,

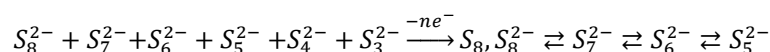
which is consisted of two parts:

For cathode potential <2.4 V,



**Equation 1.3(1)**

When cathode potential >2.4 V,



**Equation 1.3(2)**

Corresponding to **Equation 1.2** and **Equation 1.3**, the typical charge/discharge profiles of Li-S battery are plotted in **Figure 1.3**. It is worth noting that although the  $\text{S}_8$  and discharged products ( $\text{Li}_2\text{S}_2/\text{Li}_2\text{S}$ ) are solid phase, the polysulfides intermediates ( $\text{S}_n^{2-}$ ) are soluble in the organic electrolyte, especially the high-order polysulfides. Therefore, the redox process involves the interaction between liquid and solid phases. When the second discharge plateau begins, a potential dip happens due to the Li ion concentration polarization, which is caused by the accumulated dissolved polysulfides that increase the viscosity of the electrolyte [19]. Another factor is the overpotential required by the nucleation of solid  $\text{Li}_2\text{S}_2$  phase from liquid electrolyte [20]. For the charge process, similar potential barrier occurs when the solid  $\text{Li}_2\text{S}/\text{Li}_2\text{S}_2$  phase begins to be oxidized to liquid phase polysulfides. Instead of plateaus, the charge process has only one plateau which corresponds to the oxidation of polysulfides to elemental  $\text{S}_8$ .

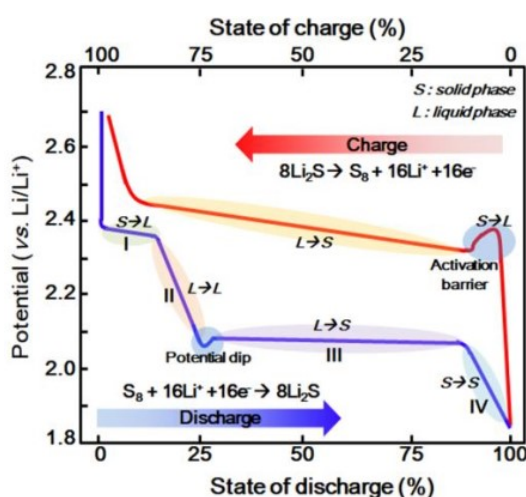


**Figure 1.3** The schematic of a theoretical charge/discharge profile of the Li-S battery [15]. Note that due to the sluggish solid phase reduction of  $\text{Li}_2\text{S}_2$  to  $\text{Li}_2\text{S}$ , the practical final reduction products are usually a mixture of  $\text{Li}_2\text{S}_2$  and  $\text{Li}_2\text{S}$ .

Despite these attractive features of the Li-S battery, some critical problems still hinder it from scalable practical application. The critical concerns are: (I) the insulating nature of the sulfur ( $5 \times 10^{-30}$  S cm<sup>-1</sup>) [21] and Li<sub>2</sub>S ( $10^{-13}$  S cm<sup>-1</sup>) [22] that greatly retards the redox in the cathode; (II) the large volumetric expansion of the sulfur upon lithiation process (~80 %) and corresponding matrix collapses [23]; (III) the dissolved high-order polysulfides that formed during the charge process diffuse to the Li anode due to the concentration gradient and then get reduced to the low-order polysulfides. The reduced polysulfides can be re-oxidized after moving back to the cathode [24-26]. This “shuttle movement” of the polysulfide is called the “shuttle effect”, which is one of the major causes for the low Coulombic efficiency and capacity degradation of Li-S batteries. (IV) On the Li anode side, the diffused polysulfides may be deposited on the anode, resulting in the insulated Li<sub>2</sub>S<sub>2</sub>/Li<sub>2</sub>S precipitation. This may affect the solid electrolyte interphase (SEI) on Li anode, which is essential in protecting the anode from electrolyte corrosion. (V) Also, the heterogeneous nucleation of Li anode during repeated stripping/plating process leads to an unwanted dendritic lithium growth, which may penetrate the separator together with a fatal short-cut. Meanwhile the shrinkage and growth of the dendrite also induce the collapse of the SEI. In conclusion, most of these issues are originated from the sulfur-related intrinsic problems and the uneven stripping/plating of the Li.

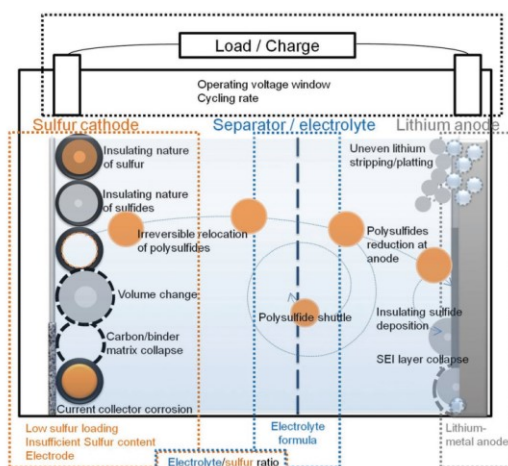


**Figure 1.4** The schematic of some intrinsic and extrinsic drawbacks of Li-S batteries [13].

## 1.2 Current research reviews of Li-S batteries

To tackle these problems, many researches have been conducted from different aspects of Li-S batteries, including cathode and anode refinement, electrolyte design, and battery configuration design

and so on. In the following part these works will be reviewed in four parts that have the most effect on the batteries' performance: Li anode, electrolyte, S-based cathode, and interlayer (battery configuration).

### 1.2.1 Li anode

Several issues that Li anode faces during the practical application are shown in **Figure 1.5**. Among all these problems, the dendrite growth and instability of SEI are the origin of other issues, so they are the research centers for Li anode refinement. In this part only the dendrite growth-related will be reviewed, as the SEI mainly involves the interaction between Li and the organic electrolyte and will be discussed in the next part.

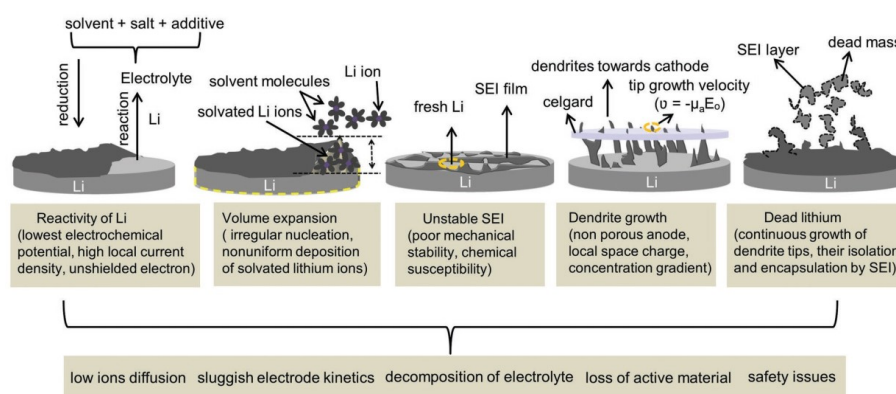


**Figure 1.5** The schematic of different issues faced by the Li metal anode during practical application [27].

The dendrite growth of Li anode in plating is originated from its crystal structure. A comparative density functional theory (DFT) study showed that the magnesium has higher free energy difference between high-dimensional and low-dimensional phases than Li [28], which explained that Mg tends to form bulk or plate shape structure, rather than one-dimensional (1D) dendrite. On the other hand, Li is more likely to generate dendrite. Another calculation study showed the Mg exhibits lower diffusion barriers than that of Li [29], therefore the latter has stronger tendency towards a rough surface growth namely having more chance of dendrite forming. Consequently, two factors, the lower surface energy and higher diffusion energy of Li result in its higher tendency in dendrite formation.

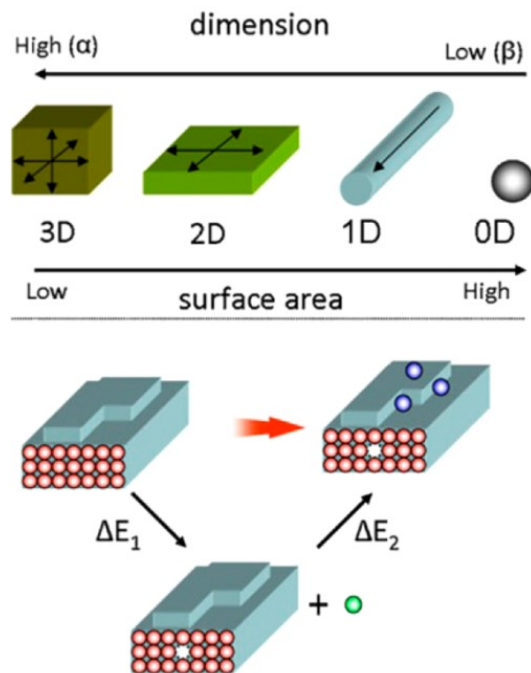


**Figure 1.6** The schematic of the high-dimensional phases to the low-dimensional phases [28].

The suppression of Li dendrite has been conducted in many ways, including electrolyte additives [30] or electrolyte formula refinement [31, 32]. More detailed discussions will be presented in the electrolyte part. Other strategies include pretreatment of Li anode (either physically [33] or chemically [34]), charging/discharging operation altering [35], and structuring of Li anode [36]. An example of nano-structured Li metal-host can be found in **Figure 1.7**, in which the graphene oxide (GO) membrane was mask-covered, flash-etched and reduced, leaving horizontal aligned pores on the reduced graphene oxide (rGO) membrane [36]. Using this porous matrix as Li host, the super-aligned pores can effectively accommodate the dendrite and prevent it from horizontal growth, which greatly reduced the risk of short-circuit and volume expansion upon stripping/plating.

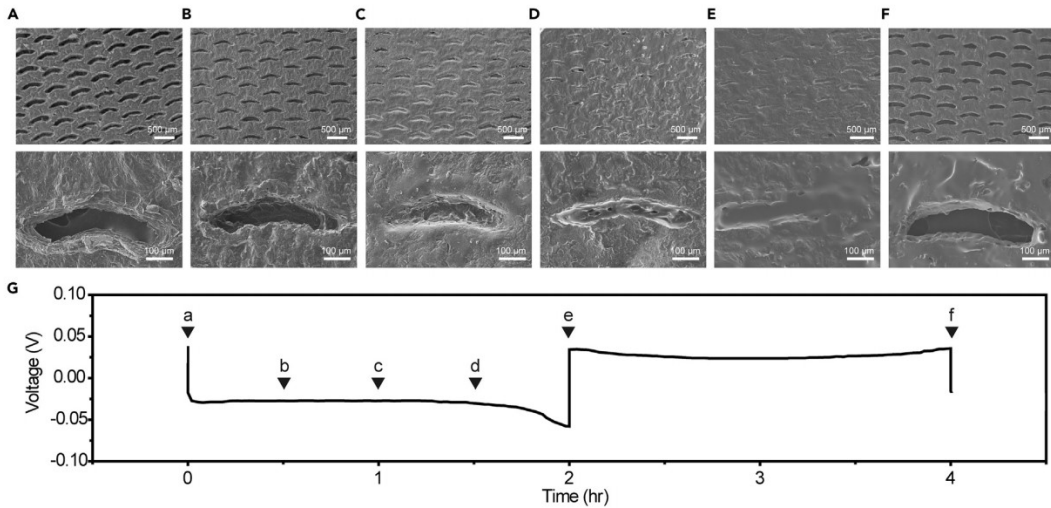


**Figure 1.7** (A–F) Surface morphology evolution characterized by scanning electronic microscope (SEM) of the P-rGO/Li anodes. (A–F) correspond to the different charge/discharge states in (G) [36].

Although these shortcomings of Li anode can be observed in any batteries applying Li anode, it is worth noting that the dendrite growth issue may be more alleviated in Li-S batteries. An *in-situ* study demonstrated that with the co-operation of  $\text{Li}_2\text{S}_8$  and lithium nitrate ( $\text{LiNO}_3$ ) additives in ether-based electrolyte, the dendrite growth is greatly suppressed [37], as shown in **Figure 1.8**. This finding suggests that for all Li-S batteries that using metal Li as anode, the dendrite situation can be superior than other batteries utilizing the same anode, for that moderate amount of the  $\text{Li}_2\text{S}_8$  that inevitably produced by the shuttle effect will be naturally introduced into the electrolyte, thus reducing the impact of dendrite growth with  $\text{LiNO}_3$  which is a common additive in Li-S electrolyte. Therefore, in the situation of Li-S batteries, more research effort was devoted to the cathode, electrolyte, separators, and other parts of batteries.

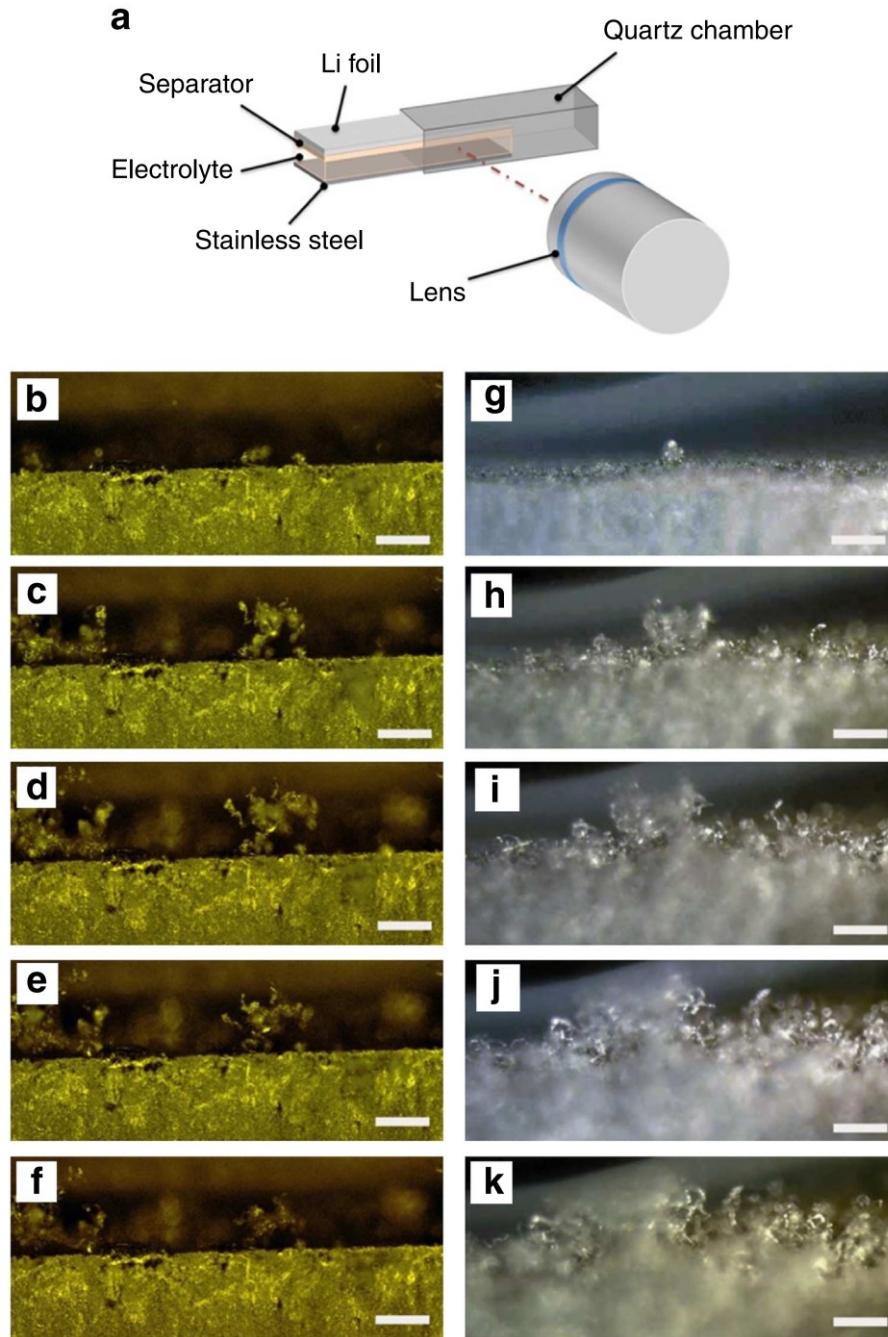


**Figure 1.8** *In-situ* optical microscopy study of the  $\text{Li}_2\text{S}_8$  and  $\text{LiNO}_3$  effect on lithium dendrite formation. (a) Schematic illustration of the *in-situ* observation equipment. (b–f) The cross-section of the cell with the addition of both  $\text{Li}_2\text{S}_8$  and  $\text{LiNO}_3$ , showing the dendrites evolution process versus increasing lithium deposition time. (g–k) The comparison with only  $\text{LiNO}_3$  addition at the same condition. All the scale bars are 100  $\mu\text{m}$  [37].

### 1.2.2 Electrolyte

The electrolyte is the internal electrochemical connection of cathode and anode in Li-S batteries. Therefore, it needs to fulfil requirements from both electrodes. Other demands include high stability and

ionic conductivity, appreciable Li salt dissociation ability, moderate polysulfides solubility, and so on [38-40]. The most commonly used electrolytes can be divided into liquid electrolytes, ionic liquid based electrolytes, and non-liquid electrolytes [38]. Their concepts, designing, and refinement have important effect on the performance of Li-S batteries.

Considering high sensitivity to water for the metal lithium, the liquid electrolytes used in Li-S batteries are usually based on the organic liquid solvent. The concept of organic liquid electrolyte is originated from LIBs, consisting of a lithium salt dissolved and a matrix of organic solvent with small molecules. The most typical Li-S electrolyte used currently is the 1:1 (v:v) mixture liquid electrolyte of 1,3-dioxolane (DOL) and 1,2-dimethoxyethane (DME), dissolving the lithium bis (trifluoromethanesulfonyl) imide ( $\text{Li}[\text{N}(\text{SO}_2\text{CF}_3)_2]$ , LiTFSI) at 1 M concentration [41]. More often it is used with ~1 wt % lithium nitrate additive [42-47].

For the Li metal anode, the electrolyte has direct influence on dendrite growing behavior. One of the most convenient and recognized approach to suppress the dendrite is the utilization of additives. It is easy to realize prominent behavior amelioration of Li anode with small concentration of additives. One typical example of these effective additives is the small molecules with sulfur or phosphorous atom that can be absorbed on the Li metal surface, such as thiourea ( $\text{S}=\text{C}(\text{NH}_2)_2$ ) [30]. As shown in **Figure 1.9**, with only 0.02 M thiourea addition, the dendrite growth can be strongly controlled even after 2 h continuous Li deposition. The mechanism of this superb performance can be ascribed to a “super filling” effect: upon the Li deposition, the thiourea tends to enrich on the concave surface, while the Li deposition energy ( $\Delta E_{\text{deposition}}$ ) with thiourea (-0.456 eV) is much lower than the one (0.029 eV) of free Li on the free (001) surface. Hence, the nucleation on the concave surface is promoted by the adsorption of thiourea, altering the dendrite growth to a smooth deposition.

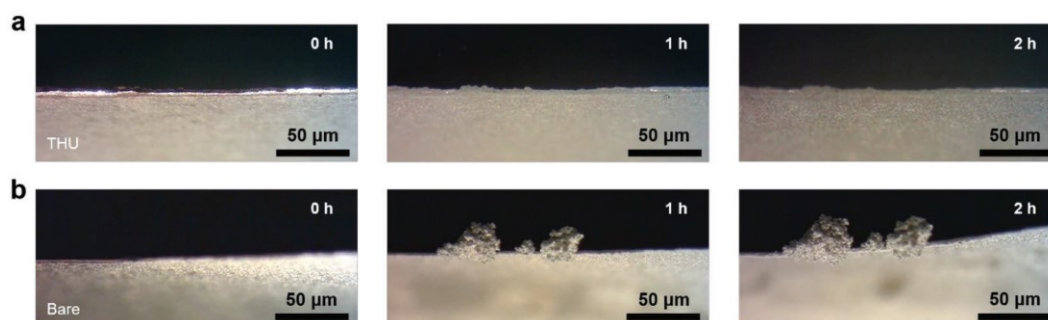


**Figure 1.9** The *in-situ* microscopy comparative observation of Li metal deposition in electrolyte (a) with and (b) without thiourea additive [30].

Early work by Sion Power had established an electrolyte solvent of DOL and DME mixture, concerning the stable SEI by DOL and high polysulfides solubility by DME [48]. This combination gives the Li-S battery good rate capability and low temperature performance ( $< -20\text{ }^{\circ}\text{C}$ ), and has become one of the most recognized electrolyte solvent formulas for Li-S researches [41-47]. Despite the well recognition, many efforts have been made to optimize the solvent to reach a better synthetic performance. In Ref.[32] the short-chain diethylene glycol dimethyl ether (DEGDME) was chosen as the new solvent for Li-S battery electrolyte, due to its high conductivity ( $> 10^{-2}\text{ S cm}^{-1}$ ), low viscosity, low flammability (Figure 1.10), and high solvating ability.

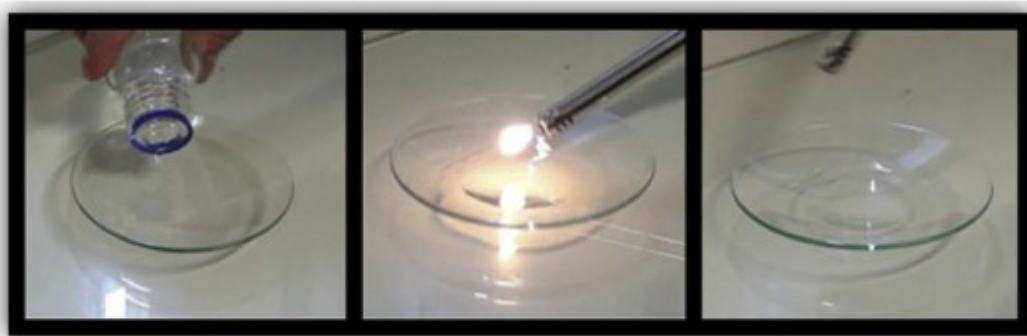


**Figure 1.10** The demonstration of low flammability of the DEGDME-LiTFSI-LiNO<sub>3</sub> electrolyte by direct ignition test [32].

In addition to electrolyte studies focusing on the formula optimizing, some researches have chosen a more radical strategies in solving the Li-S drawbacks, i.e. building up an innovated class of electrolyte. These pioneering works include ionic liquids-based electrolytes [49-51], solvent-in-salt electrolytes [52, 53], and solid-state electrolytes [54]. Owing to their unique features, although not comparable to liquid organic electrolytes in overall performance, these novel electrolyte systems exhibit attractive properties in certain aspects.

*Ionic liquids-based electrolytes:* Being non-volatile, non-flammable, high ionic conductive, the ionic liquids are also promising for its large electrochemical stability windows and strong solubility for lithium salts [55]. At the meantime, drawbacks with ionic liquids in electrolytes are obvious, including their much higher viscosities, their substantially higher costs than those of the conventional organic electrolytes, and potential toxicity. Early in 2006, Yuan *et al.* [50] have utilized the (N-methyl-N-butyl-piperidinium bis(trifluoromethanesulfonyl) imide (PP14-RTIL)) as the electrolyte for Li-S batteries. This application has achieved an initial capacity of  $1055\text{ mAh g}^{-1}$ . The cyclic voltammetry of the cell with this PP14-RTIL electrolyte presents only one cathodic peak at  $\sim 2.2\text{ V}$  from the second scanning, rather than

typical two cathodic peaks in the organic liquid electrolytes, as illustrated by **Figure 1.11**. This unusual behavior, as stated by authors, is an evidence of poor dissolvability of high-order polysulfides in this ionic liquid electrolyte. Nevertheless, more detailed studies on the interaction between ionic liquids and electrodes are needed for their due attention [38].

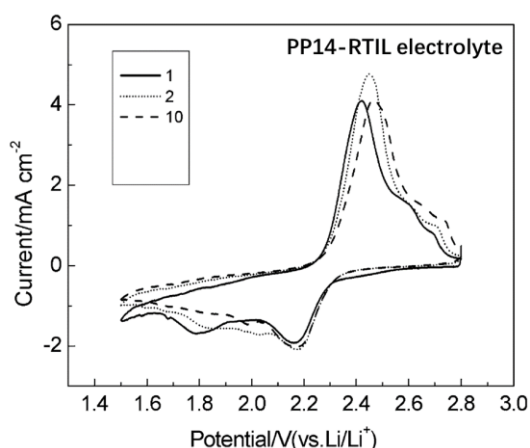


**Figure 1.11** The CV curves of the Li-S cell with PP14-RTIL electrolyte. The 1<sup>st</sup>, the 2<sup>nd</sup>, and the 10<sup>th</sup> cycles are shown in solid line, dot line, and dashed line, respectively [50].

*Solvent-in-salt electrolytes:* This concept was introduced by Suo *et al.* [52] in 2013, in which the salt concentration reaches an ultrahigh level that the ratio of salt-to-solvent exceeds 1 by either volume or weight (**Figure 1.12b**), with an optimized molar concentration of 7 mol l<sup>-1</sup> of LiTFSI in DOL : DME (1:1 by volume) solvent. This feature brings mainly two significant improvements: first, the shuttle effect is greatly suppressed, as the lithium salt is almost saturated in the electrolyte, causing high-order polysulfides barely soluble; another point is the stabilizing of the metal lithium anode. Due to the flooded anions, the anions depletion is minimized. Therefore, the overall uniformity of the lithium surface is enhanced. Therefore, the dendrite growth is also restrained. Another study reported by Shin and co-workers also applied a concentrated electrolyte for a sulfur-carbon nanocomposite cathode. They found that the overcharge capacity can be greatly reduced by this high lithium salt concentration, although the concentration of lithium salt only reaches 5 mol l<sup>-1</sup> and cannot fully suppress the polysulfides dissolution [53].

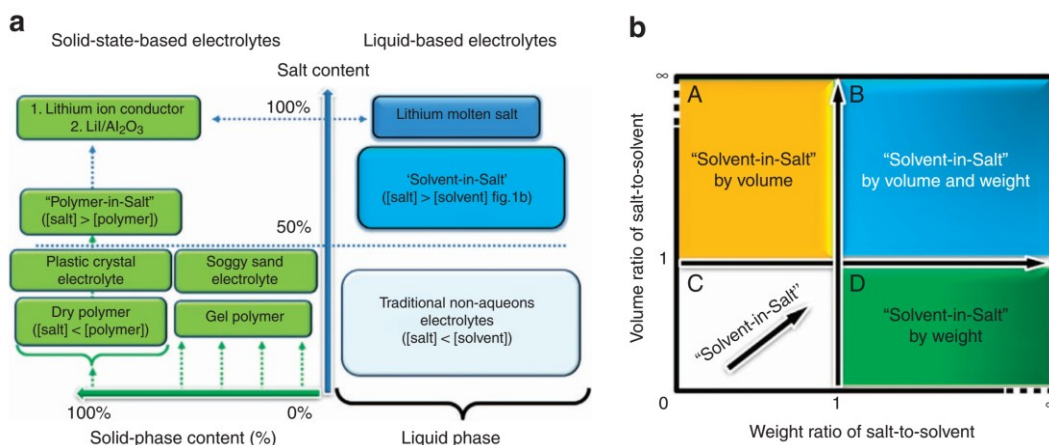


**Figure 1.12** The schematic of the concept of Solvent-in-Salt electrolyte. (a) A conclusion of currently available electrolytes and classification. (b) The distribution map of different non-liquid organic electrolytes based on volume ratio and weight ratio of salt-to-solvent [52].

*Solid-state electrolytes (SSEs)*: Despite that liquid electrolytes still being the mainstream of the Li-S batteries field, a growing amount of studies are adopting the non-liquid electrolyte concepts, especially the solid-state electrolytes (SSEs). SSEs can be classified according to their main components: polymer SSEs [56, 57], oxide SSEs [58], sulfides SSEs [59, 60], hybrid SSEs [61, 62], and other SSEs [63, 64]. Replacing the liquid electrolytes by SSEs can be very beneficial for constructing safe and high energy density Li-S batteries, due to the latter's wide electrochemical stability windows and superior thermal durability [65]. Nevertheless, there are still some challenges for Li-S batteries applying SSEs. For the battery using polymer SSEs, the multi-step reaction mechanism causes the same "shuttle effect" issue as those using the liquid electrolytes [56, 66], as indicated in **Figure 1.13C**. Nevertheless, this issue can be prevented in the all-ceramic-based SSE, especially for the sulfide SSE. Due to the solid-to-solid reaction in this system, a diverse charge/discharge profile is observed in **Figure 1.13E** with only one discharge plateau at 1.9 V. However, sulfides SSEs have a nonnegligible problem involving its chemical instability. The sulfides SSEs were reported to present a 150-300 mAh g<sup>-1</sup> discharge plateau, indicating their participation of the discharge reaction [67]. Even at open circuit state, certain types of SSEs like Li<sub>10</sub>GeP<sub>2</sub>S<sub>12</sub> [68] and Li<sub>9.5</sub>Si<sub>1.74</sub>P<sub>1.44</sub>S<sub>11.7</sub>Cl<sub>0.3</sub> [69, 70] can react with Li anode *via* direct contact, deteriorating the stability of Li-S batteries during storage. Besides, the interfacial contact between SSEs and electrodes is limited by their point-to-point contact model, causing a restricted Li<sup>+</sup> ion transportation through the interface. This restriction consequently degrades the overall electrochemical performance of the battery. This non-uniformed contact between SSEs and the anode also aggravates the Li dendrite growth on the Li metal surface, which is even more severe in the solid-phase reaction systems due to the

absence of the dissolved polysulfides, for that the dissolved polysulfides along with the lithium nitrate additive can suppress the dendrite formation [37]. Last but not the least, the volumetric change of both anode and cathode is a challenge for the SSE. The rigid SSE may apply considerable strains to the active material during cycling, resulting in the detachment between sulfur and conductive matrix. It can be concluded that applying SSE is a promising Li-S battery refinement strategy, but necessary improvements need to be done to realize scalable, durable and safe solid-state Li-S batteries.

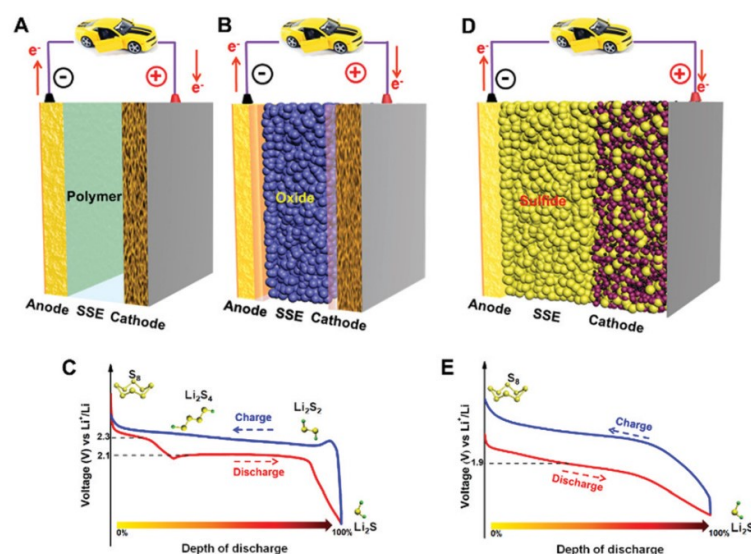


**Figure 1.13** The schematic of Li-S battery configurations with different types of SSEs: (A) polymer SSE, (B) oxide SSE, and (D) sulfide SSE. The illustration of galvanostatic charge/discharge profiles of battery systems with (C) quasi-solid and (E) solid electrolytes [65].

### 1.2.3 S-based cathode

As a result of the intrinsic drawbacks of Li-S batteries, the progression of Li-S batteries studies has been stagnant since 1962, in which the concept of Li-S battery was aroused. Later, the booming of LIB and its success in commercialization have attracted much attention. As the development of EVs urges the energy storage devices with higher energy density, researchers started to transfer their attention on Li-S batteries. A first breakthrough was achieved by Nazar *et al.* in 2009, in which a highly-ordered mesoporous carbon-sulfur composite was utilized as the cathode material [71]. Ever since then, a growing number of studies have focused on the refinement of S-based cathode and it has always been the highlight for Li-S battery study. Up to now, tremendous approaches have been applied to make refinements on the S-based cathode in aspects like capacity performance, cycling stability, self-discharge

behavior, and energy density performance. These approaches can be divided into certain categories according to their different emphasized points: sulfur-based composites as active materials, modified binders, cathode structure design, *et al.* . In this section the S-based cathode will be reviewed based on various types of refinement approaches

### **Materials as the sulfur host**

**Carbon-based materials:** The carbonaceous materials are the most widely used and investigated sulfur host material due to its high conductivity, thermal and chemical stability, and easiness in structure modification. The typical production of the sulfur-carbon composite is an isothermal treatment of the mixture of sulfur and carbon at 155 °C for 8-24 h under protective atmosphere. During this process the melted sulfur fills in the pores or coats the surface of the carbon host through capillary force. The specific temperature is chosen for the lowest viscosity of liquid sulfur at this point [72].

To achieve a perfect sulfur host, the carbon material should possess a homogenous pore-distribution, a sufficient pore volume/specific surface area, and a strong polysulfides-trapping ability to realize satisfactory sulfur distribution and sulfur content, as well as the long-term cycling stability [73]. Therefore, researchers have made tremendous effort on designing and fabricating diverse carbonaceous materials as sulfur host. Here these carbon host research will be reviewed according to their structure, morphology and interfacial modification.

#### **I. 0-dimensional structure**

A material can be defined as the 0-dimensional (0-D) structure if it's within the nanoscale by all dimensions. For carbon materials, commonly used 0-D materials as sulfur host include nanospheres, nanocages or nano-shells, and quantum dots. These structures either encapsulate the sulfur within their internal micropores and void space, or wrap the sulfur particles by themselves. For instance, Jayaprakash *et al.* fabricated a mesoporous carbon sphere by hard-template method, and yield a C@S composite by sulfur vapor exposure with nearly 70 wt.% sulfur content [21]. This C@S composite delivered an initial 1071 mAh g<sup>-1</sup> and a residual 974 mAh g<sup>-1</sup> capacity after 100 cycles at 0.5 C rate (1 C = 1675 mA g<sup>-1</sup>). Wu and co-workers also applied the template-directed method and designed the hollow graphene hollow spheres (HGs) as the sulfur host [74]. Bearing 90 wt.% sulfur in the HGs/S composite, this composite manifested a high discharge capacity of 810 mAh g<sup>-1</sup> after 200 cycles at 0.5C rate owing to its improved ion/electron conductivity and effective sulfur accommodation (**Figure 1.14**). Another novel 0D carbon material is the graphene quantum dots (GQDs) which co-worked with the carbon black (CB) as the

surface modification of sulfur particles [75]. The QGDs and the CB together formed electrical conductivity high-way for sulfur, and prohibited the lithium polysulfides loss by the chemical adsorption of oxygen-rich functional groups on the QGDs (**Figure 1.15**). The comprehensive effect of the QGDs/CB shell facilitated the QGDs-S/CB composite to achieve a 1000 mAh g<sup>-1</sup> after 100 cycles at 0.5 C rate.

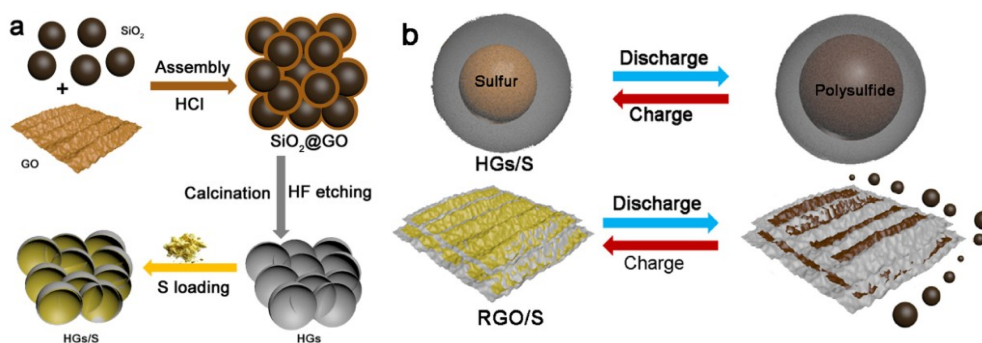


**Figure 1.14** (a) The schematic of fabrication process of the HGs/S composite by template approach. (b) A performance comparison between superior HGs/S composite and reduced graphene/sulfur (RGO/S) during cycling [74].

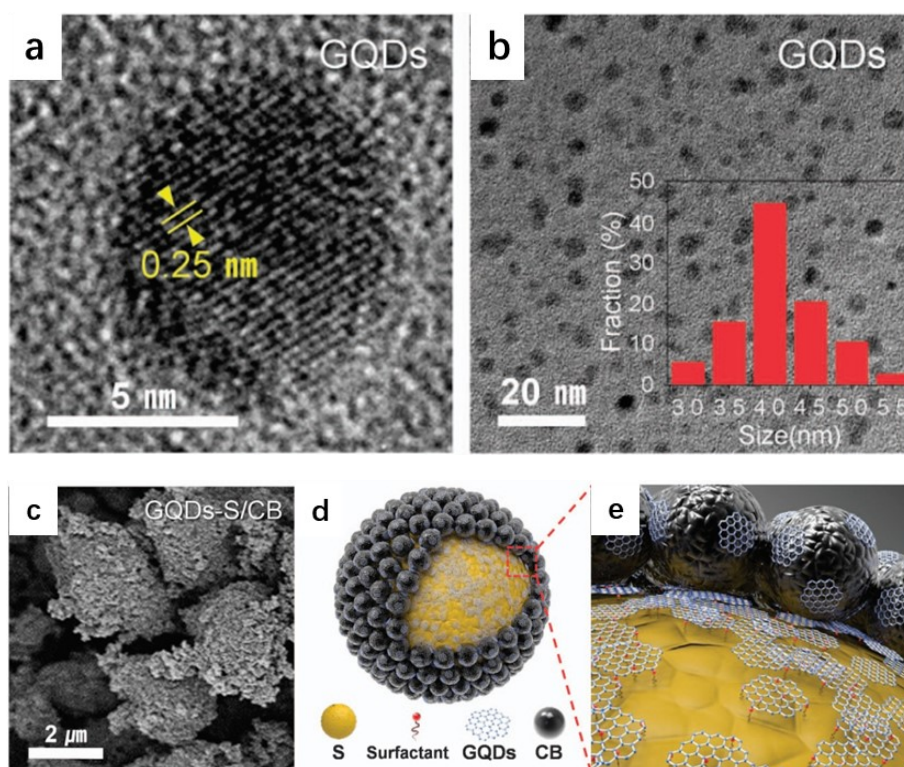


**Figure 1.15** (a)(b) The high-resolution of GQDs. The insert is the size distribution of GQDs. (c) The SEM image of GQDs-S/CB composite. (d) Schematics of GQDs-S/CB composite structure and (e) the magnified illustration near sulfur surface [75].

Apart from the carbon host, some studies focused on minimizing the size of sulfur particles to boost

the electrochemical kinetics and ameliorate the utilization of active material. An investigation designed a composite of monodispersed sulfur nanoparticles with different sizes on reduced graphene oxide (rGO), and pointed out that the smallest size (~5 nm) of sulfur nanoparticles presented an optimistic performance of an initial capacity of 1672 mAh g<sup>-1</sup> at 0.1 C, reaching the theoretical limit of Li-S battery [76]. The reduced sulfur size also resulted in the enhanced high-rate performance of 965 mAh g<sup>-1</sup> after 500 cycles at 1 C current. Such an outstanding capacity performance was ascribed to the nano-size effect (**Figure 1.16**): the small size of sulfur particles effectively increases the utilization of sulfur, leading to a direct improvement in specific performance. Besides, nano-sized particles also facilitate the lithium ion penetration through the insulating Li<sub>2</sub>S layer, thus improving the ultimate reduction of Li<sub>2</sub>S<sub>2</sub> solid core and increasing the specific discharge capacity. Another study on nano-sized sulfur used electrochemical deposition to deposit sulfur on nickel foam skeleton, and acquired sulfur nanodots with 2 nm average diameter [77]. This approach also achieved satisfying initial discharge capacity of 1458 mAh g<sup>-1</sup> at 0.1 C and high rate capability of 521 mAh g<sup>-1</sup> at 10 C. A highlight point in this electrode design was the sulfur mass loading can be adjusted from 0.21 mg cm<sup>2</sup> to 4.79 mg cm<sup>-2</sup>, which greatly enhanced the practical applicability for its high energy density.

While the nano-scaled sulfur particle exhibited attractive properties, some researchers continued to reduce the sulfur size down to less than one S<sub>8</sub> molecule. In 2010, Zhang and co-workers have fabricated carbon spheres with narrow pore size distribution of about 0.7 nm, being less than the length of one single crown S<sub>8</sub> molecule [78]. Therefore, the short linear chain configuration of sulfur at melt state could infiltrate the micro pores and be accommodated in the form of S<sub>8-x</sub> (0 < x < 8). By doing so, the high-order polysulfides that dissolves in the electrolyte were greatly reduced and the multi-step reduction of S<sub>8</sub> transformed into a one-step reduction, as evidenced in **Figure 1.17c**. This mechanism alternation radically eliminated the “shuttle effect” due to the vanish of high-order polysulfides, exhibiting superior cycling stability (**Figure 1.17d**). However, a low sulfur content is the limitation of this kind of composites, due to the necessary preserved pore space for electrolyte penetration [78-80]. When the pore space was fully filled by sulfur, as the 51 wt.% sulfur composite shown in **Figure 1.17d**, the cathode showed low sulfur utilization and resulted poor specific capacity.

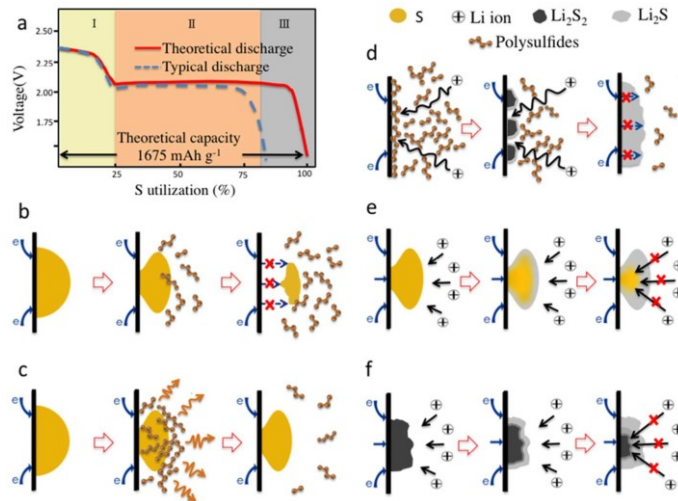


**Figure 1.16** Schematic of the nano-size effect on the sulfur particle in sulfur cathode: (a) a comparison between theoretical and practical galvanostatic discharge profiles of sulfur cathodes. (b) The dissolution of sulfur at the beginning discharge stage results in electrochemical disconnection with the electrode. (c) The diffusion of polysulfides during discharge process. (d) During the polysulfides reduction, the Li<sub>2</sub>S<sub>2</sub>/Li<sub>2</sub>S layer blocks the electron and Li ion transfer in electrode with large sulfur particle size. For the large sulfur particle, large Li ion flux may form blocking layer of Li<sub>2</sub>S on (e) sulfur and (f) Li<sub>2</sub>S<sub>2</sub> surface [76].

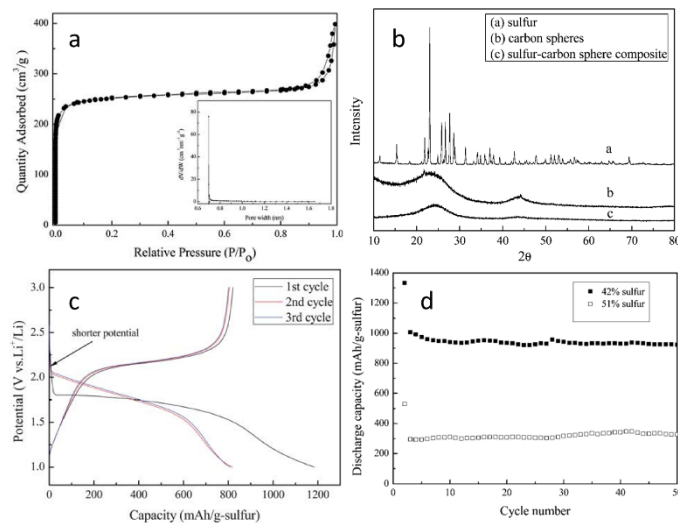


**Figure 1.17** (a) N<sub>2</sub> adsorption/desorption isotherms of the microporous carbon spheres with the insert of pore size distribution. (b) XRD patterns of sulfur, microporous carbon spheres, and microporous carbon spheres/sulfur composite. (c) The galvanostatic charge/discharge profiles of the carbon spheres/sulfur composite. (d) Cycling performance of carbon spheres/sulfur composite with 42% and 51% sulfur weight percent at 40 mA g<sup>-1</sup> [78].

## II. 1-dimensional structure

The most used 1-D carbon material in sulfur cathode is the carbon nanotube (CNT), which has high specific surface area and high electronic conductivity. Early in 2003 multiwall carbon nanotubes

(MWCNTs) were added to the cathode slurry by mechanical blending as both conductivity ameliorant and polysulfides absorber [81], but this rough application of MWCNTs showed unsatisfying cycling stability with capacity fading from about 500 mAh g<sup>-1</sup> to around 300 mAh g<sup>-1</sup> after 60 cycles at 100 μA cm<sup>-2</sup>. This result indicates that appropriate combination of CNT and elemental sulfur plays crucial role in the cathode performance. Therefore, following researches started to focus on the more intimate contact between CNT and sulfur to sufficiently take the advantage of this carbon nanostructure. Wang and co-workers fabricated the disordered carbon nanotubes (DCNTs) by an anodic aluminum oxide (AAO) membranes templated approach [82]. The obtained DCNTs array was impregnated with sulfur by S/CS<sub>2</sub> solution and subsequently heating process at different temperatures in vacuum. At high heating temperatures (300 °C and 500 °C), sulfur vapor further penetrated the void between graphitic and amorphous clusters in the DCNT, keeping the liquid electrolyte out of reach to inhibit the generation of high-order polysulfides. The physical confinement of the limited space forced the sulfur to exist in shorter chain-form, leading to divergent redox route with typical S<sub>8</sub> one's. Although improved cycling stability and Coulombic efficiency were achieved through this strategy, the limited sulfur content in the composite (40 wt%) still restricted its practical application. Cheng *et al.* also used AAO as template to build the CNT array, but the sulfur was built in the wall of CNT through the reduction of sulfate-AAO by acetylene (**Figure 1.19a**) [83]. Suffering from limited sulfur content (23-50 wt%), this free-standing film electrode by filtration provided 260 mAh g<sup>-1</sup> capacity based on the whole electrode mass. Another study used vertical aligned carbon nanotube (VA-CNT) array as the sulfur host took advantage of the void space within the CNT to reach a higher sulfur content of 69 wt% [84]. Using metal foil as the substrate, this self-standing cathode abandoned additives like binder and conductive, achieving discharge capacities higher than 800 mAh g<sup>-1</sup> of the total composite electrode mass (**Figure 1.19b**). Later, more sight was casted on an open structured sulfur on the CNT host, building up the sulfur content and utilizing the electronic conductive CNT framework to boost the redox kinetic [85, 86], as shown in **Figure 1.20**. Wang's group used the super aligned carbon nanotube (SACNT) as the matrix of sulfur nanocrystals to get a free-standing flexible electrode without other additives [85]. Benefiting from sufficient buffer volume and conductive framework of SACNT, this cathode realized high capacity of 1006 mAh g<sup>-1</sup> at 2 C and 879 mAh g<sup>-1</sup> at 10 C with sulfur content ranging from 50 wt% to 80 wt%. Another study also constructed a framework by single-wall carbon nanotube (SWCNT) as the conductive network to load the sulfur in a uniform and continuous coating form [86], as illustrated in **Figure 1.20b**. This design

maximized the sulfur loading with minimum carbon content, reaching an extremely 95 wt% high sulfur content in the whole free-standing electrode. As a result, a high areal capacity of  $8.63 \text{ mA h cm}^{-2}$  was obtained with a high areal sulfur loading of  $7.2 \text{ mg cm}^{-2}$ , which by far exceeded that of the commercial LIBs ( $4 \text{ mA h cm}^{-2}$ ).

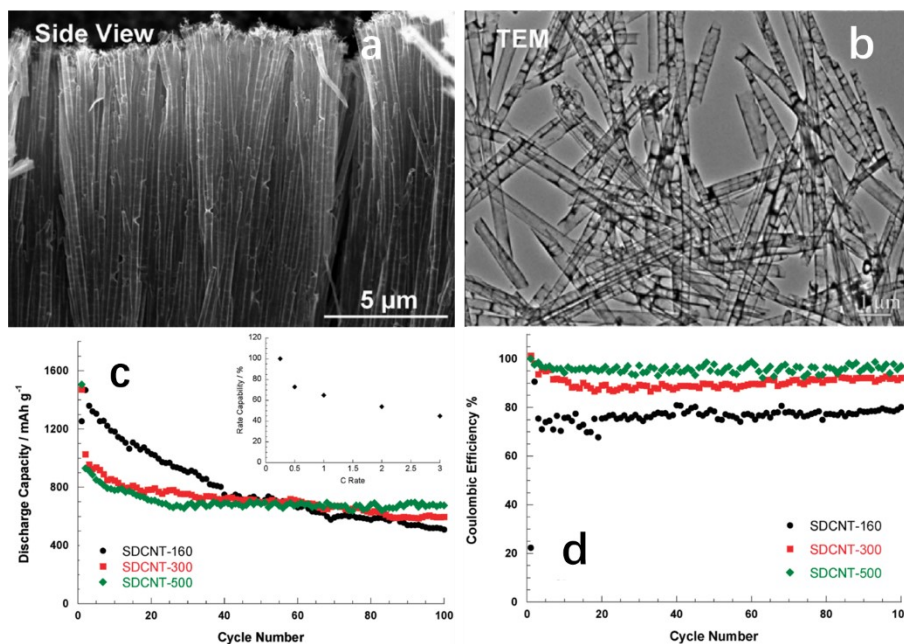


**Figure 1.18** SEM (a) and TEM (b) of the DCNTs prepared by the AAO-template method. Cycling performance (c) and Coulombic efficiency (d) of sulfur loaded CNTs (SDCNTs) samples with different sulfur impregnation temperatures [82].

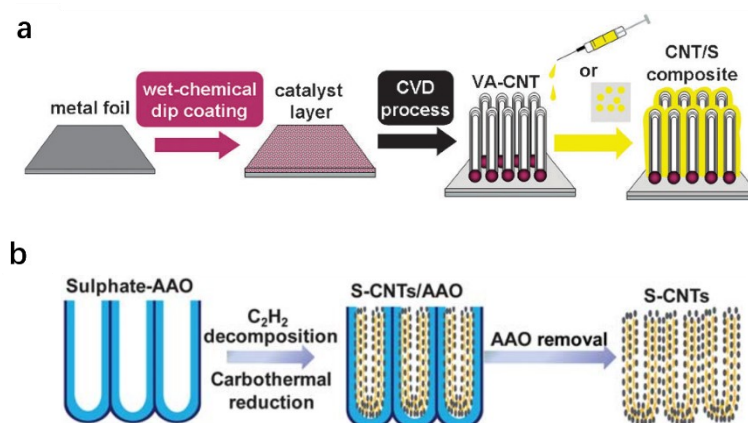


**Figure 1.19** Schematics of (a) VA-CNT/S electrode preparation [83] and (b) S-CNT electrode fabricated by AAO template and acetylene reduction of sulfate-AAO [84].

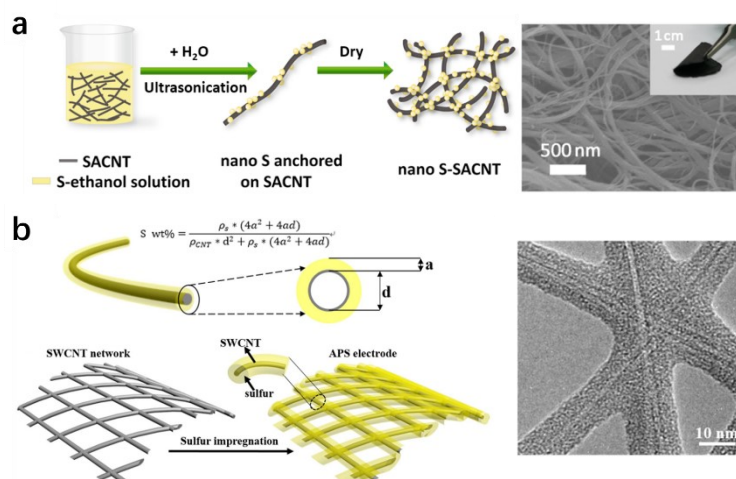


**Figure 1.20** (a) The schematic of nano S-SACNT fabrication process. The SEM image shows the morphology of the S-SACNT electrode with an insert of optical graph [85]. (b) The schematic of theoretical sulfur content calculation in a SWCNT network with uniform sulfur coating. The right image is the TEM characterization of a fabricated sulfur coated SWCNTs electrode [86].

### III. 2-dimensional structure

Typical 2-dimensional carbon nanomaterials are graphene and its derivatives. They have drawn extensive attention in the Li-S battery's cathode field for their unique 2-D structure. Graphene, as the one-atom  $sp^2$  carbon layer, exhibits high specific surface area, considerable chemical stability, high conductivity, and robust mechanical strength, while modification like oxidation and heteroatom-doping provides controllable property tailoring that meets requirements from different aspects.

Due to the flexible feature of graphene and graphene derivatives, they are often used to build buffer network to accommodate the volume expansion of sulfur particles and prevent polysulfides lose, like the poly(ethyleneglycol) (PEG) co-operated graphene oxide (GO) as the sulfur coating layer [87]. Similar design can be found in Abruna's paper, in which the graphene oxide-sulfur (GO-S) was wrapped by the amylopectin (GO-S-Amy) [88], as illustrated in **Figure 1.21**. This utilization approach of GO showed preminent cycling performance even at high sulfur loading of  $6 \text{ mg cm}^{-2}$  (**Figure 1.21 c**).

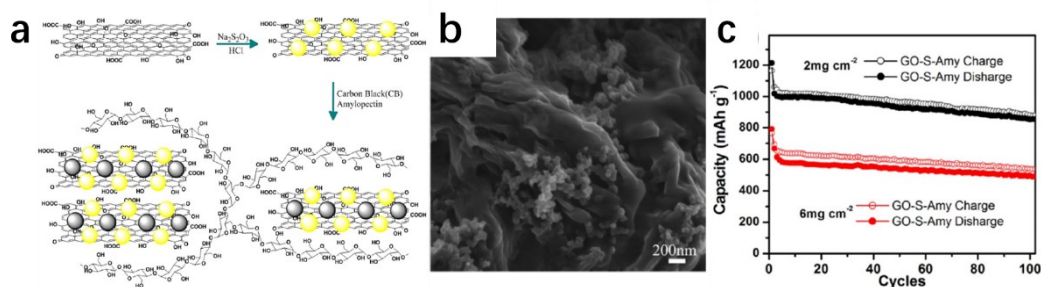


**Figure 1.21** Synthesis schematic (a) and SEM characterization (b) of GO-S-Amy composite. Cycling performance at 2 mg cm<sup>-2</sup> and 6 mg cm<sup>-2</sup> sulfur loading is shown in (c).

Besides acting as a protective wrapping layer of sulfur particles, graphene and derivatives can also become supporting matrix and current collector, leading to a self-support electrode without additional metal foil and binder. An outstanding example is the reduced graphene oxide-sulfur (rGO-S) free-standing film [89], in which the sulfur nanoparticles were deposited on the *in-situ* reduced rGO, self-assembling a compact film that can be direct used as the cathode in Li-S batteries. Due to the porous and interconnected structure of rGO, this electrode presented much superior capacity performance than the rGO-S mixture electrode (**Figure 1.22f, g**). More radical study proved that an all-graphene-based cathode can realize a high areal specific capacity of 7.5 mAh cm<sup>-2</sup> with cycling stability over 400 cycles [90].

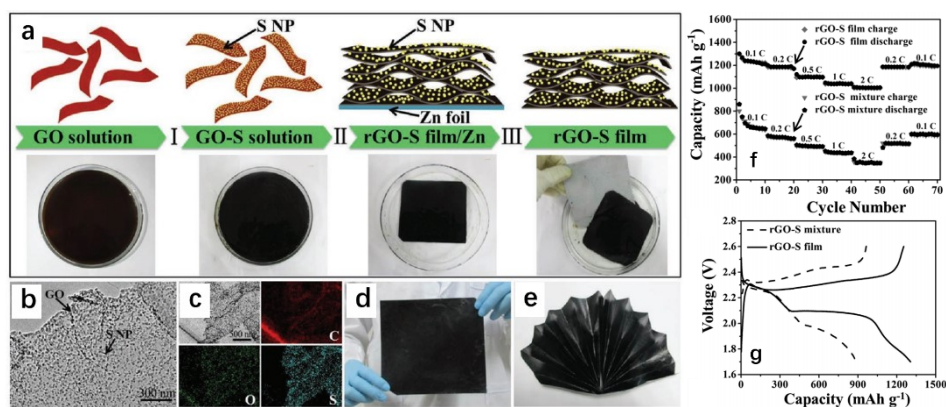


**Figure 1.22** (a) The self-assembling schematic of rGO-S film with corresponding optical image to each stage. The TEM image (b) and EDS mapping result (c). Macroscale image (d) and flexible demonstration (e) of the film. Rate performance comparison (f) and galvanostatic charge/discharge profiles (g) with the rGO-S mixture electrode, correspondingly [89].

#### IV. 3-dimensional structure

3-dimensional structured carbon hosts usually provide abundant meso/micropores and can accommodate the sulfur while enhance the electronic conductivity *via* inter-connected network. Typical examples are some graphene-constructed 3D porous structures, like the porous-graphene/sulfur (P-G/S)

fabricated by hydrothermal treatment of GO sheets of different lateral sizes [91]. By shrinking the pore size through smaller GO lateral diameters, the SP-G/S composite with 65 wt.% of sulfur can display 606.7 mAh g<sup>-1</sup> capacity after 300 cycles at 1 C with 99.0 % Coulombic efficiency. Geng's group derived a 3D sulfur@ porous carbon composite (3D-S@PGC) with extremely high sulfur content of 90 wt.% *via* a facile NaCl-templated method [92]. Due to its unique 3D networks that displays high electrical conductivities, large surface areas and high mechanical flexibility, this composite exhibited outstanding capacity performance of 1,382, 1,242 and 1,115 mAh g<sup>-1</sup> at 0.5, 1 and 2 C, respectively.

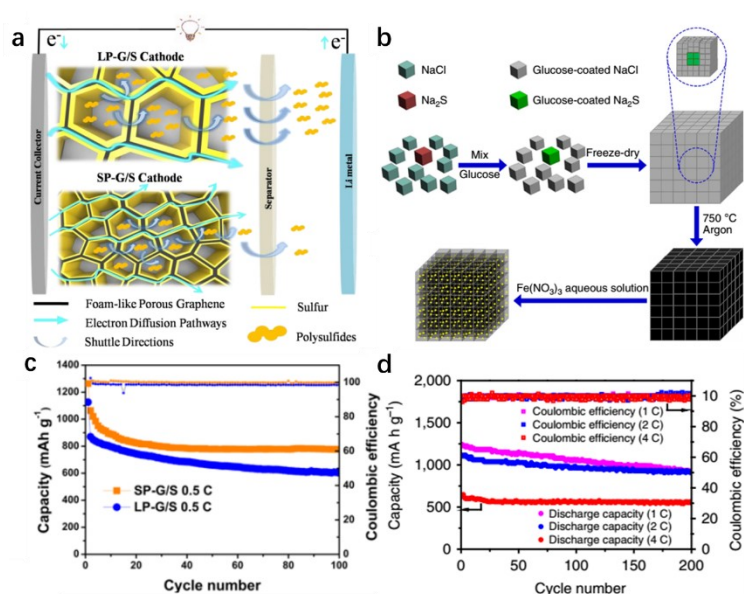


**Figure 1.23** (a) Schematic of the Li-S battery with porous-graphene/sulfur (P-G/S) with large and small pore sizes as the cathode and their cycling performance at 0.5 C (c) [91]. (b) The illustration of 3D sulfur@ porous carbon composite (3D-S@PGC) preparation and its cycling performance (d) [92].

## V. Heteroatom-doping

Although providing conductivity replenishment and robust attachment site for sulfur, carbon host with non-polar sp<sup>2</sup> bonding surface only delivers weak physical adsorption to polysulfides, like Van der Waal's force. By introducing heteroatoms, like nitrogen [93-96], sulfur [97], phosphorus [98], or their combinations [99, 100], the polysulfides adsorption ability of the carbon host can be greatly enhanced, resulting in greater sulfur utilization and more stable cycling performance. However, it should be noticed that different doping configurations may have considerable impact on the polysulfide trapping effect, sometime can be critical. one density functional theory (DFT) calculation stated that for the Li-S battery applying DME/DOL as solvent for electrolyte, only the clustered pyridinic N-dopants has higher binding

energy with polysulfides than that of solvents [101] (see the results in **Figure 1.24b**), which reminds researchers to introduce more of this configurations when designing N-doped carbon materials for sulfur host. Therefore, the regulation of the doping configuration is important in achieving desirable sulfur host for cathode.

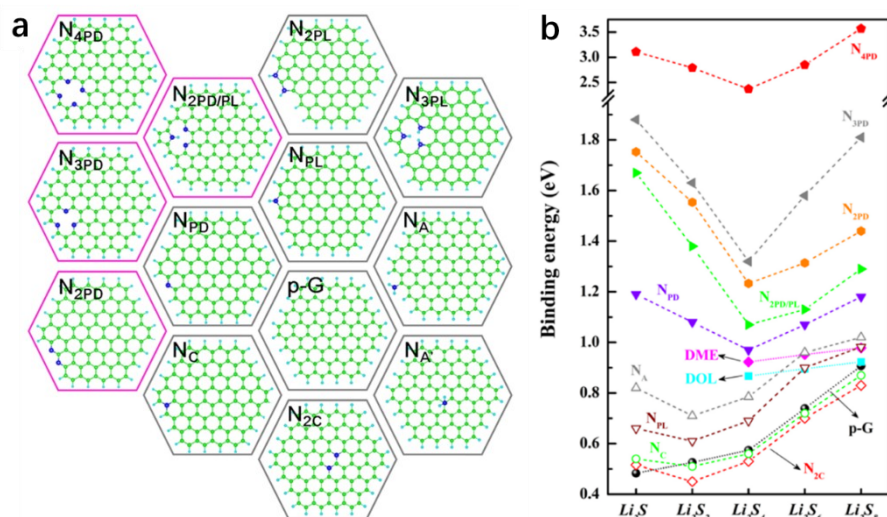


**Figure 1.24** (a) Structural illustration of pure graphene (p-G) and different N-doping configurations like graphitic N (N<sub>C</sub>), pyridinic N (N<sub>PD</sub>), and pyrrolic N (N<sub>PL</sub>). Anchoring of NH<sub>2</sub> groups are configurations of the N<sub>A</sub> at the edge and the N<sub>A'</sub> on the basal plane. (b) The conclusion of calculated binding energy between polysulfides and different N-dope configurations [101].

### ***Polymer-based materials:***

Besides the conductive carbon host, other conductive materials also drew attention for their unique features, especially the conductive polymers as they provide strong physical and chemical adsorption for polysulfides. Polyaniline (PAN or PANi), as one of conductive polymers, has been widely utilized as the protective coating material for sulfur composite due to its conductivity and easy polymerization process, like the PANi-S/MWCNT composite that showed 932.4 mAh g<sup>-1</sup> after 80 cycles [102]. Chen *et al.* used poly (3,4-ethylenedioxythiophene) (PEDOT) as the conductive polymer shell for nano sulfur particles [103], and the resulting S/PEDOT core/shell nanoparticles showed initial discharge capacity of 1117 mAh g<sup>-1</sup> and a stable capacity of 930 mAh g<sup>-1</sup> after 50 cycles. Wen and co-workers built hollow polyaniline sphere@sulfur composites with 600-800 nm diameters and 60 nm shell thickness, and this hollow design benefited the ion and electron conduction while effectively accommodated the volumetric variation of the sulfur [104], as illustrated in **Figure 1.25a**. This configuration rendered 602 mAh g<sup>-1</sup> even after 1000 cycles at 0.5 C, demonstrating its superior long-term stability. Meanwhile some tried to construct a more intimate contact between sulfur and polymers, such as the sulfur-polyaniline nanotubes

(SPANI-NT) in which the polymer was interconnected with sulfur by *in situ* vulcanization [105]. The electrode could retain a discharge capacity of 837 mAh g<sup>-1</sup> after 100 cycles at a 0.1 C rate, due to the strong physical confinement and chemical C-S bonding.

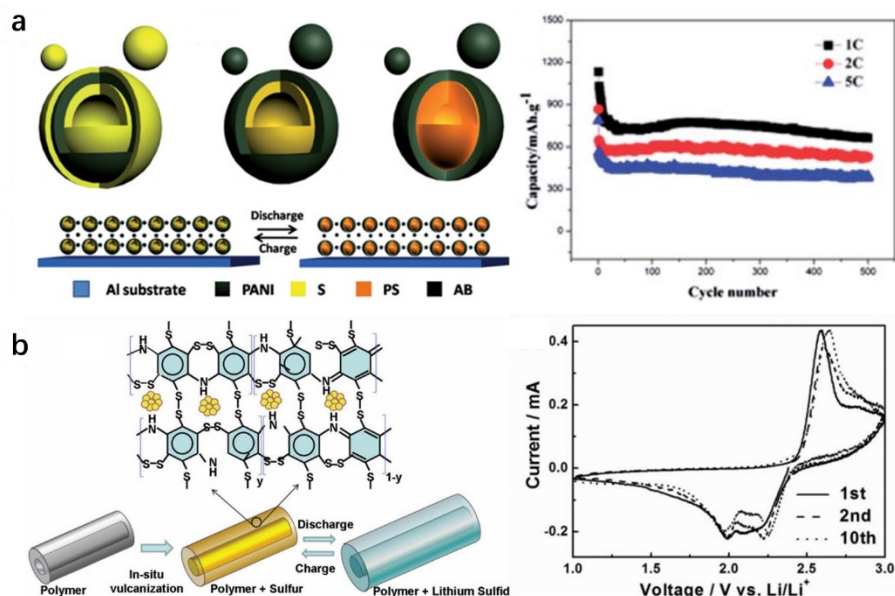


**Figure 1.25** (a) A schematic of the PANI-S composite's variation during the charge/discharge cycle, and related cycling performance at different rates [103]. (b) Schematic illustration of the SPANI-NT/ST composite structure and its cyclic voltammetry [105].

#### ***Metal oxides/sulfides/carbides/nitrides/phosphides:***

The metal compounds, especially transition metal compounds with polar surfaces, like metal oxides/sulfides/carbides/nitrides/phosphides, are considered as good sulfur host for their outstanding trapping ability of polysulfides [15]. Due to the strong electronegativity of the oxygen element, transition metal oxides often show considerable bonding energy between their surfaces and polysulfides. Tao and co-workers compared the performance of different nonconductive metal oxides (MgO, Al<sub>2</sub>O<sub>3</sub>, CeO<sub>2</sub>, La<sub>2</sub>O<sub>3</sub> and CaO) in facilitating the polysulfides adsorption and diffusion, claiming that MgO/C, La<sub>2</sub>O<sub>3</sub>/C and CeO<sub>2</sub>/C nanoflakes showed best performance due to their comprehensive properties including strong binding energy and better surface lithium ion diffusion ability [106] (**Figure 1.26**). Nazar *et al.* concluded a interaction rule between transition metal oxide and sulfur species [107]: those oxides with a redox potential within 2.4-3.05 V (vs. Li/Li<sup>+</sup>) can oxidize the polysulfides to thiosulfate/polythionate groups chemically bound to the reduced metal oxide surface. For oxides with higher redox potential (> 3.05 V), the oxidization products will be the mixture of sulfate and thiosulfate, while the sulfate is considered as electrochemically inactive and detrimental to sulfur utilization. This redox mechanism become invalid

for oxides with lower redox potential ( $< 2.4$  V). This principle, known as the “Goldilocks” principle, helped us in designing efficient polysulfides trapper with metal oxide (**Figure 1.27**).

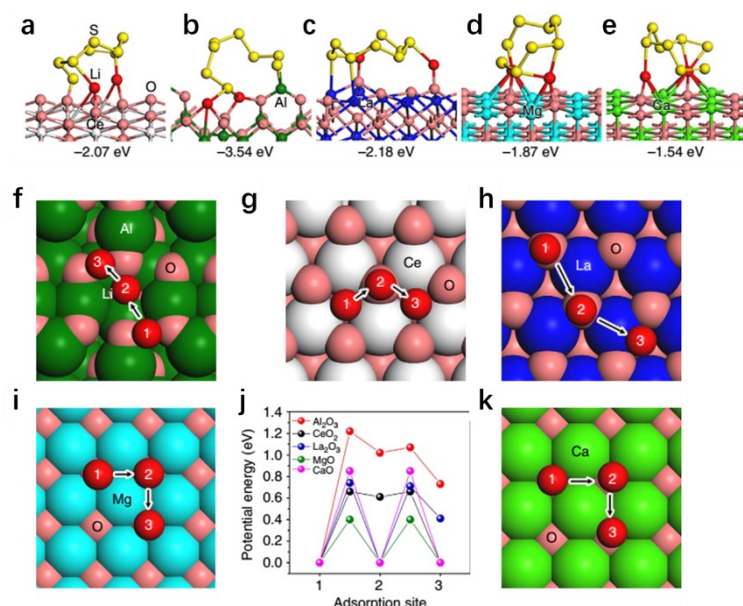


**Figure 1.26** (a-e) The binding energies of  $\text{Li}_2\text{S}_8$  on different metal oxides surface with optimized geometries. (f-k) The  $\text{Li}^+$  ion diffusion paths on different metal oxides, and the potential energy of the diffused  $\text{Li}^+$  ion on different sites of oxides [106].

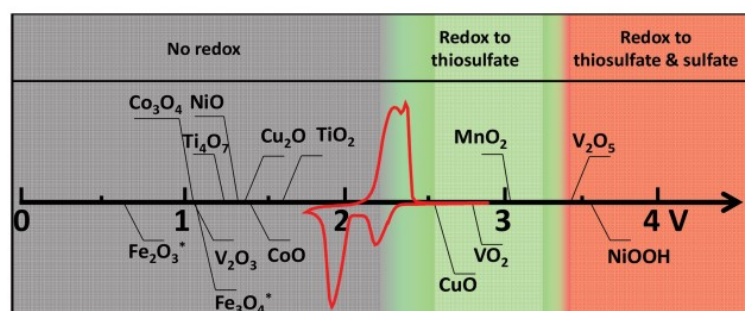


**Figure 1.27** The “Goldilocks” principle of the redox between metal oxides and polysulfides: the resulted production as a function of redox potential vs.  $\text{Li}/\text{Li}^+$  [107].

Though metal oxides often show strong chemisorption of polysulfides, these materials are considered as intrinsic insulators and have low electronic conductivity due to the strong electronegativity of oxygen atoms. By replacing the oxygen with elements with weaker electronegativity, like metal sulfides [108-110], metal nitrides [111], metal carbides [112, 113], and metal phosphides [114-116], the metal compounds usually have relatively higher electronic conductivity [108]. This will benefit the conversion of polysulfides and boost the redox at high current rates. It should be noted that the catalysis effect of some metal compounds may involve more sophisticated interfacial chemistry. Wang *et al.* [116] pointed out that the  $\text{Co-O-P}$ -like species formed by natural oxidation in air played an important role in

polysulfides adsorption, and the freshly made or reduced CoP showed much inferior performance than the former one's, as shown in **Figure 1.28**, which indicated the important catalysis effect of Co–O–P groups on the oxidized CoP surface. Therefore, we should pay more attention to the specific catalysis mechanism of different metal compounds in order to gain insights in designing proper sulfur hosts.

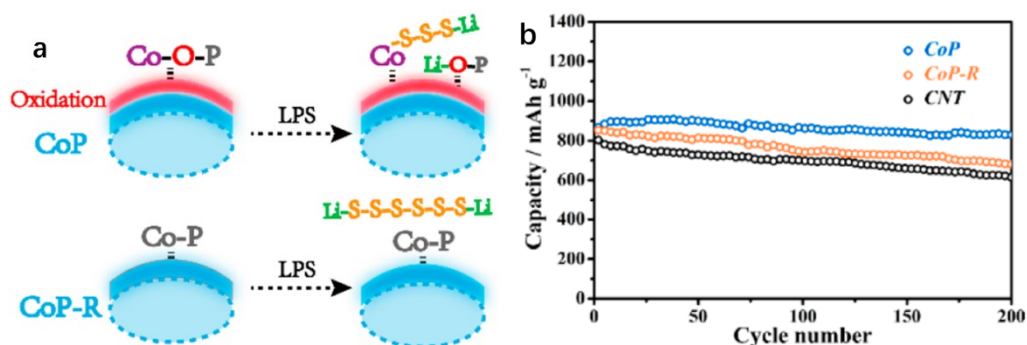


**Figure 1.28** (a) Schematic of different polysulfides adsorption mechanisms of oxidized CoP and reduced CoP (CoP-R). (b) The cycling performance with S cathodes modified with CNT, CoP-CNT, and CoP-R-CNT [116].

### Electrode structure design

While the fabrication of nano-scaled materials as sulfur host remains popular, some studies involving electrode structure reconstruction have achieved surprising refinement by electrode structure tailoring without any novel materials synthesis. One excellent example is the work from Shaibani et al. [117], in which the space between active material particles was expanded by simply minimizing the amount of binder between adjacent particles (**Figure 1.29**). Realizing expansion tolerance and unimpeded ion diffusion, this strategy delivered outstanding gravimetric capacity of >1200 mAh g<sup>-1</sup> and high areal capacity of 19 mAh cm<sup>-2</sup> with electrode sulfur loading up to 15 mg cm<sup>-2</sup>. A similar design concept was achieved by Li's group [118] using lyophilization to create ice-templated aligned canal in the coating. Besides the benefits stated in Ref. [117], this unique structure avoided the severe cracks in thick coating and elevated the absorbed electrolyte in the slurry coating (**Figure 1.30**), being opposite to conventional thermal dried electrode that cracked during desiccation and barely reserved electrolyte. What's more, the interconnected pores allowed the freeze-dried-and-compressed sulfur cathode (FDS-C) to render high full-cell energy density (481 Wh kg<sup>-1</sup>) with lean electrolyte-to-sulfur ratio (~1.2 μL mg<sup>-1</sup>). These re-constructions demonstrated the importance of proper porosity tailoring in high sulfur loading electrodes, which plays crucial roles in fabricating high energy full Li-S batteries.

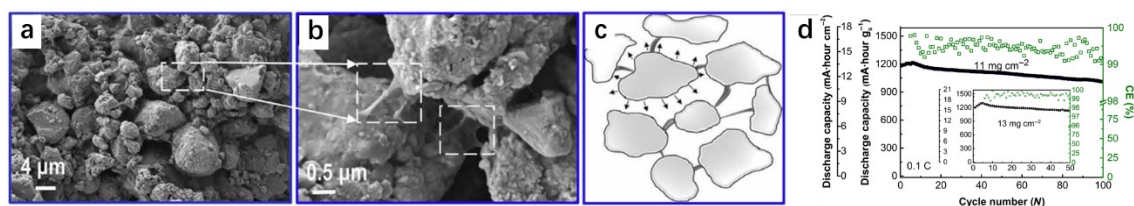


**Figure 1.29** Top-view SEM images of expansion-tolerance electrode (a,b) with growing magnifications and related schematic of web-like binder bonds holding particles while leaving expansion space. (d) The cycling performance of the expansion-tolerance electrode with high sulfur loading [117].

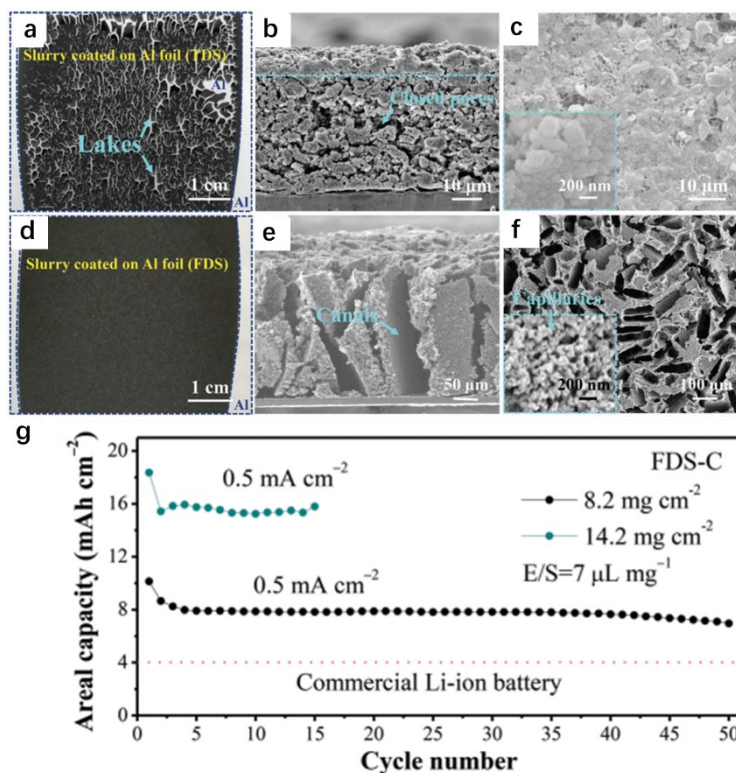


**Figure 1.30** (a-c) and (d-f): Top-view optical image, cross-section SEM image, and top-view SEM image of thermal-dried sulfur electrode (TDS) and freeze-dried sulfur electrode (FDS), respectively. (g) The cycling performance of freeze-dried-and-compressed (FDS-C) electrode with different sulfur loading at current density of  $0.5 \text{ mA cm}^{-2}$  [118].

#### 1.2.4 Multi-functional interlayers

Constructing a novel battery configuration is another approach to draw these critical issues in Li-S batteries. During the “shuttle effect”, which is the main cause of most drawbacks, the polysulfides anions diffuse through the separator and contaminate the Li anode [119]. Therefore, a counter concept is to add an extra layer between the cathode and the anode in order to avoid the contact of dissolved polysulfides and metal Li anode by adsorption of the polysulfides, which was firstly established in 2012 by Manthiram’s group [120, 121]. In most studies, this “interlayer” is also electronic conductive, acting as the secondary current-collector to boost the redox in the cathode. This interlayer concept can be usually

realized in different forms, such as a free-standing interlayer [120-123], a capping layer on the cathode [124-126], or a coating on the separator towards the cathode side [127, 128]. The materials used in interlayer construction contain carbon materials [127, 129-131], metal compounds (including oxides [132, 133], nitrides [134, 135], phosphides [136], sulfides [137] *et al.*), metal organic frameworks (MOFs) [138-140], and even elemental metal [141]. They were either applied separately or in the form of composites to serve for various targets. For the sake of polysulfide adsorption and conductivity refinement, these materials used in interlayers have largely overlapped with those used in sulfur host of cathode. Hence, for the writing conciseness, in this part the interlayer in Li-S system will be reviewed based on its working mechanisms: polysulfide confinement, conductivity refinement, and Li anode protection, along with related techniques.

### Polysulfides confinement:

The main target for the invention of the interlayer in Li-S batteries is to retard the diffusion of the dissolved polysulfides. Thus, a basic role of the interlayer should be the polysulfides diffusion barrier [128], as illustrated in **Figure 1.31** a and b. This can be achieved by either polysulfides adsorption or the rejection, in order to reserve them in the cathodic area and prevent their contact with Li anode.

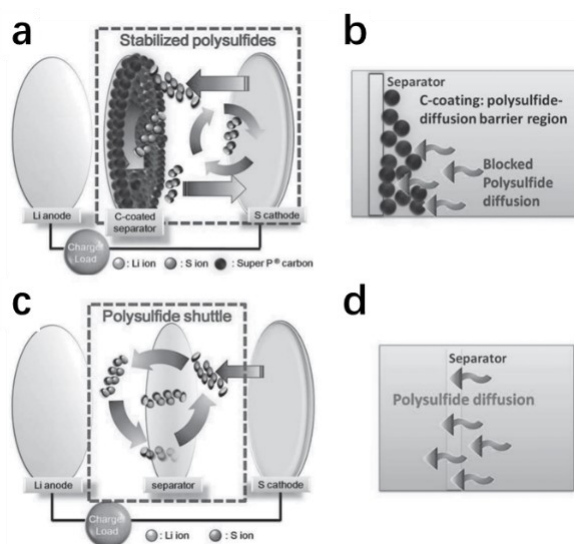


**Figure 1.31** A schematic comparison of Li-S cells with (a)(b) and without (c)(d) a carbon-coated separator as a polysulfide diffusion barrier region, showing the polysulfide-stabilization effect of interlayer [128].

Various techniques have been utilized to demonstrate the adsorption and confinement of the polysulfides. SEM images and EDS mapping usually work hand in hand to prove the distribution of sulfur species on the contacting surface, as shown in **Figure 1.32** that SEM image exhibits the

agglomerated sulfur particles and the EDS mapping confirms the sulfur distribution [120]. Another common strategy to demonstrate the restriction of polysulfides within the cathodic part is the ultraviolet-visible (UV-vis) spectra that can detect the concentration of polysulfides in the solution after the adsorption test [142]. As **Figure 1.33b** shows, the band between 400-500 nm wavelength in the solution spectrum, which was assigned to the  $\text{Li}_2\text{S}_6$ , almost completely diminished after the addition of  $\text{TiO}_2$ , proving the strong interaction between polysulfides and the interlayer material. The optical difference can also be found in **Figure 1.33a**, in which the  $\text{Li}_2\text{S}_6$  solution was found immediately faded into colorless after the  $\text{TiO}_2$  addition. X-ray photoelectron spectroscopy (XPS) is another commonly used characterization method to detect the adsorbed sulfur species, and it emphasize on the chemical bonding situation on the interlayer surface. In **Figure 1.33c**, the negative 0.3 eV shifts of the Ti 2p bands were attributed to the sulfur bonding with the Ti, indicating the electron donation from sulfides to Ti atoms.

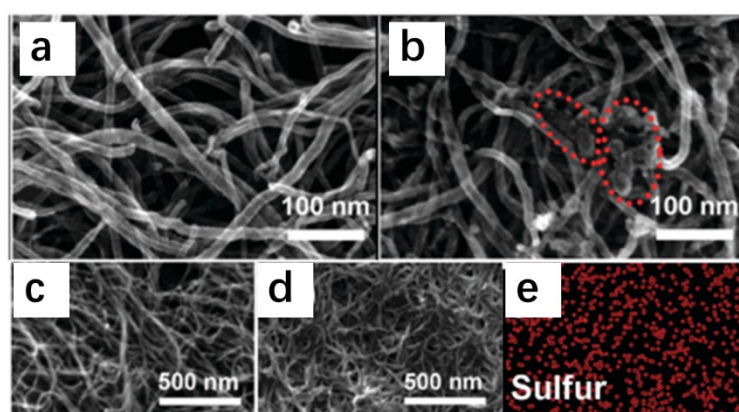


**Figure 1.32** SEM images of MWCNT paper before (a)(c) and after cycling (b)(c), in which the agglomerated sulfur particles and denoted by red circles. (e)The EDS mapping of sulfur on the surface of cycled MWCNT interlayer [120].

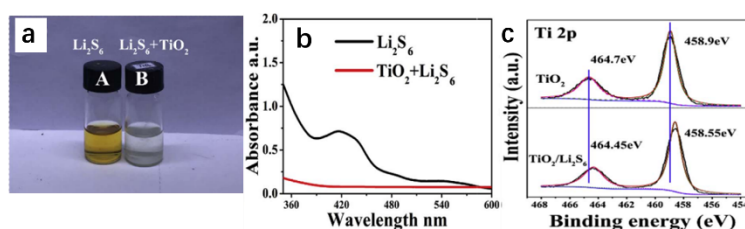


**Figure 1.33** Adsorption test of nano- $\text{TiO}_2$  with  $\text{Li}_2\text{S}_6$  solution: (a) optical image comparison, (b) UV-vis spectra of  $\text{Li}_2\text{S}_6$  solution before and after adsorption, and (c) XPS of Ti 2p of  $\text{TiO}_2$  before and after adsorption test [142].

Besides the direct evidence of adsorption, other signs of polysulfides confinement can be traced in outcomes from various electrochemical tests. The open circuit potential (OCP) test is usually used in

determining the self-discharge behavior of Li-S against shelving time. Originated from the shuttle effect, self-discharge generally causes 30% loss in capacity within several hours [25, 143], indicated by a dramatic decrease in OCP value. Zhang’s group [144] compared the OCP curves of cell with and without a graphene oxide (GO) interlayer and found that the cell with a routine separator experienced a fast decay within 5 h, while the GO membrane successfully inhibited the drop of OCP value for more than 30 h, as shown in **Figure 1.34a**. This result was assigned to the cationic permselective GO that effectively prohibiting high-order polysulfides diffusion. Another commonly used approach is the profile obtained from the galvanostatic charge/discharge test, in which the charge/discharge plateaus give information about the retained polysulfides after certain cycles. An example is shown in **Figure 1.34b** and **c**, exhibiting the distinctive plateau behavior against cycle numbers after the application of a MoS<sub>2</sub>/CNT interlayer [145]. The upper discharge plateaus, which is related to the first-step reduction of S<sub>8</sub>, were indicators of the amount of retained active sulfur in the cathodic area, and these highly overlapped plateaus over 200 cycles are electrochemical evidence of the polysulfide reservoir function of the MoS<sub>2</sub>/CNT interlayer, especially when compared with those severely shrunk plateaus of the pristine Li-S cell.

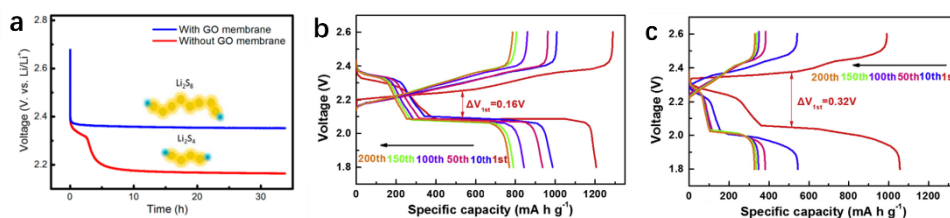


**Figure 1.34** (a) Open circuit potential (OCP) test of cells with and without GO membrane interlayer [144]. Galvanostatic charge/discharge profiles of cells with MoS<sub>2</sub>/CNT interlayer (b) and without interlayer (c) over 200 cycles [145].

Recently, a novel strategy has been applied to electrochemically demonstrate the polysulfides adsorption function of the interlayer from the reversed direction. In this special method, the interlayer was isolated with an extra separator from the cathode in order to electronically disconnect with other parts in the cell (**Figure 1.35b**). This “isolated cell” usually shows capacity level between pristine cell and cell with interlayer, along with the degraded Coulombic efficiency due to the accumulated polysulfides in the isolated interlayer [146].

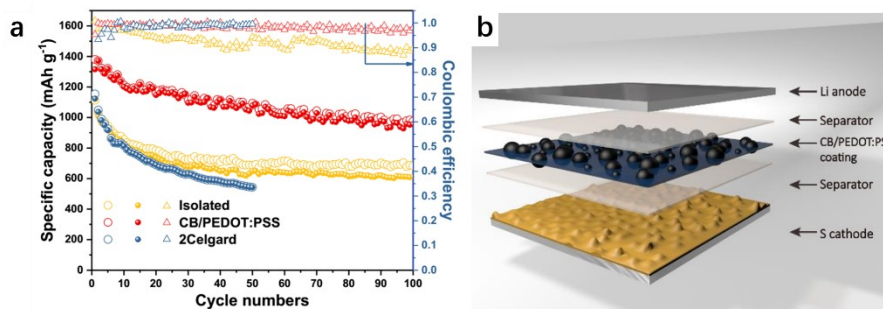


**Figure 1.35** Cycling performance of cells with CB/PEDOT:PSS interlayer, with 2 layers of Celgard separator and electrochemically isolated CB/PEDOT:PSS interlayer at 0.2 C. The schematic shows the structure of the isolated cell.

*Conductivity refinement:*

Due to the insulating sulfur and sulfur species, the electronic as well as the ionic conductivity of the cathode have always been the major concern in the Li-S study. Interlayer, as a configuration that has intimate contact with cathode upper surface, can act as the “secondary current collector” in this sandwich structure to provide external electron high-way if it’s intrinsic electronic conductive. Manthiram and Su [120, 121] first pointed out the highly conductive interlayer can reduce the effective resistance of the insulating sulfur and sulfur species in the cathode, which can be investigated by the electrochemical impedance spectroscopy (EIS). In **Figure 1.36a**, the semicircular portion of the EIS, which represents the charge transfer resistance ( $R_{ct}$ ) of the battery, has been significantly reduced by the application of the MWCNT interlayer from 277 to 38  $\Omega \text{ cm}^{-2}$ . The conductivity refinement can also be reflected by the comparison of EIS before and after cycling. Li *et al.* plotted the EIS of the cell with mesoporous  $\text{TiO}_2$ -carbon nanotubes (MTO-CNTs) interlayer before and after cycling, finding that the  $R_{ct}$  greatly decreased due to the rearrangement of the active sulfur directed by the conductive interlayer [124] (**Figure 1.36b** and c). This demonstrated the cathode resistance refinement provided by the interlayer throughout the cycling process.

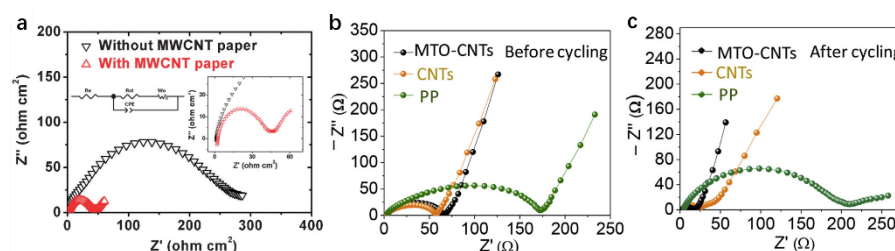


**Figure 1.36** EIS of cells with and without MWCNT paper (a) [120]; the EIS of cells with MTO-CNTs, CNTs interlayers and PP separators before and after 2 cycles [124].

Another facilitation brought by the interlayer is the ionic conductivity refinement. Some studies used cation exchange materials, like poly(styrene sulfonate) (PSS), to boost the Li ion diffusion coefficient in order to ameliorate the redox kinetic at high current density. This improvement can be quantified by the Randles-Sevcik equation:  $I_p = 2.69 \times 10^5 n^{1.5} A D_{Li^+}^{0.5} C \nu^{0.5}$ , where  $I_p$  is the peak current,  $n$  is the electron transfer number during the reaction ( $n = 2$  for Li-S batteries),  $A$  is the electrode surface area ( $\text{cm}^2$ ),  $D_{Li^+}$  is the diffusion coefficient of Li cation ( $\text{cm}^2 \text{s}^{-1}$ ),  $C$  is the concentration of Li cation in electrolyte ( $\text{mol mL}^{-1}$ ), and  $\nu$  is the scan rate ( $\text{V s}^{-1}$ ). After CV scans of the cell at different scan rates, the  $D_{Li^+}$  can be calculated for each redox peak. Using this method, the PSS in the PSS@HKUST-1 interlayer was proven to accelerate the Li cation diffusion by providing sulfonate group as a cation channel [139]. Besides the Li ion diffusion measurement in real redox process, the ionic conductivity of the interlayer can be determined from the EIS of a pure interlayer (or the modified separator) using the formula:  $\sigma = l/(R_b A)$  (in  $\text{S cm}^{-1}$ ), where the  $\sigma$  is the ionic conductivity,  $l$  is the thickness of the interlayer or modified separator,  $R_b$  is the bulk resistance which can be obtained from the intercept of the fitted straight line on the real axis ( $Z'$ ), and the  $A$  represents the area of the stainless steel disc since the separator is larger than that of the stainless steel disc. An example of this measurement is given by Guo and co-workers [147], in which  $\text{Ti}_3\text{C}_2\text{T}_x$  separator,  $\text{Ti}_3\text{C}_2\text{T}_x @$  carbon nanotube (T@C) separator,  $\text{Ti}_3\text{C}_2\text{T}_x @$  carbon nanotube/ polyethyleneimine (PEI) (T@CP) separator, and pristine glass fiber (GF) separator were subjected to this EIS test (**Figure 1.37**). The calculated conductivity of T@CP separator was  $3.08 \text{ mS cm}^{-1}$ , comparable to that of GF separator and higher than those of T@C and  $\text{Ti}_3\text{C}_2\text{T}_x$  separators, thus confirming the T@CP separator with well-organized micro/nanofluidic channels can undertake unimpeded ion transportation.

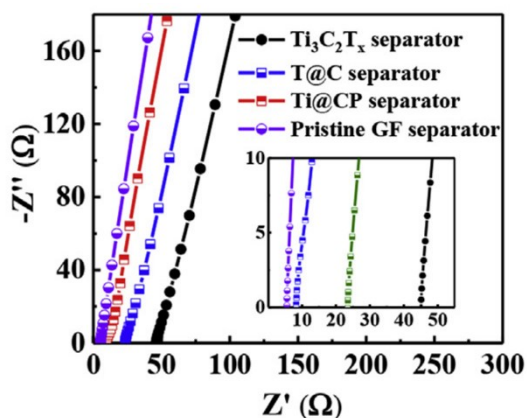


**Figure 1.37** EIS of  $\text{Ti}_3\text{C}_2\text{T}_x$  separator,  $\text{Ti}_3\text{C}_2\text{T}_x @$  carbon nanotube (T@C) separator,  $\text{Ti}_3\text{C}_2\text{T}_x @$  carbon nanotube/polyethyleneimine (PEI) (T@CP) separator, and pristine glass fiber (GF) separator [147].

### Activation of S-species:

One severe issue brought by the shuttle effect is the precipitation of insulating discharge products ( $\text{Li}_2\text{S}_2/\text{Li}_2\text{S}$ ) on the cathode surface over repeated cycles. According to Cui's group [127], the dissolved polysulfides in the electrolyte would accumulate near the surface of the cathode in the form of  $\text{Li}_2\text{S}_2/\text{Li}_2\text{S}$ . This preference of precipitation could be ascribed to that the top surface of the cathode has the shortest path distance of lithium ion flux. As a result, the reduced  $\text{Li}_2\text{S}_2/\text{Li}_2\text{S}$  would form an insulating layer on the surface of the cathode, inhibiting the following ion flux and increasing the internal resistance (**Figure 1.38a**). An interlayer effectively ameliorated this situation by facilitating the utilization of sulfur species with large conductive surface area, helping the cathode to maintain porous surface without any dense layer, as shown in **Figure 1.38g, h**. Therefore, the ionic transportation is maintained with the protection of a conductive and porous interlayer, which is crucial for

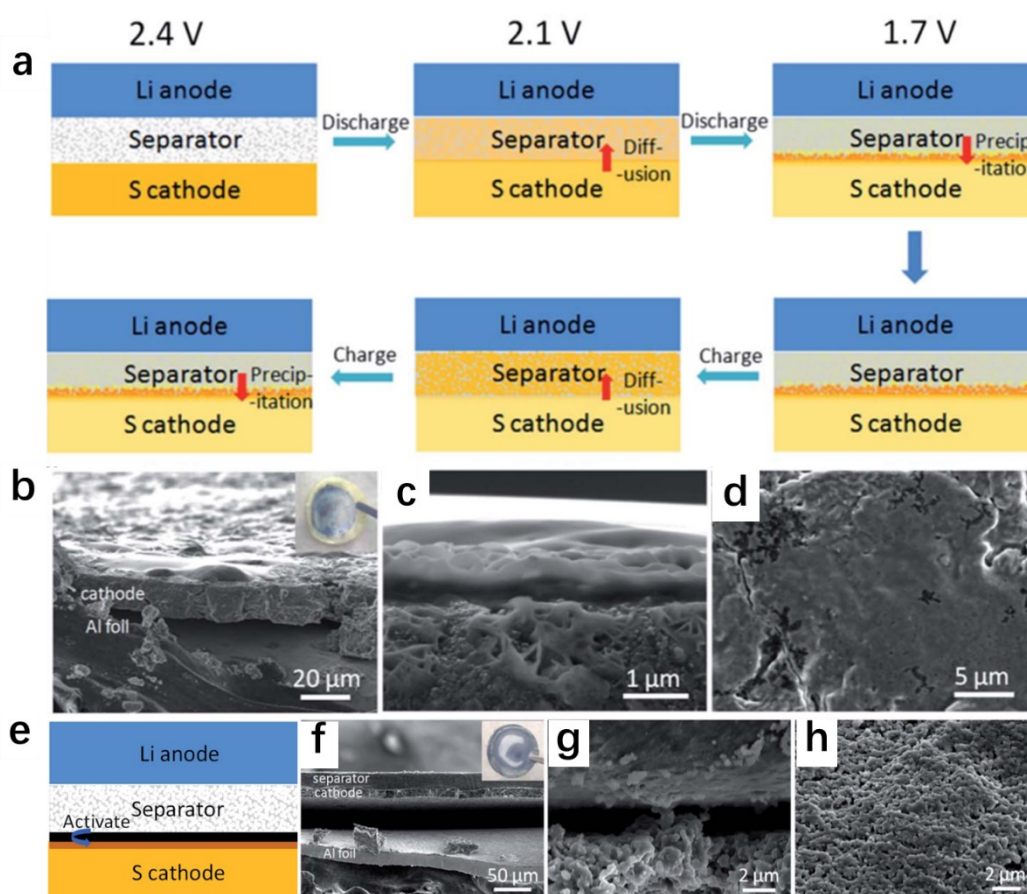


**Figure 1.38** (a) Schematic of the sulfur species precipitation on the cathode surface during charge/discharge process. SEM images of cycled cathode without conductive interlayer:(b) the cross-section image with an optical insert of corresponding separator; the magnified images of the precipitation layer: (c) the cross-section and (d) the top-view images. (e) The schematic illustration of the activate function of the conductive interlayer. (f) The cross-section image of a cell with interlayer; the insert

shows the corresponding separator. The magnified SEM images of this cathode: the cross-section (g) and the top-view (h) images [127].

### 1.3 2D materials (graphene and MXene) and their applications in Li-S battery interlayer

Due to the special function demand of the interlayer, the materials used in fabricating the Li-S battery interlayer usually need to be highly conductive and of high surface area. Therefore, conductive 2-dimensional (2-D) nanomaterials are naturally the matrix of interlayer construction. Up to now, many 2-D nanomaterials have been fabricated and utilized in battery field due to their unique features, like black phosphorus [148], 2-D borophene ( $\beta_{12}$ -borophene) [149], MoS<sub>2</sub> [150, 151], graphdiyne [152], graphene [153, 154] and 2-D metal carbides (MXene) [155, 156]. Among all these 2-D materials, the last two, graphene and MXene, have gained special attentions in the Li-S battery study for their outstanding properties and relatively easy fabrication. In this part, graphene materials and MXenes (especially Ti<sub>3</sub>C<sub>2</sub>T<sub>x</sub>) will be reviewed according to their characters and related applications in Li-S battery interlayers.

#### 1.3.1 Graphene

Being a single atomic plane of graphite, graphene has attracted tremendous attentions for its intrinsic conductivity, flexibility and stiffness [157]. Nowadays, a group of graphene derivatives, including graphene oxide (GO), reduced graphene oxide (rGO), nitrogen/sulfur/phosphorus-doped graphene (N/S/P-doped graphene), have been studied in the Li-S battery field. Early trials of fabricating Li-S interlayer with graphene materials have shown that the reduced graphene oxide (rGO) can retain the polysulfides through the functional groups on the rGO such as epoxy and carboxyl [158]. However, the interaction between each graphene derivatives sheets of the same type ( i.e. hydrophilic type and hydrophobic type) can lead to tight stack, leaving few spaces and channels for the ionic transportation (**Figure 1.39f**). Therefore, the mass loading (or the thickness for a film) is a key parameter for the interlayer of pure graphene derivatives to balance the polysulfide confinement and ionic conductivity [144], as shown in **Figure 1.39a-d**. Too much GO mass loading can significantly reduce the capacity performance at high current density, although the Coulombic efficiency is remarkably preserved for 50 cycles.

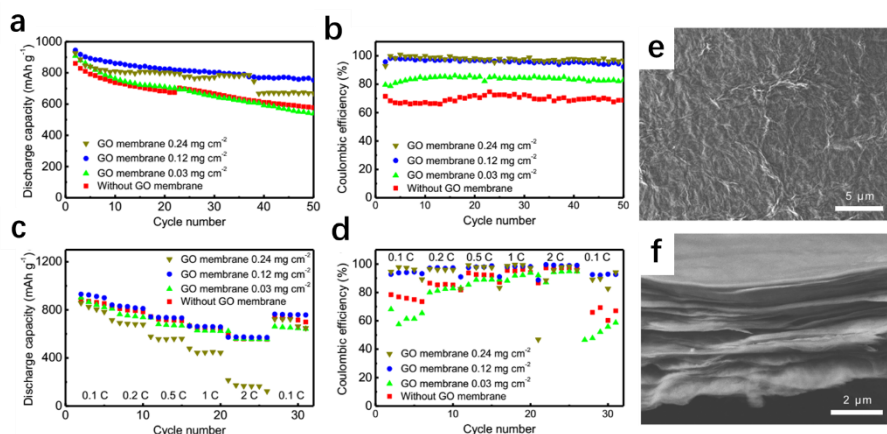


**Figure 1.39** The cycling performance of Li-S batteries of GO interlayer with various mass loadings: (a) cycling performance at 0.1 C and (b) corresponding Coulombic efficiency; (c) rate performance and (d) corresponding Coulombic efficiency. (e)(f) SEM images of the GO interlayer: bird-view and cross-section, respectively [144].

Based on this proposal, a series graphene-based interlayers have been fabricated by preventing the stacking and agglomeration of the graphene and its derivatives. A common strategy is to add other nanomaterials as the intercalator to generate additional space as ion channel, such as rGO/CB [158], GO/CNT [129], MnO<sub>2</sub>/graphene [159], and TiO<sub>2</sub>/graphene [126]. The MnO<sub>2</sub> nanosheets/graphene (MnO<sub>2</sub>/GP) [159] interlayer is a representative of this modification guideline. It is reported that the MnO<sub>2</sub> nanosheets not only served as polysulfides absorber, but also created extra supporting between graphene sheets to prevent stacking, leaving sufficient ionic transportation channels as demonstrated by the **Figure 1.40**. The optimized MnO<sub>2</sub> content achieved the balance between polysulfide adsorption and conductivity refinement, delivering a high initial specific capacity of 1395 mAh g<sup>-1</sup> at a rate of 0.5 C.

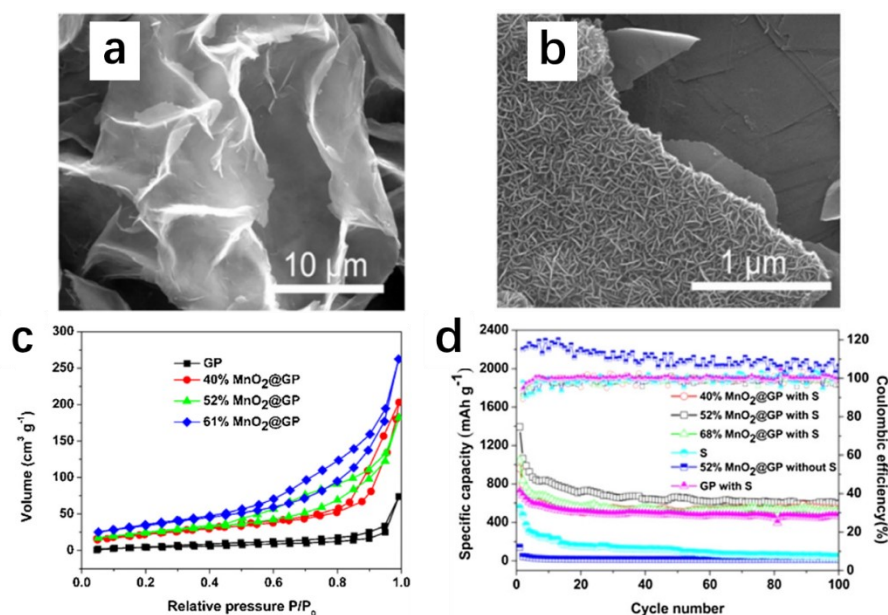


**Figure 1.40** SEM images of (a) GP and (b) MnO<sub>2</sub>/GP surface. Nitrogen adsorption/desorption curves of samples with different MnO<sub>2</sub> content were shown in (c), and their performance in cycling test were shown in (d) [159].

Another strategy to create sufficient porosity for ionic transportation and avoid layer-stacking in graphene-based interlayer is to construct 3-D structure. Usually this kind of interlayer is produced by hydrothermal process, resulting in graphene aerogel/sponge/foam materials [99, 160, 161]. These porous structures have numerous interconnected tunnels that facilitate ion transportation and present substantial surface areas for polysulfide-blocking. As shown in **Figure 1.41**, the porous nitrogen and phosphorus dual doped graphene (p-NP-G) interlayer, fabricated by Zhang's group [99], exhibited abundant mesopores by SEM observation, and the foam-like structure showed in the TEM bright field image. The p-NP-G displayed superior electronic conductivity than those of p-N-G and p-P-G due to the electron donation of N and P heteroatoms, while the porous structure of p-NP-G prevented the stacking of graphene sheets and retained free passage for electrolytes, resulting in much improved capacity performance at different current rates.

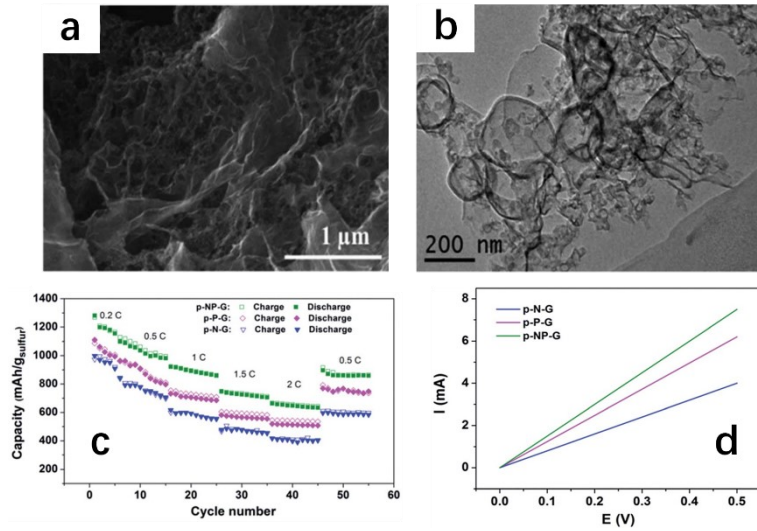


**Figure 1.41** SEM (a) and TEM (b) images of the porous nitrogen and phosphorus dual doped graphene (p-NP-G) composite. (c) Rate performance of cells with different heteroatoms doped graphene interlayers. (d)  $I$ - $V$  curves of these interlayers [99].

To sum up, graphene and its derivatives, being atomic scale-thick 2-D nanomaterials, are ideal candidates for Li-S battery interlayer. In order to make efficient use of their features, interlayer designers should avoid the stacking and agglomeration of graphene sheets, otherwise they can impede the ion transportation by the intimate contact of each sheet. Effective solution can be achieved by (i) addition of non-2-D materials as intercalators to create channels for electrolyte, and (ii) fabrication of 3-D graphene structures that leaving interconnected channels for ion transportation. However, these treatments still cannot totally avoid the re-stacking, and the introduction of heterogeneous materials usually impairs the electronic conductivity of interlayer while 3-D sponge-like graphene by the hydrothermal method may induce extra interlayer density. Hence designing more efficient ways to utilize graphene materials as interlayer requires more tactical tailoring of the nanostructure.

### 1.3.2 MXene

MXene, as its name suggests, is a group of 2-D materials derived from the  $M_{n+1}AX_n$  (MAX,  $n=1, 2,$  or 3) phase, where M represents an early transition metal, A is an element from group 13 or 14, and X stands for carbon or nitrogen. The MAX phases have layered hexagonal lattice with M atoms near-close-packed and X atoms filling in the octahedral sites, while the A atoms layer intercalate between each  $M_{n+1}X_n$  laminated structure, as illustrated in **Figure 1.42a** [162, 163]. If the A layer, either removed by

HF solution etching [162] or molten metal chloride salts [164], the MAX phase will become the accordion-like MXene, with terminals ( $T_x$ , like -OH, -Cl, and/or -F brought by etchant and solvent) as substitutes of A layer on the M atoms layer (**Figure 1.42a**). After the intercalation and delamination process, the MXene nanosheets can be detached from each other, creating graphene-like monolayer with atomic-scale thickness delaminated-MXene (d-MXene) [163]. The d- $Ti_3C_2T_x$ , as one of the most applied MXenes in electrochemical field, has demonstrated itself of high intrinsic electronic conductivity, which is ascribed to the main contribution to the density of states from Ti atoms (**Figure 1.42c**). Moreover, due to the 2-D morphology and strong interaction between nanosheets, the filtrated d- $Ti_3C_2T_x$  forms a free-standing film with excellent flexibility and considerable strength (**Figure 1.42d**), showing its high potential in electrode materials field.

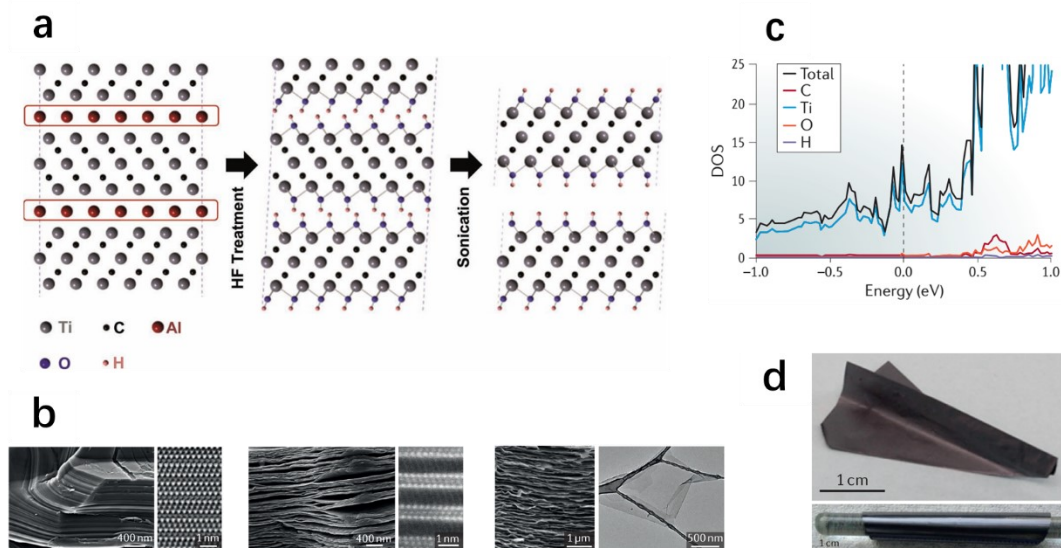


**Figure 1.42** (a) Schematic of the exfoliation of the  $Ti_3C_2T_x$  MXene [162]; (b) SEM images of the  $Ti_3AlC_2$ , the etched  $Ti_3C_2T_x$ , and the delaminated  $Ti_3C_2T_x$ , respectively. The HRTEM images are  $Mo_2TiAlC_2$ , and etched  $Mo_2TiC_2T_x$ . The bright field TEM image is a single-layer  $Ti_3C_2T_x$  flake [165]. (c) The density of states (DOS) calculation results of  $Ti_3C_2$  with all -OH terminations [166]. (d) The folded  $Ti_3C_2T_x$  filtrated paper and its flexibility demonstration [167].

While it displays attractive features in other electrochemical researches, MXenes, especially  $Ti_3C_2T_x$ , holds a unique position in Li-S studies for recent years due to their unique interaction mechanism with sulfur species. The  $Ti_3C_2T_x$  or  $Ti_2CT_x$  MXenes, with neither very high specific surface area nor porous structure to accommodate sulfur species, have showed excellent compatibility with Li-S batteries either as sulfur host [113, 168-171] or interlayer material [172-175]. This superior performance has inspired people to investigate the related chemistry. Fan *et al.* [176] analyzed the anchoring effect of different

MXenes in a density function theory (DFT) study. With the optimized configurations of adsorbed polysulfides (in which the strong Li-O covalent bond is the main force of the interaction (**Figure 1.43a-d**)), these researchers proved that the  $\text{Ti}_3\text{C}_2\text{O}_2$  has binding energies with various polysulfides higher than those of the electrolyte solvent molecules (DME and DOL), which is partially responsible for the excellent sulfur-reserve function of  $\text{Ti}_3\text{C}_2\text{T}_x$  MXenes. For the actual situation in Li-S batteries, the interaction process is much more complex, as the terminals  $\text{T}_x$  contain -F, -Cl, -O, and -OH, and each of them may have distinctive reaction behavior with polysulfides. As the paper confirmed by the XPS analysis [171], MXene terminals on the surface, mainly the -OH group, will interact with high-order polysulfides upon the first battery cycle to form thiosulfate, which later turn into sulfate by the reaction of thiosulfate and polysulfides during the following cycling. When the sulfate layer thickness reaches the critical value, polysulfides are confined under this protective layer and their redox are facilitated by the exposed bare Ti atoms on the  $\text{Ti}_3\text{C}_2\text{T}_x$  surface (**Figure 1.43e**). Therefore, the cycling stability of the S cathode with MXene host is enhanced after some initial cycles to build sulfate layer with effective thickness.

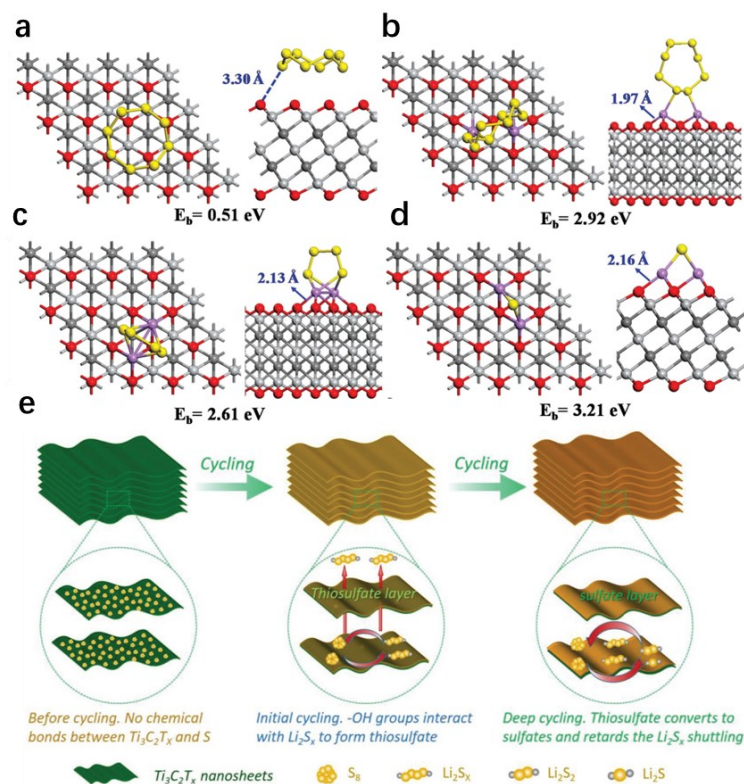


**Figure 1.43** (a-d) The optimized adsorption configurations of  $\text{S}_8$ ,  $\text{Li}_2\text{S}_8$ ,  $\text{Li}_2\text{S}_4$ , and  $\text{Li}_2\text{S}$  on the  $\text{Ti}_3\text{C}_2\text{O}_2$  surface and their corresponding adsorption energy, respectively [176]. (e) The schematic of polysulfides

reservation mechanism by the formation of a continuous sulfate protecting layer on the surface during deep cycling [171].

In addition to these highlights,  $\text{Ti}_3\text{C}_2\text{T}_x$  MXene also have similar drawbacks as those of graphene. The 2-D morphology of the delaminated  $\text{Ti}_3\text{C}_2\text{T}_x$  MXene makes it re-stacking easily, forming a compact layered structure that leaves little and tortuous tunnels for ion transmission [177, 178], as illustrated by the **Figure 1.44a**. Song *et al.* [172] filtrated the pure delaminated  $\text{Ti}_3\text{C}_2\text{T}_x$  MXene sheets on commercial Celgard separator as the interlayer. This conductive MXene membrane effectively improved the capacity performance of the Li-S battery acting as the upper current collector, delivering a discharge capacity of  $1046.9 \text{ mAh g}^{-1}$  at 0.2 C. However, the SEM image showed a rather compact surface of this membrane, and the battery performance on higher current rates ( $> 1 \text{ C}$ ) was not presented in this paper. Other  $\text{Ti}_3\text{C}_2\text{T}_x$ -based interlayer has modified the  $\text{Ti}_3\text{C}_2\text{T}_x$  sheet with various strategies to increase porosity and polysulfide-anchoring ability. Huang's group [179] managed to solve the ionic conductivity issue by introducing the  $\text{Li}^+$ -conductive and polysulfide-repulsive Nafion polymer to the filtrated  $\text{Ti}_3\text{C}_2\text{T}_x$  membrane. The height profiles measured by atomic force microscopy (AFM) proved the modification of Nafion molecules increased the thickness of the delaminated  $\text{Ti}_3\text{C}_2\text{T}_x$  nanosheets by about 1.5 nm (**Figure 1.44e**). Although still in compact stacking morphology (**Figure 1.44d**), this Nafion modified freestanding interlayer (MX-NF) greatly facilitated the ionic conductivity, resulting in high capacities of 916, 859, and  $794 \text{ mAh g}^{-1}$  at 1 C, 2 C, and 3 C, respectively. As a comparison, the pure MXene interlayer (MX) only delivered  $537 \text{ mAh g}^{-1}$  at 3 C (**Figure 1.44f**).

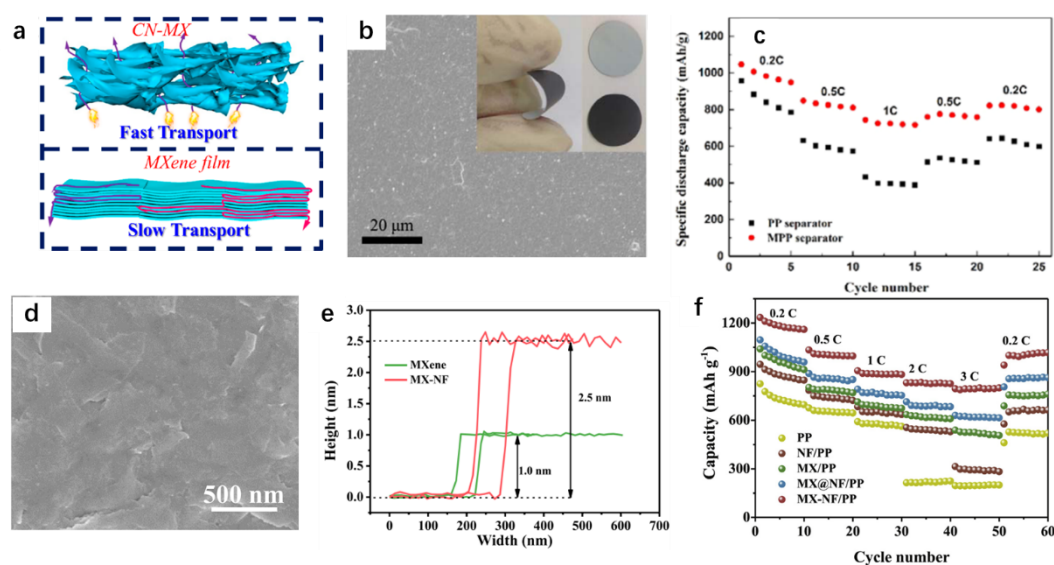


**Figure 1.44** (a) Schematic of the fast ion transportation in a compact and nano porous MXene film (CN-

MX) and the slow transportation in a tightly restacked MXene film fabricated by the vacuum filtration [177]. (b) The bird-view SEM image of pure  $\text{Ti}_3\text{C}_2\text{T}_x$  film surface with the insert of optical observation of its flexibility. (c) The rate performance of cells with and without  $\text{Ti}_3\text{C}_2\text{T}_x$  film as interlayer [172]. (d) The bird-view SEM image of Nafion-modified  $\text{Ti}_3\text{C}_2\text{T}_x$  MXene (MX-NF) film. (e) The height profiles measured by AFM of single layer  $\text{Ti}_3\text{C}_2\text{T}_x$  nanosheet and NF-MX nanosheet. (d) The rate performance cells with various interlayers and without interlayer [179].

Apart from the approach of introducing ion exchange materials in the  $\text{Ti}_3\text{C}_2\text{T}_x$  film, structural modification that creates additional space for ion transportation tunnel is another direction to enhance the  $\text{Ti}_3\text{C}_2\text{T}_x$ -based interlayer. Same as the graphene-based interlayer, porous materials are commonly used to retard the re-stacking of  $\text{Ti}_3\text{C}_2\text{T}_x$  nano-sheets. A reported  $\text{Ti}_3\text{C}_2\text{T}_x$  based interlayer used polyethyleneimine (PEI) functionalized CNTs to fabricate a CNT intercalated  $\text{Ti}_3\text{C}_2\text{T}_x$  interlayer (T@CP) [147]. The abundant amines in PEI endowed the CNT-PEI with positive zeta potential, through which it can be evenly attached to the negatively charged surface of  $\text{Ti}_3\text{C}_2\text{T}_x$  nanosheets (**Figure 1.45a**). This combination raised the specific surface area from  $25.8 \text{ m}^2 \text{ g}^{-1}$  of the pure  $\text{Ti}_3\text{C}_2\text{T}_x$  nanosheets to  $165 \text{ m}^2 \text{ g}^{-1}$ , largely increased the physical blocking area of the polysulfides. SEM characterization confirmed the regulated intercalation of the CNT-PEI in the  $\text{Ti}_3\text{C}_2\text{T}_x$  nanosheets, which helped the cell maintain better high rate performance (**Figure 1.45d**). Besides the *ex-situ* modification, some chosen *in-situ* strategies were reported to increase the specific area and inhibit the restacking of  $\text{Ti}_3\text{C}_2\text{T}_x$  nanosheets. Li *et al.* [180] grew the MOF (ZIF-67) on the delaminated  $\text{Ti}_3\text{C}_2\text{T}_x$  nanosheets as the precursor of *in-situ* grew porous carbon and the nitrogen source for doping (**Figure 1.46a**). The N-doped  $\text{Ti}_3\text{C}_2\text{T}_x$  decorated with porous carbon (N- $\text{Ti}_3\text{C}_2\text{T}_x/\text{C}$ ) by annealing in the protective atmosphere had shown better performance than that of pure  $\text{Ti}_3\text{C}_2\text{T}_x$  film interlayer and bare separator in this study (**Figure 1.46d**). The BET method proved the specific area boosted from  $10.5 \text{ m}^2 \text{ g}^{-1}$  of pure  $\text{Ti}_3\text{C}_2\text{T}_x$  to  $62.7 \text{ m}^2 \text{ g}^{-1}$  of N- $\text{Ti}_3\text{C}_2\text{T}_x/\text{C}$ , and the XPS confirmed the N-doping in both  $\text{Ti}_3\text{C}_2\text{T}_x$  and porous carbon. These improvements can benefit the polysulfide adsorption of this interlayer material.

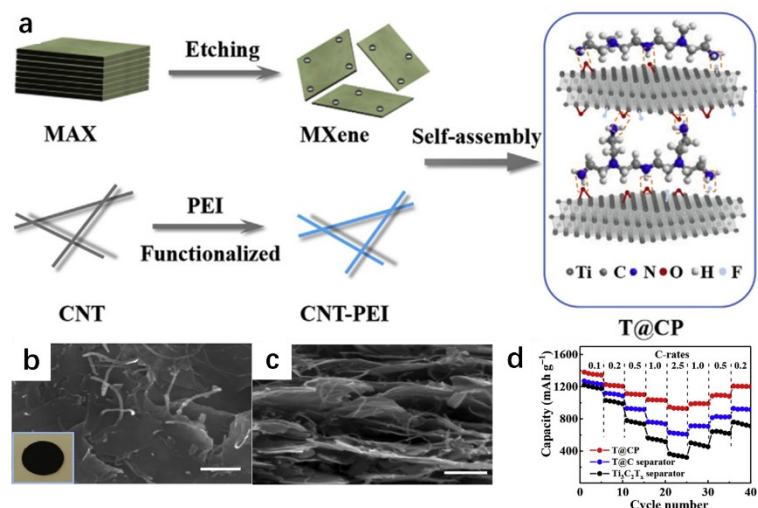


**Figure 1.45** (a) The self-assembly fabrication schematic of T@CP interlayer and its SEM images of (b) the surface and (c) the cross-section. (d) The rate test of cells with T@CP, T@C, and  $\text{Ti}_3\text{C}_2\text{T}_x$  interlayer [147].

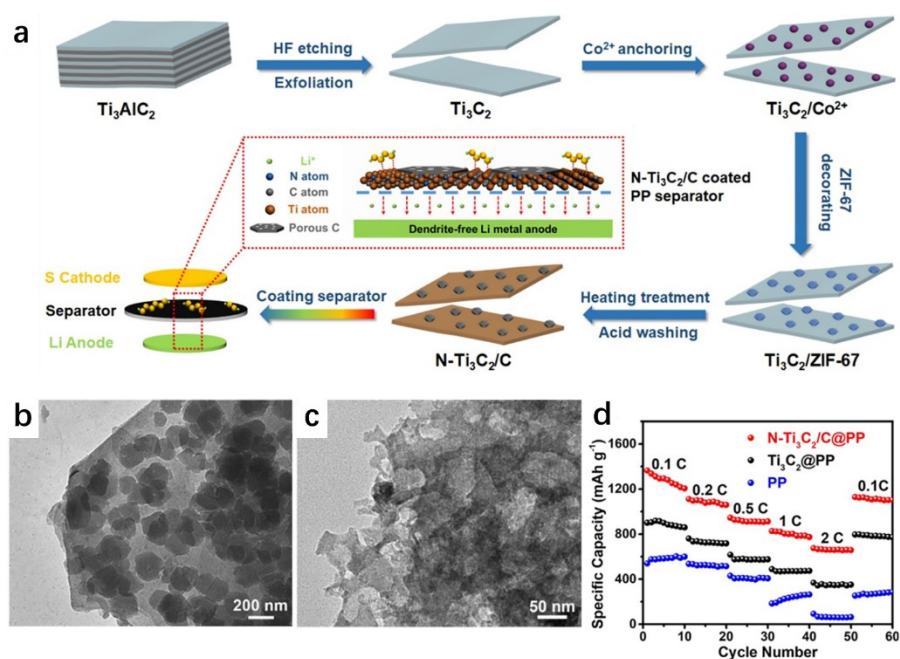


**Figure 1.46** The schematic of N- $\text{Ti}_3\text{C}_2/\text{C}$  interlayer fabrication (a), and the TEM images of  $\text{Ti}_3\text{C}_2/\text{ZIF-67}$  (b) and N- $\text{Ti}_3\text{C}_2/\text{C}$  (c). The rate performance comparison of cells with N- $\text{Ti}_3\text{C}_2/\text{C}$ ,  $\text{Ti}_3\text{C}_2$  interlayer and without interlayer is shown in (d) [180].

To conclude, the delaminated  $\text{Ti}_3\text{C}_2\text{T}_x$  nanosheet is an ideal material for Li-S battery interlayer due to its intrinsic high electronic conductivity, 2-D morphology, and strong interaction with polysulfides. But the re-stacking from the sheet-like morphology and strong hydrogen bond between surface groups greatly retard its application as the interlayer, and this issue is especially important as the original specific surface area of  $\text{Ti}_3\text{C}_2\text{T}_x$  is considerably lower than most other nanomaterials. Advanced strategies,

including the combination of  $\text{Ti}_3\text{C}_2\text{T}_x$  with ion exchange matters, *ex-situ* and *in-situ* surface decoration of  $\text{Ti}_3\text{C}_2\text{T}_x$ , can effectively mitigate these issues. These approaches are important references to build more advanced  $\text{Ti}_3\text{C}_2\text{T}_x$ -based Li-S battery interlayer.

## **1.4 Aim of study and proposals of the thesis**

### **1.4.1 Aim of study**

It can be concluded from the review that Li-S battery is one of the most promising batteries for the next-generation energy storage system. Nevertheless, intrinsic drawbacks of the Li-S battery still hinder it from scalable application, and most severe issues, like the high electrode resistance, the high volumetric expansion of sulfur species, and the “shuttle effect”, are all rooted in the S-based cathode. The interlayer between the cathode and the separator, as a novel battery configuration, is a forceful solution to these issues. Herein, this thesis will focus on the designing of appropriate interlayer and the fabrication of cathode interlayer for Li-S batteries, mainly based on two 2-D materials: graphene and  $\text{Ti}_3\text{C}_2\text{T}_x$  MXene. In order to ameliorate the drawbacks, these two nanomaterials will be modified and re-constructed to adapt to different emphasized points in each interlayer proposal.

### **1.4.2 The outline of thesis**

At the beginning, a carbon black (super-P) based interlayer was fabricated to study the basic influence of a conductive interlayer in the Li-S battery. Then the conductive and polysulfide-attractive poly(3,4-ethylenedioxythiophene)-poly(styrenesulfonate) (PEDOT:PSS) was introduced in the interlayer to enhance the chemical adsorption of polysulfides as a better improvement.

Based on the study from CB/PEDOT:PSS interlayer, a lightweight interlayer based on graphene foam (GF) was designed to decrease the mass density of the interlayer. This Ni foam-templated GF was fabricated through CVD, and then was modified by ZnO using ALD to enhance the chemical adsorption property.

In Chapter 5, the insulating ZnO nanodots were replaced by conductive  $\text{Ti}_3\text{C}_2\text{T}_x$  nanosheets, thus improving the specific surface area and conductivity of the GF. Through facile drop-coating method, the GF was modified by the  $\text{Ti}_3\text{C}_2\text{T}_x$  and acting as the 3-D frameworks to mitigate the restacking of the

Ti<sub>3</sub>C<sub>2</sub>T<sub>x</sub> nanosheets.

Finally, with the aim of creating an interlayer material that can ameliorate cathode with higher sulfur loading, a more continuous coating on the separator is more capable to fulfil the requirement. Therefore, the Ti<sub>3</sub>C<sub>2</sub>T<sub>x</sub> nanosheets was N-doped and modified with N-doped carbon nanosheet decorated with Ni nanoparticles (N-M@CNi) via the one-step *in-situ* decoration process. The synthesized N-M@CNi composite was used as the coating material on the separator to improve the performance of the high sulfur-loading cathode.

## 1.5 References

- [1] Schandl, Hatfield-Dodds, Wiedmann, Geschke, Cai, West, Newth, Baynes, Lenzen, and Owen, *Decoupling global environmental pressure and economic growth: scenarios for energy use, materials use and carbon emissions*. Journal of Cleaner Production, 2016,**132** p. 45-56.
- [2] DeCanio, *The political economy of global carbon emissions reductions*. Ecological Economics, 2009,**68** (3): p. 915-924.
- [3] Wang, Xie, and Wei, *Advanced engineering of nanostructured carbons for lithium–sulfur batteries*. Nano Energy, 2015,**15** p. 413-444.
- [4] Kim, Park, Chang, Choi, Ryu, and Song, *The Current Move of Lithium Ion Batteries Towards the Next Phase*. Advanced Energy Materials, 2012,**2** (7): p. 860-872.
- [5] Scrosati, Hassoun, and Sun, *Lithium-ion batteries. A look into the future*. Energy & Environmental Science, 2011,**4** (9): p. 3287.
- [6] Wu, Ge, Lu, Xu, and Zhang, *Graphene-based nano-materials for lithium–sulfur battery and sodium-ion battery*. Nano Energy, 2015,**15** p. 379-405.
- [7] Goodenough and Park, *The Li-ion rechargeable battery: a perspective*. Journal of the American Chemical Society, 2013,**135** (4): p. 1167-1176.
- [8] Bruce, Freunberger, Hardwick, and Tarascon, *Li-O<sub>2</sub> and Li-S batteries with high energy storage*. Nature materials, 2011,**11** (1): p. 19-29.
- [9] Manthiram, Fu, and Su, *Challenges and prospects of lithium-sulfur batteries*. Accounts of Chemical Research, 2013,**46** (5): p. 1125-1134.
- [10] Seh, Sun, Zhang, and Cui, *Designing high-energy lithium-sulfur batteries*. Chemical Society Reviews, 2016,**45** (20): p. 5605-5634.
- [11] Ji and Nazar, *Advances in Li–S batteries*. Journal of Materials Chemistry, 2010,**20** (44): p. 9821-9826.
- [12] Kim, Ocon, Park, and Lee, *Functionalized graphene-based cathode for highly reversible lithium-sulfur batteries*. ChemSusChem, 2014,**7** (5): p. 1265-1273.
- [13] Chung and Manthiram, *Current Status and Future Prospects of Metal–Sulfur Batteries*. Advanced Materials, 2019,**31** (27): p. 1901125.
- [14] Yu, Li, Wu, and Shi, *Graphene materials for lithium–sulfur batteries*. Energy Storage Materials, 2019,**15** p. 100-110.

- 2015,**1** p. 51-73.
- [15] Lim, Kim, Jo, and Lee, *A Comprehensive Review of Materials with Catalytic Effects in Li-S Batteries: Enhanced Redox Kinetics*. Angewandte Chemie International Edition, 2019,**58** (52): p. 18746-18757.
- [16] Chen and Shaw, *Recent advances in lithium-sulfur batteries*. Journal of Power Sources, 2014,**267** p. 770-783.
- [17] Birk and Steunenberg, *Chemical Investigations of Lithium-Sulfur Cells*, in *New Uses of Sulfur*. 1975, AMERICAN CHEMICAL SOCIETY. p. 186-202.
- [18] Conder and Villevieille, *Is the Li-S battery an everlasting challenge for operando techniques?* Current Opinion in Electrochemistry, 2018,**9** p. 33-40.
- [19] Yan, Liu, and Li, *Capacity Fade Analysis of Sulfur Cathodes in Lithium-Sulfur Batteries*. Advanced Science, 2016,**3** (12): p. 1600101.
- [20] Waluś, Barchasz, Bouchet, Leprêtre, Colin, Martin, Elkaïm, Baecht, and Alloin, *Lithium/Sulfur Batteries Upon Cycling: Structural Modifications and Species Quantification by In Situ and Operando X-Ray Diffraction Spectroscopy*. Advanced Energy Materials, 2015,**5** (16): p. 1500165.
- [21] Jayaprakash, Shen, Moganty, Corona, and Archer, *Porous Hollow Carbon@Sulfur Composites for High-power Lithium-sulfur Batteries*. Angewandte Chemie International Edition, 2011,**50** (26): p. 5904-5908.
- [22] Yan, Wang, Wang, Li, Gong, and Yang, *In Situ Generated Li<sub>2</sub>S-C Nanocomposite for High-Capacity and Long-Life All-Solid-State Lithium Sulfur Batteries with Ultrahigh Areal Mass Loading*. Nano Lett, 2019,**19** (5): p. 3280-3287.
- [23] Wei Seh, Li, Cha, Zheng, Yang, McDowell, Hsu, and Cui, *Sulphur-TiO<sub>2</sub> yolk-shell nanoarchitecture with internal void space for long-cycle lithium-sulphur batteries*. Nature Communications, 2013,**4** p. 1331.
- [24] Peled, Shekhtman, Mukra, Goor, Belenkaya, and Golodnitsky, *Improving the Durability and Minimizing the Polysulfide Shuttle in the Li/S Battery*. Journal of the Electrochemical Society, 2017,**165** (1): p. A6051-A6057.
- [25] Mikhaylik and Akridge, *Polysulfide Shuttle Study in the Li/S Battery System*. Journal of the Electrochemical Society, 2004,**151** (11): p. A1969.

- [26] Xu, Qian, Liu, Liu, Chen, and Yan, *Greatly Suppressed Shuttle Effect for Improved Lithium Sulfur Battery Performance through Short Chain Intermediates*. *Nano Lett*, 2017,**17** (1): p. 538-543.
- [27] Ghazi, Sun, Sun, Qi, An, Li, and Cheng, *Key Aspects of Lithium Metal Anodes for Lithium Metal Batteries*. *Small*, 2019,**15** (32): p. e1900687.
- [28] Ling, Banerjee, and Matsui, *Study of the electrochemical deposition of Mg in the atomic level: Why it prefers the non-dendritic morphology*. *Electrochimica Acta*, 2012,**76** p. 270-274.
- [29] Jackle and Gross, *Microscopic properties of lithium, sodium, and magnesium battery anode materials related to possible dendrite growth*. *The journal of chemical physics*, 2014,**141** (17): p. 174710.
- [30] Wang, Yang, Yang, Wu, Hu, Lu, Liu, Sun, Qiu, and Zhou, *Dendrite-Free Lithium Deposition via a Superfilling Mechanism for High-Performance Li-Metal Batteries*. *Advanced Materials (Weinheim, Germany)*, 2019,**31** (41): p. e1903248.
- [31] Zheng, Fan, Ji, Wang, Hou, DeMella, Raghavan, Wang, Xu, and Wang, *Manipulating electrolyte and solid electrolyte interphase to enable safe and efficient Li-S batteries*. *Nano Energy*, 2018,**50** p. 431-440.
- [32] Carbone, Coneglian, Gobet, Munoz, Devany, Greenbaum, and Hassoun, *A simple approach for making a viable, safe, and high-performances lithium-sulfur battery*. *Journal of Power Sources*, 2018,**377** p. 26-35.
- [33] Peng, Wang, Zhou, Jin, Liu, Qin, Shen, Han, and Wang, *Volumetric variation confinement: surface protective structure for high cyclic stability of lithium metal electrodes*. *Journal of Materials Chemistry A*, 2016,**4** (7): p. 2427-2432.
- [34] Koch, Morgan, Passerini, and Teobaldi, *Density functional theory screening of gas-treatment strategies for stabilization of high energy-density lithium metal anodes*. *Journal of Power Sources*, 2015,**296** p. 150-161.
- [35] Zheng, Yan, Mei, Engelhard, Cartmell, Polzin, Wang, Zhang, and Xu, *Highly Stable Operation of Lithium Metal Batteries Enabled by the Formation of a Transient High-Concentration Electrolyte Layer*. *Advanced Energy Materials*, 2016,**6** (8): p. 1502151.
- [36] Wang, Zhang, Yang, Huang, Liu, and Luo, *Horizontal Centripetal Plating in the Patterned Voids of Li/Graphene Composites for Stable Lithium-Metal Anodes*. *Chem*, 2018,**4** (9): p. 2192-2200.

- [37] Li, Yao, Yan, Zheng, Liang, Chiang, and Cui, *The synergetic effect of lithium polysulfide and lithium nitrate to prevent lithium dendrite growth*. Nature Communications, 2015,**6** p. 7436.
- [38] Scheers, Fantini, and Johansson, *A Review of Electrolytes for Lithium–sulphur Batteries*. Journal of Power Sources, 2014,**255** p. 204-218.
- [39] Barghamadi, Best, Bhatt, Hollenkamp, Musameh, Rees, and R  ther, *Lithium–sulfur batteries—the solution is in the electrolyte, but is the electrolyte a solution?* Energy & Environmental Science, 2014,**7** (12): p. 3902-3920.
- [40] Moon, Mandai, Tatara, Ueno, Yamazaki, Yoshida, Seki, Dokko, and Watanabe, *Solvent Activity in Electrolyte Solutions Controls Electrochemical Reactions in Li-Ion and Li-Sulfur Batteries*. The Journal of Physical Chemistry C, 2015,**119** (8): p. 3957-3970.
- [41] Kou, Li, Liu, Zhang, Yang, Jiang, He, Dai, Zheng, and Yu, *Triple-Layered Carbon-SiO<sub>2</sub> Composite Membrane for High Energy Density and Long Cycling Li-S Batteries*. ACS Nano, 2019,**13** (5): p. 5900-5909.
- [42] Lin, Shafique, Cai, Xiao, Chen, Wang, and Hu, *Three-Dimensional-Ordered Porous Nanostructures for Lithium-Sulfur Battery Anodes and Cathodes Confer Superior Energy Storage Performance*. ACS Nano, 2019,**13** (11): p. 13037-13046.
- [43] Du, Wu, Yang, Wang, Che, Lyu, Chen, Wang, and Hu, *Efficient synergism of electrocatalysis and physical confinement leading to durable high-power lithium-sulfur batteries*. Nano Energy, 2019,**57** p. 34-40.
- [44] Zhang, Duan, Wang, Wang, Wang, Wang, and Wang, *Natural graphene microsheets/sulfur as Li-S battery cathode towards >99% coulombic efficiency of long cycles*. Journal of Power Sources, 2018,**376** p. 131-137.
- [45] Yao, Wang, Zhao, Liu, Niu, and Chen, *A Flexible All-in-One Lithium-Sulfur Battery*. ACS Nano, 2018,**12** (12): p. 12503-12511.
- [46] Yang, Zhang, Guo, Zhu, Zhao, Wang, Fan, Xiao, and Zhang, *A N,S-codoped hierarchical carbon Foam@Porous carbon composite as freestanding cathode for high-performance lithium-sulfur batteries*. Journal of Alloys and Compounds, 2018,**768** p. 495-502.
- [47] Yan, Chen, Yu, Zhao, Li, Hu, Wu, Chen, Wang, Peng, Gao, Hasan, Li, and Su, *3D Ferroconcrete-Like Aminated Carbon Nanotubes Network Anchoring Sulfur for Advanced Lithium-Sulfur Battery*. Advanced Energy Materials, 2018,**8** (25): p. 1801066.

- [48] Mikhaylik, Kovalev, Schock, Kumaresan, Xu, and Affinito, *High Energy Rechargeable Li-S Cells for EV Application: Status, Remaining Problems and Solutions*. The Electrochemical Society, 2010, p. 23-34.
- [49] Kim, Jung, and Park, *Effects of imidazolium salts on discharge performance of rechargeable lithium-sulfur cells containing organic solvent electrolytes*. Journal of Power Sources, 2005, **152** p. 272-277.
- [50] Yuan, Feng, Ai, Cao, Chen, and Yang, *Improved dischargeability and reversibility of sulfur cathode in a novel ionic liquid electrolyte*. Electrochemistry Communications, 2006, **8** (4): p. 610-614.
- [51] Ma, Wen, Jin, Wu, zhang, Wu, and Zhang, *The enhanced performance of Li-S battery with P14YRTFSI-modified electrolyte*. Solid State Ionics, 2014, **262** p. 174-178.
- [52] Suo, Hu, Li, Armand, and Chen, *A new class of Solvent-in-Salt electrolyte for high-energy rechargeable metallic lithium batteries*. Nature Communications, 2013, **4** p. 1481.
- [53] Shin, Kim, Oh, and Cho, *Polysulfide dissolution control: the common ion effect*. Chemical Communications (Cambridge), 2013, **49** (20): p. 2004-2006.
- [54] Shin, Jung, Kim, Ahn, and Ahn, *Preparation and characterization of plasticized polymer electrolytes based on PVdF-HFP copolymer for lithium/sulfur battery*. Journal of Materials Science: Materials in Electronics, 2002, **13** (12): p. 727-733.
- [55] Armand, Endres, MacFarlane, Ohno, and Scrosati, *Ionic-liquid materials for the electrochemical challenges of the future*. Nature materials, 2009, **8** (8): p. 621-629.
- [56] Xia, Wang, Xia, Xu, Zhang, Wu, Liang, Gu, and Tu, *A Newly Designed Composite Gel Polymer Electrolyte Based on Poly(Vinylidene Fluoride-Hexafluoropropylene) (PVDF-HFP) for Enhanced Solid-State Lithium-Sulfur Batteries*. Chemistry, 2017, **23** (60): p. 15203-15209.
- [57] Zhang, Lin, Zhu, Zhang, and Liu, *Improved lithium-ion and electrically conductive sulfur cathode for all-solid-state lithium-sulfur batteries*. RSC Advances, 2017, **7** (31): p. 19231-19236.
- [58] Morimoto, Awano, Terashima, Shindo, Nakanishi, Ito, Ishikawa, and Tobishima, *Preparation of lithium ion conducting solid electrolyte of NASICON-type  $\text{Li}_{1+x}\text{Al}_x\text{Ti}_{2-x}(\text{PO}_4)_3$  ( $x = 0.3$ ) obtained by using the mechanochemical method and its application as surface modification materials of  $\text{LiCoO}_2$  cathode for lithium cell*. Journal of Power Sources, 2013, **240** p. 636-643.

- [59] Hayashi, Hama, Morimoto, Tatsumisago, and Minami, *Preparation of  $\text{Li}_2\text{S-P}_2\text{S}_5$  Amorphous Solid Electrolytes by Mechanical Milling*. Journal of the American Ceramic Society, 2004,**84** (2): p. 477-479.
- [60] Kondo, Takada, and Yamamura, *New lithium ion conductors based on  $\text{Li}_2\text{S-SiS}_2$  system*. Solid State Ionics, 1992,**53-56** p. 1183-1186.
- [61] Croce, *Nanocomposite polymer electrolytes and their impact on the lithium battery technology*. Solid State Ionics, 2000,**135** (1-4): p. 47-52.
- [62] Jayanthi, Kulasekarapandian, Arulsankar, Sankaranarayanan, and Sundaresan, *Influence of nano-sized  $\text{TiO}_2$  on the structural, electrical, and morphological properties of polymer-blend electrolytes  $\text{PEO-PVC-LiClO}_4$* . Journal of Composite Materials, 2014,**49** (9): p. 1035-1045.
- [63] Matsuo, Remhof, Martelli, Caputo, Ernst, Miura, Sato, Oguchi, Maekawa, Takamura, Borgschulte, Zuttel, and Orimo, *Complex hydrides with  $(\text{BH}_4)^-$  and  $(\text{NH}_2)^-$  anions as new lithium fast-ion conductors*. Journal of the American Chemical Society, 2009,**131** (45): p. 16389-16391.
- [64] Kim, Toyama, Oguchi, Sato, Takagi, Ikeshoji, and Orimo, *Fast Lithium-Ion Conduction in Atom-Deficient closo-Type Complex Hydride Solid Electrolytes*. Chemistry of Materials, 2018,**30** (2): p. 386-391.
- [65] Yang, Luo, and Sun, *Towards high-performance solid-state Li-S batteries: from fundamental understanding to engineering design*. Chemical Society Reviews, 2020,**49** (7): p. 2140-2195.
- [66] Eshetu, Judez, Li, Bondarchuk, Rodriguez-Martinez, Zhang, and Armand, *Lithium Azide as an Electrolyte Additive for All-Solid-State Lithium-Sulfur Batteries*. Angewandte Chemie International Edition, 2017,**56** (48): p. 15368-15372.
- [67] Hakari, Deguchi, Mitsuhashi, Ohta, Saito, Orikasa, Uchimoto, Kowada, Hayashi, and Tatsumisago, *Structural and Electronic-State Changes of a Sulfide Solid Electrolyte during the Li Deinsertion–Insertion Processes*. Chemistry of Materials, 2017,**29** (11): p. 4768-4774.
- [68] Zhang, Huang, Huang, Cai, Wu, and Yao, *CNTs@S composite as cathode for all-solid-state lithium-sulfur batteries with ultralong cycle life*. Journal of Energy Chemistry, 2020,**40** p. 151-155.
- [69] Kuhn, Gerbig, Zhu, Falkenberg, Maier, and Lotsch, *A new ultrafast superionic Li-conductor: ion dynamics in  $\text{Li}_{11}\text{Si}_2\text{PS}_{12}$  and comparison with other tetragonal LGPS-type electrolytes*. Physical Chemistry Chemical Physics, 2014,**16** (28): p. 14669-14674.

- [70] Kato, Hori, Saito, Suzuki, Hirayama, Mitsui, Yonemura, Iba, and Kanno, *High-power all-solid-state batteries using sulfide superionic conductors*. *Nature Energy*, 2016,**1** (4): p. 16030.
- [71] Ji, Lee, and Nazar, *A Highly Ordered Nanostructured Carbon-sulphur Cathode for Lithium-sulphur Batteries*. *Nature materials*, 2009,**8** (6): p. 500-506.
- [72] Evers and Nazar, *New approaches for high energy density lithium-sulfur battery cathodes*. *Accounts of Chemical Research*, 2013,**46** (5): p. 1135-1143.
- [73] Zhang, Huang, Bae, Chung, Zhang, Manthiram, and Yu, *Nanostructured Host Materials for Trapping Sulfur in Rechargeable Li-S Batteries: Structure Design and Interfacial Chemistry*. *Small Methods*, 2018,**2** (1): p. 1700279-1700310.
- [74] Wu, Wang, Wang, Chen, Li, Zhao, Sun, Chen, Ni, and Diao, *Three-dimensional graphene hollow spheres with high sulfur loading for high-performance lithium-sulfur batteries*. *Electrochimica Acta*, 2017,**224** p. 527-533.
- [75] Park, Moon, Kim, Kang, Lim, Park, Lee, Yu, Seo, Lee, Heo, Tanaka, Cho, Pyun, Cabana, Hong, and Sung, *Graphene quantum dots: structural integrity and oxygen functional groups for high sulfur/sulfide utilization in lithium sulfur batteries*. *NPG Asia Materials*, 2016,**8** (5): p. e272-e272.
- [76] Chen, Wang, Dong, Lu, Du, and Chen, *Monodispersed Sulfur Nanoparticles for Lithium–Sulfur Batteries with Theoretical Performance*. *Nano Letters*, 2014,**15** (1): p. 798-802.
- [77] Zhao, Hu, Zhang, Zhang, Hu, and Chen, *Sulfur nanodots electrodeposited on ni foam as high-performance cathode for Li-S batteries*. *Nano Letters*, 2015,**15** (1): p. 721-726.
- [78] Zhang, Qin, Li, and Gao, *Enhancement of long stability of sulfur cathode by encapsulating sulfur into micropores of carbon spheres*. *Energy & Environmental Science*, 2010,**3** (10): p. 1531.
- [79] Zhu, Zhao, An, Anasori, Wang, and Xu, *Ultra-microporous carbons encapsulate small sulfur molecules for high performance lithium-sulfur battery*. *Nano Energy*, 2017,**33** p. 402-409.
- [80] Niu, Zhou, Lv, Shi, Luo, He, Li, Yang, and Kang, *Sulfur confined in nitrogen-doped microporous carbon used in a carbonate-based electrolyte for long-life, safe lithium-sulfur batteries*. *Carbon*, 2016,**109** p. 1-6.
- [81] Han, Song, Lee, Kim, Ahn, and Lee, *Effect of multiwalled carbon nanotubes on electrochemical properties of lithium sulfur rechargeable batteries*. *Journal of the Electrochemical Society*,

- 2003,**150** (7): p. A889-A893.
- [82] Guo, Xu, and Wang, *Sulfur-impregnated disordered carbon nanotubes cathode for lithium-sulfur batteries*. *Nano Lett*, 2011,**11** (10): p. 4288-4294.
- [83] Zhou, Wang, Li, Hou, Yin, Liu, Lu, Gentle, and Cheng, *A flexible nanostructured sulphur-carbon nanotube cathode with high rate performance for Li-S batteries*. *Energy & Environmental Science*, 2012,**5** (10): p. 8901.
- [84] Dorfler, Hagen, Althues, Tubke, Kaskel, and Hoffmann, *High capacity vertical aligned carbon nanotube/sulfur composite cathodes for lithium-sulfur batteries*. *Chemical Communications (Cambridge)*, 2012,**48** (34): p. 4097-4099.
- [85] Sun, Li, Jiang, Kong, Jiang, Wang, and Fan, *Sulfur nanocrystals confined in carbon nanotube network as a binder-free electrode for high-performance lithium sulfur batteries*. *Nano Lett*, 2014,**14** (7): p. 4044-4049.
- [86] Fang, Li, Zhao, Yin, Du, Hou, Wang, Cheng, Liu, and Li, *Single-wall Carbon Nanotube Network Enabled Ultrahigh Sulfur-content Electrodes for High-performance Lithium-sulfur Batteries*. *Nano Energy*, 2017,**42** p. 205-214.
- [87] Wang, Yang, Liang, Robinson, Li, Jackson, Cui, and Dai, *Graphene-wrapped sulfur particles as a rechargeable lithium-sulfur battery cathode material with high capacity and cycling stability*. *Nano Lett*, 2011,**11** (7): p. 2644-2647.
- [88] Zhou, Chen, Yu, Wang, Cui, Disalvo, and Abruña, *Amylopectin wrapped graphene oxide/sulfur for improved cyclability of lithium-sulfur battery*. *ACS Nano*, 2013,**7** (10): p. 8801-8808.
- [89] Cao, Chen, Zhao, Zhang, Lu, Wang, Niu, and Chen, *A Flexible Nanostructured Paper of a Reduced Graphene Oxide-Sulfur Composite for High-Performance Lithium-Sulfur Batteries with Unconventional Configurations*. *Advanced Materials (Weinheim, Germany)*, 2016,**28** (43): p. 9629-9636.
- [90] Fang, Zhao, Pei, Qian, Hou, Cheng, Liu, and Li, *Toward More Reliable Lithium-Sulfur Batteries: An All-Graphene Cathode Structure*. *ACS Nano*, 2016,**10** (9): p. 8676-8682.
- [91] Deng, Zhou, Fang, and Liu, *Graphene/Sulfur Composites with a Foam-Like Porous Architecture and Controllable Pore Size for High Performance Lithium-Sulfur Batteries*. *ChemNanoMat*, 2016,**2** (10): p. 952-958.
- [92] Li, Sun, Hou, Jiang, Huang, and Geng, *Three-dimensional porous carbon composites containing*

- high sulfur nanoparticle content for high-performance lithium–sulfur batteries*. Nature Communications, 2016,**7** (1): p.
- [93] Sun, Wang, Long, Qiao, Ling, Lv, and Cai, *A high-rate lithium–sulfur battery assisted by nitrogen-enriched mesoporous carbons decorated with ultrafine La<sub>2</sub>O<sub>3</sub> nanoparticles*. Journal of Materials Chemistry A, 2013,**1** (42): p. 13283.
- [94] Tang, Zhang, Zhao, Huang, Cheng, Tian, Peng, and Wei, *Nitrogen-doped aligned carbon nanotube/graphene sandwiches: facile catalytic growth on bifunctional natural catalysts and their applications as scaffolds for high-rate lithium-sulfur batteries*. Advanced Materials (Weinheim, Germany), 2014,**26** (35): p. 6100-6105.
- [95] Wang, Zhang, Qu, Lai, and Li, *Nitrogen-doped graphene/Sulfur Composite as Cathode Material for High Capacity Lithium–sulfur Batteries*. Journal of Power Sources, 2014,**256** p. 361-368.
- [96] Li, Zhou, Yin, Koratkar, Li, and Cheng, *Stabilizing sulfur cathodes using nitrogen-doped graphene as a chemical immobilizer for Li S batteries*. Carbon, 2016,**108** p. 120-126.
- [97] Li, Gan, Wang, Chen, Chen, and He, *In situ synthesis of 3D sulfur-doped graphene/sulfur as a cathode material for lithium-sulfur batteries*. Journal of Alloys and Compounds, 2018,**754** p. 64-71.
- [98] Kim, Lee, Jeon, and Piao, *Phosphorus-doped graphene nanosheets anchored with cerium oxide nanocrystals as effective sulfur hosts for high performance lithium–sulfur batteries*. Nanoscale, 2019,**11** (29): p. 13758-13766.
- [99] Gu, Tong, Lai, Qiu, Huang, Yang, Wen, Liu, Hou, and Zhang, *A porous nitrogen and phosphorous dual doped graphene blocking layer for high performance Li–S batteries*. Journal of Materials Chemistry A, 2015,**3** (32): p. 16670-16678.
- [100] Xu, Su, Zhang, Bao, and Wang, *A Nitrogen–sulfur Co-doped Porous Graphene Matrix as a Sulfur Immobilizer for High Performance Lithium–sulfur Batteries*. Journal of Materials Chemistry A, 2016,**4** (44): p. 17381-17393.
- [101] Yin, Liang, Zhou, Li, Saito, and Cheng, *Understanding the interactions between lithium polysulfides and N-doped graphene using density functional theory calculations*. Nano Energy, 2016,**25** p. 203-210.
- [102] Wu, Chen, Li, Zhao, and Chen, *Improvement of Rate and Cycle Performance by Rapid Polyaniline Coating of a MWCNT/Sulfur Cathode*. The Journal of Physical Chemistry C,

- 2011,**115** (49): p. 24411-24417.
- [103] Chen, Dong, Ge, Wang, Wu, Lu, and Chen, *Ultrafine Sulfur Nanoparticles in Conducting Polymer Shell as Cathode Materials for High Performance Lithium/Sulfur Batteries*. Scientific Reports, 2013,**3** (1): p. 1910-1915.
- [104] Ma, Wen, Jin, Lu, Wu, Wu, and Chen, *Hollow polyaniline sphere@sulfur composites for prolonged cycling stability of lithium-sulfur batteries*. Journal of Materials Chemistry A, 2014,**2** (27): p. 10350.
- [105] Xiao, Cao, Xiao, Schwenzler, Engelhard, Saraf, Nie, Exarhos, and Liu, *A Soft Approach to Encapsulate Sulfur: Polyaniline Nanotubes for Lithium-sulfur Batteries with Long Cycle Life*. Advanced Materials, 2012,**24** (9): p. 1176-1181.
- [106] Tao, Wang, Liu, Wang, Yao, Zheng, Seh, Cai, Li, Zhou, Zu, and Cui, *Balancing surface adsorption and diffusion of lithium-polysulfides on nonconductive oxides for lithium-sulfur battery design*. Nature Communications, 2016,**7** p. 11203.
- [107] Liang, Kwok, Lodi-Marzano, Pang, Cuisinier, Huang, Hart, Houtarde, Kaup, Sommer, Brezesinski, Janek, and Nazar, *Tuning Transition Metal Oxide-Sulfur Interactions for Long Life Lithium Sulfur Batteries: The “Goldilocks” Principle*. Advanced Energy Materials, 2016,**6** (6): p. 1501636.
- [108] Pu, Shen, Zheng, Wu, Zhu, Zhou, Zhang, and Pan, *Multifunctional Co<sub>3</sub>S<sub>4</sub>@sulfur nanotubes for enhanced lithium-sulfur battery performance*. Nano Energy, 2017,**37** p. 7-14.
- [109] Dai, Hu, Li, Xu, Wang, Liu, Chen, Bao, Chen, Henkelman, Li, and Xu, *Chinese knot-like electrode design for advanced Li-S batteries*. Nano Energy, 2018,**53** p. 354-361.
- [110] Xu, Zhang, Fan, Cheng, Su, and Wang, *Promoting lithium polysulfide/sulfide redox kinetics by the catalyzing of zinc sulfide for high performance lithium-sulfur battery*. Nano Energy, 2018,**51** p. 73-82.
- [111] Jiang, Xu, Yang, Wu, Wei, and Wang, *Mesoporous, conductive molybdenum nitride as efficient sulfur hosts for high-performance lithium-sulfur batteries*. Journal of Power Sources, 2018,**395** p. 77-84.
- [112] Luo, Chung, Yaghoobnejad Asl, and Manthiram, *Long-Life Lithium-Sulfur Batteries with a Bifunctional Cathode Substrate Configured with Boron Carbide Nanowires*. Advanced Materials (Weinheim, Germany), 2018,**30** (39): p. e1804149.

- [113] Tang, Li, Pan, Cullen, Liu, Pakdel, Long, Yang, McEvoy, Duesberg, Nicolosi, and Zhang, *In Situ Formed Protective Barrier Enabled by Sulfur@Titanium Carbide (MXene) Ink for Achieving High-Capacity, Long Lifetime Li-S Batteries*. *Advanced Science*, 2018,**5** (9): p. 1800502.
- [114] Wang, Shen, Liu, Xu, Liu, Hu, Yang, Feng, Liu, Shi, Ouyang, Yu, and Zhu, *Self-Supported and Flexible Sulfur Cathode Enabled via Synergistic Confinement for High-Energy-Density Lithium-Sulfur Batteries*. *Advanced Materials (Weinheim, Germany)*, 2019,p. e1902228.
- [115] Chen, Zhang, Zhou, Tian, Su, Wang, Stockdale, Kang, Li, and Wang, *Co-Fe Mixed Metal Phosphide Nanocubes with Highly Interconnected-Pore Architecture as an Efficient Polysulfide Mediator for Lithium-Sulfur Batteries*. *ACS Nano*, 2019,**13** (4): p. 4731-4741.
- [116] Zhong, Yin, He, Liu, Wu, and Wang, *Surface Chemistry in Cobalt Phosphide-Stabilized Lithium-Sulfur Batteries*. *Journal of the American Chemical Society*, 2018,**140** (4): p. 1455-1459.
- [117] Shaibani, Mirshekarloo, Singh, Easton, Cooray, Eshraghi, Abendroth, Dorfler, Althues, Kaskel, Hollenkamp, Hill, and Majumder, *Expansion-tolerant architectures for stable cycling of ultrahigh-loading sulfur cathodes in lithium-sulfur batteries*. *Science advances*, 2020,**6** (1): p. eaay2757.
- [118] Xie, Pan, Jin, Qi, Wang, Li, Xu, Zheng, Li, Qie, Huang, and Li, *Semi-Flooded Sulfur Cathode with Ultralean Absorbed Electrolyte in Li-S Battery*. *Advanced Science*, 2020,p. 1903168.
- [119] Huang, Zhang, and Wei, *Multi-functional separator/interlayer system for high-stable lithium-sulfur batteries: Progress and prospects*. *Energy Storage Materials*, 2015,**1** p. 127-145.
- [120] Su and Manthiram, *A new approach to improve cycle performance of rechargeable lithium-sulfur batteries by inserting a free-standing MWCNT interlayer*. *Chemical Communications (Cambridge)*, 2012,**48** (70): p. 8817-8819.
- [121] Su and Manthiram, *Lithium-sulphur batteries with a microporous carbon paper as a bifunctional interlayer*. *Nature Communications*, 2012,**3** p. 1166.
- [122] Zhao, Zhu, An, Chen, Sun, Wu, and Xu, *A 3D Conductive Carbon Interlayer with Ultrahigh Adsorption Capability for Lithium-sulfur Batteries*. *Applied Surface Science*, 2018,**440** p. 770-777.
- [123] Zhang, Li, Zhang, Fang, Li, Qin, Zhang, and Lai, *From Filter Paper to Carbon Paper and*

- toward Li–S Battery Interlayer. *Materials Letters*, 2014,**121** p. 198-201.
- [124] Li, Chen, Chen, Hu, Wang, Sun, Sun, and Li, *From interlayer to lightweight capping layer: Rational design of mesoporous TiO<sub>2</sub> threaded with CNTs for advanced Li–S batteries*. *Carbon*, 2019,**143** p. 523-530.
- [125] Ma, Wen, Jin, Wu, Wu, and Zhang, *Enhanced Cycle Performance of Li–S Battery with A Polypyrrole Functional Interlayer*. *Journal of Power Sources*, 2014,**267** p. 542-546.
- [126] Xiao, Yang, Wang, Nie, Zhong, Lai, Xu, Zhang, and Huang, *A Lightweight TiO<sub>2</sub>/Graphene Interlayer, Applied as a Highly Effective Polysulfide Absorbent for Fast, Long-Life Lithium-Sulfur Batteries*. *Advanced Materials*, 2015,**27** (18): p. 2891-2898.
- [127] Yao, Yan, Li, Zheng, Kong, Seh, Narasimhan, Liang, and Cui, *Improved Lithium–sulfur Batteries with A Conductive Coating on the Separator to Prevent the Accumulation of Inactive S-related Species at the Cathode–separator Interface*. *Energy & Environmental Science*, 2014,**7** (10): p. 3381-3390.
- [128] Chung and Manthiram, *Bifunctional Separator with a Light-Weight Carbon-Coating for Dynamically and Statically Stable Lithium-Sulfur Batteries*. *Advanced Functional Materials*, 2014,**24** (33): p. 5299-5306.
- [129] Huang, Xu, Abouali, Akbari Garakani, and Kim, *Porous graphene oxide/carbon nanotube hybrid films as interlayer for lithium-sulfur batteries*. *Carbon*, 2016,**99** p. 624-632.
- [130] Zhu, Ge, Kim, Lu, Chen, Jiang, and Zhang, *A Novel Separator Coated by Carbon for Achieving Exceptional High Performance Lithium-sulfur Batteries*. *Nano Energy*, 2016,**20** p. 176-184.
- [131] Du, Guo, Wang, Hu, Jin, Zhang, Jin, Qi, Xin, Kong, Guo, Ji, and Wan, *Atom-Thick Interlayer Made of CVD-Grown Graphene Film on Separator for Advanced Lithium-Sulfur Batteries*. *ACS Applied Materials and Interfaces*, 2017,**9** (50): p. 43696-43703.
- [132] Zhao, Ye, Peng, Divitini, Kim, Lao, Coxon, Xi, Liu, Ducati, Chen, and Kumar, *Advanced Lithium-Sulfur Batteries Enabled by a Bio-Inspired Polysulfide Adsorptive Brush*. *Advanced Functional Materials*, 2016,**26** (46): p. 8418-8426.
- [133] Sun, Sun, Peng, Wang, Ge, Akhtar, Huang, and Wang, *Nano-MgO/AB decorated separator to suppress shuttle effect of lithium–sulfur battery*. *Nanoscale Advances*, 2019,**1** (4): p. 1589-1597.
- [134] Li, Ma, Wang, Chen, Wu, and Wang, *LDHs derived nanoparticle-stacked metal nitride as interlayer for long-life lithium sulfur batteries*. *Science Bulletin*, 2018,**63** (3): p. 169-175.

- [135] Qiu, An, Yan, Xu, Zhang, Guo, Wang, Zheng, Wang, Deng, and Li, *Suppressed polysulfide shuttling and improved Li<sup>+</sup> transport in Li-S batteries enabled by NbN modified PP separator*. Journal of Power Sources, 2019,**423** p. 98-105.
- [136] Luo, Luo, Kong, Wu, Wang, Fan, Duan, and Wang, *Multifunctional Interlayer Based on Molybdenum Diphosphide Catalyst and Carbon Nanotube Film for Lithium-Sulfur Batteries*. Small, 2018,**14** (8): p.
- [137] He, Chen, and Manthiram, *Vertical Co<sub>9</sub>S<sub>8</sub> hollow nanowall arrays grown on a Celgard separator as a multifunctional polysulfide barrier for high-performance Li-S batteries*. Energy & Environmental Science, 2018,**11** (9): p. 2560-2568.
- [138] Hong, Song, Yang, Tan, Li, Cai, and Wang, *Cerium Based Metal-Organic Frameworks as an Efficient Separator Coating Catalyzing the Conversion of Polysulfides for High Performance Lithium-Sulfur Batteries*. ACS Nano, 2019,**13** (2): p. 1923-1931.
- [139] Guo, Sun, Liang, Ying, Zeng, Ying, Zhou, Liang, Lin, and Peng, *Blocking Polysulfides and Facilitating Lithium-Ion Transport: Polystyrene Sulfonate@HKUST-1 Membrane for Lithium-Sulfur Batteries*. ACS Applied Materials & Interfaces, 2018,**10** (36): p. 30451-30459.
- [140] Li, Wan, Huang, Assen, Hsiung, Jiang, Han, Eddaoudi, Lai, Ming, and Li, *Metal-Organic Framework-Based Separators for Enhancing Li-S Battery Stability: Mechanism of Mitigating Polysulfide Diffusion*. ACS Energy Letters, 2017,**2** (10): p. 2362-2367.
- [141] Zhang, Qin, Fang, Li, Jia, Lai, Zhang, and Li, *Nickel foam as interlayer to improve the performance of lithium-sulfur battery*. Journal of Solid State Electrochemistry, 2013,**18** (4): p. 1025-1029.
- [142] Shao, Wang, Zhang, Wang, Chen, and Huang, *Nano-TiO<sub>2</sub> decorated carbon coating on the separator to physically and chemically suppress the shuttle effect for lithium-sulfur battery*. Journal of Power Sources, 2018,**378** p. 537-545.
- [143] Ryu, Ahn, Kim, Ahn, Lee, and Cairns, *Self-discharge of lithium-sulfur cells using stainless-steel current-collectors*. Journal of Power Sources, 2005,**140** (2): p. 365-369.
- [144] Huang, Zhuang, Zhang, Peng, Chen, and Wei, *Permselective graphene oxide membrane for highly stable and anti-self-discharge lithium-sulfur batteries*. ACS Nano, 2015,**9** (3): p. 3002-3011.
- [145] Yan, Luo, Kong, Luo, Wu, Jiang, Li, Fan, Duan, and Wang, *Enhanced performance of lithium-*

- sulfur batteries with an ultrathin and lightweight MoS<sub>2</sub>/carbon nanotube interlayer*. Journal of Power Sources, 2018,**389** p. 169-177.
- [146] Yi, Lin, Zhao, Liu, Li, Hardwick, Yang, Zhao, Geng, and Zhang, *Fabrication of a Light-Weight Dual-Function Modified Separator towards High-Performance Lithium-Sulfur Batteries*. ChemElectroChem, 2019,**6** (14): p. 3648-3656.
- [147] Guo, Ming, Su, Wu, Wahyudi, Li, Hedhili, Sheng, Li, Alshareef, Li, and Lai, *MXene based self-assembled cathode and antifouling separator for high-rate and dendrite-inhibited Li-S battery*. Nano Energy, 2019,**61** p. 478-485.
- [148] Jiang, Li, Yuan, Wu, and Tang, *Black phosphorus with superior lithium ion batteries performance directly synthesized by the efficient thermal-vaporization method*. Electrochimica Acta, 2018,**263** p. 272-276.
- [149] Grixti, Mukherjee, and Singh, *Two-dimensional boron as an impressive lithium-sulphur battery cathode material*. Energy Storage Materials, 2018,**13** p. 80-87.
- [150] Zhou, Zhang, Song, Xiao, Gao, and Ding, *Dopamine-Assisted Synthesis of MoS<sub>2</sub> Nanosheets on Carbon Nanotube for Improved Lithium and Sodium Storage Properties*. ACS Applied Energy Materials, 2018,**1** (9): p. 5112-5118.
- [151] Tan, Li, Wang, Guo, and Wang, *Lightweight Reduced Graphene Oxide@MoS<sub>2</sub> Interlayer as Polysulfide Barrier for High-Performance Lithium-Sulfur Batteries*. ACS Applied Materials & Interfaces, 2018,**10** (4): p. 3707-3713.
- [152] Wang, He, Zhang, Liu, Huang, and Jin, *Graphdiyne-Modified Polyimide Separator: A Polysulfide-Immobilizing Net Hinders the Shuttling of Polysulfides in Lithium-Sulfur Battery*. ACS Applied Materials & Interfaces, 2019,**11** (39): p. 35738-35745.
- [153] Zhang, Li, Wang, Zhang, Tan, Chu, and Guo, *Microemulsion Assisted Assembly of 3D Porous S/Graphene@g-C<sub>3</sub>*
- N4
- Hybrid Sponge as Free-Standing Cathodes for High Energy Density Li-S Batteries*. Advanced Energy Materials, 2018,**8** (14): p. 1702839.
- [154] Zhang, Xiao, Zhang, Liu, Zhang, Zhao, Wang, Zhang, and Shao, *Construction of a low-defect and highly conductive 3D graphene network to enable a high sulphur content cathode for high performance Li-S/graphene batteries*. Journal of Materials Chemistry A, 2018,**6** (45): p. 22555-

22565.

- [155] Lei, Hu, Chen, Lv, Jiao, Wang, Lv, Yan, Huang, Chu, Yan, Wu, Wang, He, and Xiong, *Genetic engineering of porous sulfur species with molecular target prevents host passivation in lithium sulfur batteries*. Energy Storage Materials, 2020,**26** p. 65-72.
- [156] Wang, Zhang, Yu, Liu, Wang, and Qiu, *Boosting redox activity on MXene-induced multifunctional collaborative interface in high Li<sub>2</sub>S loading cathode for high-energy Li-S and metallic Li-free rechargeable batteries*. Journal of Energy Chemistry, 2019,**37** p. 183-191.
- [157] Geim, *Graphene: Status and Prospects*. Science, 2009,**324** (5934): p. 1530.
- [158] Wang, Wang, and Chen, *Reduced graphene oxide film as a shuttle-inhibiting interlayer in a lithium-sulfur battery*. Journal of Power Sources, 2013,**242** p. 65-69.
- [159] Sun, Ou, Yue, Yang, Wang, Rooney, and Sun, *A simply effective double-coating cathode with MnO<sub>2</sub> nanosheets/graphene as functionalized interlayer for high performance lithium-sulfur batteries*. Electrochimica Acta, 2016,**207** p. 198-206.
- [160] Deng, Yao, Huang, Su, Zhang, and Du, *Highly improved electrochemical performance of Li-S batteries with heavily nitrogen-doped three-dimensional porous graphene interlayers*. Materials Research Bulletin, 2016,**84** p. 218-224.
- [161] Xing, Xi, Li, Su, Lai, Zhao, and Kumar, *Nitrogen, sulfur-codoped graphene sponge as electroactive carbon interlayer for high-energy and -power lithium-sulfur batteries*. Journal of Power Sources, 2016,**303** p. 22-28.
- [162] Naguib, Kurtoglu, Presser, Lu, Niu, Heon, Hultman, Gogotsi, and Barsoum, *Two-dimensional nanocrystals produced by exfoliation of Ti<sub>3</sub>AlC<sub>2</sub>*. Advanced Materials, 2011,**23** (37): p. 4248-4253.
- [163] Mashtalir, Naguib, Mochalin, Dall’Agnese, Heon, Barsoum, and Gogotsi, *Intercalation and delamination of layered carbides and carbonitrides*. Nature Communications, 2013,**4** (1): p. 1716.
- [164] Li, Shao, Lin, Lu, Liu, Duployer, Persson, Eklund, Hultman, Li, Chen, Zha, Du, Rozier, Chai, Raymundo-Pinero, Taberna, Simon, and Huang, *A general Lewis acidic etching route for preparing MXenes with enhanced electrochemical performance in non-aqueous electrolyte*. Nature materials, 2020,p.
- [165] Anasori, Xie, Beidaghi, Lu, Hosler, Hultman, Kent, Gogotsi, and Barsoum, *Two-Dimensional,*

- Ordered, Double Transition Metals Carbides (MXenes)*. ACS Nano, 2015,**9** (10): p. 9507-9516.
- [166] Anasori, Shi, Moon, Xie, Voigt, Kent, May, Billinge, Barsoum, and Gogotsi, *Control of electronic properties of 2D carbides (MXenes) by manipulating their transition metal layers*. Nanoscale Horizons, 2016,**1** (3): p. 227-234.
- [167] Ling, Ren, Zhao, Yang, Giammarco, Qiu, Barsoum, and Gogotsi, *Flexible and conductive MXene films and nanocomposites with high capacitance*. Proceedings of the National Academy of Sciences of the United States of America, 2014,**111** (47): p. 16676-16681.
- [168] Liang, Garsuch, and Nazar, *Sulfur cathodes based on conductive MXene nanosheets for high-performance lithium-sulfur batteries*. Angewandte Chemie International Edition, 2015,**54** (13): p. 3907-3911.
- [169] Zhao, Zhai, Yang, Wang, Qu, Du, and Wang, *Self-supporting Ti<sub>3</sub>C<sub>2</sub>T<sub>x</sub> foam/S cathodes with high sulfur loading for high-energy-density lithium-sulfur batteries*. Nanoscale, 2018,**10** (48): p. 22954-22962.
- [170] Tang, Li, Pan, Tu, Du, Qiu, Yang, Cullen, McEvoy, and Zhang, *A Robust, Freestanding MXene-Sulfur Conductive Paper for Long-Lifetime Li-S Batteries*. Advanced Functional Materials, 2019,p. 1901907.
- [171] Wang, Yang, Xiong, Chen, Huang, Wang, Liu, Liu, and Huang, *A robust sulfur host with dual lithium polysulfide immobilization mechanism for long cycle life and high capacity Li-S batteries*. Energy Storage Materials, 2019,**16** p. 344-353.
- [172] Song, Su, Xie, Guo, Bao, Shao, and Wang, *Immobilizing Polysulfides with MXene-Functionalized Separators for Stable Lithium-Sulfur Batteries*. ACS Applied Materials and Interfaces, 2016,**8** (43): p. 29427-29433.
- [173] Dong, Zheng, Qin, Zhao, Shi, Wang, Chen, and Wu, *All-MXene-Based Integrated Electrode Constructed by Ti<sub>3</sub>C<sub>2</sub> Nanoribbon Framework Host and Nanosheet Interlayer for High-Energy-Density Li-S Batteries*. ACS Nano, 2018,**12** (3): p. 2381-2388.
- [174] Yin, Xu, Nie, Dou, and Zhang, *MXene debris modified eggshell membrane as separator for high-performance lithium-sulfur batteries*. Chemical Engineering Journal, 2018,**352** p. 695-703.
- [175] Jiao, Zhang, Geng, Wu, Li, Lv, Tao, Chen, Zhou, Li, Ling, Wan, and Yang, *Capture and Catalytic Conversion of Polysulfides by In Situ Built TiO<sub>2</sub>-MXene Heterostructures for Lithium-Sulfur Batteries*. Advanced Energy Materials, 2019,p. 1900219.

- [176] Li, Meng, Zhu, Li, Ma, Huang, Song, and Fan, *Lattice constant-dependent anchoring effect of MXenes for lithium-sulfur (Li-S) batteries: a DFT study*. *Nanoscale*, 2019,**11** (17): p. 8485-8493.
- [177] Fan, Wang, Kang, Wang, Xie, Cheng, and Liu, *A Compact MXene Film with Folded Structure for Advanced Supercapacitor Electrode Material*. *ACS Applied Energy Materials*, 2020,**3** (2): p. 1811-1820.
- [178] Zhu, Rajouâ, Le Vot, Fontaine, Simon, and Favier, *Modifications of MXene layers for supercapacitors*. *Nano Energy*, 2020,**73** p. 104734.
- [179] Wang, Zhai, Zhao, Li, Yang, Zhang, and Huang, *Laminar MXene-Nafion-modified separator with highly inhibited shuttle effect for long-life lithium-sulfur batteries*. *Electrochimica Acta*, 2019,**320** p. 134558.
- [180] Jiang, Zheng, Chen, Ding, Li, Sun, and Li, *In-situ decoration of MOF-derived carbon on nitrogen-doped ultrathin MXene nanosheets to multifunctionalize separators for stable Li-S batteries*. *Chemical Engineering Journal*, 2019,**373** p. 1309-1318.

## **Chapter 2: Experimental section**

**I**n this section, the characterization of materials and test techniques of batteries involved in this thesis are introduced. Their operation mechanisms and functions in understanding the synthesized materials will be described briefly.

### **2.1 Structure and morphology characterization**

#### **2.1.1 Raman spectrum**

Raman spectrum is produced by the inelastic scattering of the interaction between light and material molecules. When monochromatic laser of high frequency is cast on the molecules, it will strongly interact with the electrons and induce vibration dipole moment, leading to the polarized molecules. If these polarized molecules release the scattering light with the same frequency as the incident light, this scattering is called the Rayleigh scattering and can be treated as the elastic collision between photon and molecule [1]. It is the strongest scattering phenomenon in this molecular system. For the inelastic scattering, the photons either gain or lose energy from the molecule, resulting in the different scattering light frequency with the incident light. This phenomenon is called the Raman effect and the resulted scattering spectrum is called the Raman spectrum. In a Raman spectrum, the scattering light has fixed energy difference with the Rayleigh scattering, which is called the Raman shift, and the spectrum with lower frequency than the Rayleigh line is called the Stokes line, while the line with higher frequency is called the anti-Stokes line. Both Stokes and anti-Stokes line are used for Raman spectrum analysis, but the former is the most used one [2]. In this thesis the Raman equipment used is Jobin YvonXploRA from HORIBA Scientific.

#### **2.1.2 X-ray diffraction**

X-ray diffraction, known as XRD, uses X-ray to probe the material's information of crystal structure, including the lattice system, the crystallinity degree, the grain size and so on. The working principle of XRD is based on the diffraction of X-ray in the crystal with periodic ordered atoms. Because of the

periodic arrangement, the scattered X-ray from each atom will interfere with each other due to the fixed phase relationship, and in certain directions it will form constructive interference, i.e. diffracted wave. The diffracted wave has two critical features: its distribution and intensity. The former is determined by the size and morphology and orientation of crystal cell, while the latter is the result of atom types and position in the crystal cell.

The relationship between the interlayer spacing ( $d$ ), incident angle ( $\theta$ ), and wave length ( $\lambda$ ) when diffracted wave happens can be described by the Bragg equation [3, 4]:

$$2d \sin \theta = n\lambda$$

**Equation 2.4**

where  $n$  is the diffraction series. The X-ray diffractometer type used in this thesis is D8 Advance from Bruker using a Cu  $K\alpha$  radiation source with a working voltage of 40 kV and a current of 40 mA. The wave length of the Cu  $K\alpha$  radiation is 1.544 Å.

### **2.1.3 Scanning electron microscopy**

Technically, scanning electron microscopy uses highly focused high-energy electron beam for scanning the specimen to stimulate certain physical signals, which are collected and amplified for the surface morphology observation. These stimulated signals include backscattered electrons, secondary electrons, Auger electrons and so on, as shown in the schematic **Figure 2.47** [5].

Backscattered electrons are from the electron beam reflexed by the specimen atoms, including elastic and inelastic scattered electrons. The backscattered electrons are generated from the surface depth of several hundred nanometers, and their amount are positively related to the sample's atomic number. Therefore, backscattered electrons can be used for both morphology characterization and elemental qualitative analysis.

Secondary electrons refer to the electrons that leave the surface of the sample under the bombardment of electron beam, and is a kind of free electrons in the vacuum. They come from the outer layer valence electrons of the sample atoms, which are easily ionized due to the low binding energy of the valence electrons. Usually the secondary electrons come from the surface depth of 5~10 nm from the sample, so their amount is sensitive to the surface morphology, which is applied in effective morphology

characterization.

If the energy released by the inner-shell electron transition is absorbed by other electrons and drives them detached from the atom to become the secondary electrons, then this kind of secondary electrons are called the Auger electron. Due to the characteristic energy of the electron from certain element atoms, Auger electrons also have corresponding energy values ranging from 50 to 1500 eV relating to the chemical elements. The Auger electrons can only be received from the limited atomic layers of the sample surface, therefore being suitable for surface chemical element analysis [6].

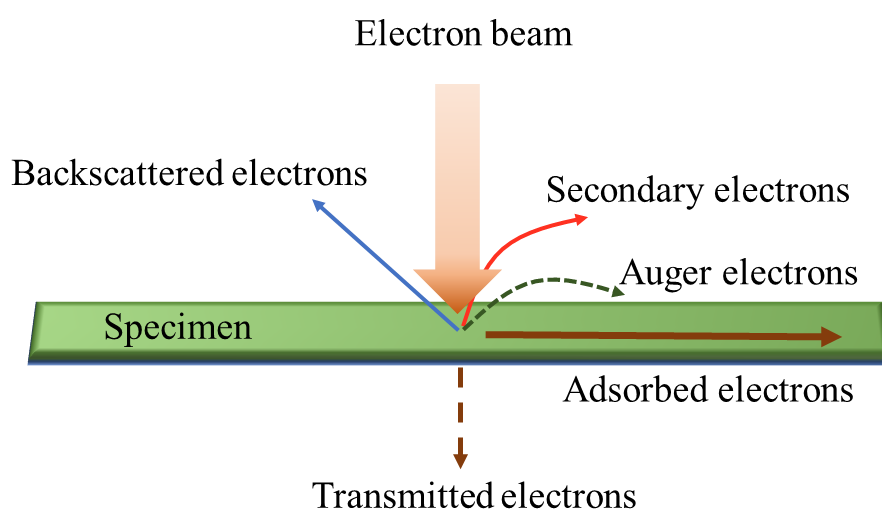


**Figure 2.47** Schematic of the physical signals from the interaction between electron beam and specimen in the SEM system (Adapted from Ref. [6]).

#### 2.1.4 Transmission electron microscopy

Transmission electron microscopy is the microscopy using electron beam as illuminant to achieve high magnification and resolution. Its light path is similar to that of optical microscopy, as shown in **Figure 2.48**. The electron beam released by the electron gun is accelerated by the high voltage and become highly focused by the condenser. This beam will penetrate through the sample and then enter the objective lens, followed by the magnification of middle lens and projection lens. The magnified image will be collected on the screen. The penetrability of the electron beam is much less than the X-ray, therefore the sample should have thickness less than 200 nm. Electrons penetrating through the sample carry the intrinsic structural information of the sample and projects it to the screen in the form of images or diffraction spectrum [7].

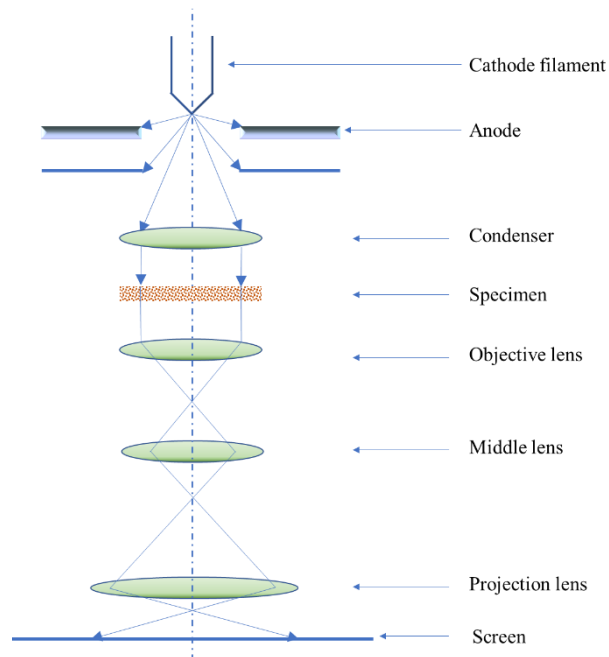


**Figure 2.48** The schematic of the optical path in the TEM system (adapted from Ref. [7]).

## 2.2 Electrochemical tests

### 2.2.1 Cyclic voltammetry

Cyclic voltammetry (CV) is the method commonly applied for the investigation of the redox process. In a typical CV profile, the  $x$ -axis parameter applied to the system is the potential ( $E$ ), while the responding current ( $i$ ) is recorded as the  $y$ -axis. The arrow indicates the direction and the beginning potential of the initial sweeping. As potential of the working electrode scans from high to low, the cathodic current ascends with the process. However, as the concentration of the reactant species near the electrode gradually deplete over time in accordance with the Nernst equation, the diffusion layer of the species increases continuously, making reactant species slower to reach the electrode surface. Consequently, a decreasing current appears as the scan goes on, resulting in a current peak [8]. When the scan is reversed, the similar process happens during the oxidation and contributes to the oxidation current peak (**Figure 2.49**).

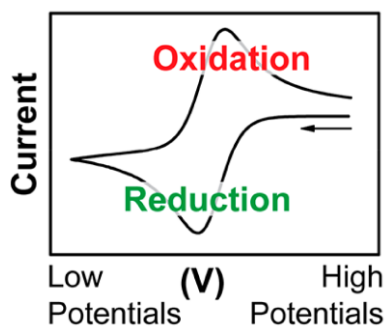


**Figure 2.49** The schematic of the oxidation and reduction peaks in a cyclic voltammetry (CV) [8].

In this thesis, the CV test was done using the two-electrode coin cell system on an Autolab electrochemical workstation (PGSTAT302N). In this method, the metal Li anode functioned both as the counter electrode and the reference electrode. The scanning window was selected as 1.5-3 V (maybe 0.1-0.2 V shifted for each chapter), for that the reduction and peaks of a typical Li-S battery with organic electrolyte fall into this range, just as in most related research papers [9-11]. The scanning rate for the CV test was as low as  $0.1 \text{ mV s}^{-1}$ , in order to minimize the polarization of Li anode (both reference electrode and counter electrode).

### 2.2.2 Galvanostatic charge and discharge

A galvanostatic charge and discharge test was used to evaluate the cycling performance of the Li-S battery. The current was fixed in each galvanostatic cell cycling, and the current value was determined by the active material mass in each cell cathode and the theoretical capacity of the elemental sulfur. The theoretical capacity can be calculated by the formula [12]:

$$Q_{\text{theoretical}} = \frac{nF}{3.6 \times M} \text{ (mAh g}^{-1}\text{)}.$$

#### Equation 2.5

Here, the  $n$  is the number of  $\text{Li}^+$  per formula unit of the elemental sulfur ( $n = 2$  for single S atom),  $F$  is the Faraday constant ( $96485 \text{ C mol}^{-1}$ ), and  $M$  is the relative mass of S atom ( $M_s = 32 \text{ g mol}^{-1}$ ). Therefore, the theoretical specific capacity of the elemental sulfur can be determined as  $1675 \text{ mAh g}^{-1}$ .

The current rate unit used for this thesis is C ( $1675 \text{ mA g}_{\text{sulfur}}^{-1}$ ), which means the current needed for the sulfur per gram to be theoretically fully discharged/charged in one hour. For instance, the 0.1 C current can fully charge/discharge the Li-S battery using 10 hours. For the low and middle current rates tests, the currents of 0.2 C ( $335 \text{ mA g}_{\text{sulfur}}^{-1}$ ) and 0.5 C ( $837.5 \text{ mA g}_{\text{sulfur}}^{-1}$ ) were used, while the 1 C ( $1675$

mA g<sub>sulfur</sub><sup>-1</sup>) and 2 C (3350 mA g<sub>sulfur</sub><sup>-1</sup>) were selected for the high rate performance.

### 2.2.3 Electrochemical impedance spectroscopy

In this thesis, the electrochemical impedance spectroscopy (EIS) is adopted as an approach to analyse the electrode structure and the dielectric and transport properties of the materials [13]. For most EIS analysis in the Li-S battery area, the results are commonly presented in the form of Nyquist plot, as shown in **Figure 2.49**. The real and imaginary impedances in the Nyquist plot can be determined by two fundamental equations [14]:

$$Z' = R_s + \frac{R_{ct}}{1 + \omega^2 R_{ct}^2 C_{dl}^2}$$

**Equation 2.6**

and

$$Z'' = \frac{R_{ct}^2}{1 + \omega^2 R_{ct}^2 C_{dl}^2}$$

**Equation 2.7**

As shown by the equivalent circuit in the **Figure 2.50**, the corresponding circuit is composed of  $R_s$ ,  $R_{ct}$ ,  $C_{dl}$ , and  $Z_w$ , and which represent the simulated circuit system of the working electrode. Here,  $R_s$  is the solution resistance,  $R_{ct}$  stands for the charge transfer resistance,  $C_{dl}$  is for the double layer charging at the electrode surface, and  $Z_w$  (also written as  $W_o$ ) symbolizes the Warburg Element. The  $Z_w$  appearing at low-frequency region is the reflection of ions diffusion in the electrolyte [13, 14].

The Autolab electrochemical workstation (PGSTAT302N) was selected to conduct the EIS tests in this thesis. All the tests were done with an amplitude of 5 mV and a frequency range of 0.01 Hz-100 kHz.

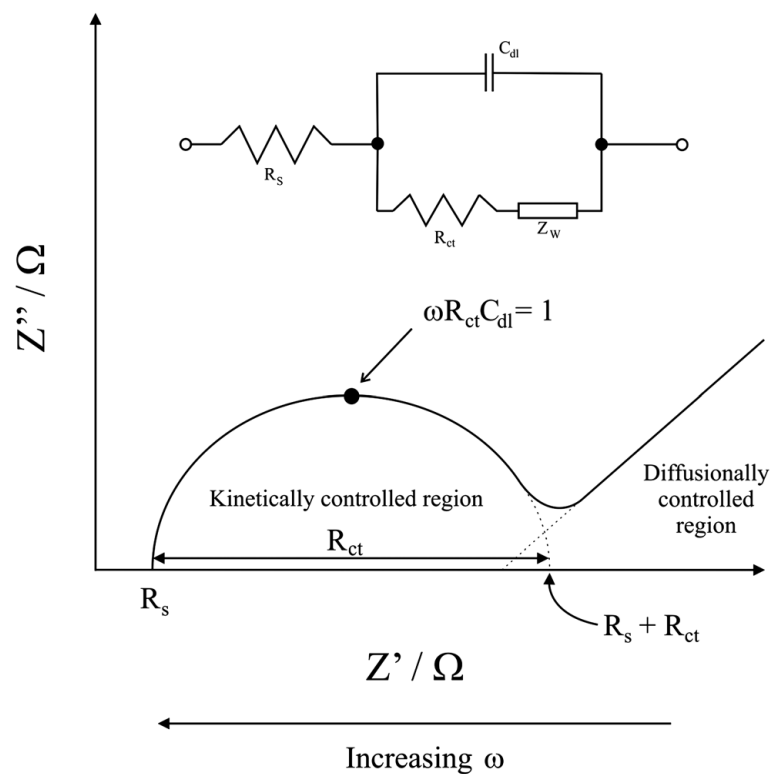


**Figure 2.50** A schematic Nyquist plot of the Randles equivalent circuit for an electrochemical cell [14].

### 2.3 References

- [1] Hendra and Stratton, *Laser-Raman spectroscopy*. Chemical Reviews, 1969,**69** (3): p. 325-344.
- [2] Rostron, Gaber, and Gaber, *Raman Spectroscopy, Review*. International Journal of Engineering and Technical Research, 2016,**6** (1): p. 50-64.
- [3] Patterson, *The Scherrer Formula for X-Ray Particle Size Determination*. Physical Review, 1939,**56** (10): p. 978-982.
- [4] Garnier, *Powder Diffraction. Theory and Practice*. Edited by R. E. Dinnebier and S. J. L. Billinge. Cambridge: RSC Publishing, 2008. Acta Crystallographica Section A, 2009,**65** (1): p. 51.
- [5] Nixon, Huxley, and Klug, *The general principles of scanning electron microscopy*. Philosophical Transactions of the Royal Society of London. B, Biological Sciences, 1971,**261** (837): p. 45-50.
- [6] Akhtar, Khan, Khan, and Asiri, *Scanning Electron Microscopy: Principle and Applications in Nanomaterials Characterization*. 2018,p. 113-145.
- [7] Tanaka, *Structure and Imaging of a Transmission Electron Microscope (TEM)*. 2017,p. 17-28.

- [8] Elgrishi, Rountree, McCarthy, Rountree, Eisenhart, and Dempsey, *A Practical Beginner's Guide to Cyclic Voltammetry*. Journal of Chemical Education, 2017,**95** (2): p. 197-206.
- [9] Yang, Luo, and Sun, *Towards high-performance solid-state Li-S batteries: from fundamental understanding to engineering design*. Chemical Society Reviews, 2020,**49** (7): p. 2140-2195.
- [10] Zhao, Li, Peng, Yuan, Wei, and Huang, *Lithium-Sulfur Batteries under Lean Electrolyte Conditions: Challenges and Opportunities*. Angewandte Chemie International Edition, 2020,**59** (31): p. 12636-12652.
- [11] Song, Cai, Kong, Cai, Zhang, and Sun, *Rationalizing Electrocatalysis of Li-S Chemistry by Mediator Design: Progress and Prospects*. Advanced Energy Materials, 2019,**10** (11): p. 1901075.
- [12] Chen, *Study on the  $Li_{1-x}Ni_{0.5}Mn_{1.5}O_4$  for Lithium Ion Batteries: a First-Principles Theory*. International Journal of Electrochemical Science, 2017,**12** p. 11309-11315.
- [13] Macdonald, *Reflections on the history of electrochemical impedance spectroscopy*. Electrochimica Acta, 2006,**51** (8-9): p. 1376-1388.
- [14] Randviir and Banks, *Electrochemical impedance spectroscopy: an overview of bioanalytical applications*. Analytical Methods, 2013,**5** (5): p. 1098.

**Chapter 3: Carbon/ Poly (3,4-ethylene dioxythiophene) : Poly (styrene sulfonate)  
(CB/PEDOT:PSS) composite modified separator as a dual-function separator for high-  
performance Li-S batteries**

### 3.1. Introduction

In this chapter, a light-weight dual-functional modified separator for lithium-sulfur batteries was prepared through a physical blend and blade-coating approach. The separator is coated with carbon black/poly (3,4-ethylene dioxythiophene):poly (styrene sulfonate) (CB/PEDOT:PSS), remarkably improving the utilization of sulfur by serving as the co-current collector. Moreover, the PEDOT:PSS effectively inhibits the diffusion of polysulfides and promotes the migration of lithium ions by providing chemical absorption and cation transport acceleration. When assembling this modified separator into the coin cell, an initial specific capacity of 1315 mAh g<sup>-1</sup> at 0.2 C is achieved with a capacity of 956 mAh g<sup>-1</sup> after 100 cycles, showing a superior performance compared to the cell without an interlayer. Meanwhile, the cell exhibits a rate capability with a discharge capacity of 699 mAh g<sup>-1</sup> at a current density of 2 C. Notably, the areal CB/PEDOT:PSS coating is as low as 0.604 mg cm<sup>-2</sup>, bringing a specific electrode capacity of 522 mAh g<sup>-1</sup> at 1 C.

The research work in Chapter 3 was mainly designed and carried out by me under the direction of Dr. Li Yang, Prof. Laurence Hardwick, and Dr. Cezhou Zhao. The result presented in this chapter was published on ChemElectroChem, 2019. 6(14): p. 3648-3656 (DOI: 10.1002/celec.201900670). Permission was sought from other co-authors to include the materials from this paper to this thesis. The manuscript was drafted by me, corrected by Dr. Li Yang and Prof. Laurence Hardwick. Prof. Laurence Hardwick also contributed to the idea of isolating the interlayer. The rest of authors helped with some supporting works, including data analysis, schematic drawing, and double check the experimental results.

### 3.2. Experiment part

#### 3.2.1. Fabrication of Carbon/ Poly (3,4-ethylene dioxythiophene) : Poly (styrene sulfonate) (CB/PEDOT:PSS) modified separator

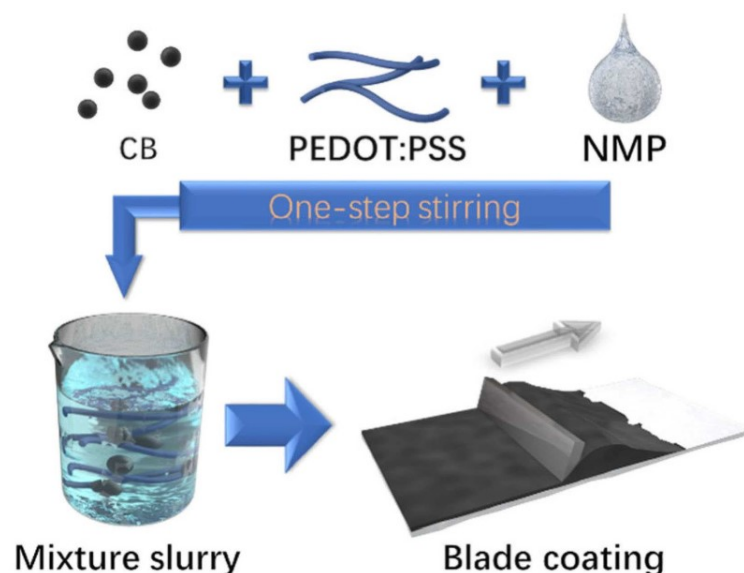


**Figure 3.51** Preparation of CB/PEDOT:PSS modified separator.

**Figure 3.51** shows the fabrication process of CB/PEDOT:PSS modified separator. The slurry was prepared by a one-step method that only involves physical mixing. Therefore, this process has great potential to be integrated into the existing industrial production. Carbon black (super-P, Timical, Switzerland), poly(vinylidene fluoride) (PVDF, >99.5%), and CB/PEDOT:PSS particles (Agfa, vacuum dried at 60°C for 12 h before used) were well mixed in a weight ratio of 40:4:5 in N-methyl-2-pyrrolidone (NMP, Aladdin). The slurry was magnetically stirred for 24 h in order to dissolve PEDOT:PSS well and improve the uniformity of the slurry. The homogeneous slurry was blade-coated on a Celgard 2400 separator via doctor blade coating. The coated separator was desiccated in vacuum at 50°C overnight. The resulting separator was denoted as CB/PEDOT:PSS separator. The pure carbon black modified separator was prepared following the same procedure and was marked as CB separator. The typical areal densities of the interlayers coating are 1.12 mg cm<sup>-2</sup> for CB and 0.604 mg cm<sup>-2</sup>.

#### 3.2.2. Electrode preparation

The S-C electrode was fabricated by mixing 60 wt% sulfur with 30 wt% conductive CB as a conducting agent and 10 wt% PVDF as a binder in the NMP. The slurry was magnetically stirred for 24 h

to achieve greater homogeneity. After stirring, the slurry was coated on a 20  $\mu\text{m}$  thick aluminum foil current collector by a blade-coating machine, followed by vacuum desiccation at 60  $^{\circ}\text{C}$  for 12 h. The prepared electrodes were cut into discs of diameter 13mm for coin cell assembling. A typical mass loading of the active materials was  $\sim 1.6 \text{ mg cm}^{-2}$ .

### 3.2.3. Materials Characterization

The morphology and elemental mapping of the CB and CB/PEDOT:PSS interlayers were observed using a scanning electron microscope (SEM, JEOL JSM-6510) and an energy dispersive X-ray spectrometer (EDS, PENTA FET Precision). The X-ray photoelectron spectroscopy (XPS, ESCALAB 250Xi, Thermo scientific) was conducted using Al K $\alpha$  X-ray source. The current-voltage curves were collected by the Autolab PGSTAT302 N electrochemical workstation using 1 cm  $\times$  4 cm rectangular samples.

### 3.2.4. Electrochemical Measurements

The S-C electrode and interlayer were tested in two-electrode 2032 coin-type cells using Li foil as counter electrodes. The cells were assembled in an argon-filled glove box. The electrolyte was 1.0 M lithium bis (trifluoromethanesulfonyl) imide (LiTFSI) in dioxolane (DOL) and dimethoxyethane (DME) (1:1 by volume) with a 1.0 wt% LiNO<sub>3</sub> additive. The amount of electrolyte is 50  $\mu\text{L}$  for each cell. The Li S cell without any interlayer is denoted as w/o interlayer. The CB and CB/PEDOT:PSS modified separators were cut into discs of 18 mm in diameter and placed with the coating facing towards the S-C working electrode. Galvanostatic charge/discharge tests were performed in the potential range of 1.5-2.8 V at 25  $^{\circ}\text{C}$  with the Neware CT-4008 battery-testing system.

## 3.3. Characterization results of the CB/PEDOT:PSS interlayer and relevant analysis

The morphology of the as-prepared CB/PEDOT:PSS interlayer surface was observed by SEM in **Figure 3.52**. The cross-section of this modified separator shows this CB/PEDOT:PSS coating has a thickness of around 6.4  $\mu\text{m}$ , as shown in Figure 1a, taking up only 35.5% of the Celgard separator's thickness (18.0  $\mu\text{m}$ ), as denoted in the figure. The specific surface area and pore information on CB/PEDOT:PSS coating were measured by nitrogen adsorption-desorption isotherms (**Figure 3.53**). The

Brunauer-Emmett-Teller (BET) specific surface area and pore volume are 52.0 m<sup>2</sup>/g and 0.18 mL/g, respectively. The pore size distribution, as shown in the inset of **Figure 3.53**, indicates abundant mesopores centered at 2.5 nm. Such a rough and porous surface of this interlayer offers a great chance to trap polysulfides and provides unimpeded channels for Li-ion between anode and cathode. The PEDOT:PSS not only enhances the physical strength by acting as the additional binder between carbon particles but also improves the electronic transmission of the CB/PEDOT:PSS composite by providing extra electron pathways between carbon particles. As a result, the CB/PEDOT:PSS interlayer presents better conductivity than the CB interlayer (see later discussion).

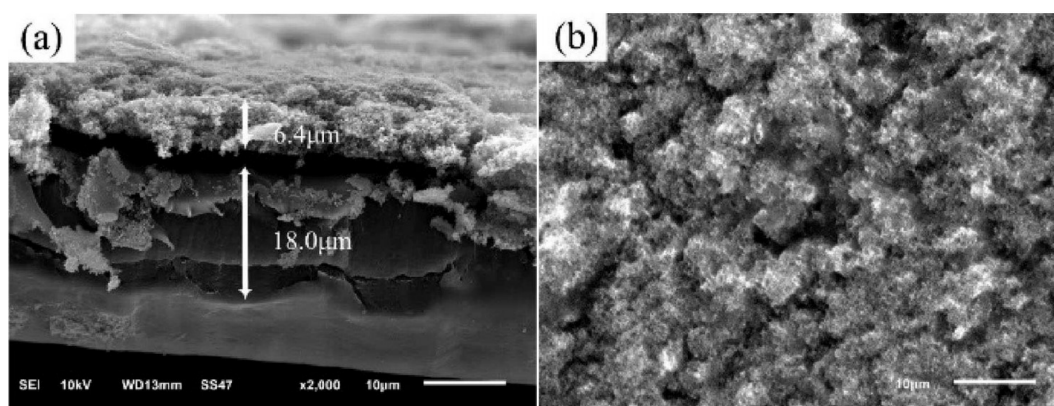


**Figure 3.52** (a) Side view of the CB/PEDOT:PSS modified separator; the thickness of the separator and coating layer were marked by arrows. (b) SEM image of the CB/PEDOT:PSS interlayer.

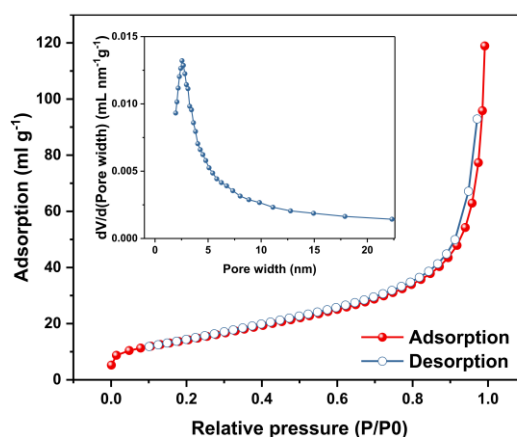


**Figure 3.53** Nitrogen adsorption-desorption isotherms of the CB/PEDOT:PSS coating. The insert shows the pore size distribution curves.

The improved conductivity of CB/PEDOT:PSS modified separator is confirmed by the comparison of current-voltage (IV) curves for pristine Celgard, CB, and CB/PEDOT:PSS modified separators (**Figure 3.54**). Tested by the linear sweep voltammetry, the CB/PEDOT:PSS modified separator shows

the largest slope value, followed by the CB and Celgard separator. Since the slope value is proportional to the electrical conductivity of the separator, this result reveals that the CB/PEDOT:PSS modified separator has the highest electrical conductivity among the three different separators. The specific resistivity values of three separators were measured by the four-probe method as shown in **Table 3.1**. This striking conductivity difference in the CB/PEDOT:PSS modified separator provides “high-way” for electron transportation. The conductivity refinement is due to that the “point-to-point” contact between two carbon particles is replaced with the large area contact brought by the PEDOT:PSS. Therefore, the CB/PEDOT:PSS modified separator can better facilitate the redox reaction of the active material than CB and pristine separators.

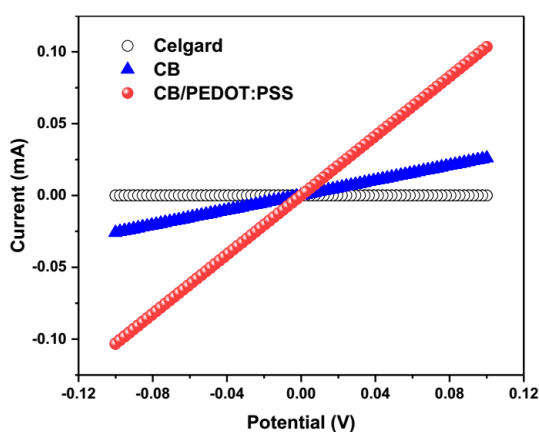


**Figure 3.54** Current-voltage (I-V) curves for pristine Celgard, CB, and CB/PEDOT:PSS modified separators.

**Table 3.1** The specific resistivity values of three separators were measured by the four-probe method.

Separators	Resistivity by four-probe/ $\Omega\cdot\text{cm}$
Celgard	N/A
CB	99.3
CB/PEDOT:PSS	22.1

Configuration of the Li S cell with the CB/PEDOT:PSS interlayer is shown in **Figure 3.55**. The CB/PEDOT:PSS was coated on one side of the Celgard separator (towards the cathode side). This conductive CB/PEDOT:PSS interlayer acts as a co-current collector to improve the specific capacity of the cell. Meanwhile, the carbon black and PEDOT:PSS components in the interlayer provide a physical

and chemical anchor for polysulfides, respectively, which greatly suppresses the shuttle effect and enhances the utilization of sulfur species.

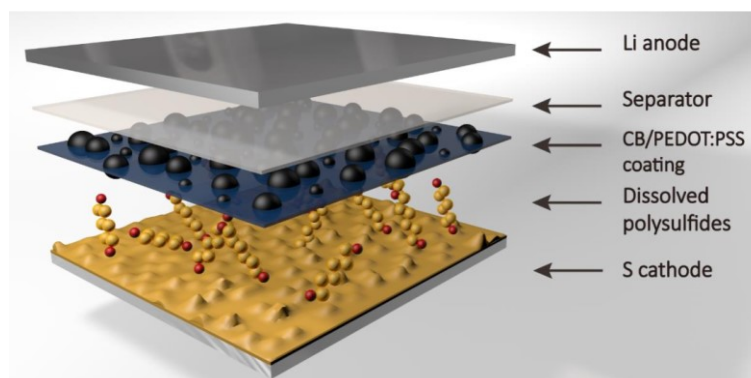


**Figure 3.55** Configuration of the Li-S cell with the CB/PEDOT:PSS interlayer.

The typical galvanostatic charge/discharge behaviors at the 2nd cycle of different cells at 0.2 C are presented in **Figure 3.56**. All the cells show one charge plateau at  $\sim 2.3$  V and two discharge plateaus  $\sim 2.3$  V and  $\sim 2.0$  V, which represent typical redox reactions of sulfides oxidation and two-step sulfur reduction [1]. The cell without interlayer shows a specific capacity of  $679 \text{ mAh g}^{-1}$ , only 40.6% of the theoretical capacity. For the cells with CB or CB/PEDOT:PSS interlayers, much higher capacities ( $947 \text{ mAh g}^{-1}$  and  $1370 \text{ mAh g}^{-1}$ ) are achieved, which are 56.5 % and 81.9 % of the theoretical capacity, respectively. The insert in **Figure 3.56** shows the enlarged part where two discharge plateaus meet. It is clear that for the cell without interlayer a “potential dip” is observed at the beginning of the low-voltage plateau. This can be attributed to the accumulation of insulating high-order polysulfides during the first reduction step, which increases the resistance of cathode and hinders further reduction [2]. Also, the concentration of the dissolved polysulfides in electrolyte reaches its maximum at this point, resulting in high viscosity of the electrolyte. Therefore, extra overpotential is needed to trigger the consequent reduction into  $\text{Li}_2\text{S}_2/\text{Li}_2\text{S}$ . When the potential drops to the value where high-order polysulfides begin to be reduced to  $\text{Li}_2\text{S}_2/\text{Li}_2\text{S}$ , the viscosity of electrolyte decreases and so does the polarization of the cell, therefore a “potential dip” occurs at the beginning of the second discharge plateau [3]. For the cell with CB interlayer, the dip is not obvious, and for the CB/PEDOT:PSS interlayer one this barrier almost disappears. This variation in the voltage barrier indicates the interlayers remit the influence of the polysulfides accumulation by improving conductivity and absorbing the dissolved polysulfides. In **Figure 3.56b–d**, the charge/discharge curves of different cells at various current rates also confirm that

the CB/PEDOT:PSS cell has superior performance in terms of sulfur utilization even at 2 C rate. By applying the PEDOT:PSS as a chemical anchor, the CB/PEDOT:PSS interlayer is evidenced to be more effective in polysulfide-trapping than the pure CB interlayer.

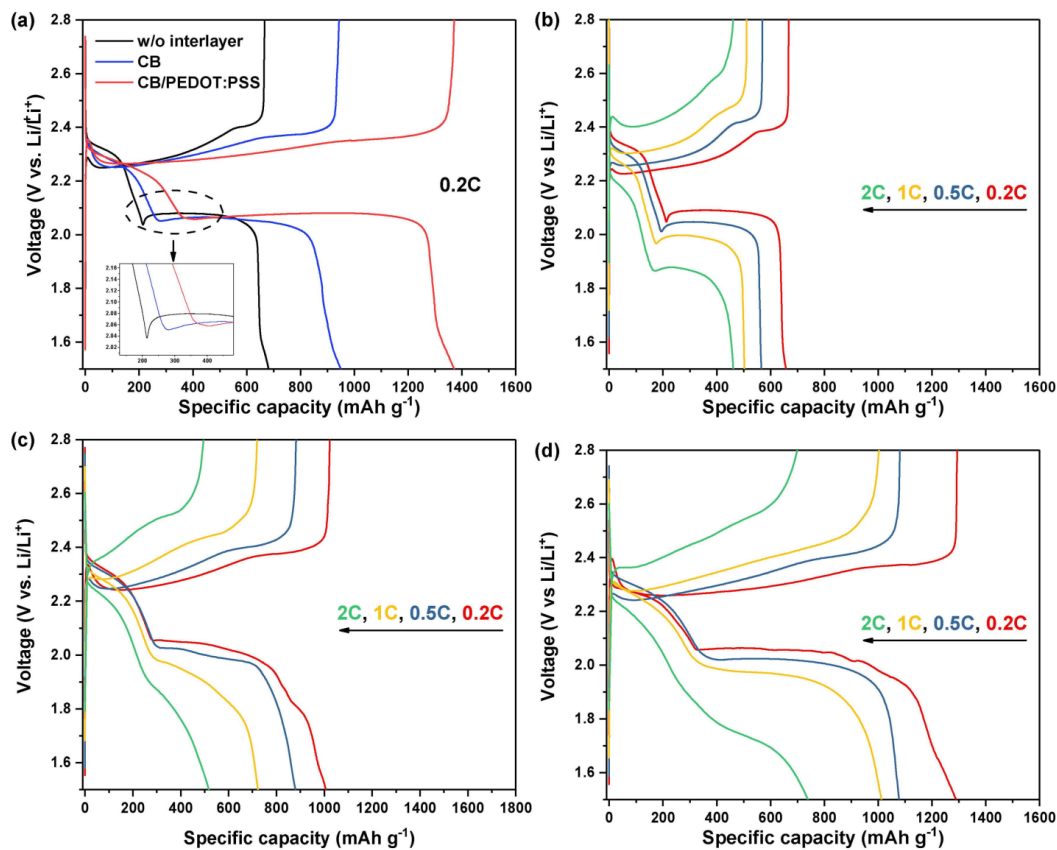


**Figure 3.56** Charge and discharge profiles (a) at 0.2 C the second cycle of cells without an interlayer, with CB and CB/PEDOT:PSS interlayers (the insert shows the enlarged part where two discharge plateaus meet); (b) at different rates of a cell without an interlayer, (c) at different rates of a cell with CB, and (d) at different rates of a cell with CB/PEDOT:PSS interlayers.

The cyclic voltammetry (CV) profiles of pristine cell and cell with CB/PEDOT:PSS interlayer help to clarify how this interlayer facilitates the redox kinetics, as shown in **Figure 3.57**. The CV curves show two prominent cathodic peaks and one anodic peak, which are typical for Li S batteries. The cathodic peaks are related to the lithiation process from  $S_8$  to long-chain polysulfides (2.2~2.3 V, Peak B) and the subsequent reduction to the insoluble short-chain polysulfides (1.9~2.0 V, Peak C), while anodic peaks (2.3~2.5 V, Peak A) are attributed to the reversed process of oxidation [4, 5]. It is clear from **Figure 3.57** that the cell with CB/PEDOT:PSS coating shows decreased voltage hysteresis, and the corresponding voltage differences between cathodic peaks and anodic peaks ( $\Delta E_A$  and  $\Delta E_B$ ) are significantly reduced in the CB/PEDOT:PSS cell ( $\Delta E_{A2} = 0.500 \text{ V} \rightarrow \Delta E_{A1} = 0.388 \text{ V}$  and  $\Delta E_{B2} = 0.222 \text{ V} \rightarrow \Delta E_{B1} = 0.105 \text{ V}$ ).

This can be explained by the effect of co-current collector provided by the CB/PEDOT:PSS coating, which leads to the improved electrochemical kinetics and decreased polarization. What's more, the higher value of the specific peak current of CB/PEDOT:PSS cell also confirms that the CB/PEDOT:PSS coating helps to maximize the utilization of active material. This is due to the outstanding polysulfides-trapping ability of this coating, as well as the improved Li-ion transport, which will be further proved by the subsequent results.

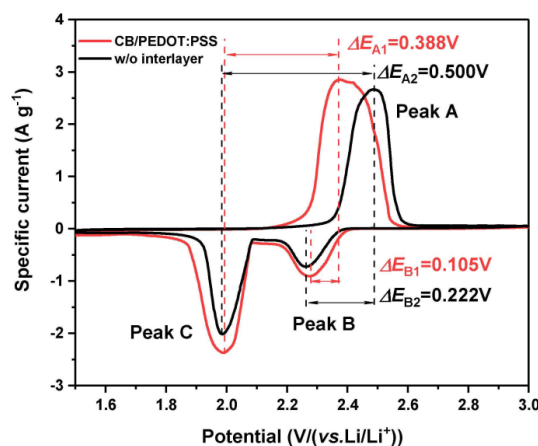


**Figure 3.57** Cyclic voltammetry profiles of pristine cell and cell with CB/PEDOT:PSS interlayer for the first cycle.

To get an in-depth understanding of the kinetic influence of the CB/PEDOT:PSS interlayer on the redox process, a comparison of the charge transfer coefficient based on Tafel equation is utilized at the electrochemical polarization voltage area of the anodic peak (peak A) and the cathodic peak (peak B). Because the scanning rate in the CV measurement is low ( $0.1 \text{ mV s}^{-1}$ ), the scanning can be treated as a quasi-steady-state process. According to the Tafel equation (for the oxidation) [6]:

$$\eta = -\frac{2.303RT}{\alpha nF} \log i_0 + \frac{2.303RT}{\alpha nF} \log i$$

**Equation 3.8**

where the  $\eta$  is the overpotential,  $R$  is the ideal gas constant,  $T$  is the temperature,  $i_0$  is the exchange current density,  $n$  is the electron transfer number,  $F$  is the Faraday constant, and  $\alpha$  is the charge transfer coefficient of the oxidation process and is the key influence of the electrode potential on the activation energy of oxidation.

The potential relationship:

$$\eta = \varphi - \varphi_e$$

**Equation 3.9**

where the  $\varphi$  is the potential of the working electrode and the  $\varphi_e$  is the equilibrium potential of the oxidation reaction.

From **Equation 3.8** and **Equation 3.9** the relationship between  $\varphi$  and  $\log i$  can be obtained as:

$$\varphi = \left( \varphi_e - \frac{2.303RT}{\alpha nF} \log i_0 \right) + \frac{2.303RT}{\alpha nF} \log i$$

**Equation 3.10**

The potential of working electrode  $\varphi$  is a linear function to the logarithmic current density  $\log i$  within the Tafel range, as shown in **Figure 3.58**. The variation in the slope reflects the change in  $\alpha$ : they are negatively correlated. Hence higher slope of the fitted line implies smaller  $\alpha$ , consequently higher activation energy for the certain electrode oxidation. The fitted slope value of the cell without interlayer ( $S_{w/o} = 243 \text{ mV dec}^{-1}$ ) is 2.4 times that of the CB/PEDOT:PSS interlayer ( $S_{CB/PESOT:PSS} = 103 \text{ mV dec}^{-1}$ ). That is to say, the  $\alpha_{CB/PESOT:PSS}$  is 2.4 times of  $\alpha_{w/o}$ , meaning a great reduction in the activation energy after the application of this CB/PEDOT:PSS interlayer.

For the reduction,

$$\eta = \varphi_e - \varphi$$

**Equation 3.11**

So, the relationship between  $\varphi$  and  $\log i$  transforms into:

$$\varphi = \left( \varphi_e + \frac{2.303RT}{\beta nF} \log i_0 \right) - \frac{2.303RT}{\beta nF} \log i$$

**Equation 3.12**

where the  $\beta$  is the charge transmission coefficient of the reduction, and  $\alpha + \beta = 1$  ( $0 < \alpha < 1$ ,  $0 < \beta < 1$ ). Similarly, the higher slope of the fitted line indicates the higher  $\beta$  value, thus smaller activation energy at the certain electrode potential. The slope of CB/PEDOT:PSS interlayer cell ( $-29.8 \text{ mV dec}^{-1}$ ) is higher than that of the pristine cell ( $-44.9 \text{ mV dec}^{-1}$ ), implying the decreased activation energy for the first-step reduction after the application of the interlayer. A similar result can also be found from the analysis of the peak C (**Figure 3.58c**), where the line slope comparison proves the same kinetic enhancement of the interlayer for the second reduction process.

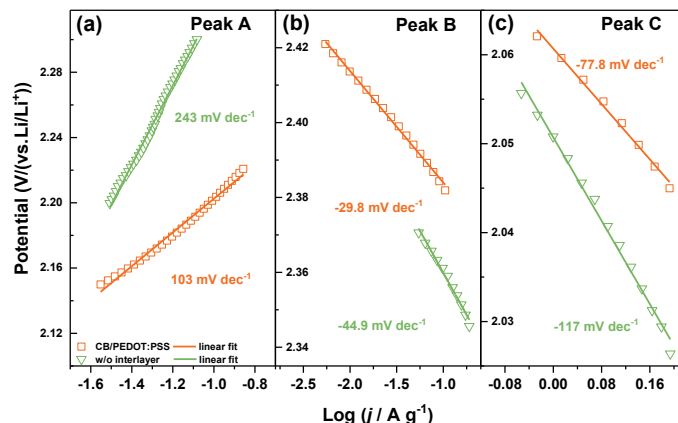


**Figure 3.58** The linear fitting result of the Tafel range in the CV curves (**Figure 3.57**): the comparison of (a) peak A and (b) peak B in different batteries.

The cyclic performances measured at 0.2 C of three different cells are compared in **Figure 3.59**. Both cells with pure CB and CB/PEDOT:PSS interlayers exhibit much higher specific capacities than the cell without the interlayer. A significant high initial specific discharge capacity of 1315 mAh g<sup>-1</sup> is delivered by the cell with CB/PEDOT:PSS interlayer, which is maintained at 956 mAh g<sup>-1</sup> after 100 cycles with a high capacity retention of 72.7% of the initial value. Correspondingly, the cell with CB interlayer shows capacities of 1019 mAh g<sup>-1</sup> and 718 mAh g<sup>-1</sup>, with a capacity retention of 70.4% under the same condition. In comparison, the pristine Li-S cell without the interlayer shows an initial capacity of 682 mAh g<sup>-1</sup> and a cycled capacity of 321 mAh g<sup>-1</sup> with poor retention of 47.1%. The cell with CB/PEDOT: PSS interlayer exhibits much superior electrochemical performance, which is also better than the cell with CB interlayer. This can be ascribed to the synergies from this dual-functional interlayer, including (i) the much better electron/ion transfer associated with the high electrical conductivity and porosity of CB/PEDOT:PSS interlayer, (ii) the heterogeneous atoms in PEDOT (thiophenic sulfur and ethylenedioxy R-O-O-R' group) which have strong interactions with soluble polysulfide species to entrap them [7], (iii) the -SO<sup>3-</sup> functional group of the PSS provides the hopping channel for Li-ion, and this mechanism facilitates the redox at high current density [8].

A further test on the rate performance of different cells has provided additional evidence that the cell with CB/PEDOT:PSS interlayer performed better than the cell with pure CB interlayer under various rates. As seen in **Figure 3.59b**, the cells were evaluated by increasing the C-rate from 0.2 C to 2 C, and then gradually back to 0.2 C. For the cell employing the CB/PEDOT:PSS interlayer, a specific capacity of 1293 mAh g<sup>-1</sup>, 1080 mAh g<sup>-1</sup>, 1002 mAh g<sup>-1</sup>, and 699 mAh g<sup>-1</sup> was achieved at 0.2 C, 0.5 C, 1 C, and

2 C, respectively, much higher than the one with CB interlayer (990, 879, 722 and 517 mAh g<sup>-1</sup> at 0.2, 0.5, 1 and 2 C). When the rate returns to 0.2 C after 60 cycles, a high reversible capacity of 1127 mAh g<sup>-1</sup> is recovered, corresponding to a capacity retention of 84.6%. As the rate capability is related to the kinetics of the cell, these results indicate the CB/PEDOT:PSS interlayer is more efficient in accelerating the velocity of the redox reaction in the Li S cell. This advantage is further demonstrated by the long-term cycling test at 1 C, as shown in **Figure 3.59c**. After 260 cycles the cell with CB/PEDOT:PSS interlayer still delivers a capacity of 674 mAh g<sup>-1</sup>, while the pristine cell only shows 370 mAh g<sup>-1</sup>. Notably, the areal density of CB/PEDOT:PSS coating is only 0.604 mg cm<sup>-2</sup> as low, bringing an outstanding specific capacity of 522 mAh g<sup>-1</sup> at 1 C based on the total mass of electrode materials and interlayer. Therefore, it can be concluded that the PEDOT:PSS has a prominent positive effect on the conventional sulfur cathode. All cells showed high Coulombic efficiencies in the range of 95–100 %

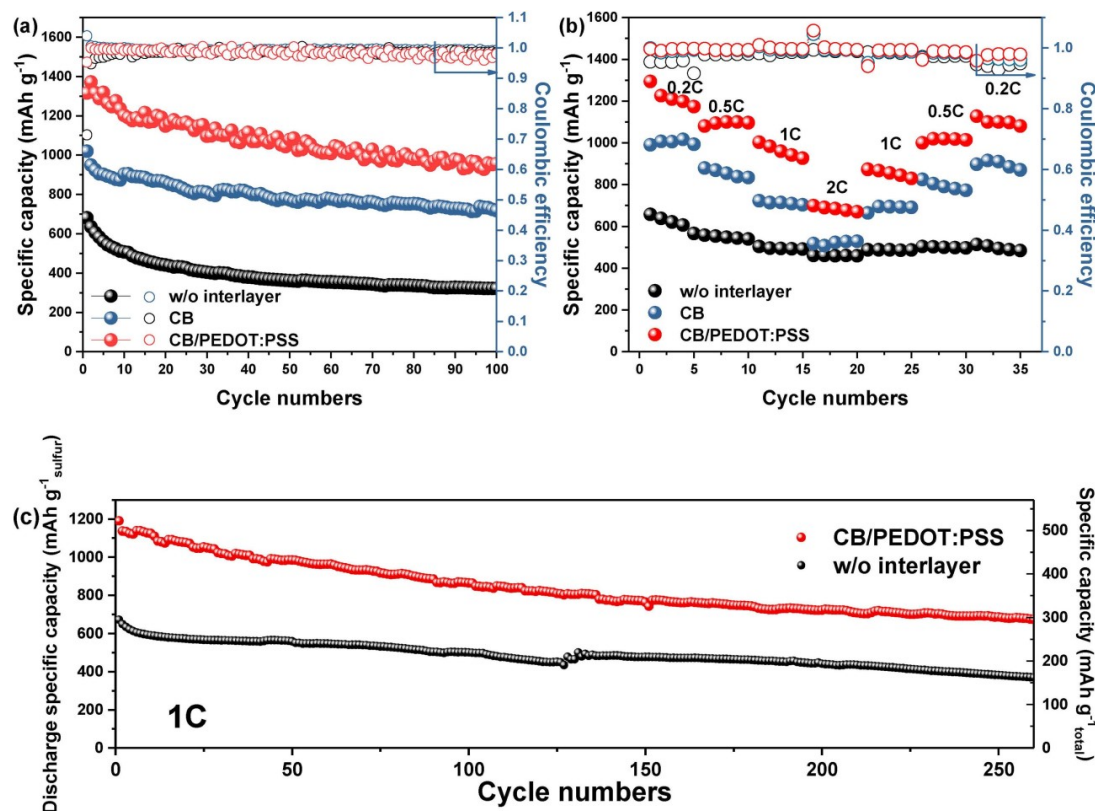


**Figure 3.59** (a) The cyclic discharging specific capacities and Coulombic efficiency of a cell without an interlayer, with CB or CB/PEDOT:PSS interlayer at 0.2 C current density. (b) The rate capacities of cells with CB or CB/PEDOT:PSS interlayer. (c) Long-term cycling of CB/PEDOT:PSS cell at 1 C.

To demonstrate the polysulfides-trapping ability, a special isolated cell was assembled and tested at 0.2 C, in which an additional separator was placed between the cathode and CB/PEDOT:PSS coating so that the coating was electrically isolated from electrodes but saturated with electrolyte [4], as shown in

**Figure 3.60.** Compared with the CB/PEDOT:PSS cell, the isolated cell showed a degraded initial specific capacity of 1113 mAh g<sup>-1</sup> and ended with 609 mAh g<sup>-1</sup> after 100 cycles. This drop of the capacity gives a further indication that the important role of the CB/PEDOT:PSS interlayer in sulfur utilization of the cell. It is also interesting to note that the Coulombic efficiency of the isolated cell continues to decline with cycles, and it drops to less than 0.9 after 100 cycles. The reason here is probably related to the dissolved polysulfides anchored by the CB/PEDOT:PSS coating during discharging cannot be further reduced or oxidized due to the isolation. Subsequently, a growing amount of active materials is accumulated and isolated in the CB/PEDOT:PSS layer, resulting in the fall of Coulombic efficiency. Cells with isolated interlayer and with 2 layers of separator show similar capacities for the initial 5 cycles and both show lower capacity than the CB/PEDOT:PSS cell due to the absence of the “co-current collector” effect. As the cycle goes on, the 2-layer-separator cell degrades more rapidly than the CB/PEDOT:PSS one. This is ascribed to the polysulfide absorption effect of the isolated interlayer that reduces the shuttle effect. These differences in capacity and Coulombic efficiency demonstrate the polysulfides trapping-ability of the CB/PEDOT:PSS coating in an indirect approach.

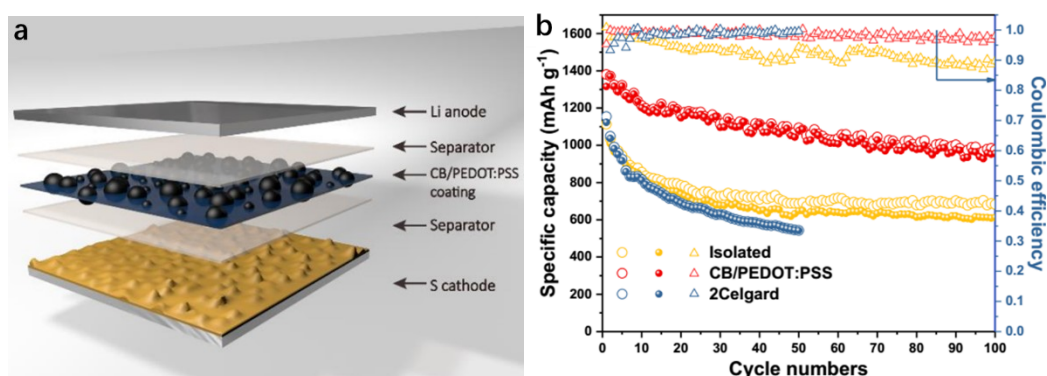


**Figure 3.60** (a) Scheme of the cell with the isolated CB/PEDOT:PSS interlayer structure. (b) Cycling performance of cells with 2-layer Celgards separator, isolated CB/PEDOT:PSS interlayer, and CB/PEDOT:PSS interlayer.

To quantify how much the modified separator promotes Li ion transference, a series of CV tests are conducted on cells with CB/PEDOT:PSS interlayer at different scanning rates (Figure 5). All the cathodic and anodic peak currents are linear with the square root of scan rate (Figure 5b, d), indicating that the reactions are diffusion-controlled [9]. The Randles-Sevcik equation was adopted to calculate the diffusion coefficients ( $D_{Li^+}$ ) (Equation 3.13) [9, 10]:

$$I_p = 2.69 \times 10^5 n^{1.5} A D_{Li^+}^{0.5} C \nu^{0.5}$$

**Equation 3.14**

Where  $I_p$  is the peak current,  $n$  is the electron transfer number during the reaction ( $n = 2$  for Li-S batteries),  $A$  is the electrode surface area ( $\text{cm}^2$ , which is undetermined in this porous sulfur cathode),  $D_{Li^+}$  is the diffusion coefficient of Li cation ( $\text{cm}^2 \text{s}^{-1}$ ),  $C$  is the concentration of Li cation in electrolyte ( $\text{mol mL}^{-1}$ ), and  $\nu$  is the scan rate ( $\text{V s}^{-1}$ ). The Li-ion diffusion coefficients of pristine cell and cell with CB/PEDOT:PSS modified separator were calculated and summarized in **Table 3.2**. It can be seen that the diffusion coefficients of lithium-ion in the CB/PEDOT:PSS covered cathode are significantly higher than those in the pristine Li S cell. Coefficients have grown by 167.8%, 144.7%, and 45.5% for peak A, B, and C, respectively. This suggested that the redox reactions, especially the anodic reaction  $\text{Li}_2\text{S}/\text{Li}_2\text{S}_2 \rightarrow \text{S}_8$  and cathodic reaction  $\text{S}_8 \rightarrow \text{Li}_2\text{S}_8$  are remarkably enhanced. This result demonstrates that the addition of the CB/PEDOT:PSS modified separator does not hinder the transport of Li cation, but in fact improves it. This prominent increase in Li-ion diffusion coefficients is probably ascribed to the sulfonate groups in PSS that allow for accelerating the Li cation transport during cycling [11].

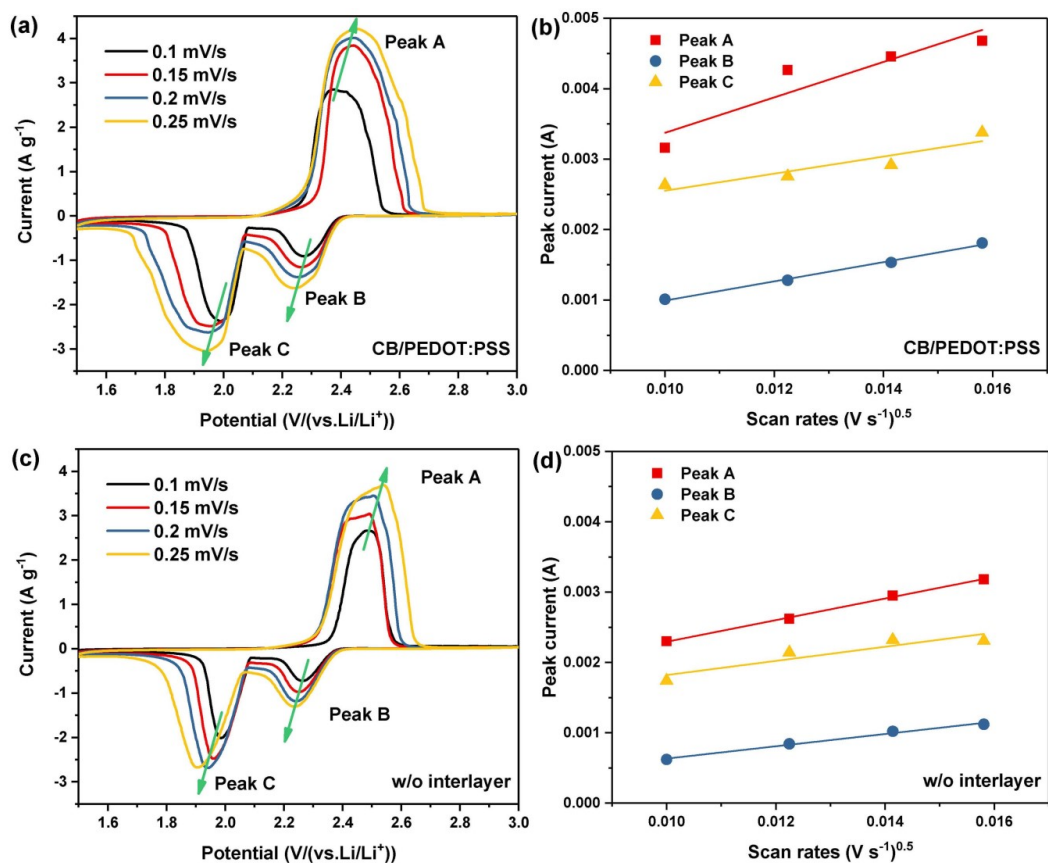


**Figure 3.61** CV curves recorded at different scan rates for Li–S batteries with (a) CB/PEDOT:PSS modified separator and (c) without interlayer. Linear fits of CV peak current dependence based on the scan rate of Li–S batteries with (b) CB/PEDOT:PSS modified separator and (d) without interlayer.

**Table 3.2** The calculated Li-ion diffusion coefficients of pristine cell and cell with CB/PEDOT:PSS modified separator.

Diffusion coefficient, $D_{Li^+}$	Peak A [ $\text{cm}^4 \text{s}^{-1}$ ]	Peak B [ $\text{cm}^4 \text{s}^{-1}$ ]	Peak C [ $\text{cm}^4 \text{s}^{-1}$ ]
without interlayer	$4.11 \times 10^{-8} \times A^{-2}$	$1.32 \times 10^{-8} \times A^{-2}$	$1.75 \times 10^{-8} \times A^{-2}$
CB/PEDOT:PSS	$11.01 \times 10^{-8} \times A^{-2}$	$3.24 \times 10^{-8} \times A^{-2}$	$2.47 \times 10^{-8} \times A^{-2}$
$D_{Li^+}$ ratio between two cells	267.8 %	244.7%	145.5%

To understand the mechanism of how the interlayer traps the polysulfide intermediates, the XPS measurement was conducted on both pristine and cycled CB/PEDOT:PSS interlayer, as shown in **Figure 3.62**. The wide survey scans before the cyclic test and after 50 cycles both present seven main peaks located at 168, 231, 285, 400, 532 and 689 eV which correspond to S 2p, S 2s, C 1s, N 1s, O 1s, and F 1s, respectively (**Figure 3.62a**). It is noted that in the cycled spectrum the S 2p and S 2s peaks are more intense than those in the pristine one, indicating the deposition of active materials on the interlayers.

There is one extra N 1s peak at 400 eV in the cycled spectrum plus with stronger intensities of the O 1s and F 1s peaks, probably rising from the LiNO<sub>3</sub> and LiTFSI salts in the remnant electrolyte.

The deconvoluted S 2p spectra (**Figure 3.62b**) obtained before cycles present two split broad peaks at around 169 and 165 eV, corresponding to the S 2p bands of PSS and PEDOT moieties, respectively [12-14]. After 50 cycles, the spectrum shows much stronger bands in the range of 168–172 eV, which can be assigned to the O=S=O bonds from the remnant LiTFSI salts. The thiosulfate -S-S\*O<sub>3</sub> band at 167.4 eV may be originated from the oxidation of the polysulfides by LiNO<sub>3</sub> [15]. The Li-S and S-S bands in the range of 162–166 eV are clearly identified [15]. For the Li 1s spectra (**Figure 3.62d and e**), a prominent peak emerges after cycling. The deconvoluted result suggests a Li-O bond (55.4 eV) [16], which indicates the chemical absorption between the lithium in polysulfide and the oxygen in PEDOT:PSS. An additional Li-N peak (55.6 eV) [17] is from the residual LiTFSI in the electrolyte.

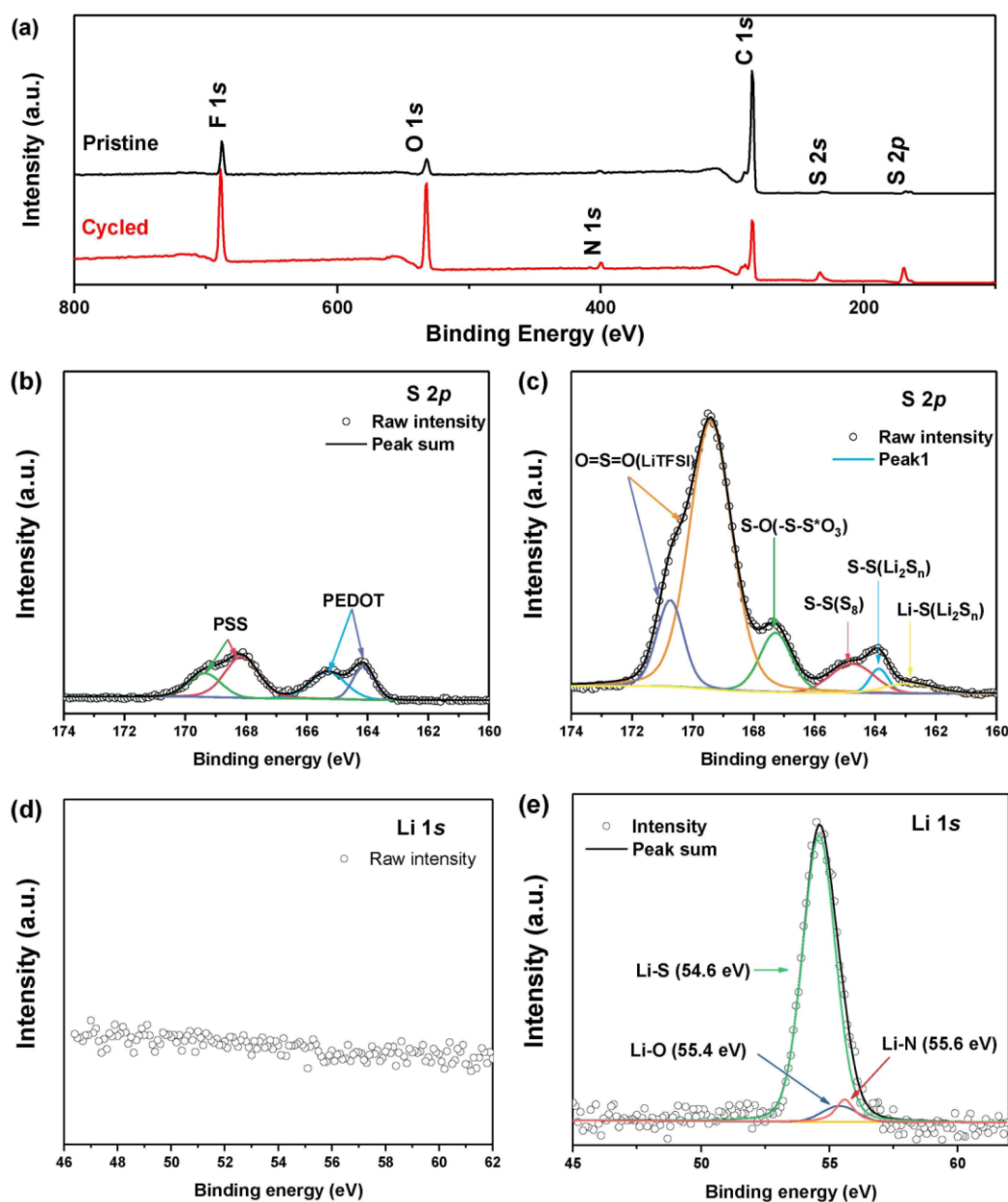


**Figure 3.62** (a) The wide survey spectra of CB/PEDOT interlayer before and after 50 cycles at 0.5 C. The deconvoluted S 2p and Li 1s XPS spectra of (b)(d) pristine CB/PEDOT:PSS interlayer and (c)(e) CB/PEDOT:PSS interlayer after 50 cycles at 0.5 C.

The Nyquist plots of different cells before and after 10 cycles at 0.2 C are shown in **Figure 3.63**. In the Nyquist plots, the diameter of the depressed semicircle in the high-to-medium frequency region corresponds to charge-transfer resistance ( $R_{ct}$ ) from the electrochemical reaction between the electrode and electrolyte [18], while the sloping line in the low-frequency region is assigned to the semi-infinite Warburg impedance ( $W_o$ ), which reflects the diffusion process of the polysulfides within the cathode [19, 20]. In the corresponding circuits, the  $R_e$  represents the resistance of the electrolyte. It is noticeable that an additional semi circle appears in the Nyquist plot of the cycled cell without interlayers, which

corresponds to the interface resistance ( $R_{st}$ ). The sum of  $R_e$ ,  $R_{ct}$ , and  $R_{st}$  is calculated as the total resistance of the cell ( $R_{total}$ ). According to the fitted results (**Table 3.3**), the most prominent difference between these two cells is the shrinkage in  $R_{ct}$  values after adding the interlayers. This amelioration should be ascribed to the highly conductive CB/PEDOT:PSS that acts as the co-current collector, which greatly facilitates the redox of dissolved polysulfides. The low  $R_{ct}$  value of the cell with CB/PEDOT:PSS interlayer indicates the highest efficiency of CB/PEDOT:PSS interlayer in reutilizing polysulfides. It is noticeable that an additional arc at medium frequency appears at the EIS of the cycled cell without an interlayer, indicating that excessive lithium sulfides deposits on the surface after cycles. Meanwhile, cells with interlayer exhibit only one arc after cycles, and the CB/PEDOT:PSS cell shows the lowest  $R_{total}$  value. The low  $R_{total}$  value of the cell with CB/PEDOT:PSS interlayer is another evidence of the remarkable effect on reducing the internal resistance.

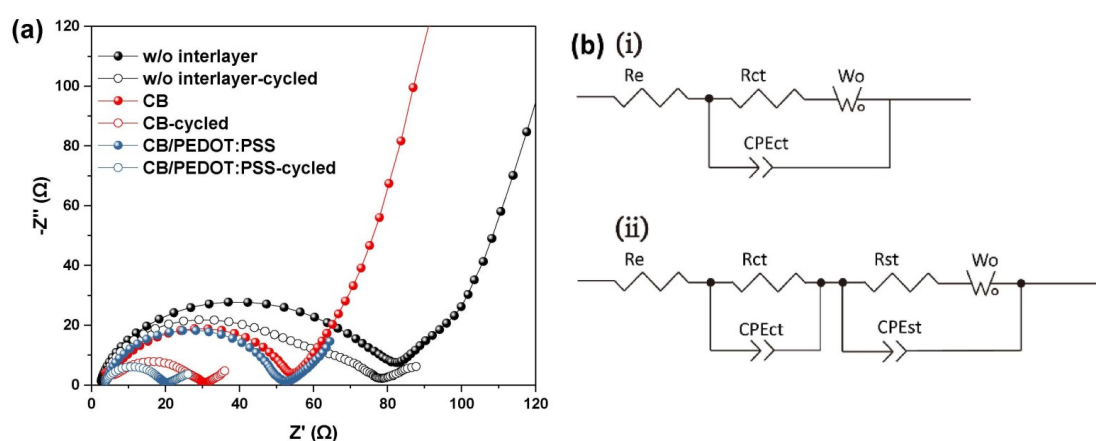


**Figure 3.63** (a) Electrochemical impedance spectra of pristine Li-S cell and cells with CB and CB/PEDOT:PSS interlayers before and after 10 cycles at 0.2 C. (b) The corresponding equivalent circuits of all the cells (i), except the cycled cell without interlayer (ii).

**Table 3.3** Fitted values of the impedance spectra in **Figure 3.13**.

		$R_e/\Omega$	$R_{ct}/\Omega$	$R_{st}/\Omega$	$R_{total}/\Omega$
cell without interlayer	pristine	1.99	79.3	/	81.3
	cycled	3.24	46.3	29.4	78.9
cell with CB interlayer	pristine	4.10	50.5	/	54.6
	cycled	4.94	25.2	/	30.1
cell with CB/PEDOT:PSS	pristine	3.57	47.8	/	51.4

---

interlayer	cycled	3.41	16.7	/	20.1
------------	--------	------	------	---	------

---

### 3.4. Conclusions

The CB/PEDOT:PSS modified separator was proposed and fabricated using a facile one-step physical approach which favors practical production, due to its low-cost and scalable process. The bi-functional modified separator not only serves as a secondary current collector but also an effective polysulfide trapper, owing to both physical and chemical absorption provided by super-P and PEDOT:PSS. Besides, this modification coating promotes chemical kinetic by enhancing Li-ion diffusion. As a result, the primitive S-C electrode with sulfur loading of  $1.6 \text{ mg cm}^{-2}$  exhibits a high initial capacity of  $1315 \text{ mAh g}^{-1}$  at  $0.2 \text{ C}$  after the application of modified separator, maintaining a retention of  $956 \text{ mAh g}^{-1}$  after 100 cycles. Even after 260 cycles at  $1 \text{ C}$ , this modified cell still holds a considerable capacity of  $674 \text{ mAh g}^{-1}$ . More surprisingly, the areal density of CB/PEDOT:PSS coating is only  $0.604 \text{ mg cm}^{-2}$  as low, bringing an outstanding specific electrode capacity of  $522 \text{ mAh g}^{-1}$  based on the total mass of electrode materials and the interlayer, which further reveals its potential application in practical high-performance Li-S batteries.

### 3.5. References

- [1] Jayaprakash, Shen, Moganty, Corona, and Archer, *Porous Hollow Carbon@Sulfur Composites for High-power Lithium-sulfur Batteries*. *Angewandte Chemie International Edition*, 2011,**50** (26): p. 5904-5908.
- [2] Wang, Wen, Yang, Jin, Huang, Wu, and Han, *Electronic and Ionic Co-conductive Coating on the Separator towards High-performance Lithium-sulfur Batteries*. *Journal of Power Sources*, 2016,**306** p. 347-353.
- [3] Ma, Wen, Wang, Shen, Peng, Jin, and Wu, *Enhanced Performance of Lithium Sulfur Battery with Self-assembly Polypyrrole Nanotube Film as the Functional Interlayer*. *Journal of Power Sources*, 2015,**273** p. 511-516.
- [4] Yi, Liu, Zhao, Hardwick, Li, Geng, Zhang, Yang, and Zhao, *A Light-weight Free-standing Graphene Foam-based Interlayer towards Improved Li-S Cells*. *Electrochimica Acta*, 2019,**299** p. 479-488.
- [5] Tan, Li, Wang, Guo, and Wang, *Lightweight Reduced Graphene Oxide@MoS<sub>2</sub> Interlayer as Polysulfide Barrier for High-Performance Lithium-Sulfur Batteries*. *ACS Applied Materials & Interfaces*, 2018,**10** (4): p. 3707-3713.
- [6] Li, Wu, Zhang, Wang, Zhang, Seh, Zhang, Sun, Huang, Jiang, Zhou, and Sun, *Fast conversion and controlled deposition of lithium (poly)sulfides in lithium-sulfur batteries using high-loading cobalt single atoms*. *Energy Storage Materials*, 2020,**30** p. 250-259.
- [7] Li, Zhang, Zheng, Seh, Yao, and Cui, *Understanding the Role of Different Conductive Polymers in Improving the Nanostructured Sulfur Cathode Performance*. *Nano Letters*, 2013,**13** (11): p. 5534-5540.
- [8] Hao, Yuan, Li, Liu, Xiang, Wu, Zeng, and Huang, *High Performance Lithium-sulfur Batteries with A Facile and Effective Dual Functional Separator*. *Electrochimica Acta*, 2016,**200** p. 197-203.
- [9] Liu, Liu, Guo, Shang, Lv, Liu, and He, *Enhanced Electrochemical Kinetics in Lithium-sulfur Batteries by Using Carbon Nanofibers/Manganese Dioxide Composite as A Bifunctional Coating on Sulfur Cathode*. *Electrochimica Acta*, 2018,**269** p. 180-187.
- [10] Wu, Hu, Shen, Chen, He, Cheng, and Pan, *Highly Efficient and Green Fabrication of A Modified*

- C Nanofiber Interlayer for High-performance Li-S Batteries*. Journal of Materials Chemistry A, 2018,**6** (6): p. 2693-2699.
- [11] Han, Chung, and Manthiram, *Designing a High-loading Sulfur Cathode with a Mixed Ionic-electronic Conducting Polymer for Electrochemically Stable Lithium-sulfur Batteries*. Energy Storage Materials, 2018,**17** p. 317-324.
- [12] Yan and Okuzaki, *Effect of Solvent on PEDOT/PSS Nanometer-scaled Thin Films: XPS and STEM/AFM Studies*. Synthetic Metals, 2009,**159** (21-22): p. 2225-2228.
- [13] Wang, Chen, Battaglia, and Liu, *Improving the performance of lithium-sulfur batteries using conductive polymer and micrometric sulfur powder*. Journal of Materials Research, 2014,**29** (09): p. 1027-1033.
- [14] Hwang, Amy, and Kahn, *Spectroscopic Study on Sputtered PEDOT-PSS: Role of Surface PSS Layer*. Organic Electronics, 2006,**7** (5): p. 387-396.
- [15] Zeng, Huang, Zhang, Zhang, Wu, and Chen, *Long-life and High-areal-capacity Lithium-sulfur Batteries Realized by a Honeycomb-like N, P Dual-doped Carbon Modified Separator*. Chemical Engineering Journal, 2018,**349** p. 327-337.
- [16] Chen, Lu, Zhou, Wu, Qin, Ogoke, and Wu, *3D Graphene Framework Supported Li<sub>2</sub>S Coated with Ultra-thin Al<sub>2</sub>O<sub>3</sub> Ailms: Binder-free Cathodes for High-performance Lithium Sulfur Batteries*. Journal of Materials Chemistry A, 2017,**5** (1): p. 102-112.
- [17] Seh, Wang, Hsu, Zhang, Li, Zheng, Yao, and Cui, *Facile Synthesis of Li<sub>2</sub>S-polypyrrole Composite Structures for High-performance Li<sub>2</sub>S Cathodes*. Energy & Environmental Science, 2014,**7** (2): p. 672-676.
- [18] Huang, Wang, Xu, Chong, Qin, Wang, and Kim, *Three-Dimensional Porous Graphene Aerogel Cathode with High Sulfur Loading and Embedded TiO<sub>2</sub> Nanoparticles for Advanced Lithium-Sulfur Batteries*. ACS Applied Materials & Interfaces, 2016,**8** (42): p. 28663-28670.
- [19] Wang, Zhang, Zhou, Yang, Li, and Zhang, *Rational design of a Nested Pore Structure Sulfur Host for Fast Li/S Batteries with a Long Cycle Life*. Journal of Materials Chemistry A, 2016,**4** (5): p. 1653-1662.
- [20] Xu, Su, Zhang, Bao, and Wang, *A Nitrogen-sulfur Co-doped Porous Graphene Matrix as a Sulfur Immobilizer for High Performance Lithium-sulfur Batteries*. Journal of Materials Chemistry A, 2016,**4** (44): p. 17381-17393.

## Chapter 4: Graphene foam-based free-standing interlayer as a light-weight dual-function cathode cover for high-performance Li-S batteries

### 4.1. Introduction

In previous Chapter 3, an interlayer coated on the separator was fabricated based on the carbon black (super-P) and conductive polymer (PEDOT:PSS). This interlayer material shows its potential in the promotion of the S-C cathode performance, especially in the specific capacity. Despite its promising potential, one critical issue for the interlayer designing is the mass addition from this configuration. This value cannot be overlooked when a high energy density battery is targeted for a Li-S battery study. While a desirable specific capacity may be achieved through the CB/PEDOT:PSS coating, it requires a high mass density interlayer (carbon black has a low specific surface area less than  $80 \text{ m}^2 \text{ g}^{-1}$ ), hence the overall energy density based on the mass of the whole battery components may be deteriorated, thus downgrading the practical potential. In order to provide more polysulfides-absorption area with less mass addition, a light material with the higher specific surface area is essential.

Graphene, since its experimental discovery in 2004, has already been foreseen as an important future technology. This carbon monolayer exhibits superior electrical conductivity, high specific surface area, and good structural stability, which has been widely used to ameliorate the challenges of the Li-S system [1, 2]. Meanwhile, recent studies have been reported that metal oxides can be effective polysulfides-trappers [3], including  $\alpha\text{-Fe}_2\text{O}_3$  [4],  $\text{MnO}_2$  [5-7],  $\text{TiO}_2$  [8, 9],  $\text{Al}_2\text{O}_3$  [10] and  $\text{ZnO}$  [11-13]. Among them,  $\text{ZnO}$  shows a strong chemical confining effect of polysulfides due to the Li-O interaction, and its binding energy for  $\text{Li}_2\text{S}_8$  is one of the highest values among other metal composites [13, 14]. Besides,  $\text{ZnO}$  has also attracted great attention due to its relative stability, low cost, and environmental friendliness [12]. However, these metal oxides are usually electrically insulating, it is essential to minimize their loadings to avoid the increase of impedance and the decline in the overall gravimetric capacity and energy density [15]. Therefore, it is desirable to effectively enhance conductivity while keeping the abilities to trap the polysulfides.

Herein, with such a target in mind, we propose to incorporate graphene with metal oxides. In this chapter, a free-standing graphene foam (GF) interlayer has been applied as an interlayer between S-C cathode and separator. The highly conductive light-weight graphene foam not only provides effective

remission for electrode polarization but also keeps the weight addition to be less than 5 wt. %, thus minimizing the decrease of whole energy density. To further enhance its polysulfide-blocking ability, the atomic layer deposition (ALD) method is used to deposit a nanoscale ZnO coating on GF interlayer (GF@ZnO) in order to minimize the deterioration on conductivity [15, 16]. With this modified separator, a sulfur cathode prepared by commercial elemental sulfur with 60 wt. % sulfur loading, reveals a high initial reversible capacity of 1051 mAh g<sup>-1</sup> at 0.5 C, with a cycle decay value of 0.36% per cycle. These fundamental studies suggest that this light-weight free-standing graphene foam interlayer has potential for next-generation high-performance lithium–sulfur batteries.

The research work in Chapter 4 was mainly designed and carried out by me under the direction of Dr. Li Yang, Prof. Laurence Hardwick, and Dr. Cezhou Zhao. The result presented in this chapter was published on *Electrochimica Acta*, 2019. 299: p. 479-488 (DOI: 10.1016/j.electacta.2019.01.015). Permission was sought from other co-authors to include the materials from this paper to this thesis. The manuscript was drafted by me and corrected by Dr. Li Yang and Prof. Laurence Hardwick. Prof. Laurence Hardwick contributed to the idea of isolating the interlayer. Dr. Chenguang Liu and Dr. Yinchao Zhao helped me with the supplementary test while I was in UoL. The rest of authors helped me with some supporting works, including data analysis, the 3D schematic drawing, and double check the experimental results.

## **4.2. Experiment part**

### **4.2.1. Fabrication of graphene foam (GF)**

Nickel foams (Liyuan Novel Materials from Changde (China), ~320 g m<sup>-2</sup> in area density and ~ 1 mm in thickness) were used as three-dimensional (3D) scaffold templates for the chemical vapour deposition (CVD) growth of GF [17]. Typically, 35 × 35 mm<sup>2</sup> of nickel foam pieces were firstly rolled to 0.3 mm thickness and heated to 1000 °C at 10 °C min<sup>-1</sup> under a mixed flow of Ar (1000 sccm) and H<sub>2</sub> (500 sccm) in a tube furnace, and annealed for 5 min. Then a CH<sub>4</sub> flow of 50 sccm was introduced into the reaction tube. After 5 min of reaction-gas mixture flow, the CH<sub>4</sub> was turned off and samples were rapidly cooled down to room temperature at a rate of ~100 °C min<sup>-1</sup>. Then the samples were etched by a 3 M HCl solution at 80 °C for 3 h and subsequently washed by deionized water to completely remove the nickel foam template. The obtained graphene foams (GFs) were dried under vacuum at 60 °C for 12

h. A typical area density of GF is  $\sim 0.15 \text{ mg cm}^2$ .

#### 4.2.2. Atomic layer deposition (ALD) of ZnO on GF

The dry GF was placed into an atomic layer deposition system (MNT Micro & nanotech f-200) for ZnO deposition. High-purity nitrogen at  $200 \text{ }^\circ\text{C}$  was used as a carrier gas for the whole process. To preserve the high conductivity of GF as much as possible, only 20 cycles of ALD were performed. Each cycle includes alternating flows of water (20 ms, oxidant) and diethyl zinc (20 ms, 99.999%, Zn precursor) separated by flows of pure nitrogen gas (20 s and 20 s, respectively, carrier and cleaning gas). The thickness of deposited ZnO flakes on GF surfaces was estimated to be 3.7 nm according to a control sample of 150 cycles,  $27.28 \pm 0.035 \text{ nm}$  thickness deposited on a silicon wafer, measured by ellipsometry (Table 4.4, Figure 4.64). The as-obtained material was denoted as GF@ZnO.

**Table 4.4** ALD growth data of ZnO on silicon wafer at different temperatures.

Temperature	Circles	Thickness (nm)			Average	Standard Deviation (nm/cycle)
		Sample 1	Sample 2	Sample 3	thickness per cycle (nm/cycle)	
150	150	28.9881	28.7492	29	0.1927	$9.43 \times 10^{-4}$
190	150	28.2151	28.3218	28.1789	0.1882	$4.95 \times 10^{-4}$
200	150	27.1282	27.1383	27.5979	0.1819	$1.79 \times 10^{-3}$
210	150	25.9309	26.5684	26.9186	0.1764	$3.34 \times 10^{-3}$
230	150	25.9071	25.6767	25.8191	0.1720	$7.75 \times 10^{-4}$

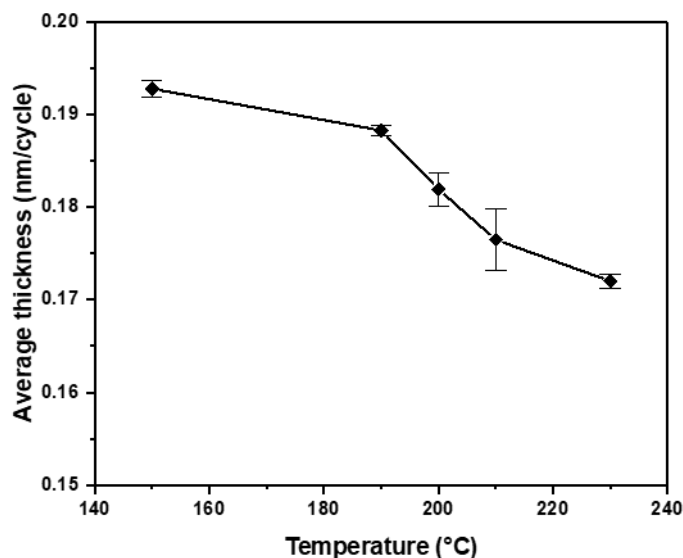


**Figure 4.64** The average growth rate of ZnO by ALD from a total 150 cycles at each temperature, measured by the ellipsometry.

#### 4.2.3. Electrode preparation

A S-C electrode was fabricated by mixing 60 wt% sulfur with 30 wt% conductive carbon black (super-P) as a conducting agent and 10 wt% poly(vinylidene fluoride) (PVDF) as a binder in the N-methyl-2-pyrrolidone (NMP). The slurry was magnetic stirred for 24 h to achieve greater homogeneity. After stirring, the slurry was coated on an aluminum foil current collector with the thickness of 20 mm by a rolling machine, followed by a vacuum desiccation at 60 °C for 12 h. The coated electrodes were cut into discs of diameter 13 mm. A typical mass loading of the active materials was  $\sim 1.5 \text{ mg cm}^{-2}$ .

#### 4.2.4. Materials characterization

The morphologies and elemental mapping of the GF and GF/GF@ZnO interlayers were observed using a scanning electron microscope (SEM, JEOL JSM-6510) and an energy dispersive X-ray spectrometer (EDS, PENTA FET Precision). The defect density and layer number of GF and GF@ZnO were estimated by Raman spectroscopy (Jobin YvonXploRA, HORIBA Scientific), excited by 532 nm laser. The ZnO atomic layer coating was characterized by using X-ray photoelectron spectroscopy (XPS, ESCALAB 250Xi, Thermo scientific) with Al K $\alpha$  X-ray source.

#### 4.2.5. Electrochemical measurements

The S-C electrode and interlayer were tested in two-electrode 2032 coin-type cells using Li foil as counter electrodes. The cells were assembled in an argon-filled glove box. The electrolyte was 1.0 M lithium bis(trifluoromethanesulfonyl)imide (LiTFSI) in dioxolane (DOL) and dimethoxyethane (DME) (1:1 by volume) with a 1.0 wt% (0.18 M) LiNO<sub>3</sub> additive (H<sub>2</sub>O < 5 ppm). The GF (or GF@ZnO, or GF/GF@ZnO) interlayers were placed between the Celgard 2400 separator and S-C electrode working electrode, with the GF@ZnO side (when GF/GF@ZnO was applied) facing towards the lithium counter electrode. Cyclic voltammetry (CV) was conducted at a scan rate of 0.1 mV s<sup>-1</sup> in a voltage range of 1.5-3.0 V using Autolab PGSTAT302N electrochemical workstation. The electrochemical impedance spectroscopy (EIS) measurements were also carried out on the same workstation with an amplitude of 5 mV and a frequency range of 0.01 Hz-100 kHz. Galvanostatic charge/discharge tests were performed in the potential range of 1.5-3.0 V at 25 °C with the Neware CT-4008 battery-testing system.

#### 3.6. Characterizations of the graphene foam-based interlayer and relevant analysis

**Figure 4.65** shows the configuration of the cell with GF-based interlayer. The interlayer is placed between a commercial separator and the S-C cathode, and the insert shows an image of the free-standing nature of as-prepared GF interlayer. To further enhance the polysulfides-blocking ability of the interlayer, we fabricated the ZnO modified GF (GF@ZnO) via ALD and overlapped it with pristine GF, which was denoted as GF/GF@ZnO. Different interlayers for example GF, 2GF (double-layered GF), GF@ZnO and GF/GF@ZnO were tested to show their effects on the electrochemical performance of S-C cathode. Specifically, the GF/GF@ZnO interlayer was inserted with the GF side towards cathode.

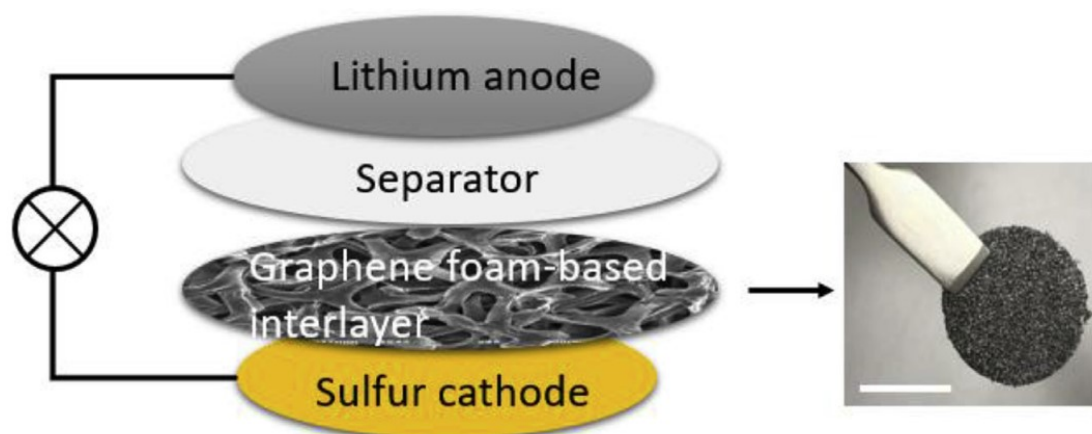


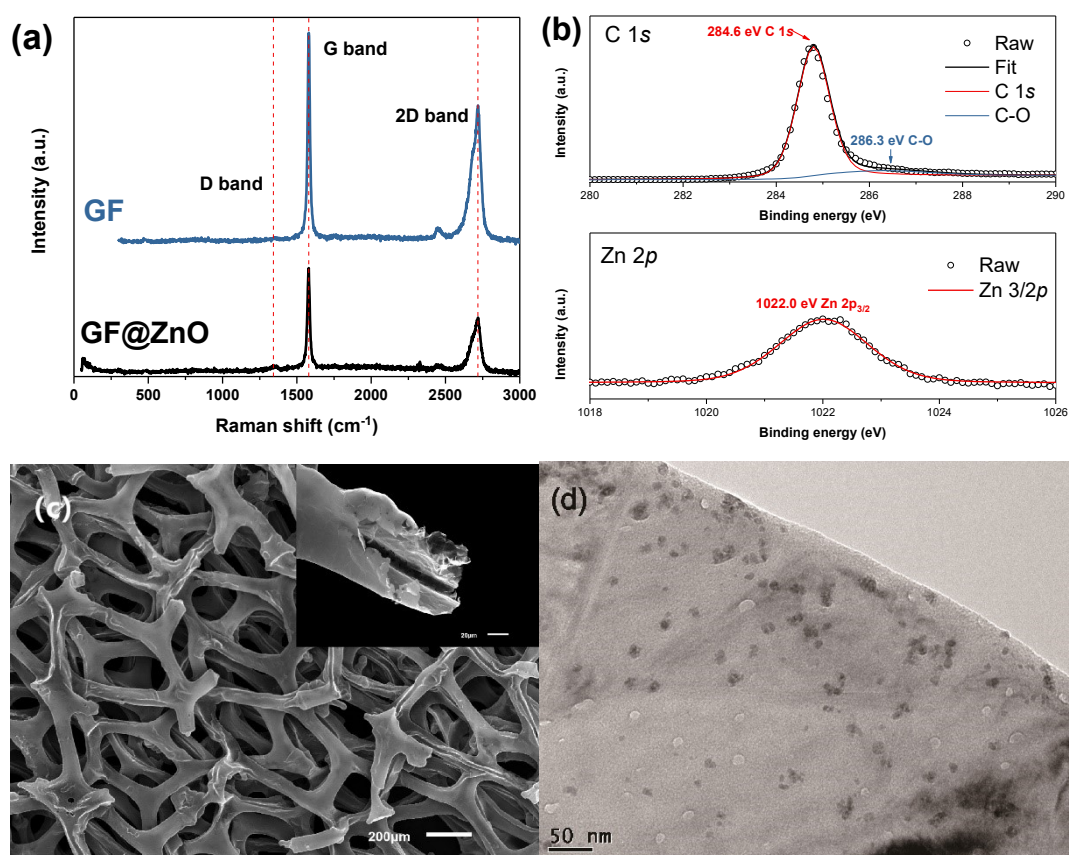
**Figure 4.65** A Li-S battery incorporated with a GF-based interlayer, with an insert showing a free-standing GF interlayer. The scale bar is 10 mm.

The structure and morphology characterizations of GF and GF@ZnO are shown in **Figure 4.66**. The as-prepared GF and GF@ZnO show two prominent peaks at 1580 and 2718  $\text{cm}^{-1}$  in Raman spectra (**Figure 4.66a**), corresponding to the G band and 2D band, respectively [18-20]. The low intensity band at 2445  $\text{cm}^{-1}$  is the G\* band [21]. Based on the integral intensity ratio of G band to 2D band ( $I_G/I_{2D} = 0.59$ ) and the full width at half maximum (FWHM) of 2D, the graphene layers of GF are estimated to be  $3e4$  layers [21, 22] (see **Table 4.5**). In addition, the strongly suppressed defect-related D band ( $\sim 1350 \text{ cm}^{-1}$ ) indicates overall high quality of the graphene in GF [17]. Due to the trace content of the ZnO, there was no obvious ZnO band in the Raman spectra (before 500  $\text{cm}^{-1}$ ), but the existence of ZnO is demonstrated by Zn 2p peak in XPS spectra (**Figure 4.66b**), with an atomic percent of 0.79% by XPS measurement. The GF perfectly inherits the interconnected 3D scaffold structure of the nickel foam template, and all the graphene sheets in the GF form hollow triangular prisms with a width of  $\sim 80 \text{ mm}$ , as shown in SEM images (**Figure 4.66c** and the insert). The macroscale pores and interior hollow space encircled by few-layer GF sheets not only lead to rapid ionic transportation but also facilitate high electron conductivity, thus potentially reducing the polarization for the S-C electrode. To visualize the morphology of the deposited ZnO, the GF@ZnO was examined under high-resolution TEM (HRTEM), as shown in **Figure 4.66d**. The deposited ZnO exhibits scattered nano-flakes morphology on the GF surface. This is likely resulting from the hydrophobic feature of the graphene surface in which no continuous nucleation sites are available to form ZnO. The HRTEM image of GF@ZnO (**Figure 4.66e**) is denoted with clear crystal lattice fringes with d-spacing of the (002) plane of the ZnO. The insert shows the layer structure of graphene edge with the fringe separation of 0.36 nm, in a good agreement with

previous reported graphene structure [20].

**Table 4.5** Analysis of Raman spectrum of GF@ZnO

	Bands	Integral intensity portion (%)	FWHM (cm <sup>-1</sup> )	Integral intensity ratio G/2D
GF@ZnO	G band (1580 cm <sup>-1</sup> )	31.42	17.2	0.59
	2D band (2718 cm <sup>-1</sup> )	53.48	59.6	
Ref. [21]				3 layers: 0.51±0.04
				4 layers: 0.62±0.08
Ref. [23]	2D band		4 layers: ~ 60	



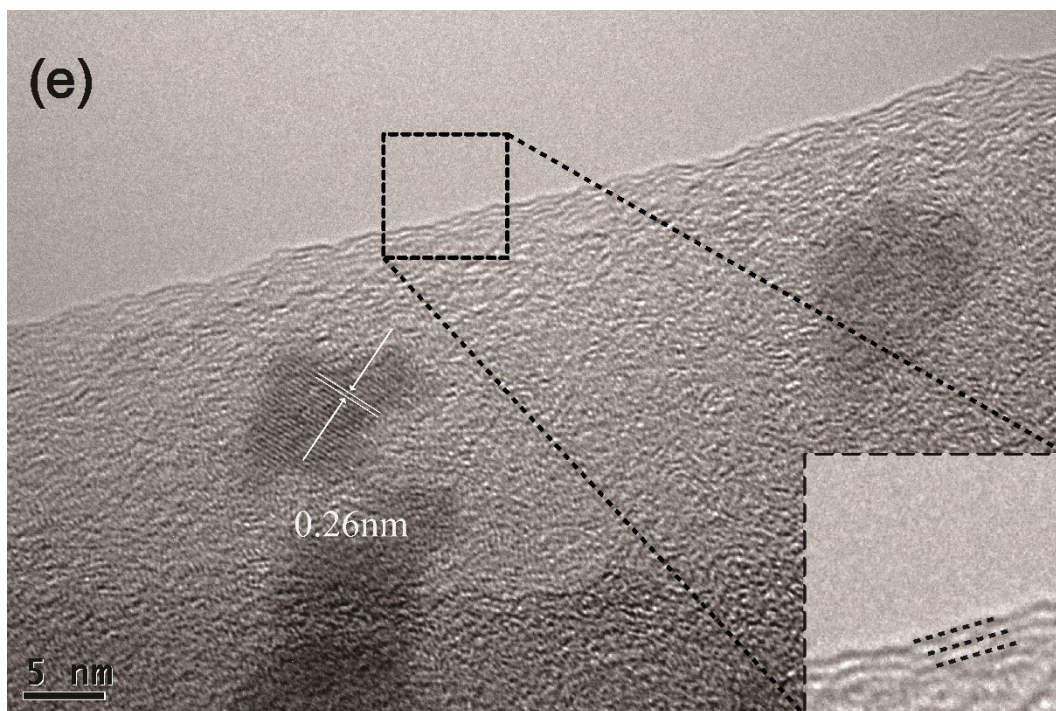


**Figure 4.66** (a) The Raman spectra of GF and GF@ZnO. (b) High resolution C 1s and Zn 2p XPS spectra of GF@ZnO. (c) SEM image of GF. The insert shows the fractured graphene triangular prism and its hollow interior space. (d) TEM image of the as-prepared GF@ZnO. (e) The HRTEM of GF@ZnO denoted with crystal lattice fringes with d-spacing of the (002) plane of the ZnO. The insert shows the layer structure of graphene edge.

**Figure 4.67** shows the cyclic voltammetry of S-C cell and cells with GF-based interlayers of the initial five cycles within a cutoff voltage window of 1.5-3.0 V at a scan rate of  $0.1 \text{ mV s}^{-1}$ . A double-layer GF (2 GF) interlayer is applied here for a more accurate comparative evaluation with GF/GF@ZnO double-layer interlayer. During the initial cycle, the cell without interlayer exhibits two broad cathodic peaks at around 1.75 and 1.85 V, which are related to the redox state from elemental sulfur to high-order polysulfides and further reduction to  $\text{Li}_2\text{S}_2/\text{Li}_2\text{S}$ , respectively [24]. The one broad anodic peak at around 2.58 V corresponds to the conversion of  $\text{Li}_2\text{S}_2/\text{Li}_2\text{S}$  to high-order polysulfides and elemental sulfur [25]. The shifts in the anodic peaks between the initial and following cycles are possibly due to the migration of the active sulfur to more electrochemically stable sites [24, 26, 27]. During the following cycles, the anodic peaks gradually shift to a lower potential, indicating the instability of pristine S-C electrode during cycling. Meanwhile, the CV curves of cell with 2 GF interlayer show similar shapes, but the anodic peak width becomes much narrower (shrinking from 0.61 V to 0.35 V) and higher than that of S-C cell (from  $\sim 1.1 \text{ A g}^{-1}$  to  $\sim 1.5 \text{ A g}^{-1}$ ), indicating that the redox reaction takes place easier in cell with 2 GF interlayer. The cathodic peaks shift to higher potentials at 1.99 and 2.29 V respectively, and display narrower peak

widths compared to those of S-C cells, suggesting the cell with 2 GF interlayer has less polarization and higher conductivity than the pristine S-C cell. Except for the initial cycle, the CV curves of the cell with 2 GF interlayer overlap without obvious shift in peak location, demonstrating the good cycling stability and reaction reversibility of this Li-S cell. The cells with GF@ZnO and GF/GF@ZnO interlayers (**Figure 4.67c and d**) exhibit similar CV profiles in **Figure 4.67b**, but possess more intense anodic peaks (1.6-2.0 A g<sup>-1</sup>). Meanwhile the redox peaks in these two cells reveal less shifting from the second cycling. These variations can be ascribed to the higher sulfur utilization efficiency brought by the ZnO layer.

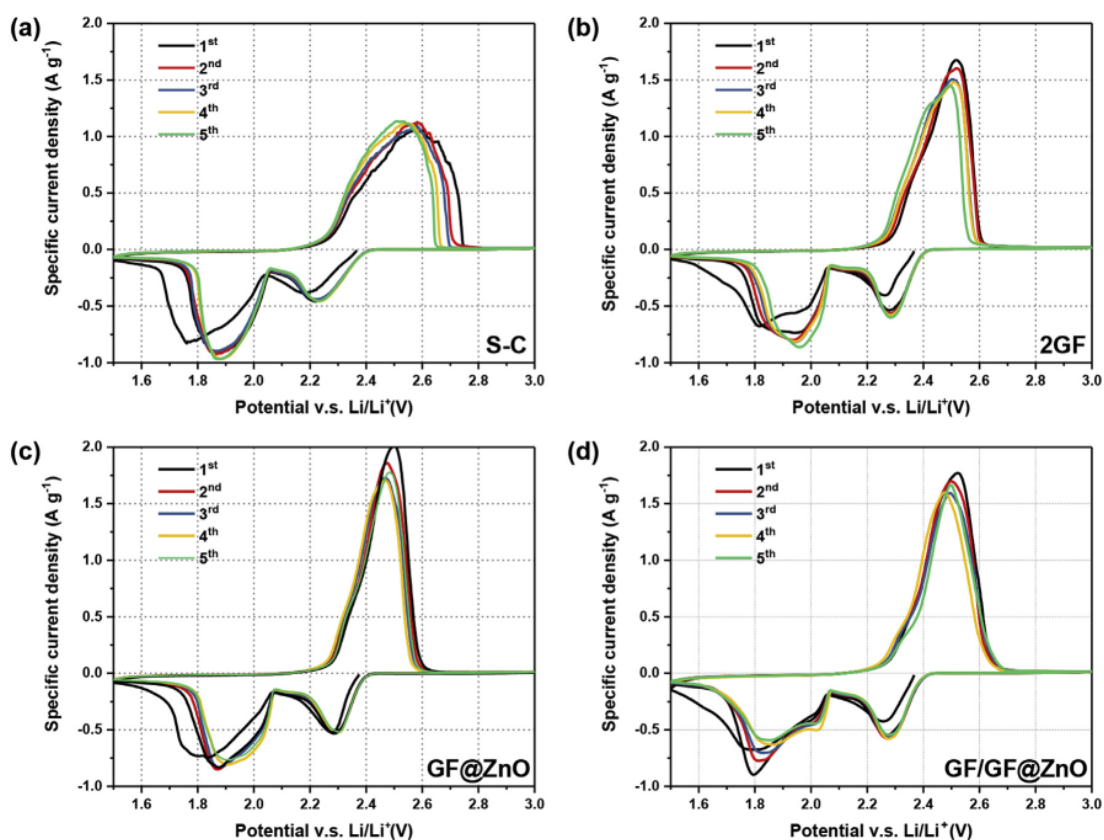


**Figure 4.67** Cyclic voltammetry profiles of the initial five cycles of the S-C cell and cells with 2 GF, GF@ZnO and GF/GF@ZnO interlayers, respectively.

The initial galvanostatic charge/discharge behaviors of different Li-S batteries evaluated at a current density of 0.5 C are shown in Fig. 3a. Two discharge plateaus and one charge plateau can be observed for all the cells, which are consistent with the CV plots. For pristine S-C cathode cell, it delivers an initial specific capacity of 595 mAh g<sup>-1</sup>), corresponding 35.5 % of the theoretical capacity (1675 mAh g<sup>-1</sup>). On the other hand, cells with different interlayers exhibit higher specific capacity and longer charge/discharge plateaus, indicating that the GF-based interlayers can effectively improve the sulfur

utilization. The meliorated specific capacity surges to 735, 805, and 1051 mAh g<sup>-1</sup> with the application of 2GF, GF@ZnO and GF/GF@ZnO interlayers, respectively. In particular, the cell with GF/GF@ZnO interlayer has the longest plateaus, with the lowest voltage hysteresis ( $\Delta E_4$ ) of 233 mV (vs  $\Delta E_1=326$  mV for S-C,  $\Delta E_2=237$  mV for 2GF and  $\Delta E_3=235$  mV for GF@ZnO) at 0.5 C, which suggests a more kinetically favored electrochemical redox reaction process and low internal resistance in the cell with GF/GF@ZnO interlayer [28, 29]. In addition, the capacities for high voltage plateau and low voltage plateau follow the order of  $C_1 > C_2 > C_3 > C_4$ , confirming the same order of the abilities for sulfur utilization when using different interlayers in cells.

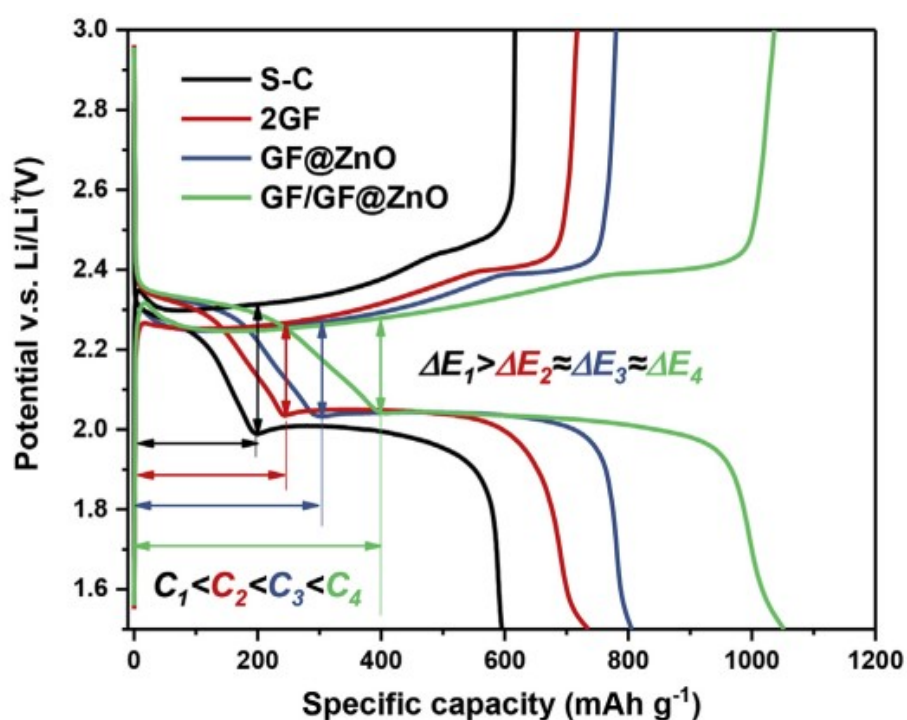


**Figure 4.68** The initial galvanostatic charge-discharge profiles of S-C cell and cells with 2 GF, GF@ZnO and GF/GF@ZnO interlayers at 0.5 C.

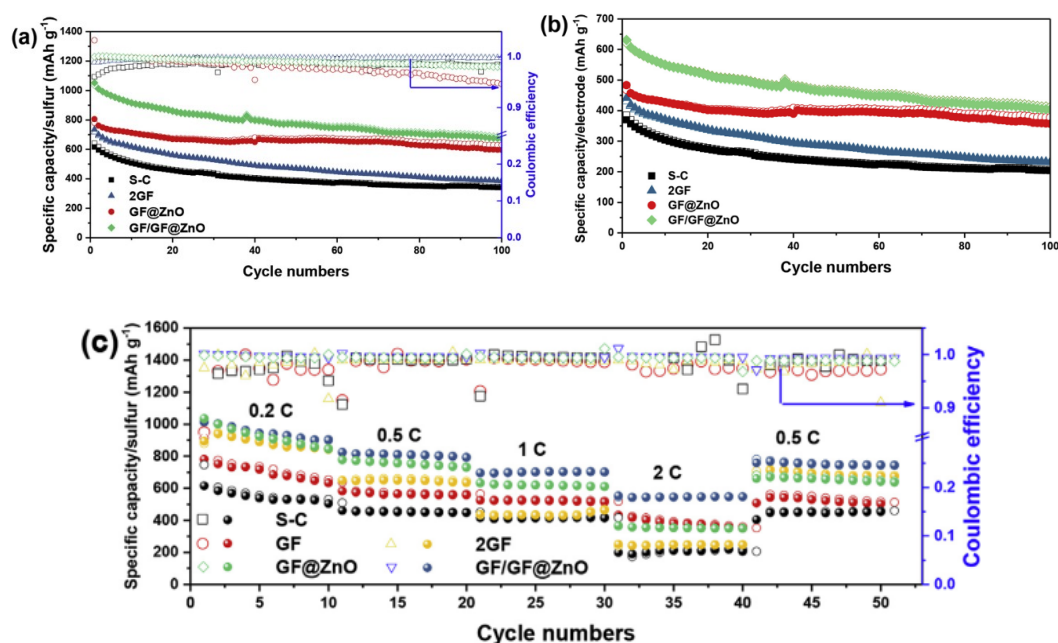
**Figure 4.69a** presents the cyclic performance of the cells with different interlayers measured at a galvanostatic charge/discharge current of 0.5 C and 0.5 C between 1.5 and 3 V. At current density of 0.5 C, the cell with pristine S-C cathode exhibits a low initial specific capacity of 681 mAh g<sup>-1</sup>, taking up only 40.6 % of the theoretical value. After 100 cycles, it drops to 326 mAh g<sup>-1</sup>, with a capacity degradation of 0.52 % per cycle. In contrast, the cells with 2GF and GF@ZnO interlayers show higher initial capacities of 735 and 805 mAh g<sup>-1</sup>, retaining a capacity of 386 and 595 mAh g<sup>-1</sup> after 100 cycles, with a relatively lower capacity decay of 0.47 % and 0.26 % per cycle. A control experiment showed that

different ALD cycles (20, 60 and 80 cycles) do not influence the capacity performance remarkably (**Figure 4.70**), so a minimum cycle (20) was selected for all the following experiments in this study. The GF/GF@ZnO interlayer delivers an improved initial capacity of 1051 mAh g<sup>-1</sup> and a stable residual capacity of 672 mAh g<sup>-1</sup> after 100 cycles, with a capacity decay of 0.36 % per cycle. The enhanced initial and residual specific capacity of the GF/GF@ZnO interlayer modified Li-S battery can be ascribed to the doubled area density of GF interlayer, which reduces the chance of polysulfides escaping through the macro-pores in GF interlayer. Another contribution to enhance the specific capacity is probably related to the chemically trapping the polysulfides by the ZnO coating. The interlayer with reverse orientation (with the GF@ZnO side towards cathode) was also tested, and corresponding cycling performance does not show prominent difference with GF/GF@ZnO one's (as shown in **Figure 4.71**). Possible reason could be that the hundred micron-scale porosity of the GF leaves enough space for the out-layer GF to get contact with the cathode surface, which means both layers will function in either situations. For the consistency of data, only the cell of GF/GF@ZnO will be discussed in the following manuscript. I also tested the triple-layer GF/GF/GF@ZnO interlayer to see if the increasing thickness of the interlayer can further improve the capacity performance. However, compared with GF/GF@ZnO cell, the triple-layer interlayer (GF/GF/GF@ZnO) cell shows shrank capacity (**Figure 4.72**). This can be ascribed to that although the additional GF provide more polysulfide-trapping sites, it hinders the transmission of Li ion from anode side to cathode, and this drawback cannot be compensated by the advantage from thickness increase, which results in capacity shrinkage. To emphasize the negligible mass addition of the interlayer, the cycling specific capacity performance based on the mass of cathode materials (including super-P, binder and interlayer) is shown in Fig. 4b, in which the cells with GF@ZnO and GF/GF@ZnO interlayers still show enhanced specific capacities. This proves the lightness of the GF-based interlayers can effectively improve the cell without impairing the overall specific capacity.

The high rate capabilities of the cells with different interlayers are shown in **Figure 4.69c**. It is clearly seen that with the gradually growing of current rate, the specific capacity of the cells with GF-based interlayers is much higher than that of cell without interlayer at the same rate. Among all cells, the cell with GF/GF@ZnO interlayer presents the highest initial discharge capacity of 1013 mAh g<sup>-1</sup> at 0.2 C. When the current rate gradually increases from 0.2 to 0.5, 1 and 2 C after every 10 cycles, the cell with GF/GF@ZnO delivers high and stable discharge capacities of 914, 721, 613 and 518 mAh g<sup>-1</sup>, respectively. After the rate reverts to 0.5 C, the capacity recovers to 688 mAh g<sup>-1</sup>, demonstrating excellent

stability and reversibility of the Li-S cell with the GF/GF@ZnO interlayer.

To further evaluate the improvement of different GF-based interlayers on electrochemical performance, the electrochemical impedance spectroscopy measurements were conducted on fresh cell of S-C cathode and cells with different GF-based interlayers, and the corresponding Nyquist plots and equivalent circuits are shown in **Figure 4.69d** and 4e. In the Nyquist plots, the diameter of the depressed semicircle in the high-to-medium frequency region corresponds to charge-transfer resistance ( $R_{ct}$ ), while the sloping line in the low-frequency region is assigned to Warburg impedance ( $W_o$ ), which reflects the diffusion process of the polysulfides [27, 30-32]. The sum of  $R_e$ ,  $R_{ct}$  and  $R_{st}$  is calculated as the total resistance of the cell ( $R_{total}$ ) [33]. According to the fitted results (**Table 4.6**), the most prominent difference between these two cells is the shrinkage in  $R_{ct}$  values after interlayers inserting. This amelioration should be ascribed to the highly conductive few-layer graphene foam that acts as the secondary current collector, which greatly facilitates the redox of dissolved polysulfides. The low  $R_{ct}$  value of cell with GF/GF@ZnO interlayer indicates the highest efficiency of GF/GF@ZnO interlayer in reutilizing polysulfides. It is noticeable that an additional semicircle in high-frequency region appears in the Nyquist plot of the cell with GF/GF@ZnO interlayer, which corresponds to the interface resistance ( $R_{st}$ ) [28, 34]. This may be caused by the increment in thickness of the two-layer GF/GF@ZnO interlayer [32, 35]. The low  $R_{total}$  value of the cell with GF/GF@ZnO interlayer is another evidence of the remarkable effect of this double-layer interlayer on reducing the internal resistance.



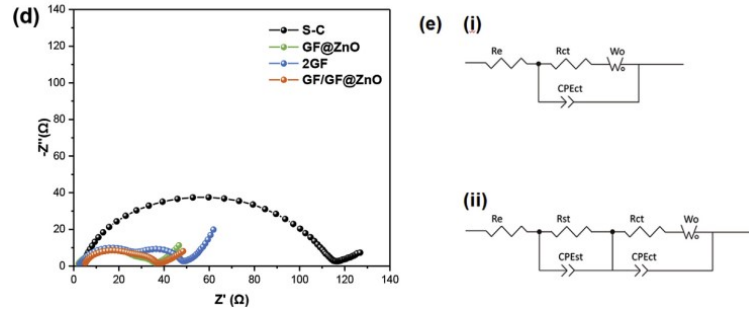


**Figure 4.69** Electrochemical performance of Li-S cells with different interlayers: (a) cyclic test performance of cells with different interlayers measured at 0.5 C and (b) the corresponding cycling specific capacity based on cathode and interlayer mass. (c) Rate performance and (d) electrochemical impedance spectra of cells with different interlayers before cycling; and (e) the corresponding equivalent circuit: (i) pristine Li-S battery and (ii) cells with different interlayers.

**Table 4.6** The fitting results of R<sub>e</sub>, R<sub>ct</sub>, R<sub>st</sub> and R<sub>total</sub> values of cells with GF/GF@ZnO interlayer and without interlayer.

	R <sub>e</sub> (Ω)	R <sub>ct</sub> (Ω)	R <sub>st</sub> (Ω)	R <sub>total</sub> (Ω)
Cell without interlayer	3.9	110	-	113.9
Cell with GF/GF@ZnO interlayer	4.3	14.0	20.2	38.5

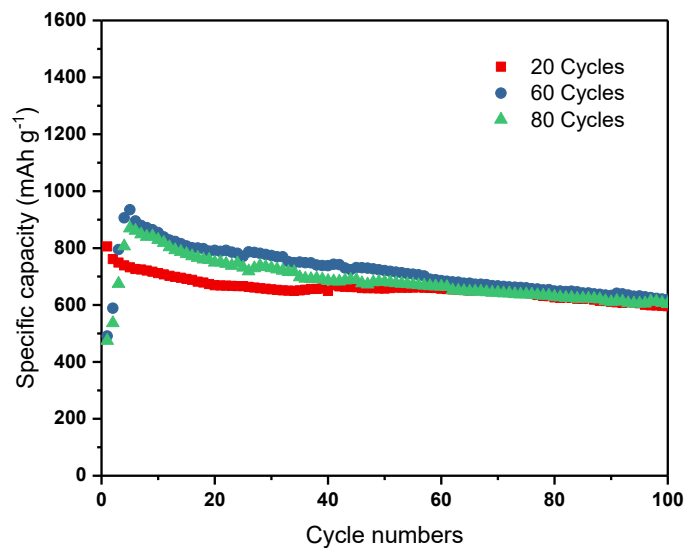


**Figure 4.70** The cycling performance of cells with different GF@ZnO interlayers: interlayers with 20, 60 and 80 ALD cycles.

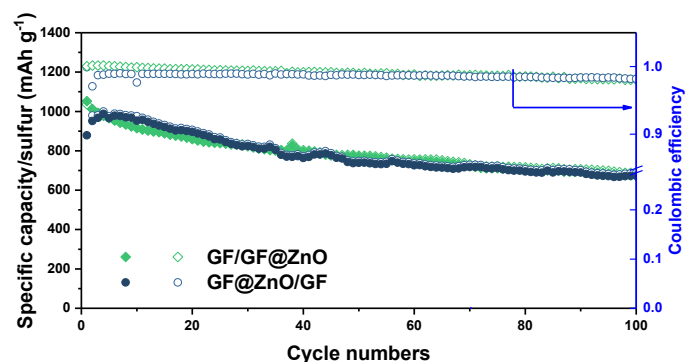


**Figure 4.71** The cycling performance of cells with GF/GF@ZnO and GF@ZnO/GF interlayers at 0.5 C.

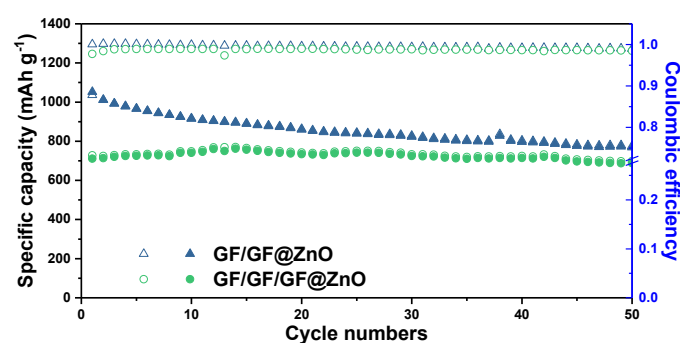


**Figure 4.72** The cycling performance of cells with GF/GF@ZnO and GF/GF/GF@ZnO interlayers at 0.5 C

To highlight the importance of the interlayer in trapping the polysulfides, a control experiment was conducted where the GF@ZnO interlayer was placed in the cell but electronically isolated, as shown in **Figure 4.73a**. An extra separator was used to avoid the contact between sulfur cathode and interlayer. Compared with the cell with the GF@ZnO interlayer, the cell with isolated separator shows impaired specific capacity. After 100 cycles at 0.5 C, it drops to 382 mAh g<sup>-1</sup>, which is much lower than the 595 mAh g<sup>-1</sup> of the GF@ZnO cell and is close to that of the pristine Li-S cell (340 mAh g<sup>-1</sup>). Due to the extra separation between sulfur cathode and interlayer, the GF@ZnO is electronically isolated and the trapped polysulfides on the interlayer cannot be utilized during the following cycles, resulting in fast capacity degrading. During the initial 50 cycles, the cell with isolated interlayer exhibited higher capacity than pristine cell, which could be attributed to the suppressed passivation layer on the Li anode surface [36].

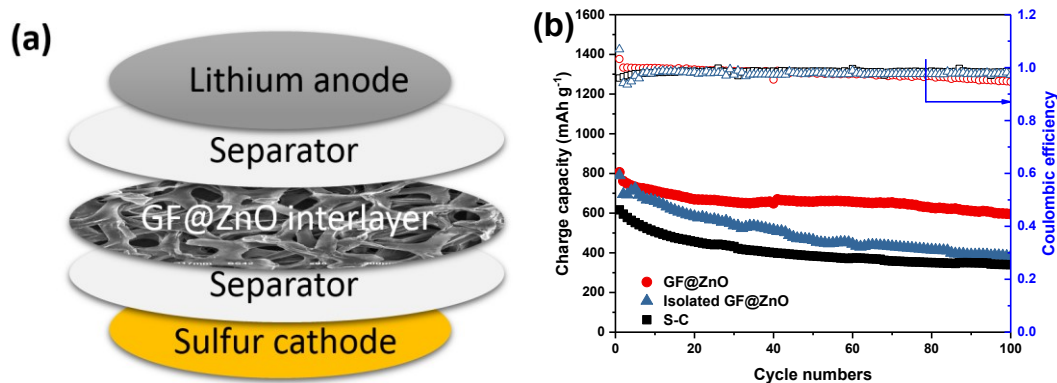


**Figure 4.73** (a) Scheme of the cell with an isolated interlayer. (b) The cyclic discharge specific capacity performance of the cell with GF@ZnO interlayer, isolated GF@ZnO interlayer and pristine cathode at 0.5 C.

The SEM image and the elemental mapping of C and S for the GF/GF@ZnO interlayer surface towards the cathode confirm the entrapment of active material. After 100 cycles at 0.5 C, the GF/GF@ZnO interlayer is taken out from the disassembled cell and characterized by SEM and EDS mapping, as shown in **Figure 4.74**. The SEM image reveals an intact structure of this GF-based interlayer with no prominent damage, suggesting its high mechanical tolerance for volumetric variation of sulfur cathode during cycling. In addition, the elemental mapping shows that carbon and sulfur signals distribute evenly on the side towards cathode without any evident agglomeration of active sulfur. The Ni foam-templated GF shows hierarchical porosity with a rather high proportion of micropores agreed well with a literature [37], which is valuable in reserving polysulfides. The mapping of the GF@ZnO side after 100 cycles shows similar result of the GF side ones, suggesting the evenly distributed sulfur within the GF/GF@ZnO (**Figure 4.75**). To make a comparison with the polysulfides-trapping ability between bare GF and GF@ZnO, the EDS was also done for both of them after cycles, as shown in **Figure 4.76**. The inserted quantitative result clearly exhibits the sulfur in the GF@ZnO sample (11.51 wt.%) is higher than that in the bare GF sample (7.19 wt.%), proving the decorated ZnO nano particles provides stronger polysulfides-trapping ability. All these mapping results confirm the function of GF/GF@ZnO interlayer as a co-current collector and recycler of the dissolved polysulfides species.

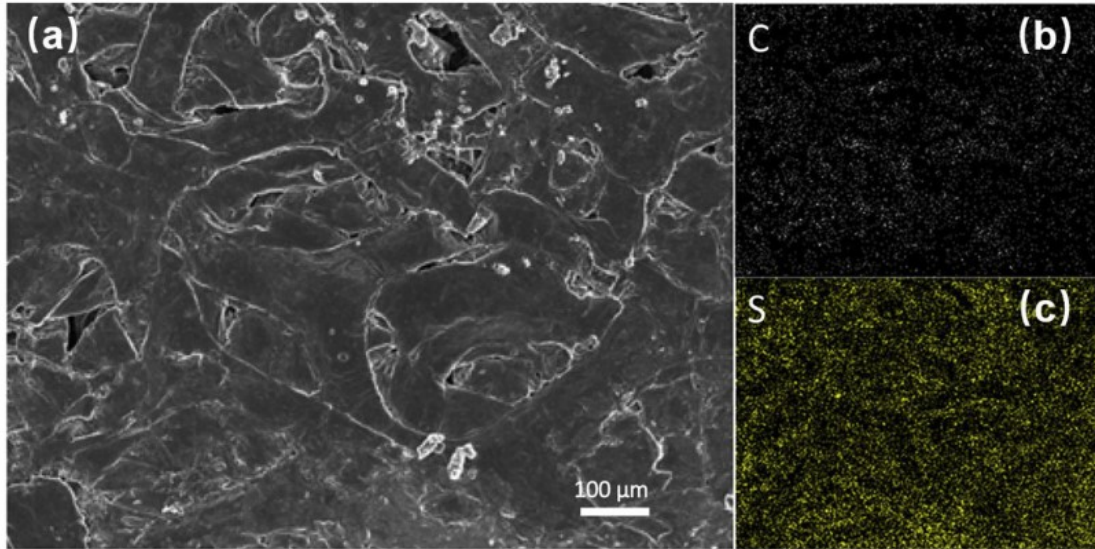


**Figure 4.74** (a) SEM image of the GF/GF@ZnO interlayer of the GF side after 100 cycles at 0.5 C; (b) corresponding EDS carbon elemental mapping and (c) corresponding EDS sulfur elemental mapping.

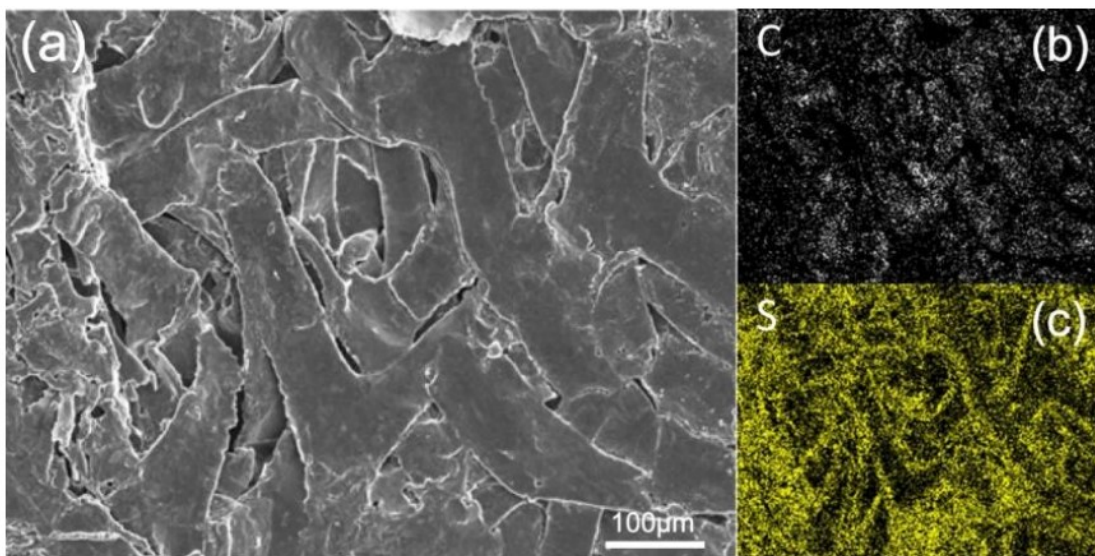


**Figure 4.75** (a) SEM image of the GF/GF@ZnO interlayer of the GF@ZnO side after 100 cycles at 0.5 C; (b) the corresponding EDS carbon elemental mapping and (c) sulfur elemental mapping.

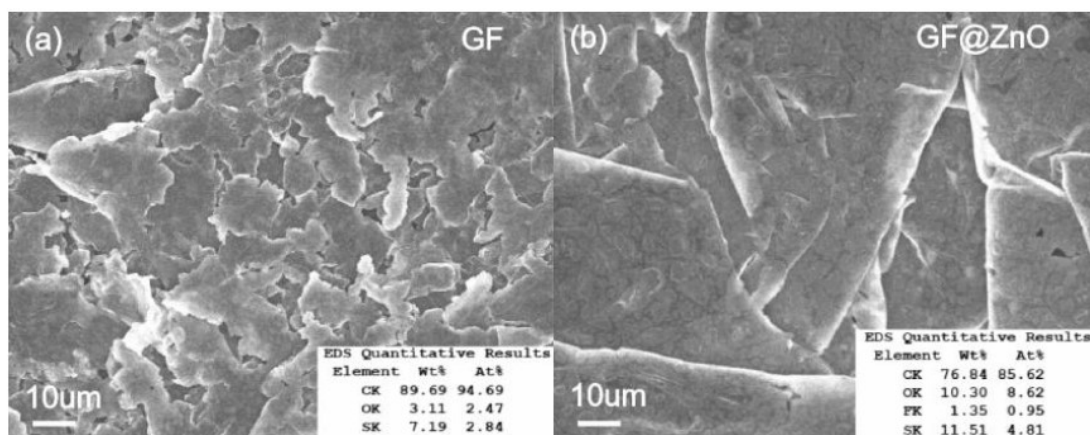


**Figure 4.76** (a) SEM image of the GF interlayer and (b) GF@ZnO interlayer after for 50 cycles at 0.5 C. Insert tables show the corresponding quantitative results of elements.

To identify the standing of this work among published results, a comparison (as shown in Table 2) is made of electrochemical performance between the current work and the cells with carbon-based and other interlayers. A parameter called “cycled capacity increment efficiency ( $A \cdot h \cdot cm^2 \cdot g^{-2}$ )” is introduced here to evaluate the interlayers’ ability to improve capacity performance by density after cycling. The cycled capacity increment efficiency ( $\Delta c$ ) is calculated as follows (**Equation 4.15**):

$$\Delta c = \frac{C_{interlayer} - C_{bare}}{\rho_{interlayer}} \quad \text{Equation 4.16}$$

Where  $C_{interlayer}$  represents the specific capacity of cell with interlayer after certain cycles, and  $C_{bare}$  is the specific capacity of the same cell without interlayer after the same cycles. The parameter  $\rho_{interlayer}$  is the density of interlayer, and here the areal density is adopted for the convenience of measurement. This  $\Delta c$  parameter is important to evaluate the comprehensive effect of interlayer on sulfur cathode, especially the degree of interlayer to “dilute” the capacity density of cathode. In this case, the effect of the additional mass of interlayer on the capacity density of cathode should be also considered. The higher the  $\Delta c$  is, the more effective an interlayer can be. Compared with all the other interlayers for Li-S batteries, the optimal GF/GF@ZnO interlayer shows a higher  $\Delta c$  value ( $1090 \text{ Ah cm}^2 \cdot g^{-2}$ ) than most other interlayers, such as  $Fe_3C/\text{carbon nanofiber}$  [38],  $MnO_2@\text{graphene}$  [39], activated carbon nanofiber [40], and super-P [41]. Although the Nafion/super-P [32] shows a higher  $\Delta c$  value, the GF/GF@ZnO presents a much higher initial discharge capacity and residual capacity after cycles at the same current rate, compensating the overall capacity performance.

**Table 2** Comparison of electrochemical performance of Li-S batteries with different interlayers and corresponding  $\Delta c$  parameters.

Interlayer materials	Current rate (mA g <sup>-1</sup> )	Cycle number	Initial discharge capacity (mAh g <sup>-1</sup> )	Residual reversible capacity (mAh g <sup>-1</sup> )	Interlayer areal density (mg cm <sup>-2</sup> )	Cycled capacity increment efficiency $\Delta c$ (Ahcm <sup>2</sup> g <sup>-2</sup> )	Ref.
Activated carbonclot	220	40	~1150	766	7.89	69.1	[16]
h @Al <sub>2</sub> O <sub>3</sub>							
Fe <sub>3</sub> C/carbon nanofiber	200	100	1177	893	2.26	218.1	[38]
Nafion/super-P	837	250	863	430	0.15	1666.6	[32]
Polypyrrole nanotube film	335	200	~1340	890	1.0	603	[42]
Polypyrrole	335	100	719	~850	0.3	833.3	[43]
MnO <sub>2</sub> @graphene	837	100	1395	600	0.8	625	[39]
Activated carbon nanofiber	Not given	100	~1200	897	1.0	851	[40]
Super-P	167.5	50	~990	~800	1.0-1.5	200-266.7	[41]
GF/GF@ZnO	837	100	1051	672	0.3	1090	This work

### 4.3. Conclusions

In this work, the light-weight and free-standing GF-based interlayers are synthesized by a facile CVD process and modified by a thin layer of ZnO using the ALD method. Being used as the interlayers between the sulfur cathode and the separator, the GF-based interlayers prove their effectiveness in serving as an electron high-way and entrapping the dissolved polysulfides. The GF/GF@ZnO interlayer shows the best amelioration for Li-S batteries, with an initial specific capacity of 1051 mAh g<sup>-1</sup> and a reversible capacity of 672 mAh g<sup>-1</sup> at 0.5 C for 100 cycles. Remarkably, the mass addition of this interlayer on the total cathode is less than 5 wt. %. This work highlights that the GF-based interlayers are suitable to improve the capacity and cycling performance of Li-S batteries without undermining their overall energy density.

### 4.4. References

- [1] Fang, Zhao, Pei, Qian, Hou, Cheng, Liu, and Li, *Toward More Reliable Lithium-Sulfur Batteries: An All-Graphene Cathode Structure*. ACS Nano, 2016,**10** (9): p. 8676-8682.
- [2] Kaiser, Ma, Wang, Han, Gao, Fan, Wang, Liu, Dou, and Wang, *Reverse Microemulsion Synthesis of Sulfur/Graphene Composite for Lithium/Sulfur Batteries*. ACS Nano, 2017,**11** (9): p. 9048-9056.
- [3] Tao, Wang, Liu, Wang, Yao, Zheng, Seh, Cai, Li, Zhou, Zu, and Cui, *Balancing surface adsorption and diffusion of lithium-polysulfides on nonconductive oxides for lithium-sulfur battery design*. Nature Communications, 2016,**7** p. 11203.
- [4] Zheng, Niu, Lv, Zhou, Li, Fan, Deng, Pan, Li, Kang, and Yang, *Propelling polysulfides transformation for high-rate and long-life lithium-sulfur batteries*. Nano Energy, 2017,**33** p. 306-312.
- [5] Cao, Liu, Li, Wang, and Jiao, *Encapsulating sulfur in  $\delta$ -MnO<sub>2</sub> at room temperature for Li-S battery cathode*. Energy Storage Materials, 2017,**9** p. 78-84.
- [6] Liang and Nazar, *In-situ Reactive Assembly of Scalable Core-Shell Sulfur-MnO<sub>2</sub> Composite Cathodes*. ACS Nano, 2016,**10** (4): p. 4192-4198.
- [7] Liang, Hart, Pang, Garsuch, Weiss, and Nazar, *A highly efficient polysulfide mediator for lithium-sulfur batteries*. Nat Commun, 2015,**6** p. 5682.

- [8] Zhao, Zhu, Chen, and Cairns, *Polypyrrole/TiO<sub>2</sub> nanotube arrays with coaxial heterogeneous structure as sulfur hosts for lithium sulfur batteries*. Journal of Power Sources, 2016,**327** p. 447-456.
- [9] Wei Seh, Li, Cha, Zheng, Yang, McDowell, Hsu, and Cui, *Sulphur-TiO<sub>2</sub> yolk-shell nanoarchitecture with internal void space for long-cycle lithium-sulphur batteries*. Nature Communications, 2013,**4** p. 1331.
- [10] Dong, Wang, Zhang, and Wu, *Preparation and electrochemical performance of sulfur-alumina cathode material for lithium-sulfur batteries*. Materials Research Bulletin, 2013,**48** (6): p. 2079-2083.
- [11] Gu, Tong, Wen, Liu, Lai, and Zhang, *Ball-milling synthesis of ZnO@sulphur/carbon nanotubes and Ni(OH)<sub>2</sub>@sulphur/carbon nanotubes composites for high-performance lithium-sulphur batteries*. Electrochimica Acta, 2016,**196** p. 369-376.
- [12] Zhang, Gu, Xu, Xue, and Pang, *High performance of electrochemical lithium storage batteries: ZnO-based nanomaterials for lithium-ion and lithium-sulfur batteries*. Nanoscale, 2016,**8** (44): p. 18578-18595.
- [13] Zhao, Ye, Peng, Divitini, Kim, Lao, Coxon, Xi, Liu, Ducati, Chen, and Kumar, *Advanced Lithium-Sulfur Batteries Enabled by a Bio-Inspired Polysulfide Adsorptive Brush*. Advanced Functional Materials, 2016,**26** (46): p. 8418-8426.
- [14] Zhang, Wang, Seh, Fu, Zhang, and Cui, *Understanding the Anchoring Effect of Two-Dimensional Layered Materials for Lithium-Sulfur Batteries*. Nano Lett, 2015,**15** (6): p. 3780-3786.
- [15] Yu, Wang, Tian, Song, Wang, Li, Hong, and Shi, *Dual-protection of a graphene-sulfur composite by a compact graphene skin and an atomic layer deposited oxide coating for a lithium-sulfur battery*. Nanoscale, 2015,**7** (12): p. 5292-5298.
- [16] Han, Xu, Chen, Chen, Weadock, Wan, Zhu, Liu, Li, Rubloff, Wang, and Hu, *Reactivation of dissolved polysulfides in Li-S batteries based on atomic layer deposition of Al<sub>2</sub>O<sub>3</sub> in nanoporous carbon cloth*. Nano Energy, 2013,**2** (6): p. 1197-1206.
- [17] Chen, Ren, Gao, Liu, Pei, and Cheng, *Three-dimensional flexible and conductive interconnected graphene networks grown by chemical vapour deposition*. Nat Mater, 2011,**10** (6): p. 424-428.
- [18] Yu, Zhao, Huang, Li, and Zhang, *Free-standing three-dimensional graphene and polyaniline*

- nanowire arrays hybrid foams for high-performance flexible and lightweight supercapacitors.* J. Mater. Chem. A, 2014,**2** (35): p. 14413-14420.
- [19] Duan, Chen, Jaroniec, and Qiao, *Porous  $C_3N_4$  nanolayers@N-graphene films as catalyst electrodes for highly efficient hydrogen evolution.* ACS Nano, 2015,**9** (1): p. 931-940.
- [20] Reina, Jia, Ho, Nezich, Son, Bulovic, Dresselhaus, and Kong, *Large Area, Few-Layer Graphene Films on Arbitrary Substrates by Chemical Vapor Deposition.* Nano Letters, 2009,**9** (1): p. 30-35.
- [21] Calizo, Bejenari, Rahman, Liu, and Balandin, *Ultraviolet Raman microscopy of single and multilayer graphene.* Journal of Applied Physics, 2009,**106** (4): p. 043509.
- [22] Bayle, Reckinger, Felten, Landois, Lancry, Dutertre, Colomer, Zahab, Henrard, Sauvajol, and Paillet, *Determining the number of layers in few-layer graphene by combining Raman spectroscopy and optical contrast.* Journal of Raman Spectroscopy, 2018,**49** (1): p. 36-45.
- [23] An, Shen, Lei, Wang, Ye, Li, Kang, and He, *An ultrathin and continuous  $Li_4Ti_5O_{12}$  coated carbon nanofiber interlayer for high rate lithium sulfur battery.* Journal of Energy Chemistry, 2018,p.
- [24] Xiao, Yang, Wang, Nie, Zhong, Lai, Xu, Zhang, and Huang, *A Lightweight  $TiO_2$ /Graphene Interlayer, Applied as a Highly Effective Polysulfide Absorbent for Fast, Long-Life Lithium-Sulfur Batteries.* Advanced Materials, 2015,**27** (18): p. 2891-2898.
- [25] Zhang, Qin, Fang, Li, Jia, Lai, Zhang, and Li, *Nickel foam as interlayer to improve the performance of lithium-sulfur battery.* Journal of Solid State Electrochemistry, 2013,**18** (4): p. 1025-1029.
- [26] Zhu, Ge, Kim, Lu, Chen, Jiang, and Zhang, *A Novel Separator Coated by Carbon for Achieving Exceptional High Performance Lithium-sulfur Batteries.* Nano Energy, 2016,**20** p. 176-184.
- [27] Wang, Zhang, Yang, Yue, Hao, Sun, Rooney, and Sun, *Flexible carbon nanofiber/polyvinylidene fluoride composite membranes as interlayers in high-performance LithiumSulfur batteries.* Journal of Power Sources, 2016,**329** p. 305-313.
- [28] Gu, Tong, Lai, Qiu, Huang, Yang, Wen, Liu, Hou, and Zhang, *A porous nitrogen and phosphorous dual doped graphene blocking layer for high performance Li-S batteries.* Journal of Materials Chemistry A, 2015,**3** (32): p. 16670-16678.
- [29] Cao, Chen, Zhao, Zhang, Lu, Wang, Niu, and Chen, *A Flexible Nanostructured Paper of a*

- Reduced Graphene Oxide-Sulfur Composite for High-Performance Lithium-Sulfur Batteries with Unconventional Configurations*. *Advanced Materials* (Weinheim, Germany), 2016,**28** (43): p. 9629-9636.
- [30] Xiao, Bu, Yang, Zhang, and Xu, *Integration of Graphene, Nano Sulfur, and Conducting Polymer into Compact, Flexible Lithium-Sulfur Battery Cathodes with Ultrahigh Volumetric Capacity and Superior Cycling Stability for Foldable Devices*. *Advanced Materials*, 2017,**29** (40): p. 1703324-1703328.
- [31] Yan, Cheng, Zhong, and Chen, *Three-dimensional nitrogen-doped graphene/sulfur composite for lithium-sulfur battery*. *Ionics*, 2016,**22** (11): p. 1999-2006.
- [32] Hao, Yuan, Li, Liu, Xiang, Wu, Zeng, and Huang, *High Performance Lithium-sulfur Batteries with A Facile and Effective Dual Functional Separator*. *Electrochimica Acta*, 2016,**200** p. 197-203.
- [33] Wang, Wen, Yang, Jin, Huang, Wu, and Han, *Electronic and Ionic Co-conductive Coating on the Separator towards High-performance Lithium-sulfur Batteries*. *Journal of Power Sources*, 2016,**306** p. 347-353.
- [34] Huang, Xu, Abouali, Akbari Garakani, and Kim, *Porous graphene oxide/carbon nanotube hybrid films as interlayer for lithium-sulfur batteries*. *Carbon*, 2016,**99** p. 624-632.
- [35] Li, Ma, Wang, Chen, Wu, and Wang, *LDHs derived nanoparticle-stacked metal nitride as interlayer for long-life lithium sulfur batteries*. *Science Bulletin*, 2018,**63** (3): p. 169-175.
- [36] Zhou, Pei, Li, Wang, Wang, Huang, Yin, Li, and Cheng, *A Graphene-Pure-Sulfur Sandwich Structure for Ultrafast, Long-Life Lithium-Sulfur Batteries*. *Advanced Materials*, 2014,**26** (4): p. 625-631.
- [37] Xi, Kidambi, Chen, Gao, Peng, Ducati, Hofmann, and Kumar, *Binder free three-dimensional sulphur/few-layer graphene foam cathode with enhanced high-rate capability for rechargeable lithium sulphur batteries*. *Nanoscale*, 2014,**6** (11): p. 5746-5753.
- [38] Huang, Zhang, Xu, Abouali, Akbari Garakani, Huang, and Kim, *Novel interlayer made from Fe<sub>3</sub>C/carbon nanofiber webs for high performance lithium-sulfur batteries*. *Journal of Power Sources*, 2015,**285** p. 43-50.
- [39] Sun, Ou, Yue, Yang, Wang, Rooney, and Sun, *A simply effective double-coating cathode with MnO<sub>2</sub> nanosheets/graphene as functionalized interlayer for high performance lithium-sulfur*

- batteries. *Electrochimica Acta*, 2016,**207** p. 198-206.
- [40] Wang, Yang, and Kang, *Porous carbon nanofiber paper as an effective interlayer for high-performance lithium-sulfur batteries*. *Electrochimica Acta*, 2015,**168** p. 271-276.
- [41] Yao, Yan, Li, Zheng, Kong, Seh, Narasimhan, Liang, and Cui, *Improved Lithium–sulfur Batteries with A Conductive Coating on the Separator to Prevent the Accumulation of Inactive S-related Species at the Cathode–separator Interface*. *Energy & Environmental Science*, 2014,**7** (10): p. 3381-3390.
- [42] Ma, Wen, Wang, Shen, Peng, Jin, and Wu, *Enhanced Performance of Lithium Sulfur Battery with Self-assembly Polypyrrole Nanotube Film as the Functional Interlayer*. *Journal of Power Sources*, 2015,**273** p. 511-516.
- [43] Ma, Wen, Jin, Wu, Wu, and Zhang, *Enhanced Cycle Performance of Li–S Battery with A Polypyrrole Functional Interlayer*. *Journal of Power Sources*, 2014,**267** p. 542-546.

## Chapter 5 Graphene foam@Ti<sub>3</sub>C<sub>2</sub>T<sub>x</sub> as an interlayer for stable Li-S batteries

### 5.1 Introduction

For the GF/GF@ZnO interlayer discussed in Chapter 4, it shows an attractive effect of improving the S-C cathode capacity and stability performance. Here, the nanoscale ZnO coating on the GF interlayer was deposited by the atomic layer deposition (ALD) method and its role is to enhance the polysulfide-blocking ability. There is a minimum amount of adding ZnO, which is a balance between prohibiting the “shuttle effect” by introducing chemical adsorption with ZnO polar surface and decreasing the conductivity brought by the insulating metal oxides. Although the improvement of the batteries is effective, the applied ALD for GF modification is a relatively sophisticated process. Also the insulating ZnO is not an ideal material considering its low conductivity. Hence, better candidates with both features of high conductivity and the polysulfides-trapping ability are sought.

MXene, standing out for its high conductivity and strong LiPS interaction, has proved itself in improving the Li-S battery performance as an MXene film-coating on the commercial Celgard separator [1]. Among all MXenes, Ti<sub>3</sub>C<sub>2</sub>T<sub>x</sub>, holds particular promise for high-performance stable Li-S batteries [2], mainly due to its high conductivity and strong interaction between polysulfides and surface functional groups, like -OH, -O-, and -F, et al. [3]. Despite its success, some drawbacks are also obvious. One of them is its limited specific surface area. Compared with the graphene with a theoretical specific surface area of 2630 m<sup>2</sup> g<sup>-1</sup>, the MXene has a much lower value in this property (21.05 m<sup>2</sup> g<sup>-1</sup> for Ti<sub>3</sub>C<sub>2</sub>T<sub>x</sub> powder [4]), which strongly hinders its application in being interlayer materials for high energy density Li-S batteries.

Herein, in this chapter, with the focus to couple with the advantages of graphene and MXene, the graphene foam@Ti<sub>3</sub>C<sub>2</sub>T<sub>x</sub> composite (GFMX) as a light-weight free-standing interlayer is fabricated. The conductive MXene provides strong polysulfides attraction with its surface functional groups, thus enhancing the ability to prohibit the “shuttle effect” by chemical adsorption; meanwhile, the GF serves as the light-weight framework for the MXene, greatly reducing the density and increasing the specific surface area of the composite. As a result, Li-S batteries with this free-standing light-weight interlayer delivers a capacity of 868 mAh g<sup>-1</sup> with a retention of 89.0 % after 120 cycles at 0.2 C. These favorable results suggest this free-standing light-weight GFMX interlayer can facilitate the high-performance Li-

S batteries.

The research work in Chapter 5 was mainly designed and carried out by me under the guidance of Dr. Li Yang and Dr. Cezhou Zhao. The result presented in this chapter was written as a paper draft and ready for a submission to a journal. The manuscript was drafted by me and corrected by Dr. Li Yang. Dr. Chenguang Liu helped me with the 3D schematic drawing and the MXene fabrication. The rest of authors helped me with some supporting works, including data analysis and double check the experimental results.

## 5.2 Experimental part

### 5.2.1 Synthesis of graphene foam (GF)

The synthesis of the graphene foam followed the process described in Chapter 4 with some minor modifications: a denser nickel foam ( $350 \pm 20 \text{ g m}^{-2}$ ) was used as the template for the CVD growth of the GF. The denser nickel foam leads to a denser GF, providing the better coverage for the cathode. After the same etching and desiccation process, a free-standing GF was obtained with a typical areal density of  $\sim 0.23 \text{ mg cm}^{-2}$ .

### 5.2.2 Synthesis of graphene foam @ $\text{Ti}_3\text{C}_2\text{T}_x$ (GFMX) interlayer

***The fabrication of  $\text{Ti}_3\text{C}_2\text{T}_x$  suspension:*** The  $\text{Ti}_3\text{C}_2\text{T}_x$  was fabricated by selectively etching the Al in the  $\text{Ti}_3\text{AlC}_2$  (MAX phase). Typically, 2 g of lithium fluoride (LiF, Aladdin, 99.9% metals basis) was added to 40 mL 9 M hydrochloric acid in a Teflon beaker, followed by a 400 rpm stirring for 30 min. Then 2 g of  $\text{Ti}_3\text{AlC}_2$  powder (MAX, 200 mesh, 11 Technology Co., Ltd.) was carefully added to the above acid mixture. The etching was conducted at 35 °C with 24 h continuous stirring. The resulting suspension was centrifugally separated (3500 rpm, 10 min), then the supernatant was carefully removed. The sediment was added with a total of 160 mL deionized water (DI water) and shaken with hand to obtain a homogeneous suspension. Afterward, the suspension was ultrasonicated (750 W, 10 min) and again centrifugally separated. These steps were repeated until a pH value of supernatant reached 5.

The  $\text{Ti}_3\text{C}_2\text{T}_x$  suspension was prepared via the delamination of the etched  $\text{Ti}_3\text{C}_2\text{T}_x$ . The ethanol of 160 mL was added to the obtained sediment as the intercalator. The mixture was shaken and centrifugally separated at 10000 rpm for 10 min. The resulted sediment was collected and added with 20 mL DI water

and then shaken by hand. The suspension was ultrasonicated (750 W, 20 min) and repeatedly centrifugal separated (350 rpm, 3 min) to collect the dark green supernatant. The resulted suspension is delaminated  $\text{Ti}_3\text{C}_2\text{T}_x$  suspension (MXene suspension). By filtrating a certain amount of MXene suspension and weighing the dried MXene film, the concentration of the resulted MXene suspension was determined as  $10 \text{ mg mL}^{-1}$ .

**The fabrication of GFMX interlayer:** The GF was firstly surface modified by the cetyltrimethyl ammonium bromide (CTAB): the GF was soaked in the 0.2 wt.% CTAB water solution for 5 minutes, and then washed by excessive DI water. Then 2 mL of  $\text{Ti}_3\text{C}_2\text{T}_x$  suspension ( $1 \text{ mg mL}^{-1}$ ) was dropwisely added to the modified GF to ensure a complete infiltration. After a 10-minute rest, the redundant suspension was adsorbed away by a tissue and the GF was vacuum dried at  $50 \text{ }^\circ\text{C}$  for 10 h to obtain the free-standing GFMX. The typical areal density of the GFMX interlayer is  $\sim 0.25 \text{ mg cm}^{-2}$ .

### 5.2.3 Physical characterization

The micromorphology was observed by the scanning electron microscope (SEM, Hitachi S4700) and the transmission electron microscope (TEM, FEI Talos F200x). The element distribution of the sample was characterized using the energy-dispersive X-ray spectroscopy (EDS). A Raman spectrometer (Jobin YvonXploRA, HORIBA Scientific) was used with a laser wavelength of 532 nm.

### 5.2.4 Electrochemical characterization

**Electrode preparation:** The S/CNT cathode composite was fabricated by a solvent-assisted sulfur deposition. In a typical process, the sulfur (0.8 g) was mixed with multiwalled carbon nanotubes (MWCNT, 0.2 g) and continuously sonicated in the ethanol (60 mL) for 2 h until most of the sulfur particles were dissolved. Then this mixture was desiccated at  $75 \text{ }^\circ\text{C}$  until the solvent was evaporated, followed by a vacuum desiccation of  $60 \text{ }^\circ\text{C}$ . The resulted cathode material was named as S/CNT. The S cathode was fabricated by mixing 80 wt.% S/CNT with 10 wt.% super-P as a conducting agent and 10 wt.% PVDF as a binder in the NMP. After being magnetically stirred for 12 h, the slurry was coated on an aluminum foil current collector by a blade-coating machine, followed by vacuum desiccation at  $60 \text{ }^\circ\text{C}$  for 12 h. The prepared electrodes were cut into discs of diameter 13 mm for coin cell assembling. The typical sulfur loading was  $\sim 1.5 \text{ mg cm}^{-2}$  if was not denoted specifically.

**Coin cell preparation:** The prepared GFMX and GF interlayers were cut into discs of diameter 15 mm, and placed between the S electrode and the separator. The interlayer was able to fully cover the cathode without touching the lithium anode. The electrolyte applied was 1.0 M lithium bis (trifluoromethanesulfonyl) imide (LiTFSI) in dioxolane (DOL) and dimethoxyethane (DME) (1:1 by volume) with a 1.0 wt% LiNO<sub>3</sub> additive. To better evaluate the performance of the interlayer, the electrolyte was overloaded with the electrolyte/sulfur (E/S,  $\mu\text{L}/\text{mg}$ ) ratio of 20:1 [5]. For the cell without an interlayer, an E/S ratio of 10:1 was used.

**Cycling test, open circuit potential measurement, and cyclic voltammetry test:** The cycling test was conducted between 1.6-2.7 V (vs. Li/Li<sup>+</sup>) using 1672 mAh g<sup>-1</sup> as the theoretical specific capacity. The cyclic voltammetry (CV) scanning rate was 0.1 mV s<sup>-1</sup> between 1.6-2.8 V using the Autolab PGSTAT302N electrochemical workstation. The electrochemical impedance spectroscopy (EIS) measurements were conducted on the same workstation with an amplitude of 5 mV and a frequency range of 10<sup>-2</sup> Hz-10<sup>5</sup>Hz.

### 3.7. Characterizations of the graphene foam@MXene interlayer and relevant analysis

The schematic of the facile fabrication process is shown in **Figure 5.77**. The surface modification by the CTAB could positively shift the zeta potential, which not only ameliorated the hydrophilicity of the GF, but also electrostatically attracted the Ti<sub>3</sub>C<sub>2</sub>T<sub>x</sub> with negative zeta potential. This method avoids the redundant Ti<sub>3</sub>C<sub>2</sub>T<sub>x</sub> nanosheets increasing the mass density of this interlayer, bringing only ~0.02 mg cm<sup>-2</sup> density addition of the Ti<sub>3</sub>C<sub>2</sub>T<sub>x</sub>. This light-weight interlayer is placed between the separator and the cathode, just like the position of GF/GF@ZnO in Chapter 4. The insert exhibits the optical image of the as-obtained GFMX interlayer, which demonstrates its implement ability at several centimeters' scale.

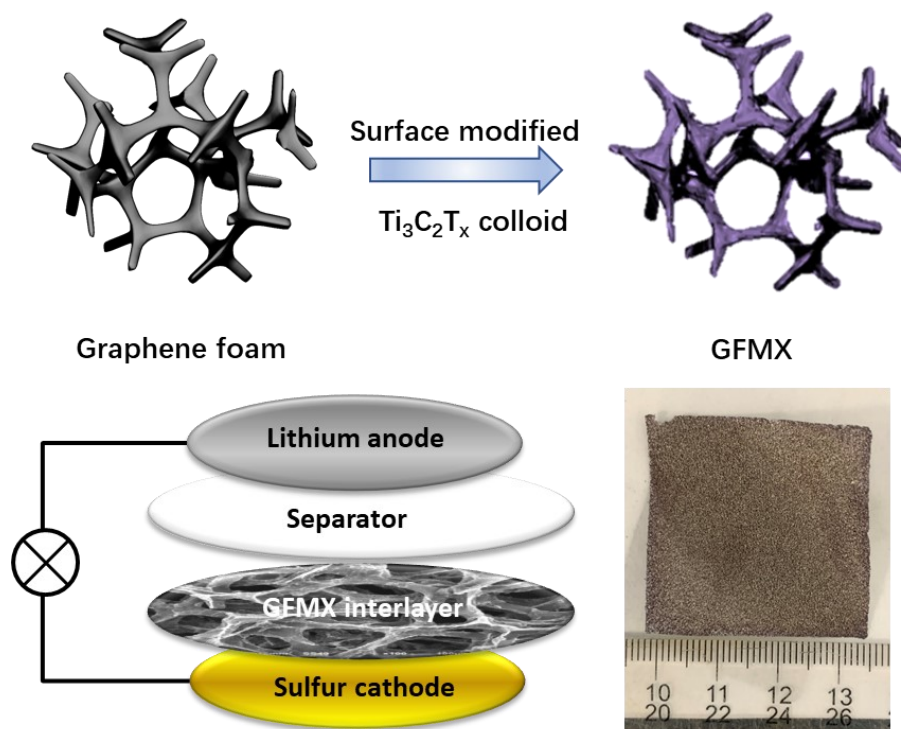


**Figure 5.77** The schematic of the fabrication of GFMX interlayer and its application in the Li-S battery. The insert is the macroscale optical image of the synthesized free-standing GFMX interlayer.

Specific physical characterizations of the obtained GFMX interlayer are shown in **Figure 5.78**. The morphology of the GFMX, as shown in **Figure 5.78a** and **c**, clearly presents the 3-D structured graphene foam with macro-scale porosity, in agreement of the GF as seen in **Figure 5.78b** and **d**. However, the surface modification of the  $\text{Ti}_3\text{C}_2\text{T}_x$  makes the smooth surface of the GF become rough, where polygonal graphene grain boundaries can be clearly identified in **Figure 5.78d**. In the case of GFMX, the crumpled  $\text{Ti}_3\text{C}_2\text{T}_x$  wraps the GF branches so that graphene grain boundaries cannot be observed directly. The TEM bright field image (**Figure 5.78e**) exhibits stacked nanosheets containing both graphene and  $\text{Ti}_3\text{C}_2\text{T}_x$ , which can be verified by the corresponding SAED patterns (**Figure 5.78f**) and the EDS mapping (**Figure 5.78g**). Discrete diffraction points on the corresponding diffraction radius indicate the overlapping multilayers of graphene [6] and  $\text{Ti}_3\text{C}_2\text{T}_x$  nanosheets [7, 8], which is consistent with the EDS mapping results of Ti and C: the distribution area of Ti and O covers the high-contrast area of C. Raman analysis is another proof of the MXene modification. Besides the G and 2D bands of graphene foam that shared by GF and GFMX, many small bands located between  $100$  and  $800\text{ nm}^{-1}$  emerge in the GFMX spectrum. The  $A_{1g}$  bands are attributed to the symmetry out-of-plane vibrations of Ti and C atoms, while the in-plane vibration modes of Ti, C, and surface functional group atoms are denoted as the  $E_g$ , as shown in **Figure 5.78h** [9]. All these physical characterizations demonstrate the successful  $\text{Ti}_3\text{C}_2\text{T}_x$  modification

of the GF surface.

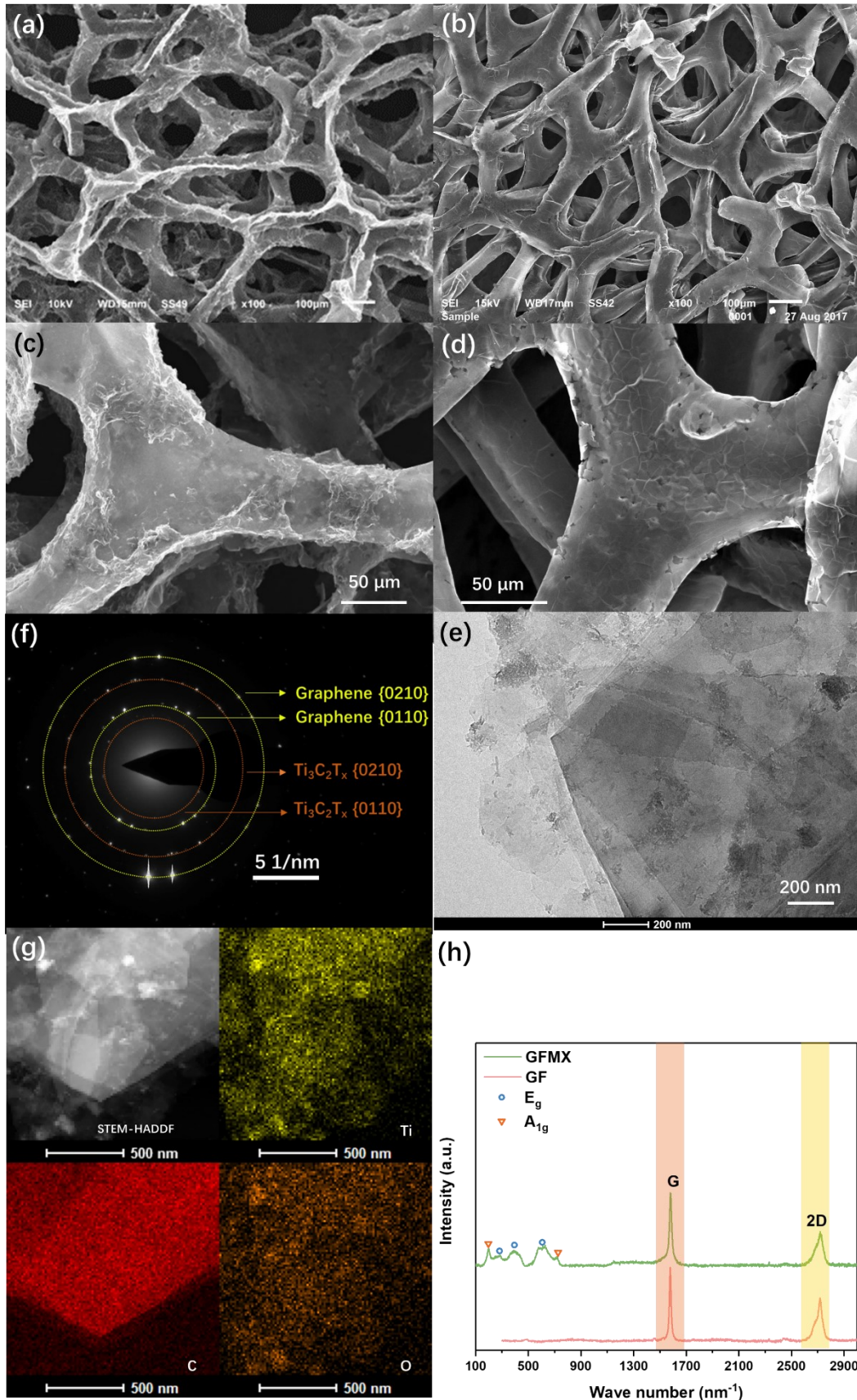


**Figure 5.78** The physical characterization of GF and GFMX: The SEM images of (a)(c) GFMX and (b)(d) GF with different magnifications. (e) The TEM bright field image of GFMX and the corresponding

(f) SEAD patterns. (g) The corresponding STEM-HAADF image and EDS element mapping of Ti, C, and O. The Raman spectra comparison of GF and GFMX is shown in (h).

To analyse the electrochemical performance, the GFMX interlayer was applied between the S cathode and the separator in Li-S cells. Firstly, the CV performance of three cells: GFMX, GF and pristine Li-S batteries, was tested and recorded in **Figure 5.79a**. All three Li-S cells show typical redox peaks of Li-S battery with organic liquid electrolyte: one merged anodic peak and two cathodic peaks which corresponding to the one-step oxidation of lithium sulfides and two-step reduction of elemental sulfur [10]. It is noted that the peak current density of cells with interlayers show higher than the pristine ones. At the meantime, the peak potential of modified cells exhibits less polarization degree. These variations indicate that GF and GFMX boost the utilization of sulfur and redox kinetic. A surge of the low-potential cathodic peak value of the GFMX cell implies that the addition of MXene extensively enhances the utilization of the dissolved high-order polysulfides, which is the main contributor of the second-step reduction's capacity. This is due to the polarized surfaces brought by the  $\text{Ti}_3\text{C}_2\text{T}_x$  nanosheets enormously amplifies the chemical adsorption ability of the graphene foam with non-polarized surface. A detailed comparison via Tafel curve analysis gives more quantitative results revealing the influence of these interlayers on the redox kinetic. As the method used in Chapter 3, the CV curves during the Tafel range were replotted in **Figure 5.79** with the current in the logarithm form. After linear fitting, fitted slopes were obtained and denoted on the plot with the same color code of corresponding curves. It can be concluded from the **Figure 5.79b** that the kinetic of three redox reactions of three cells follows the order of:  $\text{GFMX} > \text{GF} > \text{w/o}$ . The most notable kinetic elevation by the GFMX interlayer takes place in the cathodic redox, especially the final reduction process in which the  $\beta_{\text{w/o}}$  is 2.9 times of  $\beta_{\text{GFMX}}$  and 2.4 times of  $\beta_{\text{GF}}$ , implying that the activation energy of the GFMX cell is 34.4 % of the pristine cell's. This enhancement in the kinetic can be related to the adsorption ability of the  $\text{Ti}_3\text{C}_2\text{T}_x$  surface of the polysulfides.

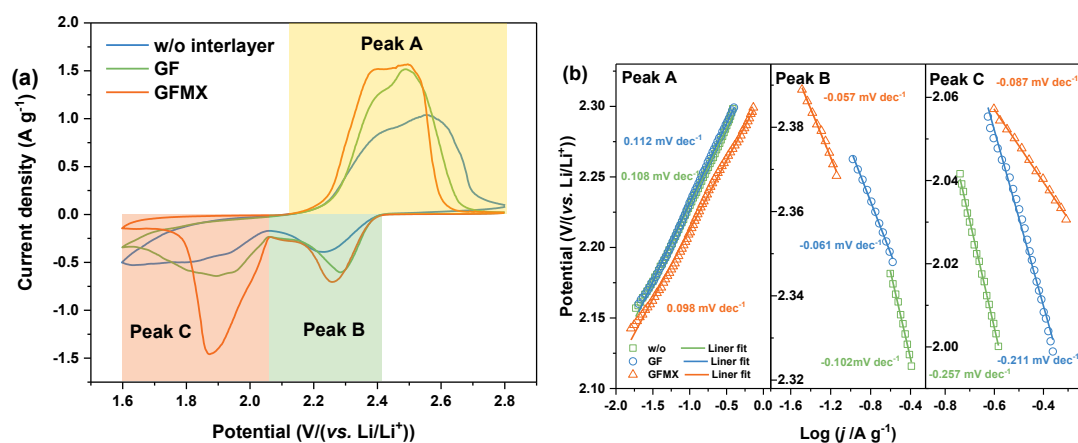


**Figure 5.79** (a) The comparison of CV curves of GFMX, GF, and pristine Li-S batteries. (b) Linear fit results of the CV curves in the Tafel range, with slopes denoted on the plot.

The cycling performance of different cells was tested using the galvanostatic charge/discharge method at various current densities. For the low-current density cycling, three types of cells were subjected to the 0.2 C cycling (**Figure 5.80a**). The cell without interlayer has an initial 818 mAh g<sup>-1</sup> discharge capacity, and being stabilized at 653 mAh g<sup>-1</sup> after 120 cycles. Meanwhile, cells with interlayers exhibit higher initial capacities at around 1000 mAh g<sup>-1</sup>, but the GFMX cell outweighs the GF one in respect of long-term cycling stability, maintaining an 867 mAh g<sup>-1</sup> after 120 cycles with an 88.8 % capacity retention. As a comparison, the GF cell only presents a residual capacity of 794 mAh g<sup>-1</sup>, accompanied with a 78.6 % retention. The upgraded capacity performance of cells with GF-based interlayers is originated from the second-current collector effect of the interlayer. This highly conductive interlayer provides extra electronic pathway to improve sulfur utilization. The higher capacity retention after cycles of the GFMX cell suggests the surface modification by Ti<sub>3</sub>C<sub>2</sub>T<sub>x</sub> nanosheets can effectively ameliorate the loss of the dissolved polysulfides, reserving the active sulfur in the cathode at a higher level. At higher current density, the GFMX cell exhibits more impressive capacity performance than the GF one's. In **Figure 5.80b**, the GFMX cell shows a capacity of ~128 mAh g<sup>-1</sup> higher than the GF one's at 1 C. This value further increases to ~279 mAh g<sup>-1</sup> as the current ascends to 2 C. The superior capacity at high current densities indicating the Ti<sub>3</sub>C<sub>2</sub>T<sub>x</sub> addition greatly enhances the kinetic at high current density by providing additional chemical adsorption of polysulfides and improved electronic conductivity. A more in-depth insight on the galvanostatic profiles can be found in **Figure 5.80c, d**. The GFMX cell maintains prominent charge and discharge plateaus at both 1 C and 2 C, while these plateaus of the GF interlayer cell present intensified polarization ( $\Delta E_{GFMX} < \Delta E_{GF}$ ). The prolonged low potential

discharge plateau (corresponding to the final reduction of the polysulfides) of the GFMX cell reveals that it can effectively boost the utilization of the dissolved polysulfides. This is consistent with the former analysis that GFMX can better assist the redox kinetic.

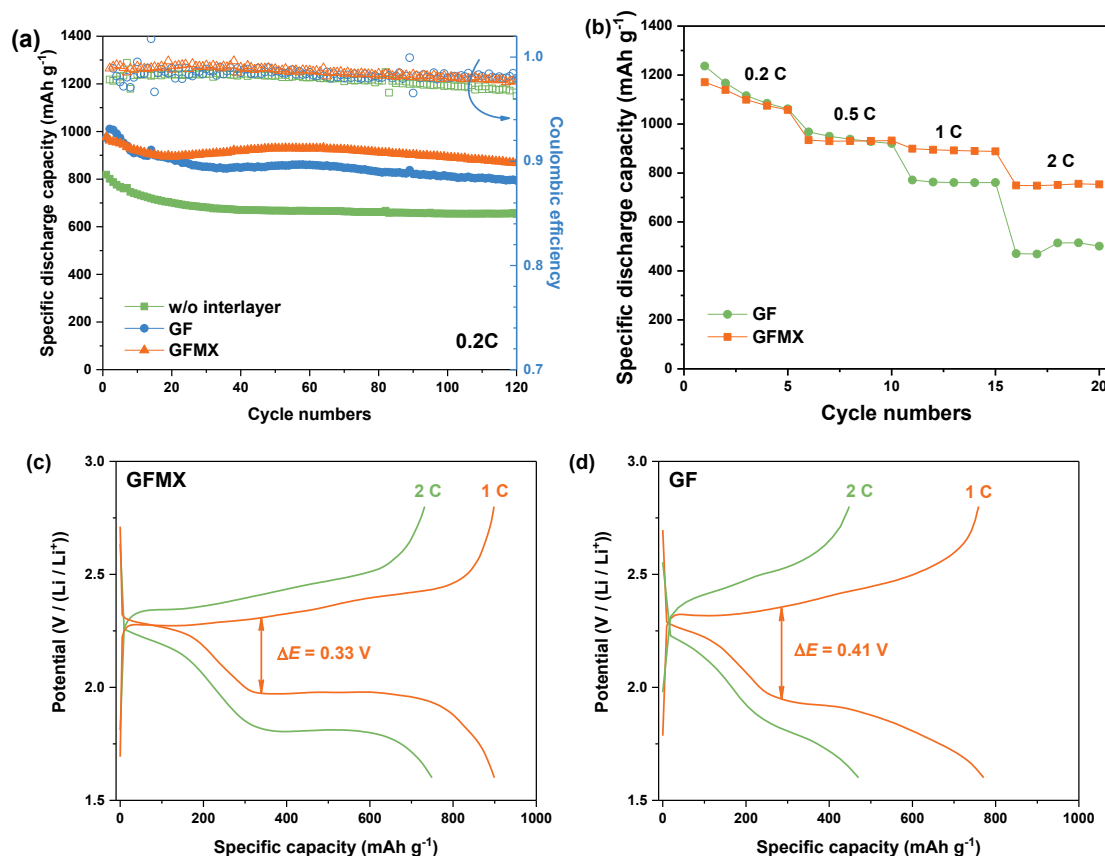


**Figure 5.80** The galvanostatic characterizations of pristine cell, GF cell, and GFMX cell: (a) cycling performance at 0.2 C. (b) The rate performance at 0.2 C, 0.5 C, 1 C, and 2 C current densities. The exhibited galvanostatic charge and discharge profiles belong to (c) GFMX cell and (d) GF cell, respectively.

EIS comparison is shown in **Figure 5.81**. Like the spectra in Chapter 3, similar shapes are observed, consisting of a depressed semicircle at high frequency region and a following sloping line in the low-frequency region. The semicircle, representing the charge-transfer resistance ( $R_{ct}$ ) from the electrochemical reaction between the electrode and electrolyte, reflects the influence of the interlayer on the internal resistance of the cell. Meanwhile the low-frequency sloping line can be ascribed to the semi-infinite Warburg impedance ( $W_o$ ), being associated with the diffusion process in the cathode [11, 12]. The second semicircle appearing at middle frequency in the GFMX one's is explained as the interface resistance ( $R_{st}$ ), which may be brought by the interface of additional  $Ti_3C_2T_x$  nanosheets. It is easy to distinguish the  $R_{ct}$  difference of three cells: the pristine Li-S cell holds the highest resistance, while the

GFMX cell has the lowest one. This difference reflects the effect of GFMX interlayer on the resistance refinement, and the prominent resistance reduction of the GFMX cell over the GF cell highlights the importance of the  $\text{Ti}_3\text{C}_2\text{T}_x$  modification. The corresponding fitting parameters are listed in **Table 5.7**.

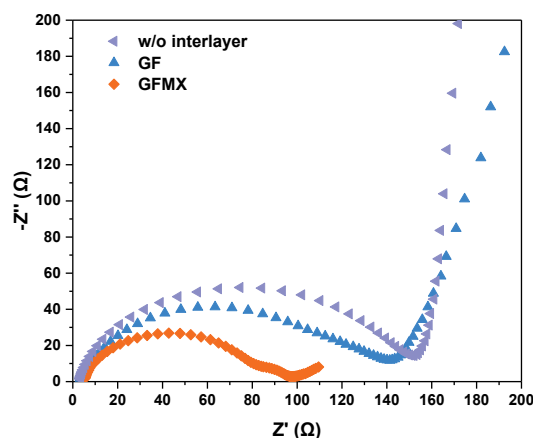


**Figure 5.81** The EIS comparison of different cells: the pristine, the GF, and the GFMX cell.

**Table 5.7** The fitted parameters of the EIS curves in **Figure 5.81**.

	$R_c/\Omega$	$R_{ct}/\Omega$	$R_{st}/\Omega$	$R_{total}/\Omega$
w/o interlayer	2.4	149.6	/	152
GF	3.2	138.1	/	141.3
GFMX	5.8	74.8	16.7	97.3

### 5.3 Conclusions

To conclude, a  $\text{Ti}_3\text{C}_2\text{T}_x$  modified graphene foam was synthesized and applied as the lightweight interlayer in Li-S batteries. The surface modification has offered the GF with polarized surface and improved electronic conductivity. These features contribute to the Li-S battery with better cyclic stability and high rate performance. Therefore, the cell with this modified interlayer delivers a capacity of  $868 \text{ mAh g}^{-1}$  and a retention of 89.0 % after 120 cycles at 0.2 C. Even at high current rate of 2 C, the GFMX cell still retains a  $749 \text{ mAh g}^{-1}$  specific capacity. These improvements indicate this free-standing light-weight GFMX interlayer can facilitate the high-performance Li-S batteries, and highlight the potential of  $\text{Ti}_3\text{C}_2\text{T}_x$  in the application of Li-S battery interlayer.

## 5.4 References

- [1] Song, Su, Xie, Guo, Bao, Shao, and Wang, *Immobilizing Polysulfides with MXene-Functionalized Separators for Stable Lithium-Sulfur Batteries*. ACS Applied Materials and Interfaces, 2016,**8** (43): p. 29427-29433.
- [2] Anasori, Lukatskaya, and Gogotsi, *2D metal carbides and nitrides (MXenes) for energy storage*. Nature Reviews Materials, 2017,**2** (2): p. 16098.
- [3] Xiao, Li, Meng, and Wang, *MXene-engineered lithium-sulfur batteries*. Journal of Materials Chemistry A, 2019,**7** (40): p. 22730-22743.
- [4] Rakhi, Ahmed, Hedhili, Anjum, and Alshareef, *Effect of Postetch Annealing Gas Composition on the Structural and Electrochemical Properties of  $Ti_2CT_x$  MXene Electrodes for Supercapacitor Applications*. Chemistry of Materials, 2015,**27** (15): p. 5314-5323.
- [5] Jiao, Zhang, Geng, Wu, Li, Lv, Tao, Chen, Zhou, Li, Ling, Wan, and Yang, *Capture and Catalytic Conversion of Polysulfides by In Situ Built  $TiO_2$ -MXene Heterostructures for Lithium-Sulfur Batteries*. Advanced Energy Materials, 2019,p. 1900219.
- [6] Wu, Zhang, Yuan, Xue, Lu, Liu, Wang, Wang, Ding, Yu, Xie, and Jiang, *Fast growth of inch-sized single-crystalline graphene from a controlled single nucleus on Cu-Ni alloys*. Nature materials, 2016,**15** (1): p. 43-47.
- [7] Naguib, Mashtalir, Carle, Presser, Lu, Hultman, Gogotsi, and Barsoum, *Two-dimensional transition metal carbides*. ACS Nano, 2012,**6** (2): p. 1322-1331.
- [8] Mashtalir, Naguib, Mochalin, Dall’Agnese, Heon, Barsoum, and Gogotsi, *Intercalation and delamination of layered carbides and carbonitrides*. Nature Communications, 2013,**4** (1): p. 1716.
- [9] Zhao, Xu, Hui, Sun, Yu, Xue, Zhou, Wang, Dai, Zhao, Yang, Zhou, Chen, Sun, and Huang, *Electrostatically Assembling 2D Nanosheets of MXene and MOF-Derivatives into 3D Hollow Frameworks for Enhanced Lithium Storage*. Small, 2019,**15** (47): p. 1904255.
- [10] Han, Song, Lee, Kim, Ahn, and Lee, *Effect of multiwalled carbon nanotubes on electrochemical properties of lithium sulfur rechargeable batteries*. Journal of the Electrochemical Society, 2003,**150** (7): p. A889-A893.
- [11] Wang, Zhang, Zhou, Yang, Li, and Zhang, *Rational design of a Nested Pore Structure Sulfur*

*Host for Fast Li/S Batteries with a Long Cycle Life.* Journal of Materials Chemistry A, 2016,4 (5): p. 1653-1662.

- [12] Xu, Su, Zhang, Bao, and Wang, *A Nitrogen–sulfur Co-doped Porous Graphene Matrix as a Sulfur Immobilizer for High Performance Lithium–sulfur Batteries.* Journal of Materials Chemistry A, 2016,4 (44): p. 17381-17393.

## Chapter 6 N-doped MXene@carbon nanosheets-Ni composite modified separator for stable Li-S batteries

### 6.1. Introduction

In previous Chapter 5, a GF@MX composite was fabricated. As an interlayer, the GF@MX has effectively increased the specific capacity and stability of the sulfur cathode, and its light-weight feature also minimizes its effect on the energy density. However, for some cathodes with higher sulfur loading, the interlayer is not capable to maintain the same level performance as those with low sulfur loading. One rational thought is to modify the MXene to enhance its polysulfide attraction, so that it becomes capable to handle the cathode with higher sulfur loading.

Although many modified separators using MXene have achieved considerable improvement in specific capacity performance, they are usually applied to cathode with an S-loading of 1-2 mg cm<sup>-2</sup> [1-5], resulting in a low energy density. Therefore, a challenge has been to develop a coating material with both highly conductive and LiPS interactive features and to be able to promote the performance of high S loading cathode.

Herein, in this work, I designed and fabricated a Ni, N-doped carbon nanosheets modified Ti<sub>3</sub>C<sub>2</sub>T<sub>x</sub> (MXene) nanosheets (N-M@CNi) as the separator coating material. The Ni, N-doped carbon nanosheets were introduced by simply annealing the mixture of dicyandiamide, Ni salt, glucose, and MXene. During the annealing, the dicyandiamide absorbed on the MXene surface through electrostatic attraction became the nitrogen source of the N-doping [6], producing the N-doped MXene that has been reported to possess more LiPS adsorption sites than those of the pristine one [7]. The N-doping of carbon nanosheets can increase the specific area of the composite, which also provides better LiPS adsorption and conductivity than the pristine sp<sup>2</sup> bonding carbon structure [8]. On the other hand, some nano-scaled transitional metal particles, like Co [9-11], Fe [12] and Ni [12-14] from the VIII B group, have been confirmed to be effective in LiPS adsorption and conversion. More attractively, the LiPS redox can be enhanced by the comprehensive effect of the N-doped carbon-coated Co nano-particles [9]. Thereby it is expected the combination of nano-scaled Ni and the N-doped carbon would have a positive effect serving as the interlayer material. For these synergistic effects, the separator decorated by the N-M@CNi showed outstanding characteristics on the Li-S batteries, including a high reversible capacity (~1300 mAh g<sup>-1</sup> at

0.2 C), an extended cycling stability (588 mAh g<sup>-1</sup> at 1 C after 500 cycles, with a capacity decay rate of 0.069 % per cycle), and an encouraging capacity from a high sulfur loading cathode of 3.18 mg cm<sup>-2</sup> (662 mAh g<sup>-1</sup> at 0.2 C after 100 cycles). These favorable results indicate that the surface modification of the N-doped MXene by the Ni, N-doped carbon nanosheets offers a novel strategy for benefiting the electrochemical performance of Li-S batteries.

The research work in Chapter 6 was mainly designed and carried out by me under the direction of Dr. Li Yang and Dr. Cezhou Zhao. The result presented in this chapter was written as a paper draft and ready for a submission to a journal. The manuscript was drafted by me and corrected by Dr. Li Yang and Prof. Laurence Hardwick. Dr. Yinchao Zhao helped me with the 3D schematic drawing. The rest of authors helped me with some supporting works, including data analysis and double check the experimental results.

## **6.2. Experiment part**

### **6.2.1. Preparation of the delaminated Ti<sub>3</sub>C<sub>2</sub>T<sub>x</sub> (MXene)**

To prepare the etched Ti<sub>3</sub>C<sub>2</sub>T<sub>x</sub>, 2 g of lithium fluoride (LiF, Aladdin, 99.9% metals basis) was added to 40 mL 9 M hydrochloric acid in a Teflon beaker, followed by a 400 rpm stirring for 30 min. Then 2 g of Ti<sub>3</sub>AlC<sub>2</sub> powder (MAX, 200 mesh, 11 Technology Co., Ltd.) was carefully added to the above acid mixture. The etching was conducted at 35 °C with 24 h continuous stirring. The resulting suspension was centrifugal separated (3500 rpm, 10 min), then the supernatant was carefully removed. The sediment was added with a total of 160 mL deionized water (DI water) and shaken with hand to obtain a homogeneous suspension. Afterward, the suspension was ultrasonicated (750 W, 10 min) and again centrifugally separated. These steps were repeated until the pH value of supernatant reached 5.

To delaminate the etched Ti<sub>3</sub>C<sub>2</sub>T<sub>x</sub>, 160 mL ethanol was added to the obtained sediment and centrifugal separated at 10000 rpm for 10 min. The resulted sediment was collected and added with 20 mL DI water and then shaken by hand. The suspension was ultrasonicated (750 W, 20 min) and repeatedly centrifugal separated (350 rpm, 3 min) to collect the dark green supernatant. The resulted suspension is delaminated Ti<sub>3</sub>C<sub>2</sub>T<sub>x</sub> suspension (MXene suspension). By filtrating a certain amount of MXene suspension and weighing the dried MXene film, the concentration of the resulted MXene suspension was determined as 10 mg mL<sup>-1</sup>.

### 6.2.2. Preparation of the nitrogen-doped MXene@nitrogen-doped carbon nanosheet-nickel (N-M@CNi)

75 mg of the nickel acetate tetrahydrate ( $\text{Ni}(\text{Ac})_2 \cdot 4\text{H}_2\text{O}$ , Aladdin, 99.9 % metals basis) was added to 30 ml of the prepared MXene suspension ( $10 \text{ mg mL}^{-1}$ ). After 10 min stirring to dissolve the  $\text{Ni}(\text{Ac})_2 \cdot 4\text{H}_2\text{O}$ , 1500 mg of dicyandiamide (DCDA, Aladdin, 99 %) was added to the suspension, followed by the addition of 150 mg glucose (AR). After adding 20 mL of DI water, the mixture was stirred for 20 min to ensure homogeneity. The mixture was vacuum dried at  $60 \text{ }^\circ\text{C}$  until all solvent was evaporated. The dark remnant was hand-ground and placed in a corundum crucible, and then kept at  $600 \text{ }^\circ\text{C}$  for 2 h, followed by  $800 \text{ }^\circ\text{C}$  for 2 h, in an argon flow. All the ramping rate was  $5 \text{ }^\circ\text{C min}^{-1}$ . The resulting black powder product was named as N-M@CNi. For comparison, the composite without Ni content was prepared by washing the prepared N-M@CNi with excessive HCl solution, and subsequently centrifugally washed and vacuum drying. The resulted product was named as N-M@C.

### 6.2.3. Preparation of the N-M@CNi modified separator

In a typical process, 120 mg N-M@CNi, 120 mg super-P and 24 mg poly (vinylidene fluoride) (PVDF) were mixed and ground, followed by the addition of 2.8 g N-methyl-2-pyrrolidinone (NMP, Aladdin, AR, > 99 %). The slurry was magnetically stirred for 12 h and coated on Celgard 2325 separator by the blade coating method. The modified separator was vacuum dried at  $60 \text{ }^\circ\text{C}$  for 12 h, with an areal coating density of  $\sim 0.7 \text{ mg cm}^{-2}$ . The N-M@C modified separator preparation followed the same process but replaced the N-M@CNi with the N-M@C. The carbon black (CB) modified separator was prepared via the same process, except for the addition of N-M@CNi.

### 6.2.4. Physical characterization

The electroconductivity of different separators was measured using the four-probe test method. The specific surface area and the pore size distribution measurement were performed on a Beishide 3H-2000PS2 instrument, and the analysis was used the Brunauer-Emmette-Teller (BET) method. The micromorphology was observed by the scanning electron microscope (SEM, Hitachi S4700) and the transmission electron microscopy (TEM, FEI Talos F200x). The element distribution of the sample was characterized using the energy-dispersive X-ray spectroscopy (EDS). The crystal structure was

investigated by an X-ray diffractometer (XRD, D8 Advance, Bruker) using a Cu K $\alpha$  radiation source from 3° to 80°, along with a Raman spectrometer (Jobin YvonXploRA, HORIBA Scientific).

### 6.2.5. Electrochemical characterization

**Electrode preparation:** The S/C electrode was fabricated by mixing 60 wt.% sulfur with 30 wt.% super-P as a conducting agent and 10 wt.% PVDF as a binder in the NMP. After being magnetically stirred for 12 h, the slurry was coated on an aluminum foil current collector by a blade-coating machine, followed by vacuum desiccation at 60 °C for 12 h. The prepared electrodes were cut into discs of diameter 13 mm for coin cell assembling. The mass loading of the sulfur was 1.0-3.18 mg cm<sup>-2</sup>, tailored by the thickness of the slurry coating. The typical sulfur loading was ~ 1.5 mg cm<sup>-2</sup> unless specifically denoted.

**Coin cell preparation:** The prepared modified separator was cut into discs of diameter 18 mm, and placed with the coating facing towards the S/C electrode. The electrolyte was 1.0 M lithium bis(trifluoromethanesulfonyl) imide (LiTFSI) in dioxolane (DOL) and dimethoxyethane (DME) (1:1 by volume) with a 1.0 wt.% LiNO<sub>3</sub> additive. To better evaluate the performance of the interlayer, the electrolyte was overloaded with the electrolyte/sulfur (E/S,  $\mu$ L/mg) ratio of 20:1 [15]. For the cell without an interlayer, an E/S ratio of 10:1 was used.

**Symmetric coin cell preparation:** To estimate the electrocatalysis effect on the polysulfide, the symmetric coin cell was tested to eliminate the influence of the reaction between electrolyte and Li anode. A 0.02 M Li<sub>2</sub>S<sub>6</sub> solution was prepared by adding the stoichiometric amount of Li<sub>2</sub>S and S<sub>8</sub> in the electrolyte and stirring for 6 h at 40 °C. Two pieces of modified separators with their uncoated-face attached together were placed in the coin cell. 60  $\mu$ L Li<sub>2</sub>S<sub>6</sub> solution was applied in each cell. The bare separators were used in the blank symmetric cell.

**Cycling test, open circuit potential measurement, and cyclic voltammetry test:** The cycling test was conducted between 1.6-2.7 V (vs. Li/Li<sup>+</sup>) using 1672 mAh g<sup>-1</sup> as the theoretical specific capacity. The cyclic voltammetry (CV) scanning rate was 0.1 mV s<sup>-1</sup> between 1.5-2.7 V using the Autolab PGSTAT302N electrochemical workstation. For the symmetric cell, the CV was performed at 10 mV s<sup>-1</sup> in the range of -1 V to 1 V. The electrochemical impedance spectroscopy (EIS) measurements were conducted on the same workstation with an amplitude of 5 mV and a frequency range of 10<sup>-2</sup> Hz-10<sup>5</sup>Hz.

### 6.3. Characterization results of the N-M@CNi interlayer and relevant analysis

**Figure 6.82** shows the process from the beginning MAX phase to the last N-M@CNi product. The aluminum layer was selectively etched from the MAX phase, resulting in the 2-D  $\text{Ti}_3\text{C}_2\text{T}_x$  material. After the delamination process, the resulted  $\text{Ti}_3\text{C}_2\text{T}_x$  suspension was mixed with  $\text{Ni}^{2+}$ , DCDA, and glucose successively, and the in-situ decoration of N-doped carbon nanosheet with nano-sized Ni particles was formed during the one-step annealing synthesis.

The morphology of the prepared N-M@CNi was characterized by SEM and TEM, as shown in **Figure 6.83**. The SEM image of N-M@CNi shows that the MXene sheets are coated with crumpled carbon nanosheets, which were formed during the annealing process. Meanwhile, the cross section in the insert exhibits compactly stacked MXene sheets. This comparison indicates the surface modification has prominent effect on preventing the self-stacking of MXene. Also, the specific surface area and porosity information of the N-M@CNi were measured by the nitrogen adsorption-desorption isotherm method (**Figure 6.84**). From the multi-point measurement, the specific surface area of N-M@CNi is  $101.8 \text{ m}^2 \text{ g}^{-1}$ , which is larger than the reported value of  $\text{Ti}_3\text{C}_2\text{T}_x$  powder ( $21.05 \text{ m}^2 \text{ g}^{-1}$ ) [16] or film ( $98 \text{ m}^2 \text{ g}^{-1}$ ) [17]. The nitrogen adsorption-desorption isotherm curve in **Figure 6.84a** was featured with a prominent H3 hysteresis loop, which was typical for type-IV curves. The surged adsorption nitrogen near  $0.0 P/P_0$  and the hysteresis during  $0.5$  to  $1.0 P/P_0$  are probably associated with the mesopores and macropores in the N-M@CNi [6, 7, 18]. On the contrary, the un-modified MXene powder (**Figure 6.84b**) is found to have much less specific area ( $41.4 \text{ m}^2 \text{ g}^{-1}$ ) and micropores volume than that of the N-M@CNi. Therefore, it can be proposed that the surface of N-M@CNi has been modified from the carbon nanosheets. A bright-field TEM image of the N-M@CNi (**Figure 6.83c**) shows that Ni nanoparticles are randomly distributed on carbon nanosheets, with their diameters ranging from 10 to 50 nm. These nanoparticles are formed during the annealing and wrapped by the carbon structure, as evidenced by the lattice fringes in the high-resolution transmission electron microscopy (HRTEM) (**Figure 6.83d**). The high-angle annular dark-field (HAADF) characterization and the EDS mapping were used to characterize the elemental distribution of the N-M@CNi. As exhibited from **Figure 6.83e**, the N element distributes evenly on the whole surface of the N-M@CNi, indicating an overall N-doping both in the carbon nanosheets and the  $\text{Ti}_3\text{C}_2\text{T}_x$  sheets is achieved. This is further confirmed by XPS in **Figure 6.86**. The clustered Ni nanoparticles in the Ni elemental mapping correspond to the high contrast points in the HAADF image,

which reflects the position of Ni nanoparticles is indeed within the carbon nanosheets.

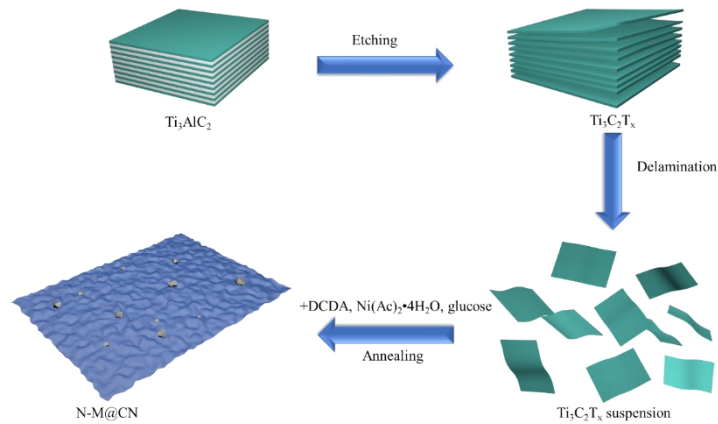


**Figure 6.82** The fabrication process of the N-doped MXene@carbon nanosheets-Ni (N-M@CNi).

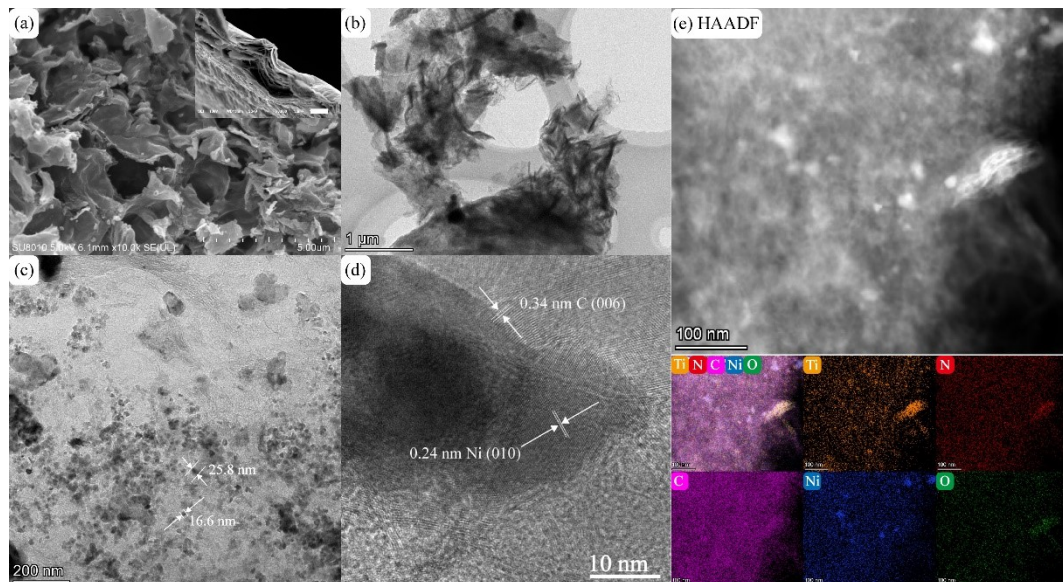


**Figure 6.83** (a) SEM image and (b) TEM bright-field image of N-M@CNi. The insert is a SEM cross-section of a  $\text{Ti}_3\text{C}_2\text{T}_x$  filtrated film (scale bar,  $5\mu\text{m}$ ). (c) The TEM bright-field image of the carbon nanosheets showing the Ni nanoparticles and their typical diameters. (d) The HRTEM image of the Ni and C lattice fringes. (e) HAADF images and corresponding elemental mapping of Ti, N, C, Ni, and O elements.

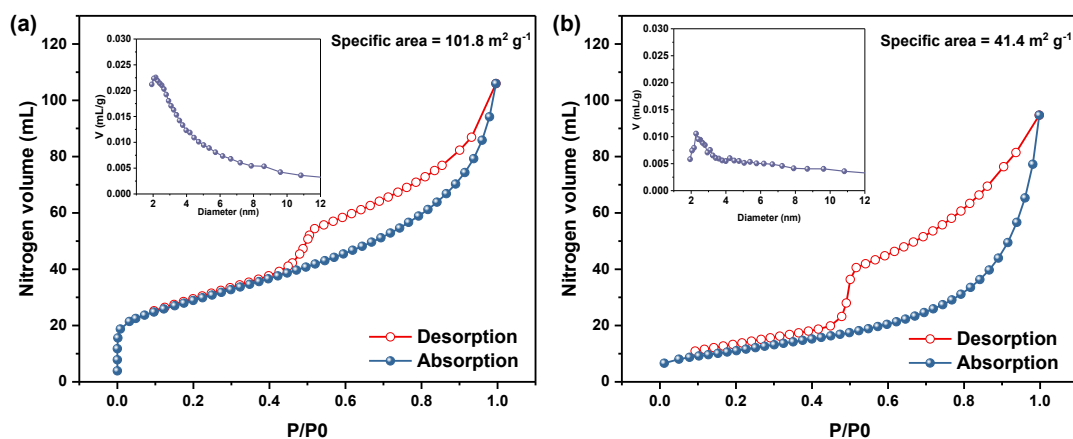


**Figure 6.84** Nitrogen adsorption-desorption isotherm of the (a) N-M@CNi and (b) MXene powder. The insert shows the pore size distribution acquired using the Barrett-Joyner-Halenda (BJH) method.

Further nanostructure analysis of the synthesized N-M@CNi was carried out by XRD and Raman spectrum, as shown in **Figure 6.85**. The XRD pattern of the pure  $\text{Ti}_3\text{C}_2\text{T}_x$  film shows only peaks of delaminated  $\text{Ti}_3\text{C}_2\text{T}_x$ , including the prominent (002) peak at  $6.8^\circ$ . This is a direct evidence of successful delamination of the  $\text{Ti}_3\text{C}_2\text{T}_x$  sheets [19]. For the pattern of the N-M@CNi sample, the low-angle shifted (002) peak reflects an enlarged interlayer spacing of the  $\text{Ti}_3\text{C}_2\text{T}_x$  sheets [20], indicating that the formation of the nitrogen-doped carbon nanosheets has a strong interaction with the MXene sheets' surface. The broad peaks at about  $17^\circ$ ,  $30^\circ$ , and  $43^\circ$  are assigned to a small amount of nanosized TiO (002), (111), and (220) planes, correspondingly (JCPDS card no. 23-1078). Also, two minor peaks at  $35^\circ$  and  $61^\circ$  could be the (111) and (220) planes for the TiC, respectively (JCPDS card no. 32-1383). Small amount of TiO and TiC are formed during the heating process. This is probably due to the conversion of the unstable Ti-O group on the MXene surface and the rearrangement of  $\text{Ti}_3\text{C}_2\text{T}_x$  after the detachment of surface groups, respectively. Two minor peaks at about  $44^\circ$  and  $51^\circ$  represent the (111) and (200) planes of Ni particles [21]. These two samples were further examined by Raman spectroscopy. As shown in **Figure 6.85b**, the bands at  $156\text{ cm}^{-1}$  (denoted by orange diamonds) are associated with the stretching vibration of the Ti-O bond [22, 23]. The enhanced band intensity of the N-M@CNi spectrum may be caused by the partial oxidation during annealing process. Three bands, denoted by green triangles ( $270$ ,  $401$ , and  $610\text{ cm}^{-1}$ ), are related to the  $E_g$  group vibrations, including the in-plane (shear) mode of Ti, C, and surface functional group atoms. The yellow circle marked band at  $703\text{ cm}^{-1}$  is indexed to the  $A_{1g}$  symmetry out-of-plane vibrations of Ti and C atoms [23-25]. At around  $1350\text{ cm}^{-1}$  and  $1580\text{ cm}^{-1}$ , two broad and weak bands (D and G) are identified in the  $\text{Ti}_3\text{C}_2\text{T}_x$  film spectrum, which can be explained by

some free carbon and the disorder of the sample [26]. Meanwhile, in the spectrum of N-M@CNi, the D and G become much more prominent, indicating the presence of graphitic carbon nanosheets [23, 27].

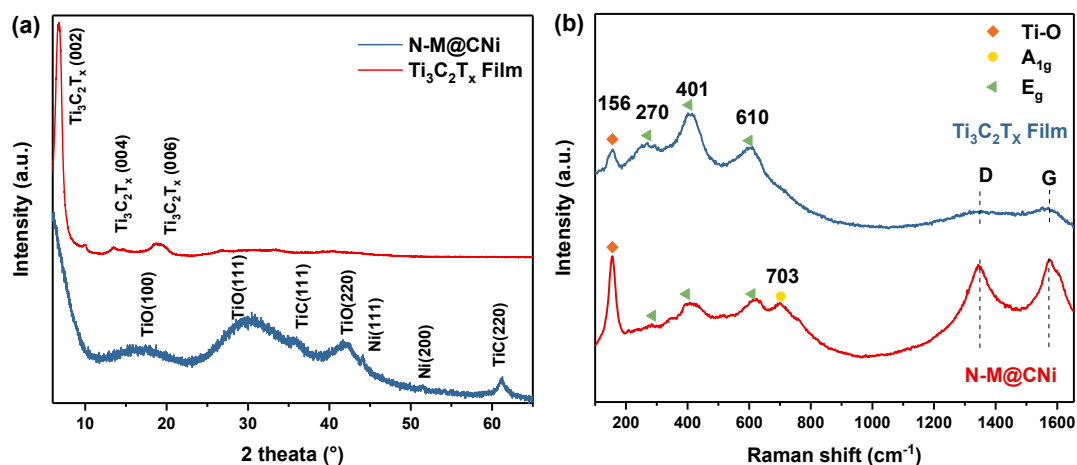


**Figure 6.85** (a) XRD patterns and the (b) Raman patterns of N-M@CNi powder and  $\text{Ti}_3\text{C}_2\text{T}_x$  film.

To further evaluate the N-doping in N-M@CNi, XPS analysis was conducted and the deconvoluted results of N 1s and Ti 2p spectra are shown in **Figure 6.86**. Deconvoluted peaks at 398.5 eV, 399.7 eV, 400.9 eV, and 397 eV are indexed as pyridinic N, pyrrolic N, graphitic N [28, 29], and N-Ti bond [6, 30] respectively. The Ti-N bond at 456.9 eV is further confirmed by the Ti 2p deconvoluted result (Figure 6.86b) [7]. It is clear that the N-doping is achieved both in carbon nanosheet and  $\text{Ti}_3\text{C}_2\text{T}_x$  in the N-M@CNi. The dual doping effect is essential for N-M@CNi to enhance the battery performance as a separator coating material, which is supported by previous reports. The N-doping in  $\text{sp}^2$  carbon materials is found not only facilitate the conductivity [31] but also absorb LiPS [32] and kinetically accelerate their conversion [8]. While compared to the pristine  $\text{Ti}_3\text{C}_2\text{T}_x$ , the N-doped  $\text{Ti}_3\text{C}_2\text{T}_x$  has higher chemical adsorption energy, preventing the diffusion of the dissolved polysulfide and consequently promoting the utilization of active material [6, 7].

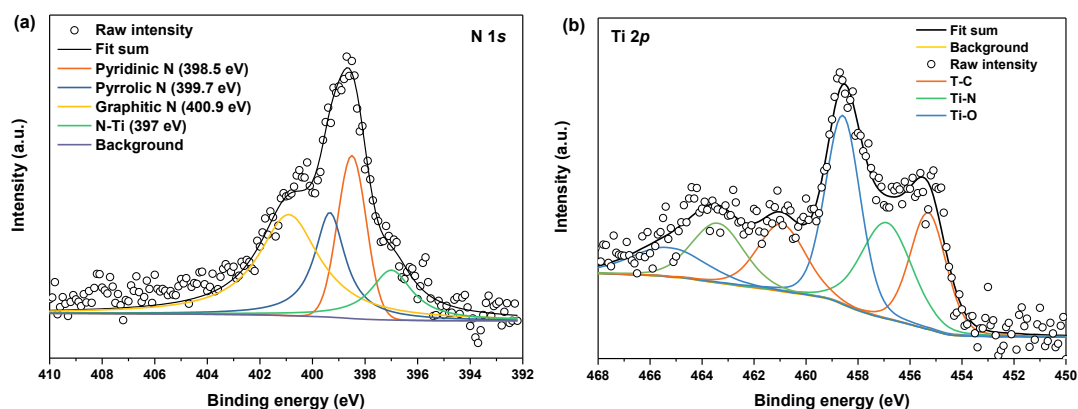


**Figure 6.86** The deconvoluted XPS of (a) N 1s and (b) Ti 2p of the N-M@CNi sample.

For Li-S batteries, one of the major challenges is the self-discharge problem induced by the shuttle effect. It is reported that almost 30 % capacity loses via self-discharge within hours [33], which is a severe drawback in practical application. In order to evaluate the effect of self-discharge on the N-M@CNi modified separator, an open circuit voltages (OCP) test was conducted on cells with CB and N-M@CNi modified separator, as well as the pristine cell with Celgard separator. The cell with pristine Celgard separator starts with an OCP of 2.25 V and ends at 2.15 V, experiencing the most severe potential variation rate of  $-6.16 \times 10^{-1} \text{ mV h}^{-1}$ . By comparing with the voltage of the first discharge plateau ( $\sim 2.3 \text{ V}$ ) in the following galvanostatic charge/discharge curves (**Figure 6.89a, b**), it is clear that a dramatic spontaneous reduction of elemental sulfur and high-order polysulfides occur in the pristine Li-S cell. The cell with the N-M@CNi separator presents the highest initial potential of 2.47 V among three cells and retains 2.42 V after over  $8 \times 10^5 \text{ s}$  (potential variation rate =  $-2.82 \times 10^{-1} \text{ mV h}^{-1}$ ), as shown in **Figure 6.87** (a) It also has a higher OCP value than those of bi-layer graphene film [34] and graphene oxide [33] interlayers at the same test duration. In contrast, the cell with CB modified separator shows an initial potential of 2.4 V and a rapid degrading is observed during the first  $0.5 \times 10^5 \text{ s}$ , ending in 2.35 V after only  $7 \times 10^5 \text{ s}$  ( $-3.95 \times 10^{-1} \text{ mV h}^{-1}$ ). This prominent anti-self-discharge effect of the N-M@CNi separator is due to its adsorption effect that effectively inhibits the loss of the LiPS.

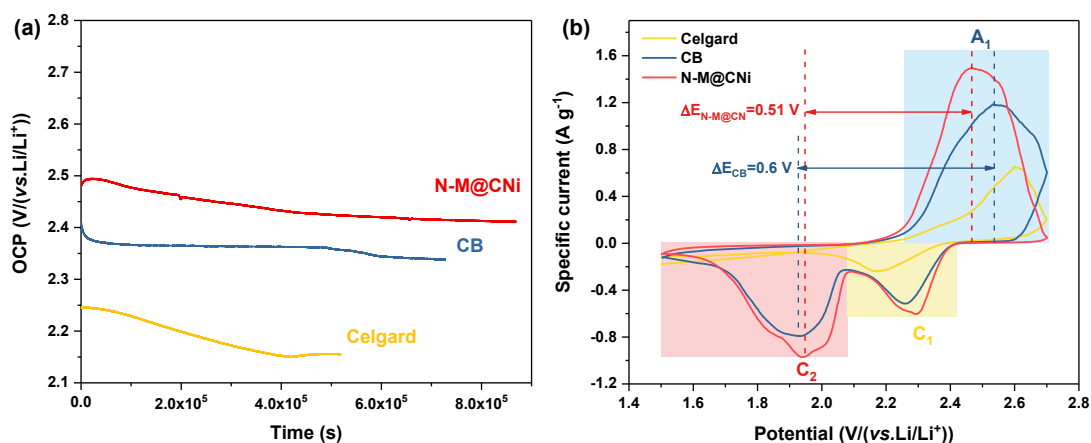


**Figure 6.87** (a) OCP test of cells with N-M@CNi or CB modified separator, or with pristine Celgard separator. (b) Cyclic voltammetry curves of cells with N-M@CNi or CB modified separator, or with pristine Celgard separator. The sulfur loading in the tested cathode was  $\sim 2.3 \text{ mg cm}^{-2}$ .

The electrochemical performance of different separators in Li-S cells were probed by the CV method, as shown in **Figure 6.87b**. The CV test was performed at a scan rate of  $0.1 \text{ mV s}^{-1}$  between 1.5 and 2.8 V. Cells with CB and N-M@CNi separators contain two cathodic peaks (C<sub>1</sub> and C<sub>2</sub>) and one anodic peak (A<sub>1</sub>). The A<sub>1</sub> peak corresponds to the oxidation of the Li<sub>2</sub>S<sub>2</sub>/Li<sub>2</sub>S to sulfur, while the C<sub>1</sub> and C<sub>2</sub> represent the reduction of the sulfur to high-order LiPS and the formation of Li<sub>2</sub>S<sub>2</sub>/Li<sub>2</sub>S [35]. The pristine cell with Celgard separator shows only one anodic peak and one cathodic peak. The C<sub>2</sub> peak is shifted beyond the voltage window [36, 37]. The second step reduction in the high sulfur loading electrode is retarded because the insulating high-order LiPS is accumulating through the reaction, causing great polarization of the cell. To evaluate the redox kinetics of the cell [36, 38, 39], we also calculated the potential difference between anodic peak and the cathodic peak. As shown by the potential difference ΔE between A<sub>1</sub> and C<sub>2</sub> in Figure 4b, the ΔE<sub>N-M@CNi</sub> is smaller than ΔE<sub>CB</sub>. Therefore, it is clear that the N-M@CNi cell facilitates a better kinetic than that of the CB cell.

A CV test of symmetric cells was used to evaluate the redox conversion kinetic of LiPS on the coating material of the separator. At a scanning rate of  $10 \text{ mV s}^{-1}$  as seen in **Figure 6.88**, it is clearly observed that the N-M@CNi modified separator has a higher current than the CB ones at the same potential, while the Celgard separator displays almost no current variation during the voltage window. This comparison indicates a very fast electrochemical reaction of the LiPS on the N-M@CNi coating, as a result from the co-operation of the stronger LiPS absorption as well as the low charge transfer resistance (as presented by the insert in **Figure 6.88a**, where the electronic resistance of N-M@CNi separator is almost two orders of magnitude lower than that of the CB) [40].

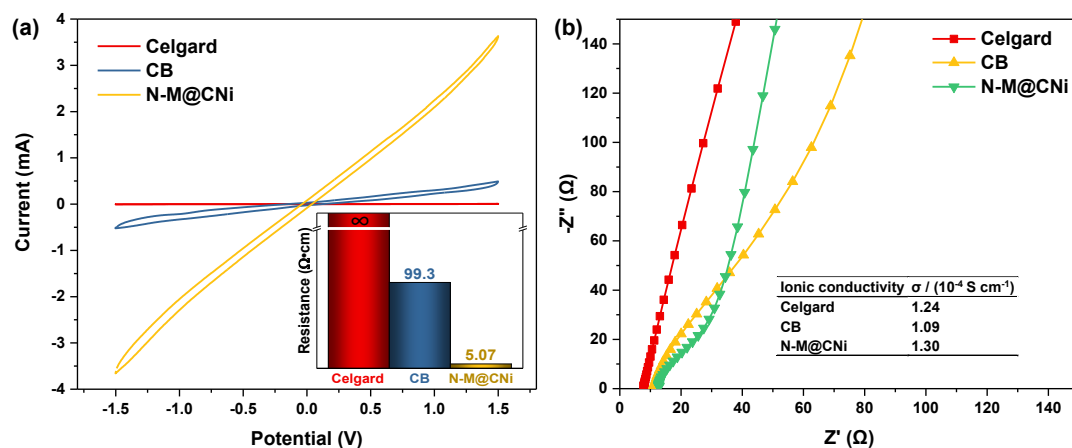


**Figure 6.88** (a) The CV of the symmetric cells (coating/Celgard/Celgard/coating) with different separators. The insert shows the resistance of different separators measured by the four-probe method. (b) The impedance plots of the stainless steel/modified separator/ stainless steel cells with different separators. The insert table summarizes the calculated ionic conductivity values of the Celgard, the CB and the N-M@CNi separators.

Apart from the electronic conductivity, the ionic conductivity was calculated from the impedance of the cell containing only the modified separator as the electrode. Unlike the typical plots consisting of a high-frequency semicircle and a low-frequency straight line, the impedance plots of these modified separators show almost only the straight-line part. This indicates that nearly all the charge carriers in these cells are ions [3]. Therefore, the ionic conductivity of the liquid could be calculated via the **Equation 6.17** [41]:

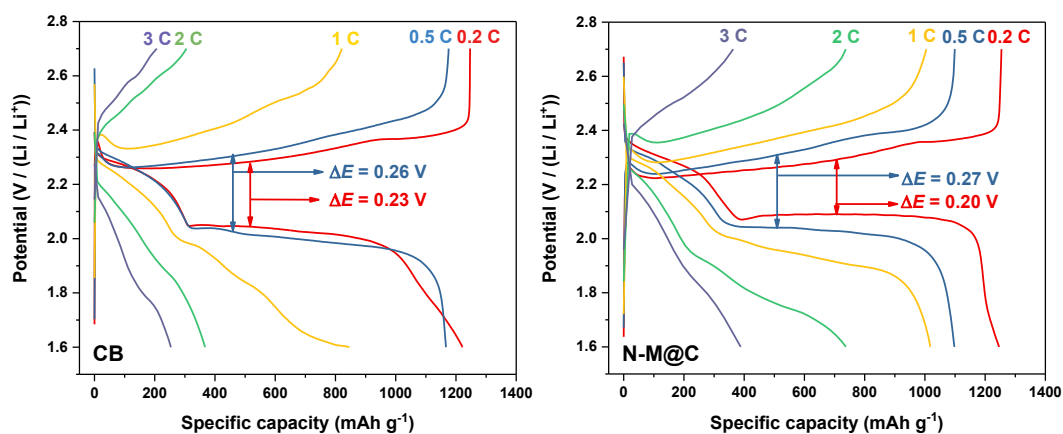
$$\sigma = I/(R_b A) \text{ (in S cm}^{-1}\text{)}$$

**Equation 6.17**

where  $\sigma$  is the ionic conductivity,  $I$  is the thickness of the separator,  $R_b$  is the bulk resistance which can be obtained from the intercept of the fitted straight line on the real axis ( $Z'$ ), and  $A$  represents the area of the stainless steel disc since the separator is larger than that of the stainless steel disc. The ionic conductivity is  $1.30 \times 10^{-4} \text{ S cm}^{-1}$  for the N-M@CNi separator, slightly higher than that of the CB ( $1.09 \times 10^{-4} \text{ S cm}^{-1}$ ) and the Celgard separators ( $1.24 \times 10^{-4} \text{ S cm}^{-1}$ ). These data confirm that the ionic conductivity of the N-M@CNi separator is at the same level as the commercial Celgard ones, which has no negative effect of the ionic transportation in the Li-S battery. This feature, along with the better electron conductivity of the N-M@CNi separator, is a crucial basis for the enhanced performance of the N-M@CNi battery at the high current rate, as discussed in the following part.

To highlight the improved electrochemical performance of the N-M@CNi separator, galvanostatic

discharge/charge profiles of cells with CB, N-M@C and N-M@CNi separators are compared and evaluated at different current rates (**Figure 6.89a-c**), and their rate performances are shown in **Figure 6.89d**. The pristine Celgard cell only delivers capacities of 964 mAh g<sup>-1</sup> and 790 mAh g<sup>-1</sup> at 0.2 C and 0.5 C and dived to 174 mAh g<sup>-1</sup> at 1 C respectively. At 2 C rate, it provides little capacity and eventually fails at a higher rate. For cells with modified separators, the CB cell shows similar specific capacity values with the N-M@CNi and N-M@C ones at low current rates (0.2 C and 0.5 C). The cycling performance of these cells at 0.2 C also exhibits the same tendency (**Figure S4**). Nevertheless, the Coulombic efficiency tendency during these 100 cycles indicates that N-M@CNi and N-M@C have stronger ability to inhibit shuttle effect than the pure CB. The N-M@CNi separator also has smaller potential hysteresis (represented by  $\Delta E$  in **Figure 6.89a, b**, the overpotential between the oxidation and the lower reduction plateaus) than the CB and N-M@C ones [18]. When the current is boosted to higher rates (i.e. 1 C, 2 C, and 3 C), the CB separator delivers much lower capacity than the N-M@CNi ones (846 mAh g<sup>-1</sup>, 367 mAh g<sup>-1</sup>, and 253 mAh g<sup>-1</sup>, compared with 1051 mAh g<sup>-1</sup>, 907 mAh g<sup>-1</sup>, and 538 mAh g<sup>-1</sup>, respectively). The N-M@C cell shows more pronounced lower capacity than that of N-M@CNi cell at higher current density (2 C and 3 C), suggesting that the Ni nano-particle plays a crucial role in boosting the redox at higher current density (**Figure 6.89d**). In addition, the potential hysteresis ( $\Delta E$ ) of the CB and N-M@C cell increases at these high currents, along with the diminishing of discharge/charge plateaus (**Figure 6.89a**). Meanwhile, the discharge/charge plateaus in the N-M@CNi cell remains distinguishable at the same current rates. This result is in good agreement with the rate test data. Therefore, from these analysis it can conclude that the N-M@CNi separator is superior to the CB and N-M@C separator in electrochemistry kinetics, facilitating the redox within a wide range of current rates.



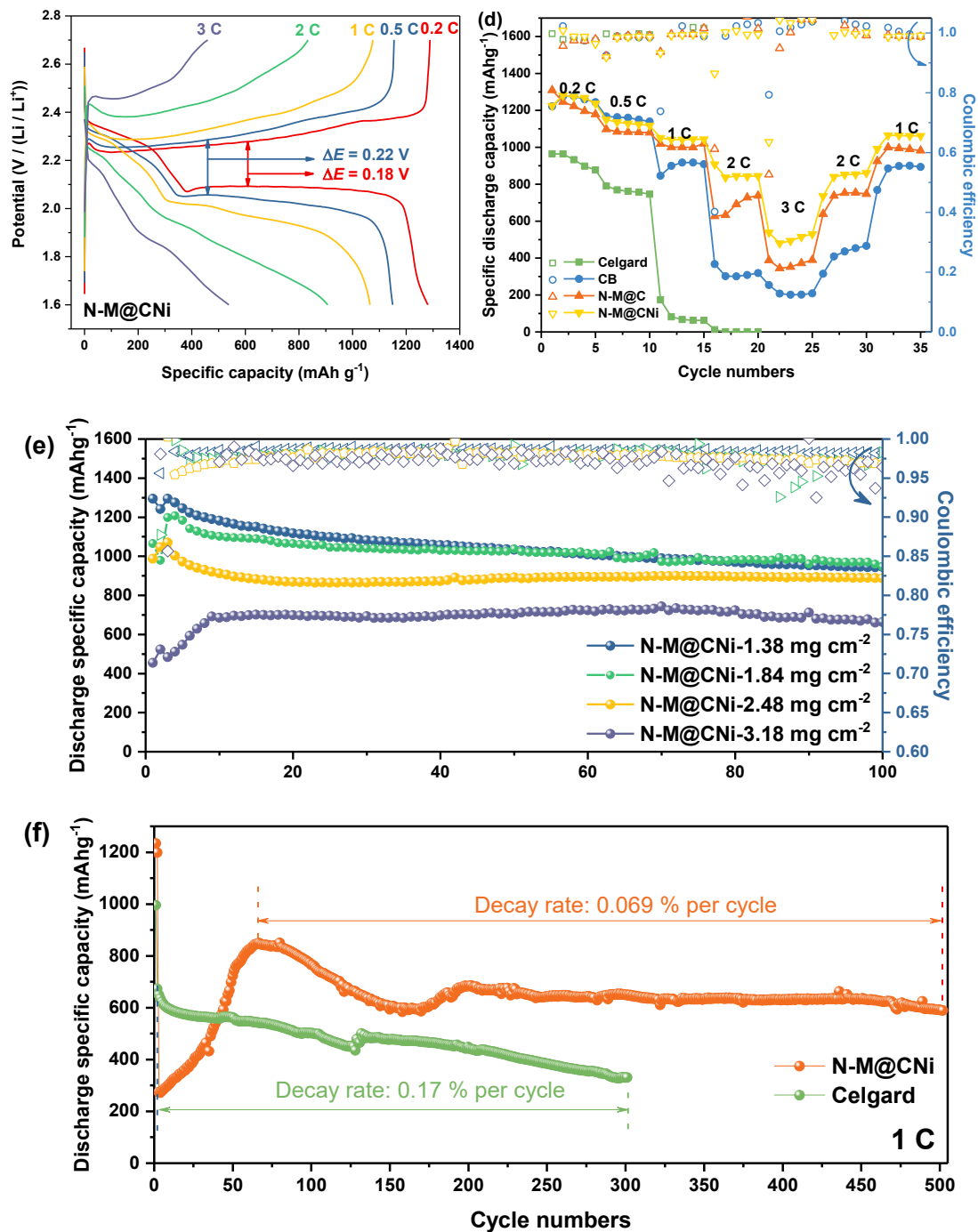


**Figure 6.89** The typical galvanostatic charge and discharge (GCD) curves of (a) CB, (b) N-M@C and (c) N-M@C/Ni cells at 0.2 C, 0.5 C, 1 C, 2 C, and 3 C. The rate performance (d) of the Celgard, the CB, the N-M@C and the N-M@C/Ni cells at a current of 0.2 C. (e) The cycling performance comparison of N-M@C/Ni cells with different sulfur mass loading cathodes at 0.2 C. (f) The long-term cycling performance of Celgard and N-M@C/Ni cells at 1 C.

Whilst the CB cell displays similar specific discharge capacity with that of the N-M@C/Ni cell at 0.2 C, the cycling stability of these two is observed a noticeable distinction at 0.2 C, as plotted in **Figure 6.89c**. Both N-M@C/Ni and CB cells start from  $\sim 1300$  mAh g<sup>-1</sup> and are stabilized at  $\sim 940$  mAh g<sup>-1</sup> after

100 cycles, during this period the pristine Celgard cell drops from 900 to 640 mAh g<sup>-1</sup>. The main difference lies in the coating used here, showing the effective promotion in sulfur utilization and cycling stabilization. Despite similar cycling capacity performance, the Coulombic efficiency of the CB cell gradually deviates from the N-M@CNi ones as the cycle continues. Unlike the N-M@CNi cell having a steady efficiency of 98–99 % throughout the whole 100 cycles, the Celgard cell and the CB cell suffer from a continuing degradation, shrinking from the initial ~ 99 % to ~ 90 % and ~ 96 %, respectively. This striking difference in the Coulombic efficiency provides an intuitive proof that the N-M@CNi has a fairly strong ability to prohibit the shuttle effect, which was the direct rationale for the Coulombic efficiency preservation [42].

To check its polysulfides-inhibiting ability on cathode with different sulfur mass loading, the N-M@CNi separator was applied to cathodes with areal sulfur loading ranging from 1.38 to 3.18 mg cm<sup>-2</sup>, and the corresponding cycling performance at 0.2 C is shown in **Figure 6.89e**. For cathodes with 1.38 and 1.84 mg cm<sup>-2</sup> sulfur loading, similar cycling performance is observed for 100 cycles. Meanwhile, the 2.48 mg cm<sup>-2</sup> cathode delivers a maximum capacity of 1070 mAh g<sup>-1</sup>, which is lower than those of the former two cathodes. However, a good capacity retention of 888 mAh g<sup>-1</sup> after 100 cycles is achieved, merely ~ 55 mAh g<sup>-1</sup> lower than those of lower sulfur loading electrodes. This performance on sulfur loading adaptability is superior to previously reported pure MXene modified separator [1]. When the areal density of sulfur surged to 3.18 mg cm<sup>-2</sup>, the maximum capacity drops to 691 mAh g<sup>-1</sup>. Nevertheless, its capacity remains fairly steady and the value is kept at 662 mAh g<sup>-1</sup> after 100 cycles, giving a capacity decay rate of 0.043 % per cycle with a high retention of 95.8 %. For the long term high rate cycling performance, the N-M@CNi separator also provides considerable improvement for the S/C electrode (Figure 6.89f). After a period of full activation process (meaning the LiPS continuous dissolution and adsorption at a high current rate [43]), the N-M@CNi cell exhibits a peak capacity of 848 mAh g<sup>-1</sup> and retains 588 mAh g<sup>-1</sup> after 500 cycles. This gives a capacity decay rate only 0.069 % per cycle. The cycling performance at 1 C is better than the reported pure Ti<sub>3</sub>C<sub>2</sub>T<sub>x</sub> modified separator [1] and many other separators modified with other composites [44, 45]. During this time the pristine Celgard cell drops from 672 to 330 mAh g<sup>-1</sup> after only 300 cycles, showing a 0.17 % decay rate per cycle. Consequently, adding the N-M@CNi separator offers a better long-term stability with strong LiPS absorption and enhances sulfur utilization at a high rate. On the other hand, the performance of the N-M@CNi separator on cathodes with different mass loading confirms its good capability of different sulfur

loading adaption. It is expected that the N-M@CNi separator might open up its potential on the cathode with more advanced sulfur-containing materials for higher demands of sulfur mass loading, facilitating the practical application of the Li-S batteries.

The electrochemical impedance spectroscopy (EIS) of Celgard, CB, and N-M@CNi cells was conducted before and after the cycling test, in order to gain better insight into the N-M@CNi separator. All curves are composed of a semi-circle at high frequency and a subsequent oblique line at low frequency. The relevant Nyquist plot is shown in Figure 6.90. The semi-circle representing the charge transfer resistance ( $R_{ct}$ ) [46] follows the sequence of Celgard > CB > N-M@CNi. This impedance ranking is a direct result of the higher conductivity of the N-M@CNi than the other two separators, which is beneficial to optimize the localized charge transfer of sulfur species [47]. After a ten-time-cycle, cells with the interlayer display a shrank semicircle, indicating the cathode impedance is ameliorated. This is explained by the diffused sulfur species from cathode to the interlayer are re-arranged at more electrochemical facilitated sites, thus the charge transfer of the active materials is reduced [48, 49]. However, for the Celgard one, no obvious change is observed from  $R_{ct}$ . An extra medium-frequency semi-circle appears after cycles, probably due to the precipitation of  $Li_2S_2/Li_2S$  layer on the cathode surface at the absence of conductive interlayer [50]. It is worth noting that after cycling the N-M@CNi cell presents much lower impedance than that of the CB cell, demonstrating its superior polysulfide-adsorption performance than the later ones. Further characterization of the cycled N-M@CNi can be found in the deconvoluted XPS results (**Figure 6.91**), in which the S 2*p* and Ti 2*p* spectra illustrate the presence of the sulfur species and the Ti-S bond. The polythionate and the thiosulfate peaks in **Figure 6.91a** are caused by the residual LiTFSI in the electrolyte and the surface redox between N-M@CNi and the polysulfides [7]. The Ti-S bond indicates the chemical adsorption by the N-M@CNi. All these results confirm an occurrence of the LiPS adsorption during the cycling process.

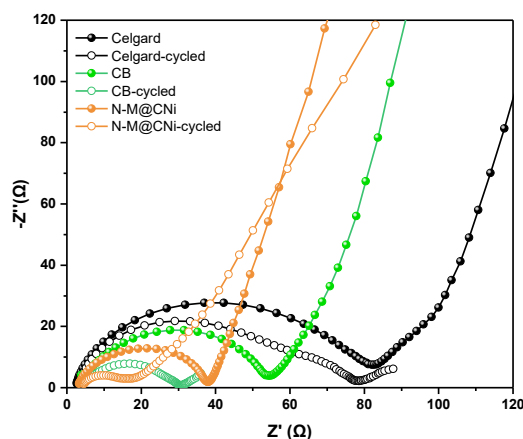


**Figure 6.90** The EIS plots of Celgard, CB, and N-M@CNi cells before (solid dots) and after 10 cycles (hollow dots) at 0.2 C.

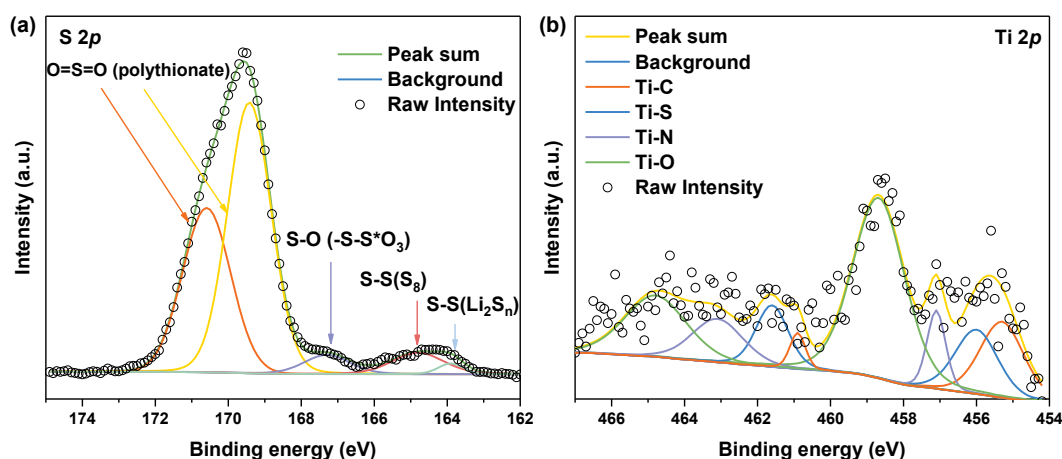


**Figure 6.91** The deconvoluted XPS of the cycled N-M@CNi separator: (a) S 2p and (b) Ti 2p. The adsorption of LiPS and the presence of the Ti-S bond are demonstrated in the deconvoluted results.

#### 6.4. Conclusions

In summary, the N-doped  $\text{Ti}_3\text{C}_2\text{T}_x$ @carbon nanosheets-Ni composite was synthesized as a separator-coating material for improved capacity and cycling stability in Li-S cells. The modified surface and the N-doped structure provide strong LiPS adsorption ability and high conductivity. Using the N-M@CNi separator in the cathode of Li-S cell offers greater sulfur utilization, better high-rate adaptability, and more stable cycling performance compared to the Celgard and CB cells. At 0.2 C the cell with N-M@CNi separator delivers an initial capacity of  $1294 \text{ mAh g}^{-1}$  and  $943 \text{ mAh g}^{-1}$  after 100 cycles. When the current at a high value of 1 C, a steady capacity of  $588 \text{ mAh g}^{-1}$  is acquired after 500 cycles with a low capacity decay rate of 0.069 % per cycle. This work may provide a feasible approach of separator modification materials toward improved stable Li-S cells.

## 6.5. References

- [1] Song, Su, Xie, Guo, Bao, Shao, and Wang, *Immobilizing Polysulfides with MXene-Functionalized Separators for Stable Lithium-Sulfur Batteries*. ACS Applied Materials and Interfaces, 2016,**8** (43): p. 29427-29433.
- [2] Wang, Zhai, Zhao, Li, Yang, Zhang, and Huang, *Laminar MXene-Nafion-modified separator with highly inhibited shuttle effect for long-life lithium-sulfur batteries*. Electrochimica Acta, 2019,**320** p. 134558.
- [3] Sun, Sun, Peng, Wang, Ge, Akhtar, Huang, and Wang, *Nano-MgO/AB decorated separator to suppress shuttle effect of lithium-sulfur battery*. Nanoscale Advances, 2019,**1** (4): p. 1589-1597.
- [4] Qiu, An, Yan, Xu, Zhang, Guo, Wang, Zheng, Wang, Deng, and Li, *Suppressed polysulfide shuttling and improved Li<sup>+</sup> transport in Li-S batteries enabled by NbN modified PP separator*. Journal of Power Sources, 2019,**423** p. 98-105.
- [5] Yin, Dou, Wang, Xu, Nie, Chang, and Zhang, *A Functional Interlayer as a Polysulfides Blocking Layer For High-performance Lithium-sulfur Batteries*. New Journal of Chemistry, 2018,**42** (2): p. 1431-1436.
- [6] Bao, Liu, Wang, Choi, Wang, and Wang, *Facile Synthesis of Crumpled Nitrogen-Doped MXene Nanosheets as a New Sulfur Host for Lithium-Sulfur Batteries*. Advanced Energy Materials, 2018,**8** (13): p. 1702485.
- [7] Jiang, Zheng, Chen, Ding, Li, Sun, and Li, *In-situ decoration of MOF-derived carbon on nitrogen-doped ultrathin MXene nanosheets to multifunctionalize separators for stable Li-S batteries*. Chemical Engineering Journal, 2019,**373** p. 1309-1318.
- [8] Du, Wu, Yang, Wang, Che, Lyu, Chen, Wang, and Hu, *Efficient synergism of electrocatalysis and physical confinement leading to durable high-power lithium-sulfur batteries*. Nano Energy, 2019,**57** p. 34-40.
- [9] Yu, Zhou, Wang, Wang, Zhang, Wang, Zhao, and Qiu, *Accelerating polysulfide redox conversion on bifunctional electrocatalytic electrode for stable Li-S batteries*. Energy Storage Materials, 2019,**20** p. 98-107.
- [10] Li, Fan, Zhang, Yang, Yuan, Chang, Zheng, and Dong, *A Honeycomb-like Co@N-C Composite for Ultrahigh Sulfur Loading Li-S Batteries*. ACS Nano, 2017,**11** (11): p. 11417-11424.

- [11] Du, Chen, Hu, Chuang, Xie, Hu, Yan, Kong, Wu, Ji, and Wan, *Cobalt in Nitrogen-Doped Graphene as Single-Atom Catalyst for High-Sulfur Content Lithium–Sulfur Batteries*. Journal of the American Chemical Society, 2019,**141** (9): p. 3977-3985.
- [12] Zhang, Sheng, Wang, Chou, Davey, Dou, and Qiao, *Long-Life Room-Temperature Sodium-Sulfur Batteries by Virtue of Transition-Metal-Nanocluster-Sulfur Interactions*. Angew Chem Int Ed Engl, 2019,**58** (5): p. 1484-1488.
- [13] Babu, Ababtain, Ng, and Arava, *Electrocatalysis of lithium polysulfides: current collectors as electrodes in Li/S battery configuration*. Scientific Reports, 2015,**5** p. 8763.
- [14] Al Salem, Babu, V. Rao, and Arava, *Electrocatalytic Polysulfide Traps for Controlling Redox Shuttle Process of Li–S Batteries*. Journal of the American Chemical Society, 2015,**137** (36): p. 11542-11545.
- [15] Jiao, Zhang, Geng, Wu, Li, Lv, Tao, Chen, Zhou, Li, Ling, Wan, and Yang, *Capture and Catalytic Conversion of Polysulfides by In Situ Built TiO<sub>2</sub>-MXene Heterostructures for Lithium–Sulfur Batteries*. Advanced Energy Materials, 2019,p. 1900219.
- [16] Rakhi, Ahmed, Hedhili, Anjum, and Alshareef, *Effect of Postetch Annealing Gas Composition on the Structural and Electrochemical Properties of Ti<sub>2</sub>CT<sub>x</sub> MXene Electrodes for Supercapacitor Applications*. Chemistry of Materials, 2015,**27** (15): p. 5314-5323.
- [17] Lukatskaya, Mashtalir, Ren, Dall'Agnesse, Rozier, Taberna, Naguib, Simon, Barsoum, and Gogotsi, *Cation intercalation and high volumetric capacitance of two-dimensional titanium carbide*. Science, 2013,**341** (6153): p. 1502-1505.
- [18] Zhang, Qi, Zhang, Zheng, Chen, Zhou, Tian, Zhang, and Sun, *Self-Assembled 3D MnO<sub>2</sub> Nanosheets@Delaminated-Ti<sub>3</sub>C<sub>2</sub> Aerogel as Sulfur Host for Lithium–Sulfur Battery Cathodes*. ACS Applied Energy Materials, 2018,**2** (1): p. 705-714.
- [19] Mashtalir, Naguib, Mochalin, Dall'Agnesse, Heon, Barsoum, and Gogotsi, *Intercalation and delamination of layered carbides and carbonitrides*. Nature Communications, 2013,**4** (1): p. 1716.
- [20] Liu, Zhang, Sun, Liu, Liu, Zhou, and Yu, *Hydrophobic, Flexible, and Lightweight MXene Foams for High-Performance Electromagnetic-Interference Shielding*. Advanced Materials (Weinheim, Germany), 2017,**29** (38): p. 1702367.
- [21] Jiang, Zhou, and Liu, *A non-polarity flexible asymmetric supercapacitor with nickel*

- nanoparticle@ carbon nanotube three-dimensional network electrodes*. Energy Storage Materials, 2018,**11** p. 75-82.
- [22] Deng, Shang, Wu, Tao, Luo, Liang, Han, Lyu, Qi, Lv, Kang, and Yang, *Fast Gelation of  $Ti_3C_2T_x$  MXene Initiated by Metal Ions*. Advanced Materials, 2019,**31** (43): p. 1902432.
- [23] Naguib, Mashtalir, Lukatskaya, Dyatkin, Zhang, Presser, Gogotsi, and Barsoum, *One-step synthesis of nanocrystalline transition metal oxides on thin sheets of disordered graphitic carbon by oxidation of MXenes*. Chemical Communications, 2014,**50** (56): p. 7420-7423.
- [24] Yan, Ren, Maleski, Hatter, Anasori, Urbankowski, Sarycheva, and Gogotsi, *Flexible MXene/Graphene Films for Ultrafast Supercapacitors with Outstanding Volumetric Capacitance*. Advanced Functional Materials, 2017,**27** (30): p. 1701264.
- [25] Zhao, Xu, Hui, Sun, Yu, Xue, Zhou, Wang, Dai, Zhao, Yang, Zhou, Chen, Sun, and Huang, *Electrostatically Assembling 2D Nanosheets of MXene and MOF-Derivatives into 3D Hollow Frameworks for Enhanced Lithium Storage*. Small, 2019,**15** (47): p. 1904255.
- [26] Melchior, Raju, Ike, Erasmus, Kabongo, Sigalas, Iyuke, and Ozoemena, *High-Voltage Symmetric Supercapacitor Based on 2D Titanium Carbide (MXene,  $Ti_2CT_x$ )/Carbon Nanosphere Composites in a Neutral Aqueous Electrolyte*. Journal of the Electrochemical Society, 2018,**165** (3): p. A501-A511.
- [27] Peng, Lu, Zhou, Sheng, Shen, Liao, Huang, Li, and Sun, *Graphitized porous carbon materials with high sulfur loading for lithium-sulfur batteries*. Nano Energy, 2017,**32** p. 503-510.
- [28] Yu, Yi, Yang, and Chen, *An easy synthesis of Ni-Co doped hollow C-N tubular nanocomposites as excellent cathodic catalysts of alkaline and neutral zinc-air batteries*. Science China Materials, 2019,**62** (9): p. 1251-1264.
- [29] Yu, Yi, Li, Chen, and Yang, *FeCo-Doped Hollow Bamboo-Like C-N Composites as Cathodic Catalysts for Zinc-Air Battery in Neutral Media*. Journal of the Electrochemical Society, 2018,**165** (11): p. A2502-A2509.
- [30] Yang, Zheng, Zhang, Chen, Zhang, Tian, and Sun, *Freestanding nitrogen-doped  $d-Ti_3C_2$ /reduced graphene oxide hybrid films for high performance supercapacitors*. Electrochimica Acta, 2019,**300** p. 349-356.
- [31] Wiggins-Camacho and Stevenson, *Effect of Nitrogen Concentration on Capacitance, Density of States, Electronic Conductivity, and Morphology of N-Doped Carbon Nanotube Electrodes*.

- The Journal of Physical Chemistry C, 2009,**113** (44): p. 19082-19090.
- [32] Yin, Liang, Zhou, Li, Saito, and Cheng, *Understanding the interactions between lithium polysulfides and N-doped graphene using density functional theory calculations*. Nano Energy, 2016,**25** p. 203-210.
- [33] Huang, Zhuang, Zhang, Peng, Chen, and Wei, *Permselective graphene oxide membrane for highly stable and anti-self-discharge lithium-sulfur batteries*. ACS Nano, 2015,**9** (3): p. 3002-3011.
- [34] Du, Guo, Wang, Hu, Jin, Zhang, Jin, Qi, Xin, Kong, Guo, Ji, and Wan, *Atom-Thick Interlayer Made of CVD-Grown Graphene Film on Separator for Advanced Lithium-Sulfur Batteries*. ACS Applied Materials and Interfaces, 2017,**9** (50): p. 43696-43703.
- [35] Kou, Li, Liu, Zhang, Yang, Jiang, He, Dai, Zheng, and Yu, *Triple-Layered Carbon-SiO<sub>2</sub> Composite Membrane for High Energy Density and Long Cycling Li-S Batteries*. ACS Nano, 2019,**13** (5): p. 5900-5909.
- [36] Zhao, Zhu, An, Chen, Sun, Wu, and Xu, *A 3D Conductive Carbon Interlayer with Ultrahigh Adsorption Capability for Lithium-sulfur Batteries*. Applied Surface Science, 2018,**440** p. 770-777.
- [37] Zeng, Huang, Zhang, Zhang, Wu, and Chen, *Long-life and High-areal-capacity Lithium-sulfur Batteries Realized by a Honeycomb-like N, P Dual-doped Carbon Modified Separator*. Chemical Engineering Journal, 2018,**349** p. 327-337.
- [38] Hong, Song, Yang, Tan, Li, Cai, and Wang, *Cerium Based Metal-Organic Frameworks as an Efficient Separator Coating Catalyzing the Conversion of Polysulfides for High Performance Lithium-Sulfur Batteries*. ACS Nano, 2019,**13** (2): p. 1923-1931.
- [39] Shao, Wang, Zhang, Wang, Chen, and Huang, *Nano-TiO<sub>2</sub> decorated carbon coating on the separator to physically and chemically suppress the shuttle effect for lithium-sulfur battery*. Journal of Power Sources, 2018,**378** p. 537-545.
- [40] Zhong, Yin, He, Liu, Wu, and Wang, *Surface Chemistry in Cobalt Phosphide-Stabilized Lithium-Sulfur Batteries*. Journal of the American Chemical Society, 2018,**140** (4): p. 1455-1459.
- [41] Zhu, Xiao, Shi, Yang, Hou, and Wu, *A Composite Gel Polymer Electrolyte with High Performance Based on Poly(Vinylidene Fluoride) and Polyborate for Lithium Ion Batteries*.

- Advanced Energy Materials, 2014,**4** (1): p. 1300647.
- [42] Lim, Kim, Jo, and Lee, *A Comprehensive Review of Materials with Catalytic Effects in Li-S Batteries: Enhanced Redox Kinetics*. Angewandte Chemie International Edition, 2019,**58** (52): p. 18746-18757.
- [43] Wang, Wang, and Chen, *Reduced graphene oxide film as a shuttle-inhibiting interlayer in a lithium-sulfur battery*. Journal of Power Sources, 2013,**242** p. 65-69.
- [44] Tan, Li, Wang, Guo, and Wang, *Lightweight Reduced Graphene Oxide@MoS<sub>2</sub> Interlayer as Polysulfide Barrier for High-Performance Lithium-Sulfur Batteries*. ACS Applied Materials & Interfaces, 2018,**10** (4): p. 3707-3713.
- [45] Dong, Zheng, Qin, Zhao, Shi, Wang, Chen, and Wu, *All-MXene-Based Integrated Electrode Constructed by Ti<sub>3</sub>C<sub>2</sub> Nanoribbon Framework Host and Nanosheet Interlayer for High-Energy-Density Li-S Batteries*. ACS Nano, 2018,**12** (3): p. 2381-2388.
- [46] Li, Chen, Chen, Hu, Wang, Sun, Sun, and Li, *From interlayer to lightweight capping layer: Rational design of mesoporous TiO<sub>2</sub> threaded with CNTs for advanced Li-S batteries*. Carbon, 2019,**143** p. 523-530.
- [47] He, Chen, and Manthiram, *Vertical Co<sub>9</sub>S<sub>8</sub> hollow nanowall arrays grown on a Celgard separator as a multifunctional polysulfide barrier for high-performance Li-S batteries*. Energy & Environmental Science, 2018,**11** (9): p. 2560-2568.
- [48] Huang, Zhang, Xu, Abouali, Akbari Garakani, Huang, and Kim, *Novel interlayer made from Fe<sub>3</sub>C/carbon nanofiber webs for high performance lithium-sulfur batteries*. Journal of Power Sources, 2015,**285** p. 43-50.
- [49] Huang, Xu, Abouali, Akbari Garakani, and Kim, *Porous graphene oxide/carbon nanotube hybrid films as interlayer for lithium-sulfur batteries*. Carbon, 2016,**99** p. 624-632.
- [50] Yao, Yan, Li, Zheng, Kong, Seh, Narasimhan, Liang, and Cui, *Improved Lithium-sulfur Batteries with A Conductive Coating on the Separator to Prevent the Accumulation of Inactive S-related Species at the Cathode-separator Interface*. Energy & Environmental Science, 2014,**7** (10): p. 3381-3390.

## Chapter 7 Conclusion and perspective

This thesis addresses the critical cathodic issues in Li-S batteries by the interlayer design and fabrication. Being fabricated from conductive carbon materials and  $Ti_3C_2T_x$ , these dual-functional interlayers not only provide extra electronic enhancement for the cathode but also act as the reservoir of the dissolved polysulfide. The present research demonstrates that adding an interlayer in the battery is an effective way to enhance the electrochemical performance compared with the one without the interlayer.

For the first attempt, a carbon black-based CB/PEDOT:PSS modified separator was proposed and fabricated using a facile one-step physical approach which favors practical production, due to its low-cost and scalable process. This dual-functional modified separator provides both physical and chemical absorption. Besides, the Li-ion diffusion coefficient calculation shows this modification coating promotes chemical kinetic by enhancing Li-ion diffusion. As a result, the primitive S-C electrode with sulfur loading of  $1.6 \text{ mg cm}^{-2}$  exhibits a high initial capacity of  $1315 \text{ mAh g}^{-1}$  at  $0.2 \text{ C}$  after the application of modified separator, maintaining a retention of  $956 \text{ mAh g}^{-1}$  after 100 cycles. Even after 260 cycles at  $1 \text{ C}$ , this modified cell still holds a considerable capacity of  $674 \text{ mAh g}^{-1}$ .

While a desirable specific capacity may be achieved through the CB/PEDOT:PSS coating, it requires a high mass density interlayer (carbon black has a low specific surface area less than  $80 \text{ m}^2 \text{ g}$ ), hence the overall energy density based on the mass of the whole battery components may be deteriorated. In order to provide more polysulfides-absorption area with less mass addition, a light material with the higher specific surface area is essential. In Chapter 4, the 2-D carbonaceous material, graphene, was selected as the interlayer matrix. The CVD-produced graphene foam was modified by a thin layer of ZnO using the ALD method. This approach endows the graphene foam with a polarized surface and minimizes the mass addition at the same time. The results from the GF-based interlayers confirm their effectiveness in serving as an electron high-way and entrapping the dissolved polysulfides. The GF/GF@ZnO interlayer shows the best amelioration for Li-S batteries, with an initial specific capacity of  $1051 \text{ mAh g}^{-1}$  and a reversible capacity of  $672 \text{ mAh g}^{-1}$  at  $0.5 \text{ C}$  for 100 cycles. Remarkably, the mass addition of this interlayer on the total cathode is less than  $5 \text{ wt. \%}$ .

To explore a more facile method to modify the graphene foam, the conductive  $Ti_3C_2T_x$  (MXene)

was used to replace the ZnO. This highly conductive 2-D material with the polarized surface not only enhances the polysulfide attraction but also ameliorates the electronic conductivity. Meanwhile, the GF serves as the light-weight framework for the MXene, greatly reducing the density and increasing the specific surface area of the composite. As a result, Li-S batteries with this free-standing light-weight interlayer delivers a capacity of 868 mAh g<sup>-1</sup> with a retention of 89.0 % after 120 cycles at 0.2 C.

In Chapter 6, with a research objective to make a cathode with higher sulfur loading, a Ni, N-doped carbon nanosheets modified N-doped Ti<sub>3</sub>C<sub>2</sub>T<sub>x</sub> (MXene) nanosheets (N-M@CN) as the separator coating material was fabricated by simply annealing the mixture of dicyandiamide, Ni salt, glucose, and MXene. During the annealing, the dicyandiamide absorbed on the MXene surface through electrostatic attraction became the nitrogen source of the N-doping, producing the N-doped MXene. The N-doping of carbon nanosheets can increase the specific area of the composite, which also provides better LiPS absorption and conductivity than the pristine sp<sup>2</sup> bonding carbon structure. The Ni nano-particles can provide catalysis for the polysulfide. Owing to these synergistic effects, the separator decorated by the N-M@CN shows outstanding characteristics on the Li-S batteries, including a high reversible capacity (~1300 mAh g<sup>-1</sup> at 0.2 C), an extended cycling stability (588 mAh g<sup>-1</sup> at 1 C after 500 cycles, with a capacity decay rate of 0.069 % per cycle), and an encouraging capacity from a high sulfur loading cathode of 3.18 mg cm<sup>-2</sup> (662 mAh g<sup>-1</sup> at 0.2 C after 100 cycles).

With the advancement of the interlayer in Li-S batteries, many pronounced achievements have been realized through structure tailoring and material designing. An excellent interlayer to be applied in practical Li-S batteries should be able to facilitate the capacity performance, cycling stability, energy density, and kinetics at high-rates. Therefore, some critical pending issues need to be solved before the practical applications: (I) the fabrication of the interlayer material should be facile and scalable, being feasible for industrial applications; (II) the material should have some essential intrinsic features to meet the requirements, including high electronic conductivity, necessary porosity, and the ability to absorb and catalysis the polysulfide. Therefore, the material needs to be rationally selected and modified for the interlayer; (III) most of the interlayer studies lately used coin cells as the testing system to evaluate the effect on the cathode. But the case of the coin cell has some crucial differences with the one in pouch cell, which is related to the magnified electrode area and active material mass. Thus, it is necessary to test the practical performance of interlayer in the pouch cell; (IV) the safety issue of the interlayer is also an inevitable concern for its application, as the conductive coating layer on the separator may ascend the

risk of short-circuit. Nevertheless, all the interlayers reported in this thesis have achieved high electrochemical performance (e.g. high capacity and cycling stability etc.). This work might bring a novel idea and facile method to develop MXene/graphene-based materials as promising interlayer materials for future practical Li-S batteries.